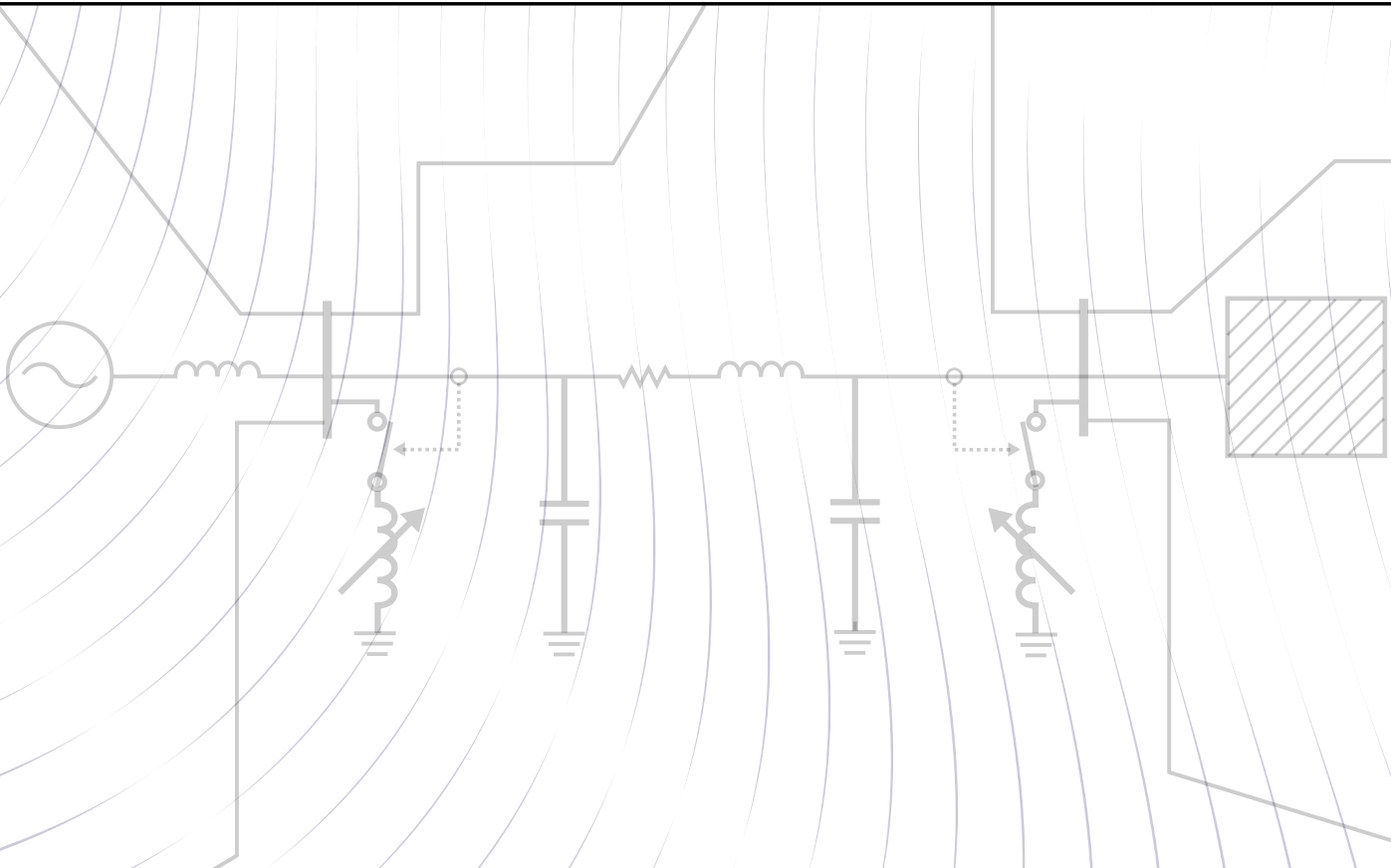

Power system stability analysis of cable based HVAC transmission grids with reactive power compensation



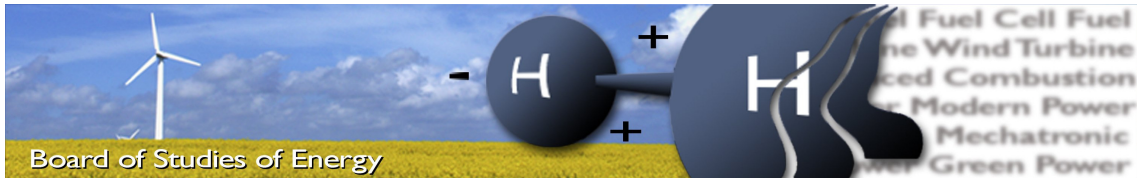
Master thesis by

Foo Yi Wern
&

Laurids Martedal Bergholdt Dall

June 2016





Title: Power system stability analysis of cable based HVAC transmission grids with reactive power compensation

Semester / theme: 10th semester / Master thesis

Project period: 1.2.2016 to 1.6.2016

ECTS: 30

Supervisor: Filipe Miguel Faria da Silva

Project group: EPSH4-1031

Yi Wern Foo

Laurids Martedal Bergholdt Dall

Copies: 4
Pages, total: 189
Appendix: 10
Supplements: 1 CD

SYNOPSIS:

This thesis presents a study of the electromechanical dynamics associated with the implementation of long HVAC cables in power transmission. Transient stability and large-disturbance voltage stability of generic multi-machine power systems is assessed by RMS simulations in Digsilent PowerFactory. The stability performance of the OHL base case system is compared against an equivalent cable system. Results show that the 100 % compensated equivalent cable system has longer CCT than the OHL base system in most cases. Increasing the SR compensation degree may improve the CCT, while voltage stability analysis show that under-compensation improve the V, P load-ability. The cable system displays larger P_{max} than the OHL base system. An advantage of the cable system is the availability of switch-able SRs. By decreasing X_{SR} during a large disturbance, the capacitive current generated by the cables is injected into the network to impose a voltage. Case studies show that SR-switching can improve system voltages. A smooth voltage recovery is achieved by sequentially switching the buses measuring the lowest voltages. Further work is required in order to generalize and quantify the properties of SR-switching.

By signing this document, each member of the group confirms that all group members have participated in the project work, and thereby all members are collectively liable for the contents of the report. Furthermore, all group members confirm that the report does not include plagiarism.

Preface

This thesis is written by group EPSH4-1031, during the 4th and final semester of the 'Electrical Power Systems and High Voltage Engineering' programme at Aalborg University. The work presented has been carried out from the 1st of February to the 1st of June 2016.

We would like to direct a special thank you to our supervisor, Filipe Faria da Silva for guidance, comments and weekly meetings throughout the project period.

Reading Guide

This thesis is divided in eight chapters and ten appendices, containing references, illustrations, tables and equations. The literature references are referred to according to the IEEE citation style, numbered in the order of appearance. The bibliography is located at the end of the report, containing further information about the source. Books are listed with author, year, title, edition and publisher; Websites are listed with author, title, date and URL. Figures, tables and equation will be referred to by a chapter and a number [chapter, number], including a word or an abbreviation indicating what is being referred to. The words/abbreviation are Figure for illustrations and Table for tables. If no reference is given on a figure it means that the figure was created by the project group.

Software

The following software has been used during the project:

- DigSILENT PowerFactory version 15.1.6
- LaTeX is used to write the report.
- Matlab is used for coding scripts and plotting.

Abstract

Danish TSO Energinet.dk is in the process of undergrounding parts of the AC transmission grid in Denmark. Undergrounding involves the replacement of conventional overhead line (OHL) transmission with underground cables. The electrical behaviour of a HVAC cable is substantially different to that of an equivalent OHL. The most significant difference is the capacitance, where cables display values typically 10-20 times greater than OHL.

The focus of this thesis is to study the electromechanical dynamics associated with the implementation of long HVAC cables in the power transmission network. The main objective is to assess and study the transient stability and large-disturbance voltage stability of generic multi-machine power systems.

This is accomplished by simulating large-disturbance electromechanical transients in DIgSILENT PowerFactory. The analysis is initiated on a simple single-machine infinite bus system, and is expanded to the IEEE 9-bus and 39-bus multi-machine power systems. The stability performance of the OHL base case system is compared against an equivalent cable system.

Transient stability studies are performed with variations to fault locations, and critical clearing time (CCT) is chosen as stability index. For voltage stability assessment both steady state analysis of V, P and Q, V -characteristics and RMS simulation based voltage trajectory analysis are performed.

Comparison of the transient stability performance in both SMIB and multi-machine systems show that the equivalent cable system with 100 % compensation has consistently longer CCT than the OHL base system, provided that the corresponding shunt reactors (SR) of the faulted line are disconnected when the line is taken out of service.

Increasing the SR compensation degree has an improving effect on the CCT. This was tested up to 115 %, and is a confirmation of the findings in the state of the art. However, this result is not explicitly conclusive for every aspect of power system stability. In contradiction the voltage stability analysis show that under-compensation of cables improve the V, P load-ability of the network. Being under-compensated, the cables supply reactive power to line inductance, inductive loads and transformers locally. Hence the optimal compensation degree is concluded to be a balance of both synchronous generator excitation level and the ability to supply reactive power locally in the network.

The V, P -characteristics in both 9-bus system and 39-bus system show that the 100 % compensated equivalent cable system display higher steady state load-ability than the OHL base system. This result is in line with the overall CCT observations, and is ascribed to the L and R difference. Similarly Q, V -curves of the equivalent cable systems prove to be slightly steeper, indicating lower voltage sensitivity to changes in reactive power flow.

The bus voltages following large-disturbances are evaluated against an under-voltage limit.

An advantage of the cable based system is the presence of SRs. The cable based system is equipped with a significant amount of local reactive power support, by assuming that SRs can be switched in and out of service as fast as necessary. By decreasing the shunt reactance during an electromechanical transient, the large amount of capacitive current generated by the cables is injected into the network inductance and thereby imposing a voltage.

It is shown for various cases that SR-switching can improve voltage trajectories to satisfy the under-voltage limit. This ability is unavailable in the OHL base system, where compensation for steady-state operation is unnecessary.

It is concluded that the SR-switching should be performed progressively to reduce the risk of transient over-voltages. A smooth voltage recovery can be achieved by sequentially switching the buses measuring the lowest voltages. The overall system improvement should be considered and not limited to the lowest voltage buses. The amount of SR-switching necessary could be based on the magnitude of the post-disturbed voltage and dQ/dV -sensitivities of the network. Further work is required in order to generalize and quantify the properties of SR-switching.

Furthermore, it is shown how SR-switching may reduce the need of dynamic voltage regulation in the form of FACTS. By performing SR-switching the necessary capacity of STATCOMs may be significantly reduced or completely substituted.

Table of contents

Chapter 1 Introduction	1
1.1 Background	1
1.2 Types of power system stability	6
1.3 Principles of transient stability	8
1.4 Principles of voltage stability	14
1.5 Transmission lines in power system stability studies	20
1.6 State of the art review	25
Chapter 2 Problem statement and methodology	35
2.1 Problem statement	35
2.2 Delimitations	36
2.3 Methodology	37
Chapter 3 Stability analysis of single-machine infinite bus system	39
3.1 Single-machine infinite bus system	39
3.2 Introducing the DIGSILENT PowerFactory SMIB system	41
3.3 Sensitivity study of line parameters on the SMIB system	44
3.4 Comparison of OHL and cable transmission lines in the SMIB system	54
Chapter 4 Transient stability analysis	59
4.1 Introduction	59
4.2 IEEE 9-bus transient stability analysis	61
4.3 IEEE 39-bus transient stability analysis	68
4.4 Transient stability summary	74
Chapter 5 Large-disturbance voltage stability analysis: IEEE 9-bus system	77
5.1 Load modelling in voltage stability analysis	77
5.2 Q,V-characteristics of load buses in the IEEE 9-bus system	79
5.3 Voltage stability of Bus 8 in the IEEE 9-bus system	81
5.4 Discussion of reactive power capability limits in the IEEE 9-bus system	83
5.5 Voltage trajectory analysis of Bus 8 in the IEEE 9-bus system	86
5.6 Forcing voltage instability in the IEEE 9-bus system	90
5.7 Summary of voltage stability analysis in the IEEE 9-bus system	100
Chapter 6 Large-disturbance voltage stability analysis: IEEE 39-bus system	103
6.1 Identification and characterization of weak areas in the IEEE 39-bus system	104
6.2 V,P-characteristics of areas in the IEEE 39-bus system	107
6.3 Q,V-characteristics of areas in the IEEE 39-bus system	109
6.4 Large-disturbance case studies in the IEEE 39-bus system	111
6.5 Summary of voltage stability analysis in the IEEE 39-bus system	126

Chapter 7 Discussion of results	129
7.1 Comparison of results with published research	129
7.2 Discussion of methodology and validity of results	131
7.3 Future work	133
Chapter 8 Conclusion	135
Bibliography	137
Appendix A Accounting for capacitance in SMIB systems	141
Appendix B Basic voltage regulation and reactive power control of synchronous generators	147
B.1 Control of active and reactive power	147
B.2 Automatic voltage regulator	151
B.3 Excitation system influence on power system stability	152
B.4 Influence of governors and power system stabilizers compared to AVR . . .	154
Appendix C Modelling parameters in 9-bus and 39-bus systems	157
C.1 9-bus system	157
C.2 39-bus system	159
Appendix D DIgSILENT Programming Language used in studies	163
Appendix E Pole-slip function in PowerFactory	167
Appendix F PowerFactory simulation results for 9-bus and 39-bus system	171
Appendix G Simple model of a generic STATCOM in DIgSILENT PowerFactory	179
G.1 Modifications to the generic model	180
Appendix H Additional case studies of SR-switching and STATCOM	183
Appendix I Utilizing Q,V-characteristics for SR-switching	185
Appendix J CD content	189

List of symbols

Table 1. List of symbols used in this report - Part 1.

Symbol	Unit	Name
C	[F]	Capacitance
d	[m]	Distance
e	[-]	Exponent coefficient
E	[V]	Voltage
F	[-]	Factor
G	[S]	Conductance
H	[MWs/MVA]	Inertia constant
I	[A]	Current
J	[kg · m ²]	Mechanical inertia
K	[-]	Gain
k	[-]	Coefficient
l	[m]	Length
L	[H]	Inductance
n	[-]	Number of
P	[W]	Active Power
Q	[var]	Reactive power
p, q	[-]	Coefficients
R	[Ω]	Resistance
S	[VA]	Apparent power
T	[N · m]	Torque
T	[s]	Time constant
t	[s]	Time
V	[V]	voltage
X	[Ω]	Reactance
x	[-]	State variable
Z	[Ω]	Impedance
z	[m]	Distance

When a symbol has a subscript, the text is used to refer to a specific value, function or component, for example x_l may refer to the line reactance.

Table 2. List of symbols used in this report - Part 2.

Symbol	Unit	Name
β	[rad/m]	Phase constant
δ	[deg]	Power angle
Γ	[-]	Coefficient
λ	[m]	Wavelength
ω	[rad/s]	Rotational speed
ω	[rad/s]	Electrical Frequency
θ	[deg]	Power factor angle

When a symbol has a subscript, the text is used to refer to a specific value, function or component, for example ω_s may refer to the synchronous speed.

Table 3. List of abbreviations used in this report.

Abbreviation	Name
AC	Alternating Current
AVR	Automatic Voltage Regulator
CCT	Critical Clearing Time
DFIG	Doubly Fed Induction Generator
DPL	DIgSILENT Programming Language
FACTS	Flexible AC Transmission Systems
HVAC	High Voltage Alternating Current
HVDC	High Voltage Direct Current
OEL	Over-Excitation Limiter
OHL	Overhead Line
OLTC	On Load Tap Changer
PF	Power Factor
PSS	Power System Stabilizer
PV	Photovoltaic
SG	Synchronous Generator
SI	Surge Impedance
SIL	Surge Impedance Load
SMIB	Single-Machine Infinite Bus
SR	Shunt Reactor
STATCOM	Static Compensator
SVC	Static Var Compensator
TL	Transmission Line
TSO	Transmission System Operator
VSC	Voltage Source Converter

Introduction

1

The focus of this thesis is to investigate the electromechanical dynamics associated with the implementation of long HVAC cables in the power transmission network. More specifically multi-machine power systems with various line parameters are to be analysed with respect to transient and voltage stability. A special emphasis is directed towards the issue of reactive power compensation, and its significance in a cable based power system.

The following chapter introduces the basic concepts concerning power system stability, while describing the background of the project. The terms transient stability and voltage stability are discussed and defined according to relevant IEEE and CIGRE recommendations to specify the terminology according to the project goals. The main differences on overhead line (OHL) and cable based networks are briefly discussed, with focus on the important characteristics in stability studies. Finally, the most recent research in stability studies with HVAC cable power systems is discussed and the initiating problem is described.

1.1 Background

Power system stability is a mature and well researched branch of power system analysis. Mathematical models and tools for stability analysis have been developed since the early 1920s, where the first instability issues in AC power systems were experienced [1]. Accurate stability studies demand thorough dynamic modelling of power system components, with particular emphasis on the differential equations describing the electromechanical dynamics of the electrical machinery. The dynamic models for the most traditional power system components and their application are well described by the author of [2], and is widely recognized as the state of the art for power system stability studies.

Power system stability is an extensive technical term, involving every aspect of power generation, transmission and distribution. Thus, assessing the stability of a given power system can turn out to be a cumbersome and complex task. In year 2004 the authors of [3] published the efforts of a combined IEEE and CIGRE taskforce with the objectives of defining and classifying various power system stability topics and categorizing power system instability phenomena. Furthermore the authors of [3] highlight the realisation that complete mathematical modelling of power system stability is generally unachieved, especially for large systems. Typically what is referred to as *partial stability* analysis is applied in studies of transient and voltage stability [3]. Here the focus is on the behaviour of a subset of variables, while the remaining system states may be ignored for simplicity. Thus, when analysing power system stability, simplifications are generally favourable. As a result, careful attention should be paid towards the absence of unmodelled interactions of the power system environment.

Examples could be unmodelled electrical machinery dynamics and controls, protection topologies and variations of line switching, altering the system topology.

Instability of the power system can in the most severe cases result in a total system collapse leading to what is often referred to as a *blackout*. Fortunately blackouts are rare, but historically they do occur, even as stability-improvement methods have been continuously developed and implemented. On the 14th of August 2003 the United States and Canada experienced a blackout in the north-eastern part of North America. A task force was formed in order to investigate the causes of the blackout and to elaborate future preventive methods. However, the answer to the cause of the system collapse turned out not to be a simple one, as stated by the task force in [4]. Largely the initial cause is described as a failure of both equipment and human action in control center of a local energy company, when three 345-kV and one 138-kV transmission lines started tripping due to transient currents related to line faults caused by partial discharges to the nearby vegetation. The following undetected overloading of several transmission lines, combined with an already voltage depressed power system due to inadequate reactive power supply, caused an cascading outage throughout the region. The aftermath of the 2003 blackout was a wake-up call resulting in government enforced regulations and an extensive use of the terminologies: power system reliability and security.

For scientists and engineers working in the field of power system stability, the terms reliability and security may seem redundant in the presence of the technical stability definitions. However, the authors of [3] describe power system reliability as "the ability to supply adequate electric service on a nearly continuous basis, with few interruptions over an extended time period" and power system security as "the degree of risk the power systems ability to survive imminent disturbances (contingencies) without interruption of customer service". Evidently these formulations are easily confused with the classical definition of power system stability: "The continuance of intact operation following a disturbance", but the members of the joint IEEE and CIGRE task force seek to distinguish between the terminologies. Power system contingencies involving explosive cable failures, fall of transmission towers or sabotage, are recognized as reliability issues, while security issues are defined as the resulting consequences of power system instability. However, the system wide behaviour following a disturbance, regardless of the cause or terminology used, is dependant of the electromechanical behaviour of the power system and the classical electrical engineering definitions. Thus, the subject of power system stability is treated in the classical term throughout this thesis, and the terms reliability and security are not applied.

Although stability is a mature topic in power systems, on both theoretical and practically applied level, it is a topic which demands continuous attention. The power system is changing, and now possibly faster than ever. On a global level the amount of renewable power capacity is increasing, and throughout year 2014 renewables made up 58.5 % of the globally installed capacity that year. Thus, reaching a total capacity figure of 1.712 GW by the end of year 2014, corresponding to 22.8 % of the global electricity demand [5]. Renewable resources such as wind and solar imply a fluctuating and uncontrollable nature of power supply, consequently demanding extra focus on the constant balancing of generation and load, and increasing the complexity of power system control.

Furthermore, the implementation of renewables has influenced the transient stability limits of the power system. According to the authors of [6], the influence of a high penetration of doubly-fed induction generators (DFIG) can have an either beneficial or destructive impact on power system stability. The impact of wind power penetration is largely dependant on the DFIG insertion point in the grid and the location of disturbances. An increasing problem is the loss of mechanical inertia utilized in maintaining synchronism, and delivering short-circuit power during large disturbances. On the other hand, the increased penetration of DFIG can result in an indirect dampening effect of the power system oscillations associated with instabilities, due to the reduction in synchronous generators (SG) participating. However, with the wind penetration numbers reaching as high as 42.1 % [7], the impact of wind power on stability limits is arguably mainly negative. Similarly, the impacts of high photovoltaic (PV) penetration is investigated in [8]. The results indicate that power systems with high PV penetration levels (20 % to 50 %), suffer from large bus voltage dips during transients, indicating the need for dynamic reactive power compensation in order to mitigate possible voltage collapses.

In order to distribute the large amount of fluctuating power produced from renewables, some countries are expanding their transmission systems by investing in interconnections across country borders. One of the benefits of such interconnections is the ability to utilize regional unbalances in generation and load, and by cross country transmission and distribution, limit local bottlenecks. Danish TSO Energinet.dk is participating in the preparations of two new high-voltage direct current (HVDC) connections in the North Sea. The COBRACable (700 MW), which is expected to connect Denmark and Holland by 2019 [9] and the Viking Link (1.4 GW), connecting Denmark and England by 2022 [10]. Furthermore, Energinet.dk is cooperating with TenneT in Germany on expanding the existing 1.5 GW HVAC connection crossing the Denmark-Germany border to 2.5 GW by 2020 [11]. Finally, near the construction of the 600 MW Kriegers Flak offshore wind farm, is the establishment of a 400 MW HVDC connection between East Denmark and Germany by 2018 [12].

The increasing interconnection of power systems, on both national and international level, is influencing the stability limits of the system significantly. Expansion of the power system, by the addition of transmission lines, improves the power system's ability to remain stable following contingencies, such as the loss of generation or transmission lines. As power can be transmitted between generation and load without violation of stability limits. The authors of [13] investigate how issues with uncontrollable cascading effects of large interconnected power systems can be mitigated by the implementation of HVDC connections with voltage-source converters, such as the ones being installed in Denmark. It is found that HVDC connections acts as blocking of power angle oscillations related to transient stability, and provides voltage stability improvement by reactive power control. Thus, interconnecting by HVDC-VSC is expected to have an improving effect on power system stability.

Another major topological change of the danish power system, is the ongoing undergrounding of the high voltage AC grid, as published by Energinet.dk in [14] and [15]. In the grid development plan it is stated that it has been politically decided, to replace a big part of the overhead lines in the transmission network with underground transmission cables. The main motivation is to improve the aesthetic look of the danish landscape. Traditionally the majority of power system transmission lines are OHL, and a CIGRE study [16] show that underground cables are mainly represented in 50 kV to 109 kV distribution networks. Figure 1.1 shows a map of the future Danish high voltage power system. The 132 kV to 150 kV overhead lines (OHL) are to be fully replaced by HVAC cables, while the 400 kV lines are to be partially replaced by cables.

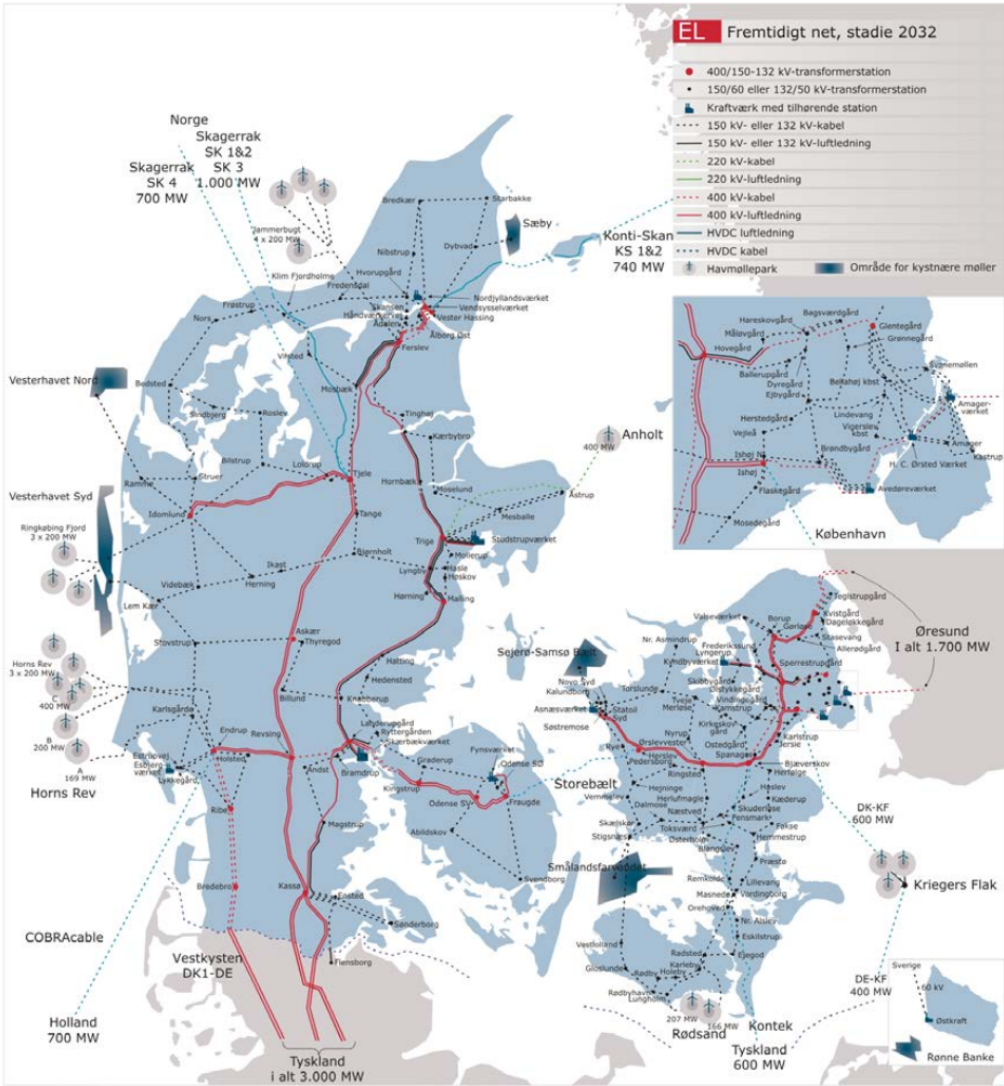


Figure 1.1. Future Danish power system anno 2032 according to Energinet.dk grid development plans, showing the 150 kV to 400 kV system [14]. The plan does not display the Viking Link.

The electrical behaviour of a HVAC cable is substantially different to that of an equivalent OHL. The most significant difference is the capacitance, where cables display values typically 10-20 times greater than OHL [17]. As a result the HVAC cables generally inject a substantial amount of capacitive current, whereas OHLs mainly draw inductive current. Consequently, the change from OHL to cable-based power transmission imply a drastic change of reactive power flow of the system. Historically, transmission line susceptance has been ignored for short line modelling (lengths shorter than 80 km), due to negligible capacitance [2]. However, for cable modelling such practice is erroneous for any given length. As voltage levels are increased (400 kV and higher) for both OHL and cables, the reactive power generated by even small values of capacitance and line lengths is considerable. This is due to the V^2 proportionality. In order to avoid over-voltages during steady state operation HVAC cables must be compensated by the connection of inductive shunt reactors, whereas OHLs are compensated by series capacitors if necessary. However, the implementation of HVAC transmission cables does not only affect the steady state performance of the system. The nature of electromagnetic transients in power transmission cables is analysed and discussed by the authors of [18], explaining how the physical characteristics of cables alter line parameters and effectively influence switching phenomena, travelling waves and more.

Being established, that the topologically fundamental change from OHL to cables in the HVAC power system, has a significant influence on multiple aspects of the power system as a whole, it becomes relevant to consider the impact on power system stability. As described in [2] transmission network topology influence both transient stability and voltage stability. The transient stability limits are altered as equivalent network impedances influence the non-linear power-angle relationship of the interacting electrical machinery. An influence which is present in both pre-disturbance, disturbance and post-disturbance conditions. The large-disturbance voltage stability is mainly an issue addressing the balance of reactive power at local system weak-points during and following major disturbances, such as line faults and switching. Thus, it is impending to believe that there exist one or more voltage stability related consequences, following the change from OHL to cable based transmission.

Undergoing any major system restructuring, such as the one described by Energinet.dk in [14], it seems vital to consider a reevaluation of the power system stability. However, a problem appear to be the lack of available research and guidelines on the topic of HVAC cables in power system stability studies. Some publications address the issue, such as [19] [20] [21] [22]. These studies are discussed in further detail in Section 1.6.1. A quick review reveal that the few studies published are very different in their use of stability terminology and methodology towards the topic of HVAC cables in stability analysis. The study presented in [19] is limited to a simple single-machine infinite bus (SMIB) with focus on transient stability. The research in [20] treat small-signal voltage stability in the case of a specific island grid in Taiwan. While [21] address power system stability in the context of undergrounding of a part of the Dutch HV network, more similar to the Danish case. And finally [22] investigates the idea of utilizing a mixed OHL and cable system for mutual reactive power compensation.

Due to the sparsity in available literature, and motivated by the Danish grid development plans, this thesis seek to investigate both transient and voltage stability limits for multimachine power systems with cable based HVAC transmission. In the case that instability issues are discovered, the aim is to discuss and point towards possible solutions.

The focus in this thesis, is the use of power system simulation software and generic power system models, to explore the stability during large disturbances. While the results are to be discussed on the basis of the theoretical principles, a detailed mathematical study of the stability phenomena is not the objective. Instead, parametric sensitivity studies are performed in order to provide understanding and highlight the key issues of assessing stability of power transmission networks with HVAC cables.

In summary the question to be answered is: How does undergrounding of the HVAC power system affect power system stability limits, and how should reactive power compensation be utilized to improve the stability?

1.2 Types of power system stability

Power system stability is a major issue of concern for continuous system operations. However it comes in many forms and cannot be treated as a single whole entity. Therefore it is important to identify and define the various instabilities and their respective dynamic behaviour in a system for assessment purposes.

The type of dynamic behaviour can be classified according to its response time. Electromagnetic transients are the fastest transients which occur in the time range of μs and are related to events such as switching surges and lightning propagation [23]. In contrast, electromechanical transients are slower transients which can be detected in the time span of 3-10 s and up to a few minutes. The project focuses only on the issues regarding electromechanical dynamics namely transient stability and voltage stability. The theory and principle behind each of these stabilities are further expanded in Sections 1.3 and 1.4. The classification of electromechanical stability in power system is shown in Figure 1.2.

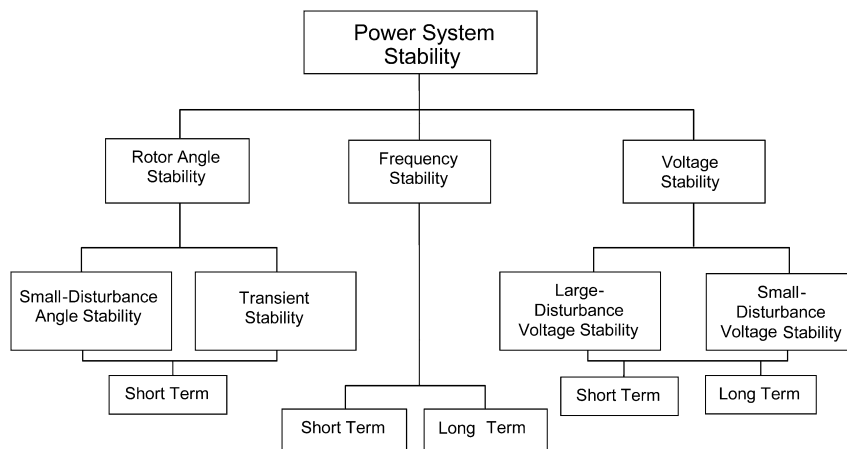


Figure 1.2. Classification of electromechanical power system stability topics [3].

1.2.1 Transient stability and voltage stability

As can be seen from Figure 1.2, transient stability is a subform of rotor angle stability. In synchronous generators terminology, rotor angle could also be referred to as power angle and load angle whereby the terms are inter-changable. For standardization purposes, the term power angle will be used from here onwards in the project. According to CIGRE and IEEE, transient stability is defined as the "*ability of the power system to maintain synchronism when subjected to a severe disturbance* [3]." Examples of large disturbances are fault on transmission line and loss of generating units.

Transient instability of a synchronous generator involves a deviation of its power angle beyond the critical value which causes loss of synchronism. The duration of transient could vary from three to five seconds up to 10 seconds depending on different factors [2]. It is practised by authors in [24] to carry out simulations up to 10 seconds after the disturbance in order to verify unstable cases.

Figure 1.3 depicts the time response of the power angle following a disturbance. Case 1 represents the instantaneous form of instability and is commonly called first-swing instability where the power angle is increased continuously beyond its critical value. As for large power systems, instability may not be from the first swing but as a consequence of cascading interarea oscillations between groups of machines as shown in Case 2 [2].

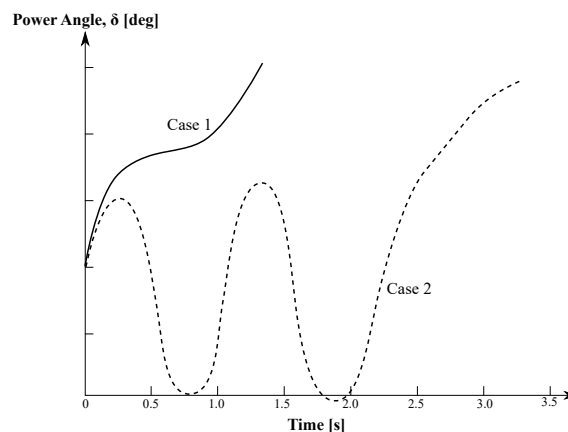


Figure 1.3. Power angle response to a disturbance.

Voltage stability is the "*ability to maintain steady voltages at all buses in the system after being subjected to a disturbance* [3]." It is also categorised according to the severity of the disturbance to the power system. Small signal voltage stability is analysed when the system experiences small perturbations. In this thesis, voltage stability refers to the large disturbance voltage stability during which the power system is subjected to disturbances of similar severity as transient stability.

It is common that angle stability and voltage stability do not present the effects individually. Instead, often instability in one would greatly affect the other due to strong coupling between them following large disturbances [3]. Though it may be hard to distinguish between the two, it is important to identify the underlying causes of the problem for precise protective operations. The basis of distinction lies in the variable which is more evident in the instability [3].

1.3 Principles of transient stability

This section illustrates the dynamic response of a synchronous machine in a system when subjected to a disturbance and provides an elementary view on transient stability. The topic related to multi-machine systems will also be briefly discussed.

1.3.1 Single machine infinite bus system

The study of transient stability of a system begins with a simple base model as shown in Figure 1.4. This model is well known as single machine infinite bus (SMIB) system, which is used to illustrate the power angle response in stability studies [2]. The SMIB system is made up of a generator connected to an infinite bus through a transmission network comprised of two lines. The infinite bus is an ideal voltage source with constant voltage and frequency under all conditions behind a reactance.

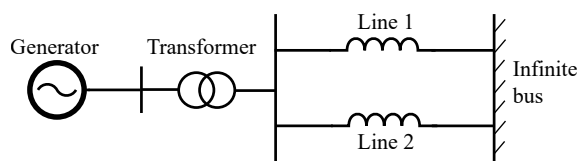


Figure 1.4. Single-line diagram of a SMIB system.

The schematic representation of the model is shown in Figure 1.5(a). The system is assumed lossless without any resistive element. The infinite bus is modelled as an ideal voltage source E_B , and is the voltage reference with zero angle. X_{tr} represents the transformer reactance while X_1 and X_2 are the respective line reactances. The generator modelling is based on the classical representation of a synchronous machine as presented in [25]. It is represented by a constant internal voltage source, E_g behind the stator reactance, X_d and the terminal voltage is denoted by V_T . Power angle δ is the angular difference between the internal voltage and infinite bus voltage. This is a simplified transient model in stability studies as described in [2].

Finally, the equivalent circuit could be simplified as shown in Figure 1.5(b). Terminal voltage, V_T is eliminated and X_T is the only reactance term of the final circuit summing the reactance by all the elements between the two sources.

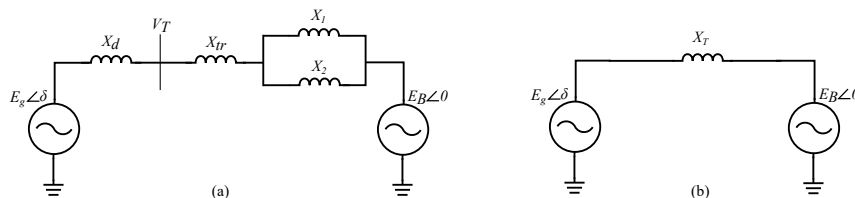


Figure 1.5. (a) Single-line diagram of SMIB. (b) Final equivalent circuit.

The electrical power delivered from the generator to the infinite bus according to the equivalent circuit in Figure 1.5(b) can be modelled using equation (1.1).

$$P_e = \frac{E_g E_B}{X_T} \sin \delta \quad (1.1)$$

Under steady state operation, the electrical power output is balanced by the mechanical power input to the generator. This forms a set of opposing forces acting on the rotating shaft of the generator as shown in Figure 1.6. The input mechanical torque T_m is the driving force, whereas electrical torque T_e is the retarding force of the rotation [26]. ω is the speed of the shaft and is in the same direction as mechanical torque T_m . The input mechanical power is the product of mechanical torque T_m , and speed ω .

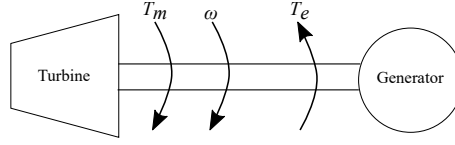


Figure 1.6. Mechanical and electrical torque on the shaft.

The governing equation for the rotor motion with respect to the set of forces is given by the *swing equation*, which may be written as in (1.2) [2].

$$\frac{2H}{\omega_0} \frac{d^2\delta}{dt^2} = P_m - P_e \quad (1.2)$$

Where input mechanical power P_m , and output electrical power P_e , are in per-unit (p.u.), H is the inertia constant of the rotating mass in MWs/MVA and ω_0 is the synchronous speed.

Equation (1.2) is derived based on the resultant torque acting on the rotating mass as a result of any imbalance in mechanical and electrical torques. The assumption made is that the angular speed remains constant. The left hand side has a second derivative of the power angle with respect to time and basically the acceleration or deceleration of the rotor due to kinetic energy gained or expended by the rotating mass in the event of a disturbance.

Transient response to a disturbance

The initial condition of the system is considered to be under steady state operation. Hence, the initial mechanical power, P_{m0} is equal to the electrical output, P_e at point A with a power angle value of δ_0 as shown in Figure 1.7(a). The curve of P_e is determined by the power-angle relationship established in (1.1).

To study the dynamics of the system, it is subjected to a sudden increase in mechanical power from P_{m0} to P_{m1} . The new equilibrium point B corresponds to a new power angle position, δ_1 . However the power angle can not change immediately owing to the inertia of the rotor. This results in an imbalance between the mechanical power and electrical power, and the resultant power is known as accelerating power [2]. This accelerating power forces the rotor to accelerate, and therefore the power angle increase from point A to point B along the P_e curve.

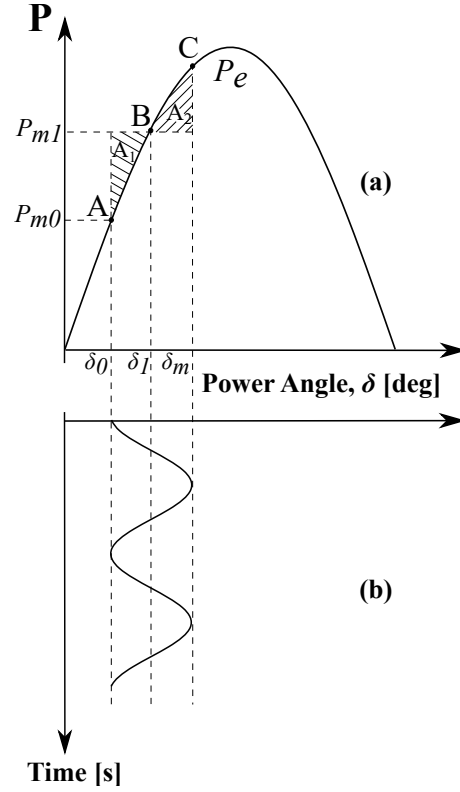


Figure 1.7. Transient response to a disturbance.

At the time instant when the power angle reaches point B, the rotor speed is higher than the synchronous speed, ω_0 , therefore the power angle continues to increase. P_e is greater than P_{m1} beyond point B and the imbalance produces a decelerating power to the rotor. While the rotor decelerates, the power angle increases until a maximum angle of δ_m at point C is reached, where the rotor speed returns back to ω_0 . However, there still exists an imbalance between P_e and P_{m1} at point C, hence the rotor speed continues to decrease. The operating point traces along the P_e curve back to point B and subsequently to point A again. This process would continue indefinitely, and the power angle would oscillate about the new equilibrium angle point, δ_1 as can be seen in Figure 1.7(b). This is because all the resistive elements are neglected in the system modelling, and therefore no damping effects are considered.

Equal area criterion

The stability of the SMIB system could also be processed graphically by using the power angle diagram in Figure 1.7. This method utilises the energy function of the acceleration and deceleration with respect to angle to determine if the system is stable. Basically, when the rotor experiences a resultant accelerating power it gains kinetic energy, as the power angle increases from δ_0 to δ_1 . The kinetic energy accumulated by the rotor is highlighted by area A_1 . On the other hand, kinetic energy is lost to the system during deceleration, when power angle changes from δ_1 to δ_m . A_2 shows the area which represents the total lost energy during deceleration.

For the system to be stable, these two areas have to be at least equal or A_1 smaller than A_2 . If A_1 is greater than A_2 , the system would experience instability as there is insufficient synchronizing torque to stop the increase of the rotor angle and the consequence is loss of synchronism. If A_1 is equal to A_2 the system is at its stability limit and δ_m is the maximum allowed excursion of δ before instability. The stability criterion is named the equal area criterion. The mathematical approach used in the criterion is given by (1.3) which can be deduced from equation (1.2) [2].

$$\int_{\delta_0}^{\delta_m} (P_m - P_e) d\delta = 0 \quad (1.3)$$

This method presents an alternative to finding the transient stability limit without having to solve (1.2) using analytical and numerical methods. Though it requires some modification to be applied to multimachine systems as proposed in [27], it is sufficient for providing an overview on the influence of elements on transient stability of any system [2].

Critical clearing time (CCT)

Critical clearing time (CCT) is a common stability index used for assessing the transient stability of a system. It can be defined as the maximum time after fault occurrence at which the fault needs to be cleared without resulting in power angle instability [19]. This is an important parameter for designing protection systems. As the accuracy of this index is vital to the system operation coupled with the need to shorten computing time, extensive research efforts are continuously carried out in this topic [28, 29, 30].

To illustrate the CCT for the SMIB system in Figure 1.5 using the equal area criterion, a short-circuit fault condition is introduced to the system. Short-circuit on the transmission line is one of the most common large-disturbances for transient stability analysis. The considered fault is a three-phase ideal fault located at Line 2, some distance away from the generator side marked by F in Figure 1.8(a). The equivalent schematic of the faulted circuit is shown in Figure 1.8(b).

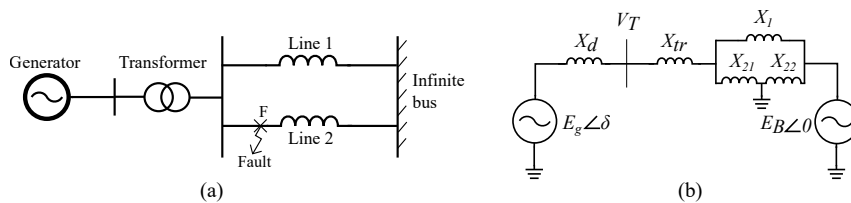


Figure 1.8. Graphical representation and schematic of faulted system.

Figure 1.9 shows the power-angle graphical diagram with multiple P_e curves under different network conditions. The pre-fault curve represents power delivered by the generator P_e , before the fault using (1.1). During fault, the active power delivered will be much less as compared to before fault. This is because most of the short circuit current will be flowing through inductive reactance to the fault, which causes a reduction in the active power flow to the infinite bus. The power flow is greatly affected by the location of the fault with respect to the sending end busbar. The closer the fault is to the busbar, the lesser the active power transfer. An arbitrary curve is chosen to represent P_e during fault.

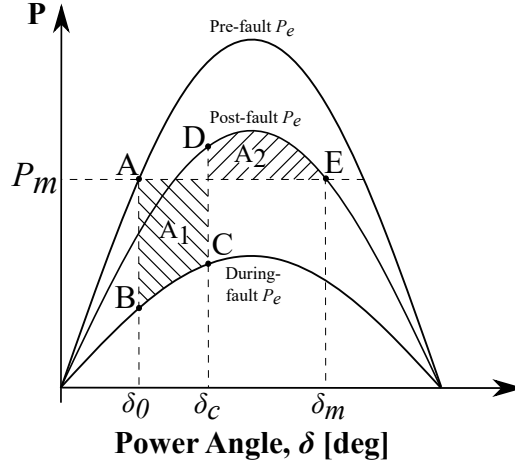


Figure 1.9. Power-angle representation of system transient with fault.

When the line fault is of permanent nature, the fault has to be cleared by operating the circuit breakers at both ends of the line. As a result, a larger current would flow through Line 1 increasing in active power transfer. However the post-fault P_e curve is still lower than the pre-fault curve. This is because with Line 2 out of service, the equivalent reactance X_T of the system is larger, and P_e is lowered according to 1.1. In contrast, a temporary fault without any line disconnection would produce the same post-fault P_e curve as the pre-fault curve. The input mechanical power, P_m remains constant throughout the entire period.

The initial operating point of the system is at point A in Figure 1.9, where the system is assumed to be in steady state. The power angle, δ corresponding to this position is denoted by δ_0 . When the system is subjected to a fault, the operating point drops to point B. Similar to a sudden increase in input mechanical power, there is an excess of mechanical power P_m over electrical power P_e , which accelerates the rotor, hence δ increases. The rotor speed increases until point C, where the fault is cleared and the operating point moves to point D.

From point D onwards, P_e is larger than P_m and the rotor experiences deceleration. Nevertheless, δ continues to increase as the speed is still above synchronous speed, until point E, where the rotor speed recovers back to synchronous speed, and δ_m is the maximum swing value of δ . The operating point would then trace back along the post-fault P_e curve to point D and further on. Assuming the absence of any damping components, the end result is continuous power angle oscillations about a new equilibrium point.

The kinetic energy gained during the transient period is highlighted by area A_1 in Figure 1.9, whereas the energy lost is marked by area A_2 . In order for a system to maintain stability, these two areas have to be equal thus satisfying the equal area criterion of the postfault system. Supposed that A_1 is greater than A_2 , the system would become unstable. This is because beyond point E, the resultant power turns back to an accelerating power that would cause the δ to increase further until loss of synchronism. In view of that, if A_1 is indeed equal to A_2 , the system is considered to be critically cleared and δ_c is the critical clearing angle of the system beyond which the system would become unstable [25]. The time taken to clear the fault at δ_c is the CCT of the system.

Generally there is no set of values for δ_c for a single generator as it is dependent on many factors such as system composition, fault conditions and fault clearance method [21]. For example, if the post-fault P_e curve is greater, a larger δ_c is obtained and the CCT would also increase. Introduction of underground HVAC cables in the system would alter the overall electrical parameters substantially, in particular the equivalent system reactance X_T in equation (1.1). Thus, the influence of undergrounding with respect to CCT is investigated in this thesis.

1.3.2 Multimachine system

A multimachine system is a power system with several interconnected generators in the network. The stability of the system is not dependent on the individual power angle of each generator which is measured relative to a rotating reference frame. Instead, the important factor in this case is the angular separation between generators, which is the difference in power angles from one generator to another [25].

Suppose a multimachine system is subjected to a large disturbance resulting in an excess of accelerating power. All the generators would absorb the majority of the extra power and begin to accelerate. The simultaneous increase in speed for all generators is acceptable as long as the power angles are relatively close to one another. The system would eventually stabilize itself because there is sufficient dampening torque in such case [2]. However in the case where one or more generators is deviating greatly from the rest, after a certain limit the critical generators would be forced to be disconnected and cause subsequent disturbance to the system which may lead to instability.

The transient behaviour of the system can be illustrated by using the rubber band analogy as shown in Figure 1.10 [26]. The weights represent the inertias of the generators and the rubber band corresponds to the inductance of the transmission lines. The weights are initially in their equilibrium positions and when one of them is pulled and let go, its movement would cause an oscillation with the other weights connected by rubber bands. As a weight is swinging downwards, the rubber band connected to it would stretch as a result, and this would brake the weights movement and exert a pulling force on the other weights. The motion would eventually come to a halt depending on the damping characteristics. If the stress on any rubber band is greater than its strength, it would snap and the system is no longer intact.

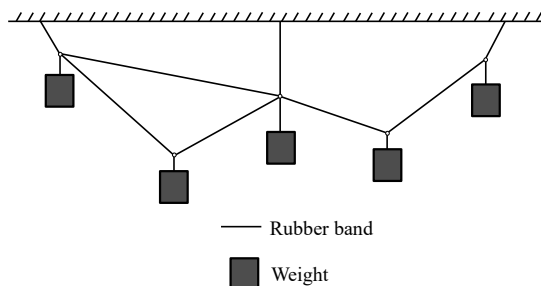


Figure 1.10. Rubber band analogy for illustration of multimachine power angle stability.

In a large system consisting of many generators, the identification of angular separation limits is of high complexity [2].

It is highly dependant on the location of the disturbance and subsequent power distribution among the generators determined by the layout of the system. Therefore direct methods are not used to obtain the CCT of multimachine systems, but instead through iterative simulations.

1.4 Principles of voltage stability

Following the classifications and definitions by the IEEE and CIGRE Taskforce [3], voltage stability is defined as:

"The ability of a power system to maintain steady voltages at all buses in the system after being subjected to a disturbance from a given initial operating condition."

The main cause of voltage instability is the inability of the power system to balance reactive power between generation, lines and loads. Thus, voltage stability is a partial stability problem which is focused on the behaviour of transmitted power P_R , bus voltages V_i and the reactive power injection Q_i at relevant nodes in the system. During a large disturbance a power system might be exposed to a sudden decrease or increase in reactive power demands. Such a disturbance could be the loss of generation, line or load, changing the topology of the system temporarily. Following a disturbance the restoration of loads can cause stress on the HVAC network by increasing reactive power consumption. Loads such as induction motors draw increased reactive current during start-up. If the system is weakened in a post-disturbance condition, due to the disconnection of lines or generation, it may be pushed beyond its stability limit when exposed to load dynamics. The load dynamics may attempt to restore power consumption beyond the capability of generation and the transmission network [3]. For this reason, voltage instability is more likely to occur when faults are near loads, compared to transient instability, which is more typical when faults are near generation [3].

If generators are unable to absorb or generate the required reactive power, or if compensation is insufficient, the power system risk a voltage collapse. According to the authors of [3] a major factor leading to voltage instability is the voltage drop that occurs due to reactive power flow through inductive reactances of the network. This voltage drop limits the power transfer capabilities of the system.

The change from OHL to cable based AC transmission is hypothetically particularly interesting considering large disturbance voltage stability. The reactive power behaviour of cables is substantially different to that of equivalent OHLs, which is elaborated in Section 1.5. Traditionally transmission systems based on OHL require additional reactive power during a disturbance, in order to raise the voltage and keep it nearer 1 p.u. The extra reactive power must be supplied by electrical machines, power electronics and switching of compensation reserves. Synchronous generators have the ability to change their excitation levels through field current control. Considering the classical model of synchronous generators in Figure 1.11, a basic understanding of the reactive power capabilities of electrical machines can be gained.

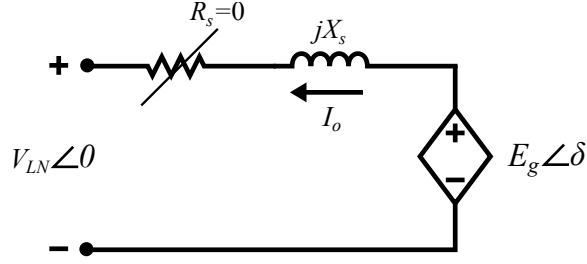


Figure 1.11. Classical equivalent circuit of phase (a) for a three-phase synchronous machine. The stator coil resistance is neglected, $R_s = 0$.

E_g is often referred to as internal voltage, field voltage or excitation voltage. The angle δ is the power angle as explained in Section 1.3. The magnitude of E_g is modelled by a dependent voltage source, as its value is a function of the field current I_f .

The relationship between E_g and I_f is expressed in equation (1.4), where M is the mutual inductance linking stator and rotor, assuming a non-salient air-gap, and ω_s is the synchronous speed.

$$E_{g,rms} = \frac{\omega_s M I_f}{\sqrt{2}} \quad (1.4)$$

From the model in Figure 1.11 the apparent three-phase power output $S_{o,3ph}$ is expressed in (1.5), from where the expressions for active and reactive power are derived by taking the real and imaginary part.

$$S_{o,3ph} = 3V_{LN}I_o^* = 3V_{LN} \left(\frac{E_g - V_{LN}}{jX_s} \right)^* \quad (1.5)$$

$$P_{o,3ph} = \text{Re} \{S_{o,3ph}\} = \frac{3V_{LN}E_g}{X_s} \sin(\delta) \quad (1.6)$$

$$Q_{o,3ph} = \text{Im} \{S_{o,3ph}\} = \frac{3V_{LN}E_g}{X_s} \cos(\delta) - \frac{3V_{LN}^2}{X_s} \quad (1.7)$$

Considering both (1.6) and (1.7) it is observed that both active and reactive power are proportional with the excitation voltage E_g , which can be controlled indirectly through the field current I_r [2]. When $Q_o > 0$ the machine is producing reactive power, which is defined as over-excitation. Decreasing E_g is decreasing Q_o , and when $Q_o < 0$ the machine is absorbing reactive power, which is defined as under-excitation. In other words, regulation of E_g implies power factor control. Figure 1.12 show how different excitation levels affect the P, δ -characteristics of a synchronous generator. The limit between over- and under-excitation is arbitrarily displayed in Figure 1.12. In reality this limit is dependent on the machine design and resulting parameters.

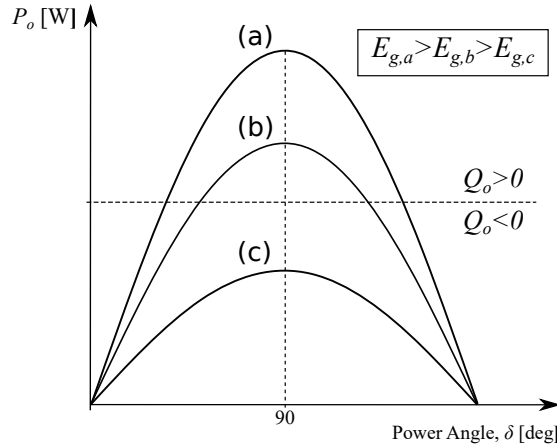


Figure 1.12. P, δ -characteristic of a SG with various levels of excitation voltage E_g .

The excitation level of synchronous machines and its effect on the P, δ -curve, indicate the existing coupling between transient stability and voltage stability. The excitation is changed in order to respond to a change of reactive power in the power system. Either the machine is controlled to produce more or less reactive power, or is changed from over- to under-excited, in response to excessive reactive power in the network. When the machine excitation is changed drastically, and the P, δ -curve in Figure 1.12 changes from (a) to (c) or vice versa, the power angle stability limits are influenced. The consequence may be power swings similar to the ones presented in Figure 1.7 in Section 1.3. However, now initiated by a drastic change in reactive power flow.

Reactive power flow and bus voltages are directly related. A simple two bus system with a generator, line and load is shown in Figure 1.13. The voltage drops from the sending to the receiving end of the line, due to the flow of current through both resistance and inductive reactance. Figure 1.14 show the superposition of the voltage drop across the resistor, and the voltage drop and 90° phase shift due to jX . The resistive voltage drop is illustrated with real and imaginary part in (a), while the voltage drop of the reactance is illustrated with real and imaginary part in (b). From Figure 1.14 the sending end voltage phasor V_S can be written as the super position of real and imaginary voltage drops. This operation is expressed in equation (1.8). Substitution of the expressions in (1.9) into (1.8) yields equation (1.11), which is the voltage drop equation of the line without capacitance and conductance to ground. The equation is sometimes presented where δ is assumed negligible, which eliminates the imaginary part of the expression. The significance of (1.11) is the relation between the voltage drop ΔV and reactive power transmitted to the receiving end Q_R . The voltage drop is proportional to Q_R , as transmitting more reactive power increases the voltage drop across the line. The equation indicate that reactive power should be supplied locally, rather than transmitted, in order to avoid detrimental voltage drops throughout the system. It is important to note that there always exist an inevitable voltage drop due to the line resistance and the transfer of active power.

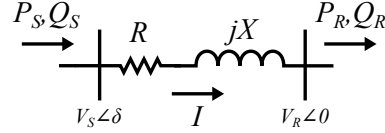


Figure 1.13. A simple line with impedance $Z = R + jX$. The current is lagging the voltage by an angle θ , and δ is the voltage angle at the sending end with reference to the receiving end.

$$\widetilde{V}_S = \widetilde{V}_R + RI \cos(\phi) + XI \sin(\phi) + jXI \cos(\phi) - jRI \sin(\phi) \quad (1.8)$$

$$P_R = V_R I \cos(\phi) \quad \text{and} \quad Q_R = V_R I \sin(\phi) \quad (1.9)$$

$$\widetilde{V}_S = \widetilde{V}_R + \frac{R}{V_R} P_R + \frac{X}{V_R} Q_R + j \frac{X}{V_R} P_R - j \frac{R}{V_R} Q_R \quad (1.10)$$

$$\Delta V = \widetilde{V}_S - \widetilde{V}_R = P_R \left(\frac{1}{V_R} \right) (R + jX) + Q_R \left(\frac{1}{V_R} \right) (X - jR) \quad (1.11)$$

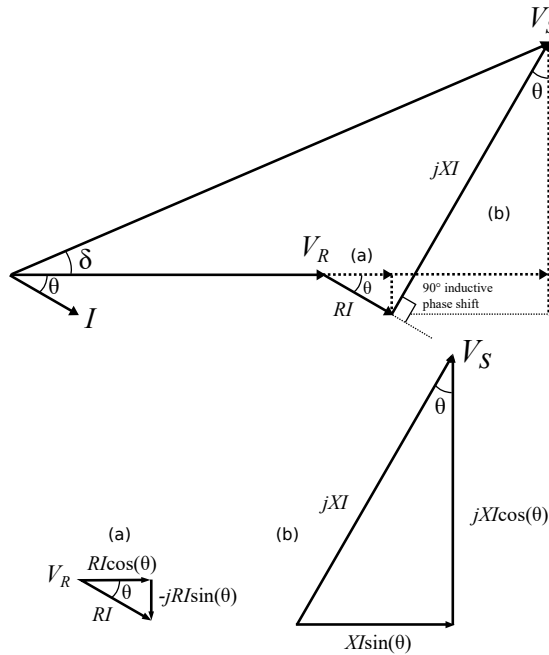


Figure 1.14. Superposition of the voltage drops of a transmission line with line impedance $Z = R + jX$. The power factor is lagging, so that the current is lagging the voltage by θ .

An interesting consideration is the behaviour of cables in the AC transmission system under large disturbances. Cables in HVAC networks generate large amounts of reactive power, which is typically compensated by shunt-reactors. During a fault the system requires injection of reactive power to maintain voltage. Hypothetically the shunt-reactors of nearby substations could be controlled, or even switched-out, during a fault.

As a result the reactive power demand of the system would be decreased, and the HVAC cables would act as reactive power sources to aid the voltage. Although, an important note is that the local generation of reactive power will be affected by the drop in voltage.

Another important characteristic in voltage stability studies is the V, P -characteristics of the system. The V, P -characteristics can be applied to the classical SG model under load, a line under load, or an equivalent network representing multiple machines, lines and loads. For a simple radial system under load, such as the one presented in Figure 1.13, the relationship between P_R and V_R is displayed in Figure 1.15 and 1.16. The values displayed are arbitrarily chosen, and does not represent a real system. The receiving end power P_R is normalized against the maximum power transfer at unity power factor ($\cos(\theta) = 1$), denoted $P_{R,MAX}$. The receiving end voltage V_R is normalized by the sending end voltage V_s . The power transmitted to the receiving end is maximum when the voltage drop across the length of the line is equal in magnitude to V_R , which is voltage across the load. This occurs when the impedance of the load is matched to the line, a condition that is elaborated in Section 1.5. Moving out of the horizontal axis on Figure 1.15, the power transfer is increased by a drop in load impedance Z_L . As Z_L is decreasing, and more power is transferred, the current I goes up and V_R is dropping. At first the increase in I is dominating the decrease in voltage V_R , in the standard impedance formulation in (1.12). Thus the power transmission is increasing, with the decrease in Z_L .

$$Z_L = \frac{V_R}{I} \quad (1.12)$$

As Z_L drops and approaches the impedance of the line, the decrease in V_R and the increase in I are balancing each other. The voltage V_R is recognized as the critical voltage around the point of impedance matching, where $P_R/P_{R,MAX} = 1$. Further lowering of Z_L beyond the critical point, makes the decrease in V_R dominate the increase in I , which effectively lowers the power transmission P_R . The critical voltage point indicates the existence of a voltage stability limit, which is affected by the load demand. Figure 1.16 show that the V, P -characteristics are greatly dependent of load power factor. This is a natural consequence of the relationship between reactive power transfer and voltage drop as former expressed by equation (1.11). Figure 1.16 is showing cases of both inductive (PF lag) and capacitive load (PF lead). A key observation is that when the load is injecting reactive power (PF lead), the relationship $V_R/V_S > 1$, indicating that the receiving end voltage is higher than sending end. As the system consists of an inductive line, the maximum power transfer increases as the load changes from consuming to supplying reactive power. Additionally, the critical voltage operation point is increasing, as the power factor is changed from lagging to leading. Normally only operating points above the critical values are satisfactory for voltage stability [2]. In power systems with cable based transmission, lines can represent capacitive loads, which have increased critical voltage limits, compared to that of equivalent OHL system. The dependency on loading and power factor is illustrated in Figure 1.16. If a system is operated close to the critical voltage limit in Figure 1.15, a sudden change in active power demand, can push the voltage below the critical limit. Thus, V, P -characteristics are likely to be essential in the study of voltage stability in cable based power systems.

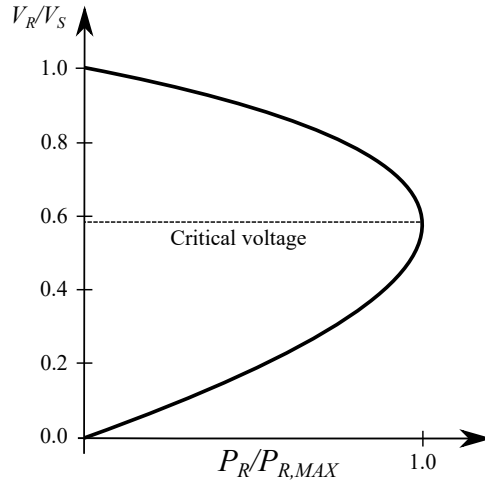


Figure 1.15. V, P -characteristic of the system shown in Figure 1.13. $P_{R,MAX}$ is the maximum power transfer at unity power factor. Operation below the critical voltage is considered unstable.

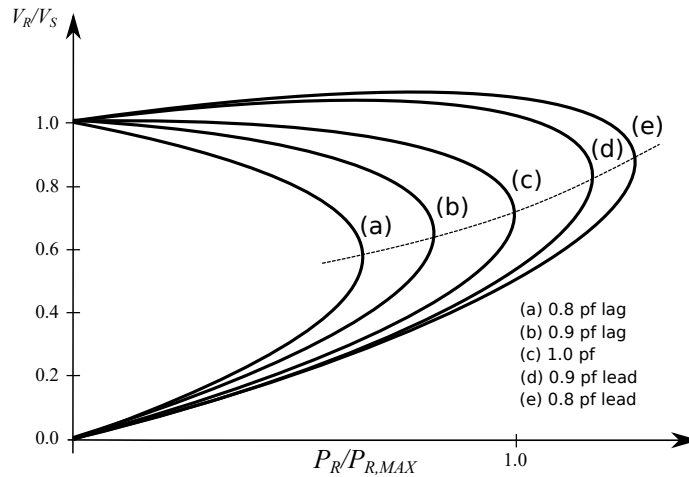


Figure 1.16. V, P -characteristic of the system shown in Figure 1.13 at different load power factors. The characteristics show cases of both leading, unity and lagging power factor.

Figure 1.17 show the Q, V -characteristics of the system in Figure 1.13. The values displayed are arbitrarily chosen. As in Figure 1.16 the locus of the critical points are indicated by a stippled line. The Q, V -characteristics indicate the voltage stability of the system for fixed values of active power transfer P_R . Stable voltage stability operation is in the region where $\frac{dQ}{dV}$ is a positive value, while the stability limit is at the minima of the Q, V -curves where $\frac{dQ}{dV} = 0$. Stable operation can be achieved in the negative region of the Q, V -curves. However, such operation requires controlled reactive power compensation, with a high capacity and Q/V -gain [2]. Q_R is the reactive power injected at the receiving end bus in the system in Figure 1.17. For voltage stable operation, a positive increment in Q_R should result in a positive increment in bus voltage V_R . As the loading of the system is increased from case (a) to (c), the minimum value of V_R is increased and the range of stable voltage operation is decreased. This is a consequence of the voltage of the system being a function of both active and reactive power transfer, as it was derived in (1.14).

The behaviours displayed in Figures 1.15, 1.16 and 1.17 are for the simplified system in Figure 1.13. As a whole, the behaviours presented highlight the most basic voltage stability phenomena. In a comprehensive and complex power system, the voltage stability limits are functions of load characteristics, generator reactive power capability limits, characteristics of reactive power compensation elements, power transfer levels and the strength of the transmission network [2]. All of which influences the voltage stability in local buses and for the system as a whole.

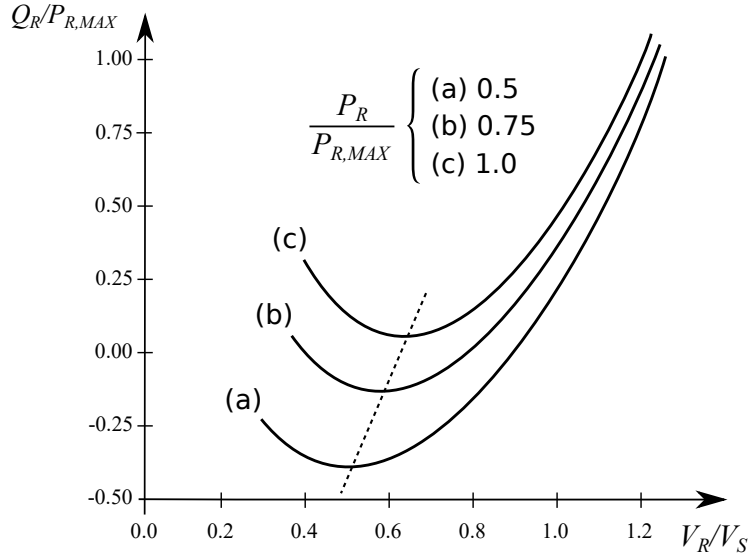


Figure 1.17. Q, V -characteristic of the system shown in Figure 1.13 at three active power loadings.

1.5 Transmission lines in power system stability studies

In power system stability studies transmission lines are represented by classical algebraic equations in a common real-imaginary reference frame. Modelling of lossy transmission lines with distributed parameters involves series resistance R , series inductance L , shunt conductance G and shunt capacitance C . G is often neglected due to its insignificant value, while some stability studies also neglect R . Neglecting line resistance is a typical partial stability study, with the purpose of limiting line influence to power angle and reactive power [2]. As the majority of transmission lines are OHL, C is typically neglected for short lines. The line parameters expressed in equation (1.13) and (1.14) are distributed throughout the length of the transmission line. Thus, a full model of the transmission line performance involves the application of Maxwells's equations to express the telegraphers's equations and applying the d'Alembert general solution [31]. Typically, equivalent circuit modelling with lumped parameters is utilized for stability studies, such as the equivalent π or nominal π models, just as it is the practice in power flow studies [2].

$$z = R + j\omega L \quad (1.13)$$

$$y = G + j\omega C \quad (1.14)$$

However, the exact model and its properties are relevant to consider in order to understand the behaviour of transmission lines in dynamic studies.

An interesting transmission line property following the general solution to telegrapher's equations is the characteristic impedance Z_0 . By defining the characteristic impedance as in equation (1.15) the distributed circuit can simply be represented by the transmission line (TL) shown in Figure 1.18. Where Z_0 express the magnitude of the relationship between propagating voltage $V(z, t)$ and current $I(z, t)$ at any point z and time t along the length of the line.

$$Z_0 = \sqrt{\frac{R + j\omega L}{G + j\omega C}} \quad (1.15)$$

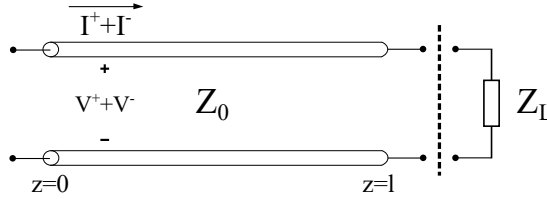


Figure 1.18. Transmission line representation with forward and backward propagating voltage $V(z, t)$ and current $I(z, t)$, and characteristic impedance Z_0 .

If an arbitrary load Z_L is impedance matched to Z_0 , the reflection coefficients $\Gamma_v = -\Gamma_i = 0$, and no reflection occurs at the boundary between the line and the load. This principle is valid at any boundary in the system. The voltage reflection coefficient is expressed by equation (1.16).

$$\Gamma_v = \frac{V^-}{V^+} = \frac{Z_L - Z_0}{Z_L + Z_0} \quad (1.16)$$

If the transmission line is considered lossless, and $R = G = 0$ in (1.15), the value of Z_0 in (1.15) is reduced to a purely real number, expressed by equation (1.17). As the practical value of G is close to zero for transmission lines, and $R \ll \omega L$, high-voltage lines are often assumed to be lossless in dynamic studies. Historically this practice originates from the study of lightning and switching surges. Thus, the characteristic impedance Z_0 of a lossless line is known as the *surge impedance* (SI) [2].

$$Z_0 = \sqrt{\frac{L}{C}} = \text{SI} \ [\Omega] \quad (\text{lossless}) \quad (1.17)$$

When a transmission line is loaded by an impedance equal to its SI, the voltage and current amplitudes are constant along the length l of the line, and the voltage and current are in phase, resulting in unity power factor. The phase angle between the sending and the receiving end is $\delta = \frac{2\pi l}{\lambda}$, where λ is the wavelength of the travelling wave [2]. The *surge impedance load* (SIL) is the power delivered to the SI matching load, and is defined in equation (1.18).

$$\text{SIL} = \frac{V_{LL}^2}{Z_0} \ [\text{W}] \quad (\text{three-phase}) \quad (1.18)$$

So why is surge impedance an important parameter in power system stability? At SIL the reactive power generated due to the distributed capacitance C , is exactly equal to the reactive power absorbed, due to the distributed inductance L of the line. This effect can be realized by observing the current and voltage at any point of the line, showing that they are in phase.

The result is a flat voltage profile of the line, meaning no voltage magnitude variation throughout the total length. Thus, indicating that no reactive power is absorbed or generated at the ends of the line. For this reason SIL is considered an optimum state in voltage stability, which is directly related to the control of reactive power and voltage at specific network points. Hence, SI and SIL are often utilized as a reference values for transmission lines in voltage stability studies [2].

The electrical characteristics of a HVAC cable is different to that of an equivalent OHL. Table 1.1 show a comparison of field measured parameters, performed in the project presented in [21]. The rated apparent power of the cable in Table 1.1 is 987.27 MVA, while the OHL is rated at 2635 MVA. An interesting observation is the significant difference in SI and SIL. The main cause is the higher value of C for the cable according to equation (1.17), in this case 17.5 times higher compared to the OHL. The lower value of SI, and inversely higher value of SIL of the cable, mean that the cable is more likely to be lightly loaded with respect to SIL, under normal operation. Whereas the low value of SIL for the OHL, means that it is more likely to be heavily loaded with respect to SIL. The nominal apparent power load of the OHL is 2635 MVA, while it is 987 MVA for the cable [21].

Table 1.1. Comparison of electrical parameters for 400 kV- 50 Hz OHL and cable. The rated ampacity of the OHL is 4 kA, while it is just 1.5 kA for the cable. SIL is calculated for 380 kV. The OHL conductor is a bundle of 4 sub-conductors [21].

Type	Cross-section [mm ²]	R+jX [Ω /km]	C [nF/km]	SI [Ω]	SIL [MW]
OHL conductor	2483.6	0.0092+j0.2452	13.2	243.2	593.8
XLPE Cable	2500	0.0227+j0.1712	231.5	48.5	2976.2

Figure 1.19 show the Q-P characteristic of transmission lines at various lengths. An important observation is that if the line is operating below SIL ($P_R < SIL$), the reactive power is negative at the sending end and positive at the receiving end. This indicates that the line is supplying reactive power at both ends, which is absorbed by the system. When $P_R < SIL$ reactive power is being supplied by the system to the line. Underground cables have high values of SIL, as can be seen in Table 1.1, hence cables are typically operated with $P_R < SIL$ in the Q-P characteristic.

If a transmission line is operated below SIL, which would be the typical case of an uncompensated cable (or in the case of open-circuit), the Ferranti effect can be observed [2]. In this case excessive amounts of capacitive current are supplied by the distributed capacitance of the line, flowing through the inductive reactance of the line, towards the sending end. The result is a higher magnitude of voltage at the receiving end of the line than the sending end, as illustrated in Figure 1.20. The shape of the voltage magnitude as a function of the line length appears from the solution to the telegraphers equations. For a lossless line the voltage phasor at any position z along the transmission line can be expressed as in equation (1.19), where β is the phase constant expressing the phaseshift in radians per meter. β is the imaginary part of the propagation constant γ as expressed in (1.20). Typical values of β are within the range of 0.001 rad/km for OHL, and 0.009 rad/km for cables [2]. The relatively low value of β result in the slowly changing sinusoidal voltage shape across the length of the line.

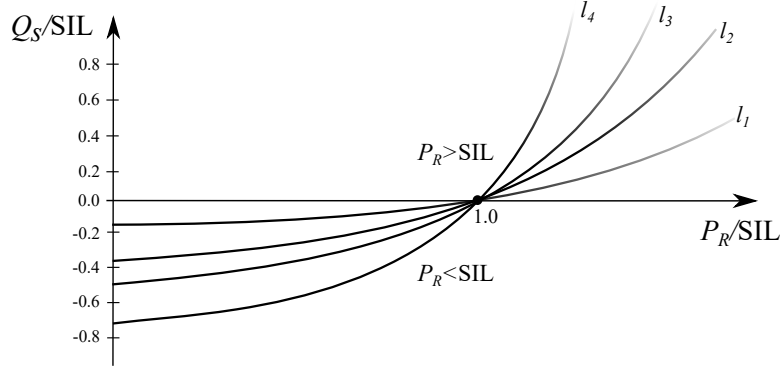


Figure 1.19. Q-P characteristic of transmission lines at different lengths normalized with SIL. The lengths are so that $l_1 < l_2 < l_3 < l_4$. The voltages at the ends are assumed equal so that $Q_r = -Q_s$.

$$\tilde{V}(z) = \tilde{V}_R \cos(\beta z) \quad (1.19)$$

$$\beta = \text{Im} \{ \gamma \} = \text{Im} \left\{ \sqrt{(R + j\omega L)(G + j\omega C)} \right\} \quad (1.20)$$

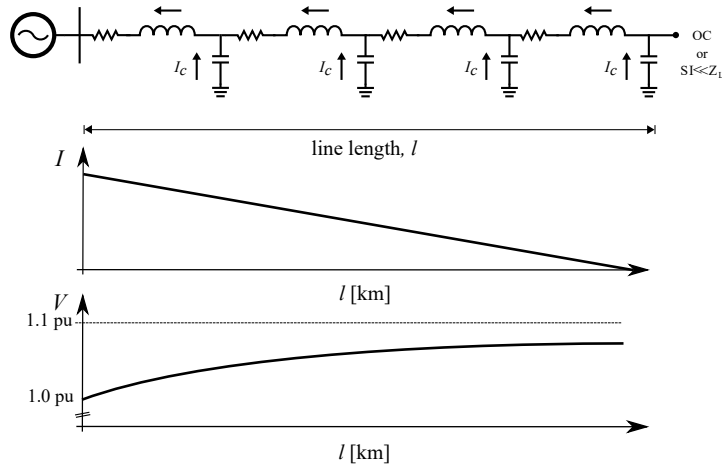


Figure 1.20. Reactive current and voltage profiles for a lightly loaded ($SI \ll Z_L$), or open-circuited, transmission line with distributed parameters.

Light loading $SI \ll Z_L$, is primarily caused by capacitive behaviour of the load. This could be continuation of the line by an underground cable. A way of avoiding over or under voltages caused by the flow of reactive power, is to compensate the line. Compensation refers to the implementation of reactive power balancing units, such as inductors or capacitors in series or parallel (shunt), which effectively change the characteristic impedance Z_0 of the line. Another method for reactive power control is the implementation of synchronous condensers with excitation control. In Figure 1.21 a transmission line is connected to under-excited synchronous generators at both ends. No active power is transmitted between the line ends, and the voltage is fixed at 1 p.u. at both ends.

The figure displays how capacitive current is supplied to both ends of the line, implying a voltage maximum point on the middle of the line. In this configuration the synchronous condensers are absorbing all the excessive reactive power generated by the transmission line.

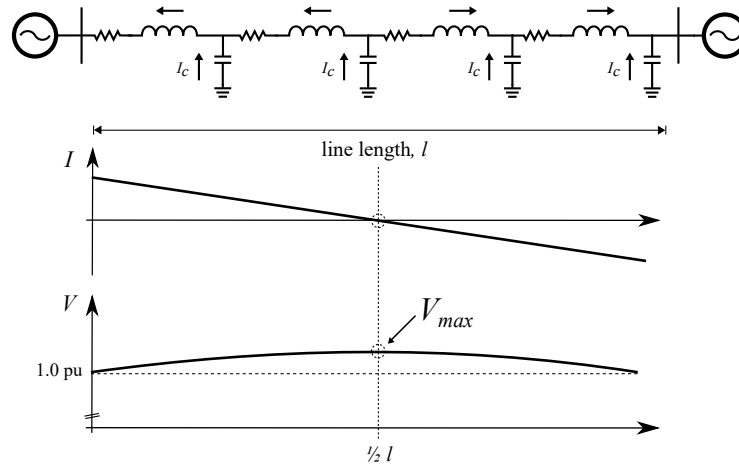


Figure 1.21. Reactive current and voltage profiles for a transmission line connected to external grids fixed at 1 pu voltage. The networks represented at both ends are considered under-excited, thus absorbing reactive power. No active power are transmitted from sending to receiving end, $P_s = P_r = 0$.

Figure 1.22 shows a cable with reactive power compensation in the form of shunt reactors (inductors), located at different points. The distributed capacitance C of the cable produces an excessive amount of capacitive current which must be balanced by the inductors. The location and size of the inductors influence the reactive current flow, and the voltage profile of the cable. Case (a), with compensation at just one line end, results in the largest reactive current flow and a steeper voltage profile. The reason is the accumulative reactive current flowing through the entire length of the cable. Whereas the reactive current flow in case (b) and (c) is in both directions, either towards the ends or towards the middle. By dividing the compensation more evenly throughout the length of the cable, which is shown in case (d), the reactive current flow in the cable is limited, resulting in a more flat voltage profile. Essentially this brings the characteristic impedance Z_0 of the transmission line closer to impedance matching with the load, and the cable will display similar characteristics. Sizing and placement of compensation is not only important in steady state operation and for small-signal stability. In large-disturbance stability studies the compensation plays an important role with regards to the initial conditions (post-disturbance) of the stability problem. Likewise, any possible dynamic compensation will influence the stability limits during the full duration of the electromechanical transient.

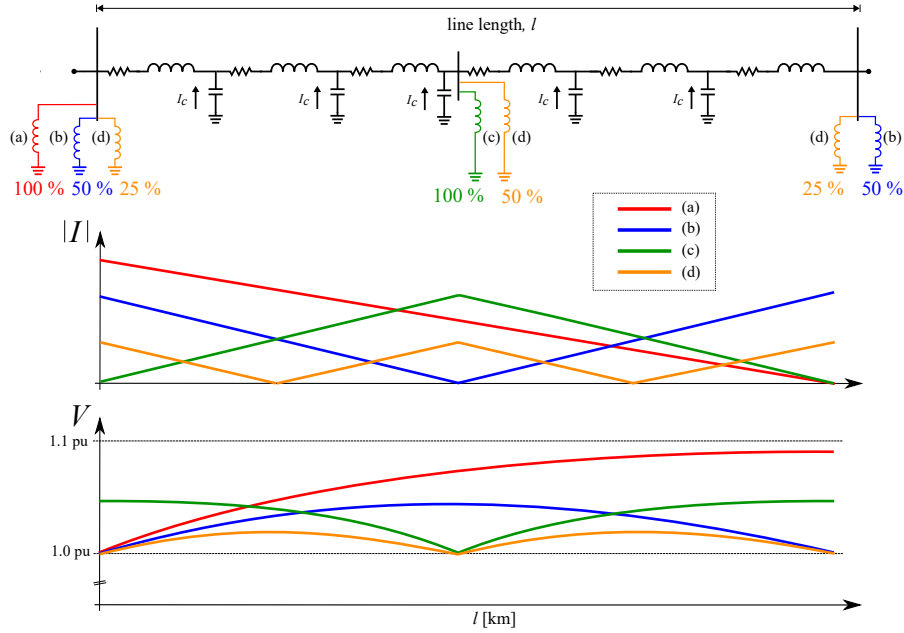


Figure 1.22. Reactive current and voltage profiles for a cable with distributed parameters and different location and size of inductive shunt compensation. Only the current magnitudes are shown, however the waveform indicates the direction of flow. 4 cases are shown. (a) 100 % compensation at the sending end, (b) 50 % compensation at both ends, (c) 100 % compensation at the middle of the cable, and (d) 50 % compensation on the middle, and 25 % on the ends.

1.6 State of the art review

The following section is a brief review of the latest research and state of the art in stability studies involving HVAC cables, planning of reactive power and stability indices. The methodologies and results are discussed, with focus on the applicability and influence on the scope of this thesis.

1.6.1 HVAC cables in stability studies

HVAC cables gained traction recently due to growing concerns over the construction of new high voltage overhead lines. The concerns are related to environmental and landscape issues. Denmark is one of the few countries that is heading this transition in their transmission network as described in Section 1.1. As it is not widely adopted yet in many countries, there is relatively little literature available on stability studies related to cable systems.

Authors in [19] have made a comparative analysis on transient stability for different system configurations under fault condition. The comparison is done between SMIB systems that contain cables and with overhead lines only. It is shown in certain cases that the systems that are made up of uncompensated cables in part of the transmission system display shorter CCT than the overhead line system. The adverse effect becomes clearer with the increase of the line length. Figure 1.23 shows the CCT of the investigated systems in [19] with respect to the length of L2 stretch.

L2 is a stretch on the transmission line that was used to carry out the sensitivity analysis. MLC represents a mixed line system that is made up of both cable and overhead line with compensation whereas ML is the uncompensated counterpart. OHL denotes the system in which the line is composed of overhead line only.

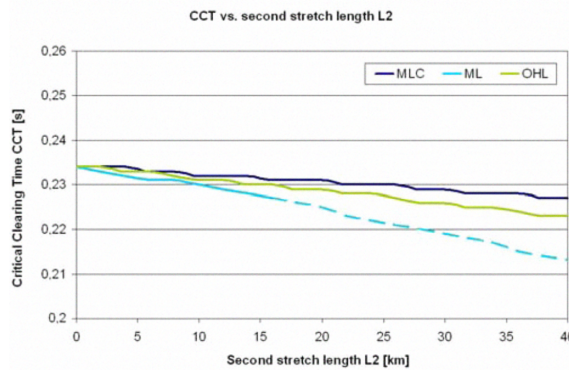


Figure 1.23. CCT of investigated systems [19]. System with a higher CCT is more stable.

From Figure 1.23, it can also be observed that compensation helps to improve the stability of the system. This observation is backed up by studies conducted in [20] and [21]. The type of stability investigated in [21] includes transient and voltage stability whereas [20] concentrates on the latter only. The study in [20] is about the voltage stability of an island grid in Taiwan which is connected to a large grid via submarine cables. Compensation devices such as static var compensators (SVC) and static synchronous compensators (STATCOM) are included in the case study as a form of reactive power support. The disturbance in is the disconnection of one of the cables. The voltage response to the disturbance of the island grid terminal, Bus 01 for two scenarios is shown in Figure 1.24. The connection of compensating devices helps to reduce the sudden voltage drop at the disturbance instance and to restore the voltage level at a much shorter time. In contrast, the uncompensated system requires the slow acting tap changer on the transformer to bring the voltage back close to nominal value. The long duration of undervoltage may be detrimental to the system and components.

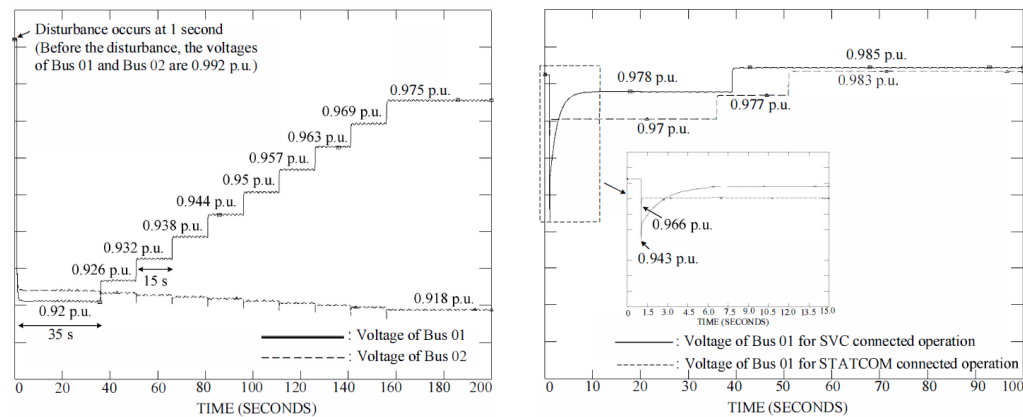


Figure 1.24. Voltage response of Bus 01 and Bus 02 when a cable is disconnected at 1 second [20]. (Left) Without compensators. (Right) With compensators. Bus 01 is the island grid side terminal of the cable.

In addition to fault and disconnection of a line, [21] also covers the connection of a line as a form of severe disturbance to investigate the transient dynamics of the system in the presence of cables. The investigation is conducted on the prospective Dutch transmission network in 2020. The findings is the same as the one observed in [19] with higher degree of undergrounding being more vulnerable to instability unless compensated. Figure 1.25 illustrates the voltage transient at the terminal BSL380 during line connection. Nevertheless, the paper also proposes alternative switching sequences of compensators to help minimize the effects of voltage variation during line connection and disconnection. The change is suggested to relief the generators of acting in under-excitation mode for sustained period of time due to the excess reactive power generated by the cable.

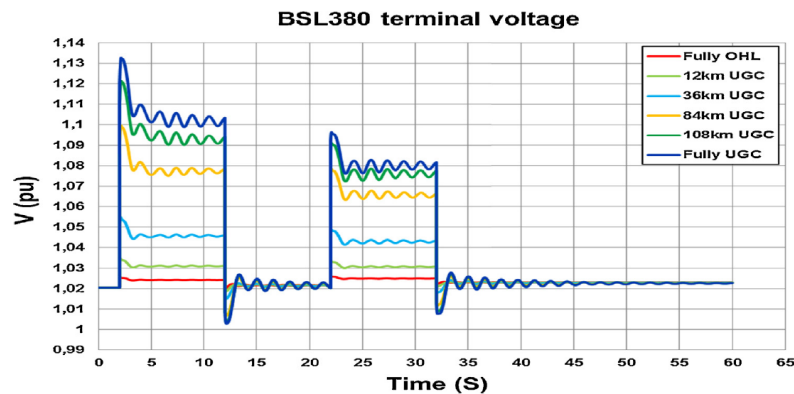


Figure 1.25. BSL380 terminal voltage for different degree of cabling during line connection [21]. Total length of the line is 120 km. OHL and UGC are the abbreviations for overhead lines and underground cables respectively.

The location of compensators is also of great influence according to [19] and [21], though with different findings. The benefits of enhancing the system dynamics may outweigh the extra cost incurred in proper allocation of compensators. The authors in [22] have presented the idea of utilizing capacitive cables to fully compensate the reactive power requirement of the overhead lines. This approach may be analytically useful to provide power correction and result in improved transient stability, however the practical applicability is limited to a certain extend due to the constraints imposed by political, environmental and technical feasibility factors.

1.6.2 Planning of reactive power compensation for improved voltage stability

Following the change from OHL to cable based HVAC transmission, danish TSO Energinet.dk is implementing reactive power compensation in the form of shunt reactors. Carsten Rasmussen, Engineer and grid planner, comments on the sizing and positioning of reactive power in the Danish transmission network:

"The maximum size of the reactors are mainly determined by the maximum allowed voltage jump when switching the reactors in or out. For screening purposes we use static calculations (short circuit calculations), where we assume that a voltage jump of 3 % is OK. If we for instance have a minimum short circuit level, SCL, in a station of 1500 MVA, then the maximum-size of the reactor is: $1500 \text{ MVA} \cdot 0.03 = 45 \text{ Mvar}$.

The standard sizes in the 132 kV or 150 kV grid is either 40 Mvar, 70 Mvar or variable 40 Mvar to 100 Mvar. The last one is chosen for Copenhagen. When the reactor is switched it should be adjusted to 40 Mvar (to limit the voltage jumps). If the Cable Action Plan is continued (we should know in half a year from now) we will have reactors in many stations. Probably in every second 132 kV station in East-Denmark and in almost every 150 kV station in West-Denmark." - Carsten Rasmussen, date: 3.3.2016

Furthermore Carsten Rasmussen comment that no static synchronous compensators (STATCOM) are implemented in the danish transmission network, while there is one static VAR compensator (SVC). However, he does point out that one of the HVDC connections to Norway (Skagerak 4) uses the voltage source converter technology (VSC), which allows for reactive power control. While more VSCs are following the upcoming HVDC connections to Holland and England.

The authors of [32] address the issue of optimal planning of dynamic reactive power compensation. The motivation is the lack of compensation planning based on large-disturbance voltage stability studies. The authors state that most publications on the topic of dynamic reactive power planning are based on static small-signal voltage stability analysis. In order to optimize dynamic reactive power planning, the authors formulate two sub-problems, (1) optimal siting (i.e. location), and (2) optimal sizing. Optimal sizing and siting of reactive power compensation is important as devices are expensive, especially dynamic compensation, such as SVC and STATCOM. Furthermore, the number of available compensation locations is limited by external interests.

The first issue is to identify weak buses of the system, as reactive power should be compensated locally to avoid the voltage drops associated with long distance transmission. However, it is not enough to only consider the compensated weak point (bus), as local compensation will affect the voltage stability at neighbouring points. Thus, it is necessary to consider the correlation between system busses when formulating a siting model. Ideally every weak point should be dynamically compensated, but due to economical and external limitations, this is not possible. For this reason it is essential to identify locations which will improve the voltage stability limit of all busses of interest.

The authors of [32] identify the weak busses of the system by voltage trajectory analysis. During a fault the bus voltage drops, which is depicted in Figure 1.26(A). The bus voltage drops below a threshold value of 0.75 p.u. and the time $T_{Ri,k}$, from that point to recovery back to 0.75 p.u. is recorded. The index i denotes the bus number and k denotes the fault condition. If $T_{Ri,k}$ exceeds 1.0 s, the authors consider the system unstable. In weak areas of the power system, buses display similar voltage trajectories and their recovery times are similar. This difference is defined in (1.21).

$$T_{Ci,j,k} = |T_{Ri,k} - T_{Rj,k}| \quad (1.21)$$

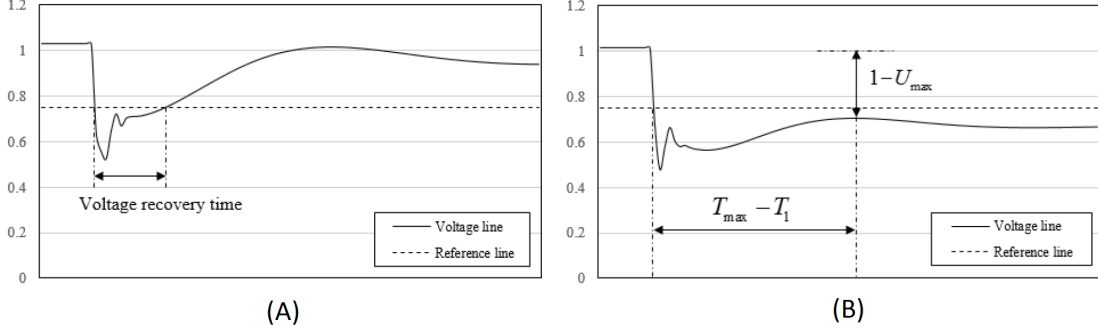


Figure 1.26. Bus voltage trajectories in response to a fault. In (A) the voltage is able to recover above the threshold value, while it is unable in (B). The threshold value of 0.75 p.u. is indicated by the dashed line. [32]

In some cases the voltage cannot recover to the threshold voltage of 0.75 p.u. This is depicted in Figure 1.26(B). In this case the recovery time is defined as in equation (1.22), where T_m is a fixed large recovery time of 10s, T_1 is the incident time of the fault, T_{max} is the time of maximum recovery voltage post fault, and U_{max} is the maximum post fault voltage.

$$T_{Ri,k} = T_m + (1 - U_{max}) \cdot (T_{max} - T_1) \quad (1.22)$$

Based on simulations the recovery times $T_{Ri,k}$ of weak buses are recorded and stored in a matrix \mathbf{T} in (1.23). The row number m is the specific weak bus, while the column number n is the fault type.

$$\mathbf{T} = \begin{bmatrix} T_{R1,1} & T_{R1,2} & \cdots & T_{R1,n} \\ T_{R2,1} & T_{R2,2} & \cdots & T_{R2,n} \\ \vdots & \vdots & \ddots & \vdots \\ T_{Rm,1} & T_{Rm,2} & \cdots & T_{Rm,n} \end{bmatrix} \quad (1.23)$$

The authors of [32] use the voltage trajectory analysis to perform an optimization of size and location of reactive power compensation. In short, their proposed method optimizes the reactive power compensation by identifying the most improved voltage trajectories according to the definitions. It is concluded that the method proposed provides a efficient way of planning reactive power compensation based on large disturbance voltage stability. It is highlighted how the compensation at one bus will affect other buses, and how the method secures that the individual bus is neither over compensated nor under compensated.

1.6.3 Stability indices for transient and voltage stability analysis

Choosing an appropriate stability index for assessment of power system stability is essential in stability analysis. Firstly, the index should be relevant according to the questioned instability type. Whether it is a transient stability or voltage stability problem, or even a specific sub-type as categorized in [3] and presented in Figure 1.2. Secondly the index and the associated methodology should be suitable for the scope of the analysis. Overall, power system stability can be assessed in two different ways. Either from a mathematical stability theoretical approach, or from what in [3] is referred to as the practitioners way. The power system practitioner asses the stability through software simulations.

Mathematical stability analysis of large systems is very complex and is not achieved for large disturbances according to [3].

"The construction of Lyapunov functions for detailed power system models, particularly accounting for load models, is still an open question... The stability of power systems to large disturbances is typically explored in simulations. Advances in this direction come from improved computer technology and from efficient power system models and algorithms."

From a mathematical point of view Lyapunov stability is considered to be the state of art in determining power system stability. This method includes many definitions with different sets of stability criteria. Since large-disturbance power system dynamics are nonlinear, the definitions for stability and asymptotic stability are most suitable [3].

The typical definitions for power systems are concerned with the equilibrium point and its stability assessment. A time varying system is considered in (1.24) where x is the state vector, \dot{x} is the derivative and f is a function in which the domain includes the origin. The origin ($x = 0$) is assumed to be an equilibrium point.

$$\dot{x} = f(t, x) \quad (1.24)$$

The basis for the origin or equilibrium point, $x = 0$ to be stable is that equation (1.25) has to be satisfied. In other words, the initial conditions starting in a small spherical neighbourhood of radius δ result in the trajectory of the system which is subjected to disturbance to be bounded by a cylindrical shape of radius ϵ at all time. The graphical illustration of the definition is shown in Figure 1.27.

$$\|x(t_0)\| < \delta \Rightarrow \|x(t)\| < \epsilon, \forall t \geq t_0 \geq 0 \quad (1.25)$$

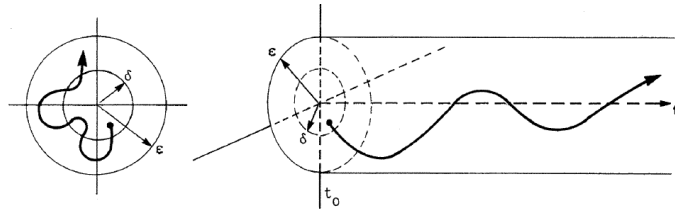


Figure 1.27. Illustration of the Lyapunov stability definition [3].

In addition to the definition given in (1.25), asymptotic stability definition also require the system to return to the equilibrium point eventually as shown in Figure 1.28. The stricter requirement may only be applied to systems which has a post-disturbance condition similar to the pre-disturbance condition (i.e. initial conditions) and therefore it is not practical for disconnection of power system components resulting in topology changes.

The definitions that are presented require detailed construction of functions for power system models and it is normally limited to small systems like SMIB. In the case of large multimachine systems, like the ones to be investigated in this thesis, this stability approach is not feasible within the time constraints of the project period and will not be applied.

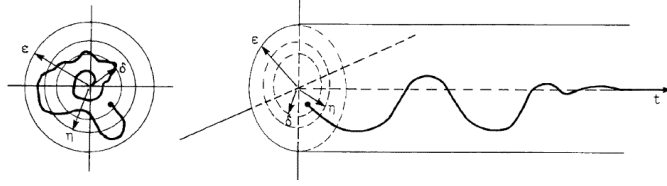


Figure 1.28. Illustration of Lyapunov asymptotic stability definition [3].

In this thesis both transient stability and large-disturbance voltage stability is to be analysed. This is done for systems larger than the SMIB system, more specifically the IEEE 9-bus system and IEEE 39-bus system. Thus stability indices, which are suitable for large system analysis are to be chosen, for both partial stability problems.

In transient stability the parameters of interest are mainly the active power transmission and power angle, (P, δ) -characteristics. The most used index for transient stability is the critical clearing time (CCT), which is elaborated in Section (1.3.1). CCT can be assessed both mathematically and by simulations. Through simulations the CCT can be obtained by iterative sensitivities of the system.

For voltage stability studies the choice of stability index is not as straight forward. The author of [2] comments on stability margins and indices of voltage stability: *"There are at present no widely accepted guidelines for selection of the degree of margin and the system parameters to be used as indices. These are likely to be system dependent and may have to be established based on the characteristics of the individual system."*

The work in [2] was published in year 1993, but as of today indices for voltage stability is still a research topic.

Voltage stability is concerned with the parameters V , P and Q at critical nodes of the system. Thus assessing voltage stability by CCT, which is associated with the power angle δ , is an indirect way of analysing voltage stability. Recent voltage stability studies utilize a form of simulation based trajectory analysis for analysing instabilities [20]. However, other studies are still based on determining δ , even if the topic is compensation of voltage by reactive power [22]. Thus, no general consensus regarding the use of voltage stability index exist. For small-signal voltage stability several alternative indices have been used. The authors of [33] compare and discuss previous methods and propose a new index. However, the methods are focused on the voltage collapse following small-signal load variations, and have not been verified for large disturbances.

The authors of [34] discuss the advantages and disadvantages of large-disturbance stability indices, while proposing a new method. In papers [32] and [21] the large-disturbance voltage stability is assessed by evaluating voltage waveforms in different dynamic situations. The effect of reactive power compensation is analysed directly by observation of $v(t)$ following a large disturbance, and doing incremental $\frac{\partial v(t)}{\partial Q} \approx \frac{\Delta v}{\Delta Q}$ sensitivities. This method is simple, but has the disadvantage of not providing a qualitative definition of stability margins.

1.6.4 Evaluation criteria of large-disturbance voltage trajectories

As it was discussed in Section 1.6.3, there is no standard method for assessment of voltage stability for large-disturbances. In this thesis a voltage trajectory method similar to the one presented in [32], and discussed in Section 1.6.2, is to be utilized for comparison of OHL and cable based networks. Voltage trajectory analysis is considered a simple method for comparing different cases of system topology with respect to voltage stability performance. However, a disadvantage of the method is that it does not assess the voltage stability margin, and the so called distance to instability. Thus, the method is not suited for determining if an actual case will lead to instability, but rather for comparing and determining whether a given case has an improving or decreasing effect on voltage stability.

Following a large disturbance, the voltage trajectory (i.e. voltage waveform) at a given node in the power system, will display certain characteristics. Here the focus is on the power systems ability to recover local voltages within a certain time frame. Thus, observing the voltage trajectory, the important parameters are the voltage recovery time t_R from the incident of the disturbance, to a voltage above a certain threshold, and the recovery voltage v_R .

In this thesis, it is decided to evaluate the voltage trajectories against an under-voltage limit provided by Nan Qin, Ph.d. student and employee at danish TSO Energinet.dk. The under-voltage limit is displayed in Figure 1.29. The original figure is published in [35], displaying both under-voltage and over-voltage limits.

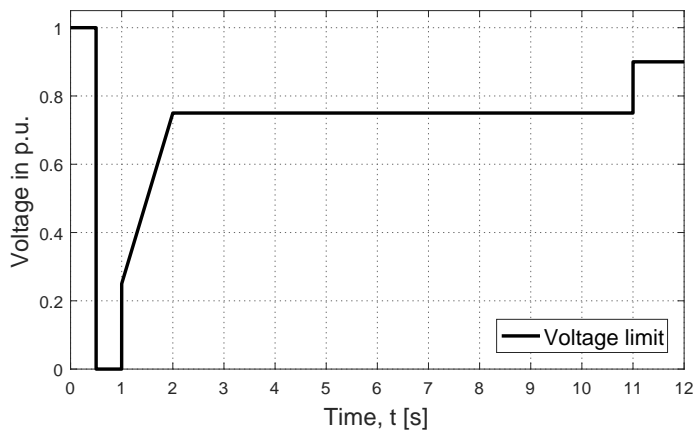


Figure 1.29. Under-voltage limits following large-disturbances for assessing voltage stability [35].

The under-voltage limit is not part of a grid-code, but is an evaluation criterion used to assess voltage stability under large disturbances. It is used to assess the voltage profile at any node in the transmission grid, and it considers protection and operational limits of the system and equipment.

The under-voltage limit displayed in Figure 1.29 dictates that in order to consider voltage stable operation, the voltage should be able to recover to atleast 0.75 p.u. within 1 s of clearing the disturbance. Thus, the minimum slope of recovery from 0.25 p.u. to 0.75 p.u. should be $\Delta V/\Delta t = 0.5$. Furthermore, 10 s after clearing the disturbance the voltage should have recovery to more than 0.90 p.u.

If the voltage trajectory of any node following a disturbance, does not satisfy these limits in the given time, the continuous operation at the specific node cannot be guaranteed. Consequences of under-voltage operation may be increased current drawn by constant power loads and stalling of induction motors, which may further detriment the system voltage. Under-voltage load shedding and tripping of under-voltage protection may be a necessary resort to avoid a system collapse.

Problem statement and methodology 2

This chapter lists the problem statement of the thesis together with the specific objectives realized to answer the problem. The delimitation of the thesis scope is described together with the chosen methodology.

2.1 Problem statement

Danish TSO Energinet.dk is in the process of undergrounding parts of the AC transmission grid in Denmark. The affected voltage levels range from 132 kV to 400 kV. Undergrounding involves the replacement of conventional OHL transmission with underground cables. A major difference in terms of electrical parameters is that cables are mainly capacitive and a source of reactive power, in contrast to the inductive OHL, that absorbs reactive power due to typical operation above SIL.

The focus of this thesis is to study the electromechanical dynamics associated with the implementation of long HVAC cables in the power transmission network. The main objective is to assess and study the transient stability and large-disturbance voltage stability of generic power systems. The analysis is to be initiated on a simple single-machine infinite bus system, and then expanded to IEEE 9-bus system and IEEE 39-bus multi machine systems. The stability of power systems with OHL and cable based HVAC transmission is to be compared through sensitivity studies of fault duration, fault location, reactive power compensation degrees, load levels and more.

Transient stability studies are to be performed with critical clearing time (CCT) as index for power angle stability assessment.

In the case of voltage stability, V, P and Q, V -characteristics are used as static indices for comparing the performance of the two different systems. It is to be investigated how varying the degree of reactive power compensation can influence the steady state stability performance.

The dynamic large-disturbance voltage stability is to be assessed by observing voltage trajectories at load buses following a series of large-disturbance events. The analysis is focused on the effects of dynamic switching of compensation devices (i.e. shunt reactors) on the voltage trajectory.

The questions to be answered are: *Does undergrounding of HVAC transmission networks influence the transient and voltage stability limits of power systems? How can the stability be improved by utilizing reactive power compensation?*

Objectives

- Analysis of the basic electromechanical dynamics in OHL and cable based transmission systems.
- Initial studies on a SMIB system with focus on modelling and parametric influence on transient and voltage stability.
- Assessment of transient stability and comparison of CCT for IEEE 9-bus and IEEE 39-bus systems..
- Assessment of voltage stability by comparison of V, P and Q, V -curves for IEEE 9-bus and IEEE 39-bus systems.
- Assessment of large-disturbance voltage stability by observing voltage trajectories for cable based systems.
- Analysis and comparison of various reactive power compensation schemes for improved stability.
- Discussion of considerations for dynamic switching of reactive power compensation devices for stability improvement.

2.2 Delimitations

System models: No detailed modelling is carried out for the power system components that are presented in this thesis. Dynamic modelling of a system component involves the application of the algebraic and differential equations that govern its dynamic behaviour. Instead, each component model is generic and obtained directly from the DIGSILENT PowerFactory library.

Simulation duration: Simulations are carried out for a duration of up to 40 s. In a real power system voltage instability may occur 300 s after a disturbance due to small-signal interactions of power system components with slow dynamics. Examples of some slow acting devices include OLTC transformers and OEL, both of which are not included in the thesis.

Voltage stability margins: An analytical assessment index is not defined and applied for the study of large-disturbance voltage stability. The voltage trajectory method to be used does not reveal the actual margin to instability. However the method is convenient for easy comparison between OHL and equivalent cable cases.

No validation: The results obtained from the analysis are not compared and validated by measurements or results from other software and models. Hence the validity of the results rely on the models and their use, which is unverified. However, the results and tendencies are to be compared with published research within the scope of the thesis.

Simplified system and results: The results are based on simplified standard benchmark systems, which do not cover every component of an actual modern power system. For this reason the results can only be used for comparative studies of tendencies.

2.3 Methodology

Software and models: DlgSILENT PowerFactory is the software used for performing all necessary simulations of the project. An SMIB model is constructed by connecting the respective elements found in the software. In this software the basic tap and load flow data of the elements need to be defined for power flow solutions. As in the case of 9-bus and 39-bus systems, both models are taken from the examples given in this software. Additionally Matlab is used to process the results exported from PowerFactory and to plot figures presented in the thesis.

Simulations: Dynamic RMS simulations are carried out to obtain the critical clearing time and voltage trajectory of the systems. Simulation events are defined to initiate disturbances and SR-switching. A DPL script is also used to automate the clearing time increment during simulations in order to determine the critical clearing time. Meanwhile, load flow calculations are performed in steady state analysis from which the V , P and Q , V -characteristic curves are obtained. The short-circuit power of each bus in the network can be computed using short-circuit calculations command in the software.

Result analysis: Results from simulations are compared and analysed based on theoretical principles. In the transient stability study, the focus is on interpreting the tendencies displayed by the CCT values from varying line parameters and compensation schemes. As for voltage stability, the voltage trajectories are used to illustrate considerations for dynamic SR-switching.

Stability analysis of single-machine infinite bus system 3

This chapter is an introduction to the transient and voltage stability analysis presented in this thesis. It is an initial comparison of OHL and cables in stability studies, with focus on their parametric differences. The purpose is to illustrate and highlight the main electromechanical dynamics and present those in a simplistic and clear way. A single-machine infinite bus system is used for the analysis which is performed using DIgSILENT PowerFactory.

A discussion of the influence of transmission line capacitance on the classical P, δ -equation for a SMIB system is located in Appendix A.

3.1 Single-machine infinite bus system

The single-machine infinite bus system (SMIB) is described in Section 1.3.1, and reproduced in Figure 3.1 for convenience. The SMIB system is widely used in stability studies for its simplicity, especially when a mathematical approach is desired. The infinite bus is characterized by a constant voltage at constant frequency, regardless of active and reactive power flow. In reality infinite buses do not exist, and does not represent a real power system with electromechanical dynamics. However, with a fixed frequency (e.g. 50 Hz), the infinite bus is providing a convenient reference frame for the display of bus angles for the study of stability in simplified cases. The purpose of the parallel line configuration is for the two ends of the transmission system to maintain connection during and after a large disturbance in Figure 3.1(B).

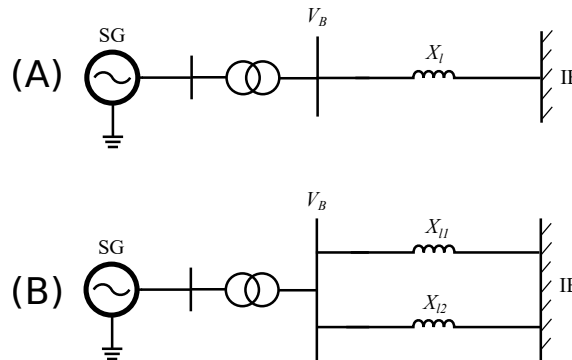


Figure 3.1. (A) Single-line diagram SMIB with one line connecting the electrical machine to the infinite bus, and (B) two parallel and equal lines connecting the two ends.

3.1.1 SMIB in faulted condition

In Section 1.3.1 it is explained how the P, δ -curve change during a fault. When applying a three-phase to ground fault to the SMIB system represented in Figure 3.1(A), all the the current from the generator flows through the fault. This current lags the field voltage E_G by 90° , due to the transient inductance X'_d . Thus, the real power output of the generator is effectively zero. Therefore, if the fault is sustained, the power angle δ will increase indefinitely because the entire input power will be used for acceleration. As described in Section 1.3.1 this may lead to transient instability.

However, P, δ is not the only relevant characteristic of the SMIB system during a fault. Recalling the voltage drop equation presented in (1.11), excessive active and reactive power must be supplied during a fault in order to maintain bus voltage due to the rapid ΔV following the fault. Considering the SMIB system presented in Figure 3.2(A), all of the short-circuit current is reactive, due to the system being purely inductive. The SG and IB must supply reactive power in order to maintain voltage. The SG does so by field current control, resulting in a change of excitation level. An example of this is given later in this chapter. Considering a system with a capacitive line, lumped at the sending end, in Figure 3.2(B). The lumped shunt capacitance acts as a source of reactive power according to (3.1), where $|V|$ is the voltage magnitude across the shunt capacitor. If the voltage across the lumped capacitance drops to $\frac{1}{2}V$ due to the fault, the reactive power is reduced by $\frac{1}{4}$. Thus, during system conditions with low voltage, such as a fault, the unregulated generated reactive power drops, which essentially compound the problem. Realistically the capacitance of the line is distributed, and as such the lumped model presented in Figure 3.2(B) does not account for the change in capacitive current as the fault location is changed. As mentioned in Section 1.4 the issue of bus voltages and reactive power balance is a matter of voltage stability. In the SMIB model, which is absent in load dynamics, the voltage stability problem is mainly centred around the reactive power capabilities of the synchronous machine, the voltage control and the parameters of the transmission line.

$$Q_C = \frac{|V|^2}{X_C}, \quad \text{where} \quad X_c = -\frac{1}{\omega C} \quad (3.1)$$

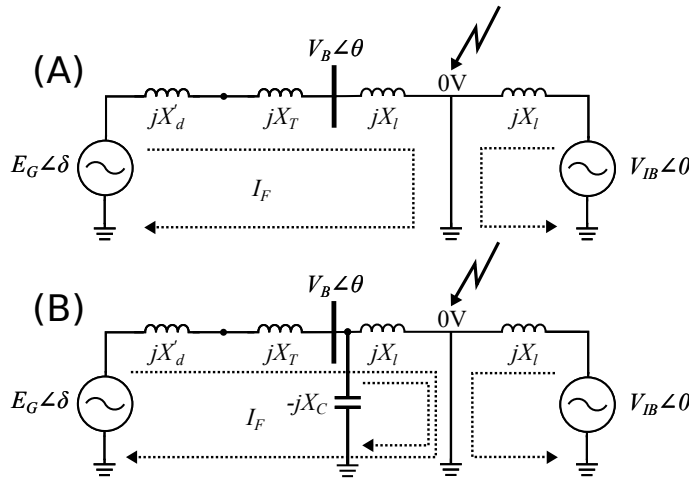


Figure 3.2. Single-line diagram SMIB system under three-phase to ground fault. (A) purely inductive line, (B) line with lumped capacitance.

3.2 Introducing the DIgSILENT PowerFactory SMIB system

In order to analyse the dynamic behaviour of the SMIB system it is modelled using DIgSILENT PowerFactory version 15.1.6. The SMIB system is constructed with two parallel lines, as displayed in Figure 3.3. The system frequency is 50 Hz. The components of the system are the following:

- (A) DIgSILENT standard model synchronous machine. Nominal apparent power: 255 MVA. Nominal voltage: 19 kV. Transient reactance, $X'_d = 0.21$ p.u. Inertia constant, $H = 10$ s.
- (B) 2-Winding 19/220 kV Transformer. Y-Y connected, with both neutrals grounded. Rated apparent power: 500 MVA. Leakage reactance $X_T = 0.5$ p.u.
- (C) Line 1: Lumped parameter nominal pi modelled line. Length, $l = 100$ km. Initially lossless, $R = G = 0$. RMS-simulation applies a three-phase fault at $t_{f,0} = 0.1$ s at a distance d_f from the sending end bus BB1. The fault is cleared by opening the line at both ends at t_c , so that the time under which the SMIB system is faulted is $t_f = t_c - t_{f,0}$.
- (D) Line 2: Lumped parameter nominal pi modelled line. Line parameters and length are exactly equivalent to those of Line 1 (C). This line is not faulted, and remains in service in any operation condition.
- (E) External grid acting as infinite bus. The voltage is 1 p.u. in steady state and acts as angle reference fixed at 0° . The external grid is not an ideal voltage source. Thus, it is not able to keep the voltage at 1 p.u., and the frequency at 50 Hz during a fault. However, it resembles a strong grid with a short-circuit power of 10 000 MVA.

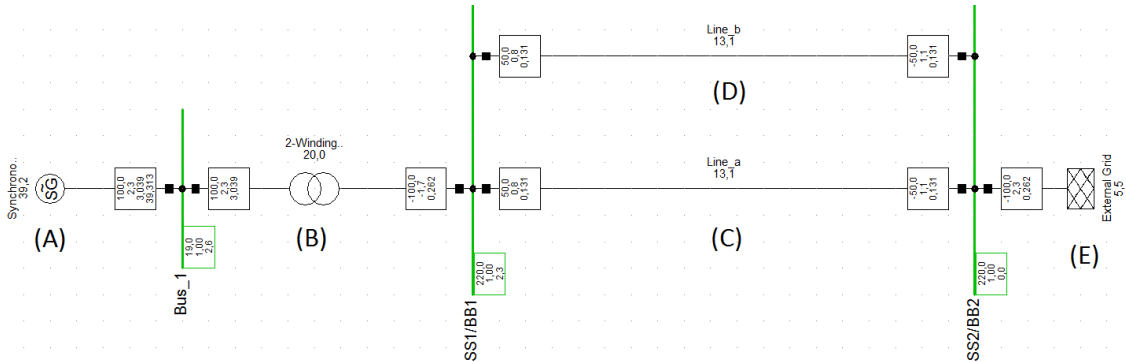


Figure 3.3. Single-line diagram of the SMIB system modelled in DIgSILENT PowerFactory. The markings (A) through (E) indicate the components listed.

3.2.1 Synchronous machine controls in PowerFactory

In PowerFactory v. 15.1.6 the synchronous machine can be modelled as either voltage controlled or power factor controlled. As stated in DIgSILENT documentation [36] the voltage controlled mode is the typical setting for large synchronous generators. Thus, voltage controlled mode is used for the results presented, unless it is desired to force the reactive power output of the generator to highlight certain dynamics. In such case, the use of power factor control will be stated explicitly.

The Local Controller defined as "Const. V" is typically used for large synchronous generators at large power stations which operate in voltage control mode ("PV" mode). When enabling this option, the generator will control the voltage directly at its terminals. As basis for the controlled [p:u:] value, the voltage of the connected terminal is used.

The Local Controller defined as "Const. Q" is typically used for smaller synchronous generators, like the ones embedded in distribution grids, where the power factor is kept constant ("PQ" mode). With this type of control, the user can specify the active and reactive power dispatch of the generator.

Besides the choice of local controller, various plant models can be added to the synchronous machine. The three main control systems are:

- Automatic voltage regulator (AVR), also referred to as excitation system. The purpose of the AVR is to adjust the generator field current to maintain a constant terminal voltage.
- Governor: Used to control the generator speed, helping to maintain a desired frequency.
- Power System Stabilizer (PSS): The purpose of the PSS is to add a signal to the excitation system proportional to shaft speed deviation, and electrical power in case of dual input stabilizer. This adds dampening to the power oscillations following a large disturbance.

A discussion of the impact of the different machine controls is located in Appendix B. The SMIB results presented in this chapter are produced with AVR as the only added control. The argument is that AVR is the most relevant control in the study of large-disturbance stability and the regulation of voltage and reactive power with respect to line parameters and compensation.

3.2.2 Increasing the duration of the fault

Increasing the time under which the SMIB system is faulted t_f , will affect the transient response of the system. In Section 1.3.1 it is described how the swing equation governs the power angle oscillations in response to a fault. If the power angle exceeds a critical value during a fault the machine becomes unstable, unless the fault is cleared before reaching this limit. Figure 3.4 displays how the power angle oscillations increase as a consequence of increased fault duration. When t_f is increased the amplitude of the oscillations increases. The power angle reaches a higher value in the post-fault state, before the rotor speed recovers back to synchronous speed. This concept is further explained in Section 1.3.1 Figure 1.9. In all the cases displayed the SMIB system is stable as it recovers to steady state. However, the post-fault steady state power angle is increased compared to the pre-fault value, as the faulted line is taken out of service, resulting in an increased system reactance.

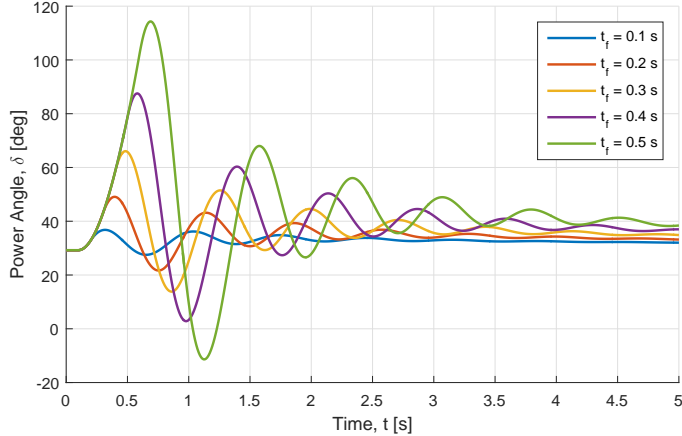


Figure 3.4. Power angle fault response of the SMIB system, as a result of a fault at $t_{f,0} = 0.1$ s. The duration of the fault is increased from 0.1 s to 0.5 s.

3.2.3 Obtaining the CCT in PowerFactory

As t_f is increased the system is approaching its transient stability limit. The maximum permissible t_f for stable operation was defined as CCT in Section 1.3.1. In order to evaluate CCT in PowerFactory a transient stability limit must be defined to enable the detection of instability. DIgSILENT PowerFactory has a built-in function to detect whether an electrical machine has lost synchronism. The function is referred to as out of step detection or "pole-slip" in the DIgSILENT manual. Initially this method is used to evaluate CCT for transient stability studies in this thesis. However, after experiencing examples of inconsistency in the method and results, the evaluation of CCT by the pole-slip function is discontinued. A description of the pole-slip method is located in Appendix E together with a discussion of the inconsistencies which are discovered.

Instead a fixed power angle limit δ_{lim} is set. If the power angle δ reaches δ_{lim} , the machine is considered unstable. In [2] it is stated that 90° is considered the nominal limiting value for a two machine system. However, in [2] the following is emphasized: "*Limiting values of power transfers and angular separation are a complex function of generation and load distribution.*" Thus, δ_{lim} is dependent on the network topology and the transmission of active and reactive power. In this thesis δ_{lim} is chosen at 180° separation, as acceleration beyond this angle theoretically implies that the electrical machine changes from a generator to a motor. δ_{lim} should not be confused with the critical clearing angle. The critical clearing angle is the maximum allowed angular separation at the time of fault clearing, whereas δ_m is the maximum angle reached after clearing. When the fault is cleared the machine continues to accelerate till it reaches δ_m .

Having defined $\delta_{lim} = 180^\circ$, the CCT becomes the maximum allowed clearing time t_c , which ensures that the power angle separation never reaches or exceeds 180° . In order to assess CCT for the SMIB system in PowerFactory a simple DPL (DIgSILENT Programming Language) script is executed. The DPL script runs a for-loop, which performs RMS simulations while increasing the clearing time t_c , and thus the fault duration t_f . This procedure is iterated until $\delta_m \geq 180^\circ$, and the fault duration t_f reached in that iteration is the CCT. The DPL code used is located in Appendix D.

It can be argued that the choice of $\delta_{lim} = 180^\circ$ is weakly motivated, as it is chosen without consideration of machine parameters and initial conditions of the system. Undoubtedly the method introduces a large uncertainty to the actual CCT values obtained. However, the purpose of this thesis is to compare generic OHL and cable based networks, and study the tendencies and sensitivities of line parameters. Thus, the differences in system behaviour are more relevant than the actual values obtained.

3.3 Sensitivity study of line parameters on the SMIB system

Now, sensitivity studies of the line parameters L , C and R are performed on the SMIB system in PowerFactory. Studies of shunt conductance G are not performed, due to its typically negligible value. When a parameter is changed, it is done to both parallel lines simultaneously, so that they are always equal. Variations in power angle response and CCT are presented to study the impact on transient stability, while voltage and reactive power trajectories are displayed for the study of voltage stability.

3.3.1 Sensitivity of transmission line inductance

The transmission lines of the SMIB system are initially chosen to be purely inductive. The first step of the line parameter sensitivity study is to investigate the influence of increasing X_l . Figure 3.5 show how the CCT is decreased as the reactance of the line is increasing. Two cases are displayed, one where the fault is at the sending end $d_f = 1$ km, and one where the fault is at the receiving end $d_f = 99$ km. The CCT is longer if the fault is located at the receiving end of the system. In other words, the system is more stable for faults farther away. Both SG and IB supplies reactive power to the fault, but as the distance to the fault is increased, less reactive short-circuit current from the SG will be transferred through the purely inductive faulted line. When the fault is located at 99 km from the SG bus, the reactance of the fault loop, illustrated in Figure 3.2, is significantly bigger than when it is at 1 km. This is simply due to the total line impedance being a linear function of the length:

$$Z_l = (R + j\omega L)l \quad [\Omega] \quad (3.2)$$

The SG has finite short-circuit capability, and if less reactive power is supplied to the fault, more active power can be transferred to the IB on the healthy parallel line. In other words the P, δ -curve of the generator does not drop to zero during the fault, and it is able to supply active power to the IB. Recalling Figure 1.9, this results in a steeper P, δ -characteristic during the fault. As it is explained in Section 1.3.1, the shape of the P, δ curve is directly influencing the kinetic energy areas A_1 and A_2 . When the fault is far away, $d_f = 99$ km, the kinetic energy gained due to acceleration A_1 is smaller, due to the steeper P, δ -curve during the fault. The equal area criterion states that if $A_1 > A_2$, the system becomes unstable.

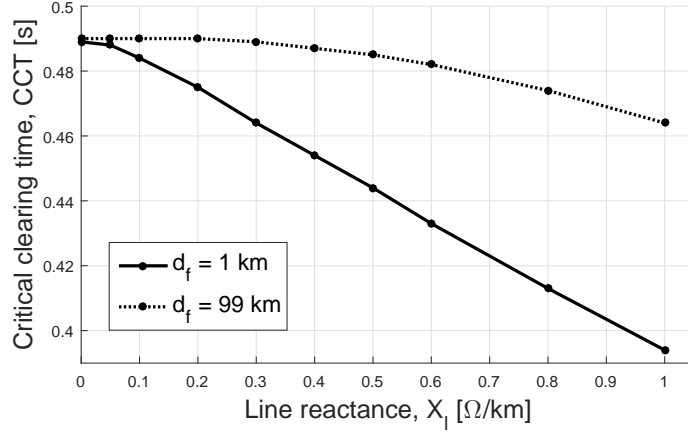


Figure 3.5. CCT sensitivity of line reactance X_l in the SMIB system. The line is purely inductive, so that $R = C = G = 0$. Total length of the line, $l = 100$ km.

The distance to the fault d_f impacts the CCT mainly by influencing the during-fault power transfer capabilities. When observing Figure 3.5 it may seem misleading that increasing line reactance detriment the CCT, when it is just deduced how an increased reactance has a positive effect on CCT. However, increasing X_l affects the impedance seen by the SG in every operational state, pre-fault, during fault and post-fault. The absolute difference in pre-fault and post-fault reactance increases as the line reactance goes up, due to the topological change from parallel line configuration to single-line configuration, as the faulted line is taken out of service. This is illustrated arbitrarily in Figure 3.6. Thus, increasing X_l implies a greater and greater difference between the pre-faulted and post-faulted SMIB systems. The P, δ -curve is governed by the equation (3.3), which is repeated here for convenience. The active power output is inversely proportional to the system reactance.

$$P = \frac{E_g V_b}{X} \sin(\delta) \quad (3.3)$$

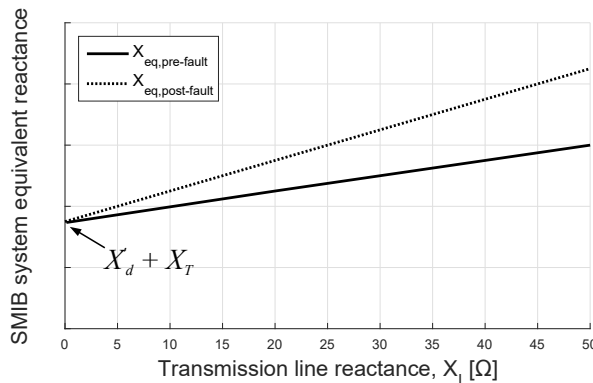


Figure 3.6. Comparison of pre-fault and post-fault SMIB system equivalent reactances, as a function of line reactance X_l . The offset is due to the SG reactance X'_d and transformer reactance X_T . The values are arbitrarily chosen.

When the difference between pre-fault and post-faulted systems changes, it impacts the change in system states A, B, C, D and E, in Figure 1.9. An increased difference in the P, δ -curve between the systems states, will affect the stability negatively by causing increased power angle oscillations.

An observation is that the difference in CCT between having a fault at $d_f = 1$ km and $d_f = 99$ km, increases as X_l increases. The slope of the two curves in Figure 3.5 are different, so that:

$$\frac{\Delta \text{CCT}(d_f = 1 \text{ km})}{\Delta X_l} > \frac{\Delta \text{CCT}(d_f = 99 \text{ km})}{\Delta X_l} \quad (3.4)$$

The increasing X_l decreases the CCT due to an increased difference in P, δ -curves, while moving the fault farther away from the SG improves the CCT by improving the during-fault P, δ -curve. Increasing line reactance is equivalent of increasing the distance in faulted condition. Thus, the observation that the CCT is lowered as X_l increases, indicate that the increasing difference between pre-fault and post-fault systems has a dominant negative impact on the stability.

The behaviour of power angle δ and active power output P in response to a three-phase fault is displayed in Figure 3.7. The fault location d_f and fault duration t_f are constant. The figure shows how there is only a small difference in post-fault (steady state) power angle between the cases. The first swing behaviour from when the fault is applied at $t_{f,0} = 0.1$ s to when it is cleared at $t_c = 0.5$ s is very similar.

However, the case of low reactance displays a slightly larger first swing compared to higher values of X_l . The reason is a bigger change in P, δ -curve when going from pre-fault to during fault condition, as the reactance between the fault and SG is lower, which allows for more active power transfer. The effect is exactly similar to the case of changing the fault location.

After the fault is cleared, the δ oscillations are larger and continues for a longer duration, the higher value of X_l . This is due to the machine accelerating to a higher δ_m value, with reference to Figure 1.9, as a result of the increasing difference between pre-fault and post-fault systems. The behaviour can be confirmed by comparing different scenarios of fault clearing.

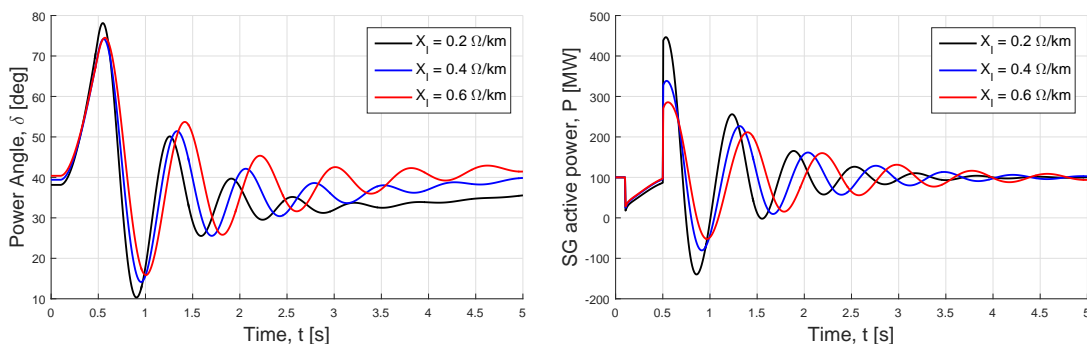


Figure 3.7. SG power angle and active power output for various values of X_l . The fault is applied at $t_{f,0} = 0.1$ s and cleared at $t_c = 0.5$ s, so that $t_f = 0.4$ s. The fault location is $d_f = 25$ km.

In Figure 3.8 two cases of fault clearing are compared. The system parameters, initial conditions and fault duration are exactly equal in the two cases. The difference on the two cases displayed is the method of fault clearing. In Case 1, the fault is cleared by taking the line out of service, which cause the post-fault reactance to be higher than the pre-faulted one. In Case 2, the fault is removed, and the system returns to its pre-faulted topology. Figure 3.8 shows that up until the point of fault clearing, the two systems behave identically. The system which is changed to its pre-fault topology (Case 2) accelerates to a lower maximum angle δ_m . This realisation supports the observation that increasing X_l in the SMIB system, increases the difference between pre-fault and post-faulted systems, which impacts the power angle oscillations.

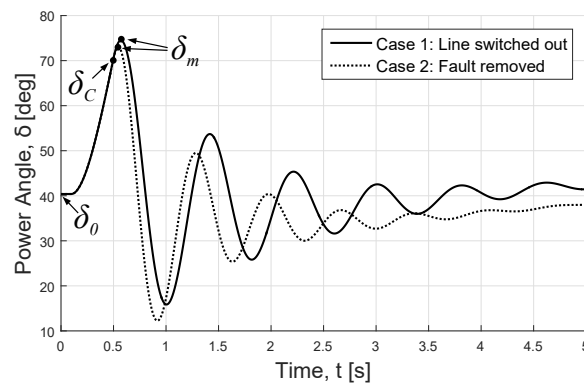


Figure 3.8. Comparison of power angle response in two cases of fault clearing. In Case 1 the line is switched out of service. While in Case 2 the fault is removed, and the line stays in service.

Line reactance influence on voltage and reactive power trajectories

The increase in line reactance X_l is not only affecting the P, δ -characteristics related to transient stability. In Figure 3.9 the reactive power output of the generator, and the generator bus voltage fault response are displayed. The figure gives indications towards the voltage stability of the system. When the fault occurs the voltage at the SG bus drops, and the reactive power output increases due to the purely inductive faulted system and the ΔV between the ideal fault and the bus. The V, Q -behaviour is highly dependant on the AVR system of the synchronous generator. During the fault the AVR system will try to bring the bus voltage back to 1 p.u. by increasing the field current. The increased field current, will in turn increase the excitation voltage E_g in equation (3.3), leading to what is referred to as a higher excitation level, and the SG is outputting more reactive power. When the fault is cleared, the SG becomes under-excited as it is absorbing reactive power supplied by the IB. The main observation however, is that increasing the line reactance, results in an increased bus voltage during the fault. The reason is the increased reactance between the SG and the fault, limiting the local voltage drop.

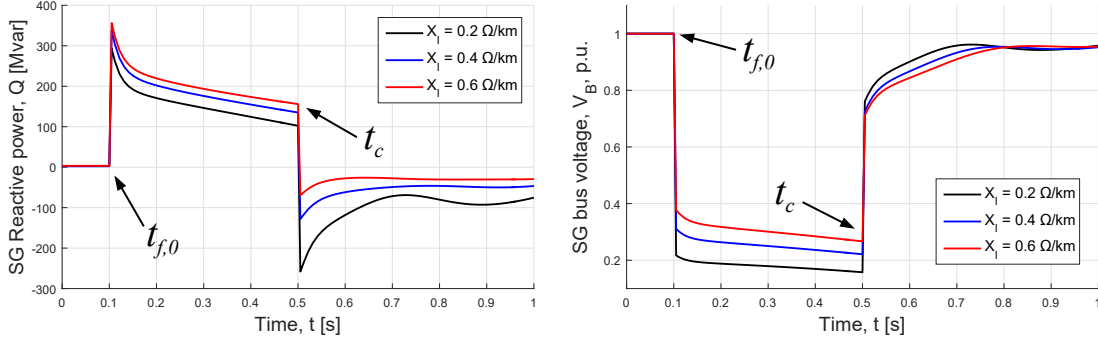


Figure 3.9. SG reactive power output and bus voltage for various values of X_l . The fault is applied at $t_{f,0} = 0.1$ s and cleared at $t_c = 0.5$ s, so that $t_f = 0.4$ s. The fault location is $d_f = 25$ km.

3.3.2 Sensitivity of transmission line capacitance

Now capacitance is added to the lossless transmission line. The line reactance is now fixed at a value of $X_l = 0.181 \Omega/\text{km}$ ($L = 0.576$ H), which is an example value of underground cables given by CIGRE in technical brochure B1.30 [37].

Figure 3.10 show the behaviour of CCT on the SMIB system as the transmission line capacitance is increased. An observation is that there is an insignificant difference in CCT between the two cases of fault location (1 km and 99 km), as the capacitance is increased. The small difference between the two cases, comes from the difference in line reactance between the SG and the faulted location. Transmission line capacitance is a parallel component, and does not affect the equivalent reactance between the SG and the fault in the same way as line inductance or resistance does. This behaviour indicates that the main influence of capacitance on transient stability, lies in the impact on post-fault and pre-faulted system power angle, rather than the faulted network topology.

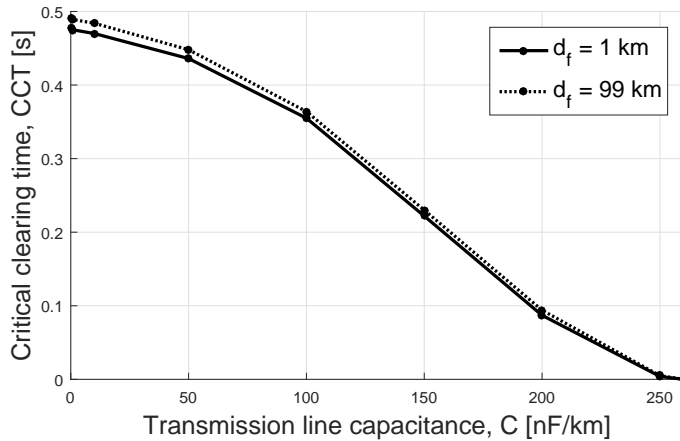


Figure 3.10. CCT sensitivity of line capacitance C in the SMIB system. The line is lossless, with $X_l = 0.181 \Omega/\text{km}$. Total length of the line, $l = 100$ km.

In order to exclude that the result is significantly influenced by the modelling of the line, the study is repeated for a SMIB system with a line divided in 5 π -sections of 20 km each, to be compared with the results of the 100 km π -modelled line.

Table 3.1 compares CCT values calculated for the two different models. The difference between the models is 0 % in most cases, with a solution time step-size of 1 ms. There is a slight indication that the difference increases as the stability limit of the system is lowered and the CCT approaches 0s. However, the differences of 50 % and 25 % are meaningless at a resolution of 1ms, as the absolute difference is just 1ms and 2ms. Furthermore, comparison of the two different line models at various fault locations ($d_f = [1\ 25\ 50\ 75\ 99]$ km) shows that there is no significant difference in CCT results.

Table 3.1. Comparison of CCT values calculated for different capacitance values in two cases of line modelling: (1) single π -model, (2) series of 5 equal π -sections.

C	Single π -section		5 π -sections		Relative difference	
	CCT ₁	CCT ₉₉	CCT ₁	CCT ₉₉	1 km	99 km
0 nF/km	0.477 s	0.491 s	0.477 s	0.491 s	0 %	0 %
10 nF/km	0.470 s	0.484 s	0.470 s	0.484 s	0 %	0 %
50 nF/km	0.436 s	0.448 s	0.436 s	0.448 s	0 %	0 %
100 nF/km	0.355 s	0.364 s	0.355 s	0.363 s	0 %	0.27 %
150 nF/km	0.222 s	0.230 s	0.221 s	0.229 s	0.45 %	0.43 %
200 nF/km	0.087 s	0.094 s	0.085 s	0.093 s	2.30 %	1.06 %
250 nF/km	0.004 s	0.005 s	0.002 s	0.003 s	50 %	25 %

Improving the distribution of capacitance by including more π -sections, has no important influence in the tested cases of fault location. However, the actual value of capacitance influences the CCT considerably. Figure 3.11 compares CCT values for $C = 10$ nF/km and $C = 200$ nF/km at various fault locations d_f . Generally the CCT is lowered for every fault distance as the capacitance is increased. This is in agreement with the overall sensitivity in Figure 3.11. However, the dependency on fault location is substantially different in the case of $C = 10$ nF/km compared to that of $C = 200$ nF/km. When the capacitance is low, the transient stability is mainly influenced by the inductive reactance between the generator and the fault, as it is described in Section 3.3.1. As the distance to the fault approaches the middle of the line, the stability limit is highly improved. As the capacitance is increased the tendency of CCT as a function of d_f remains. However, the dependency on d_f due to X_l is less distinct, as it is dominated by the impact of the capacitance. In other words, transmission line capacitance appears to be influencing the transient stability differently than line inductance. This result support the aforementioned observation that series and parallel components affect the large-disturbance stability differently as d_f is changed.

Figure 3.12 show power angle and active power output of the SG in response to a three-phase fault at $d_f = 25$ km with a duration $t_f = 0.4$ s. As the capacitance of the uncompensated transmission line is increased the steady state power angle is increased from 40° to 157° .

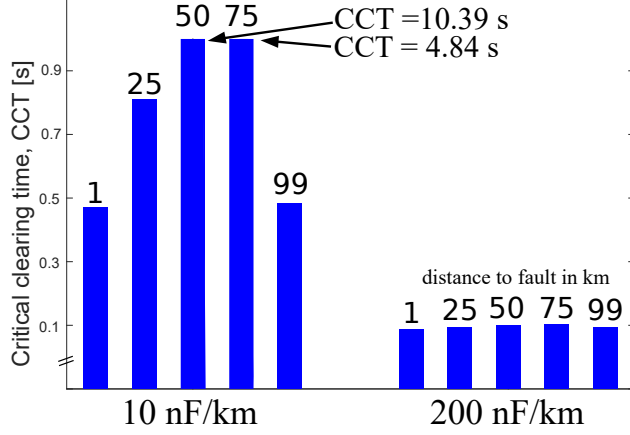


Figure 3.11. Comparison of CCT values for two cases of transmission line capacitance and various fault locations: $d_f = [1 \ 25 \ 50 \ 75 \ 99]$ km.

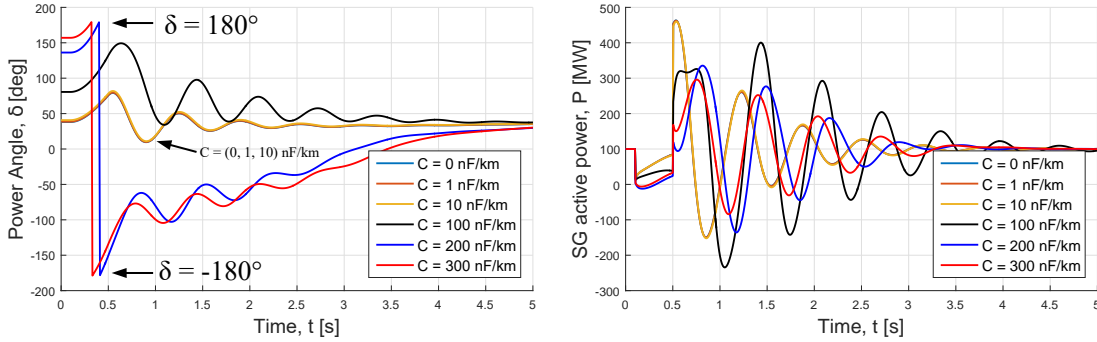


Figure 3.12. SG power angle and active power output for various values of C . The fault is applied at $t_{f,0} = 0.1$ s and cleared at $t_c = 0.5$ s, so that $t_f = 0.4$ s. The fault location is $d_f = 25$ km.

At 220 kV and 50 Hz adding $C = 300$ nF/km to each of the two π -modelled parallel lines in the SMIB system, is equivalent of inserting a source of reactive power at both ends of the system equal to:

$$Q_c = \frac{V_{LL}^2}{X_C} \Rightarrow Q_c = V_{LL}^2 \cdot \omega C \quad (3.5)$$

$$Q_c = (220 \cdot 10^3 \text{V})^2 \cdot 2\pi \cdot 50 \text{ Hz} \cdot 300 \cdot 10^{-9} \frac{\text{F}}{\text{km}} \cdot 100 \text{ km} = 456.16 \text{ Mvar} \quad (3.6)$$

As the line generates more reactive power, the SG becomes increasingly under-excited in order to absorb the excessive reactive power. The SG changes from outputting 2.47 Mvar to absorbing 352.9 Mvar as the capacitance is changed from 0 nF/km to 300 nF/km. The heavily under-excited state results in a flat P, δ -curve as illustrated previously in Figure 1.12 in Section 1.4. Thus, in order to output 100 MW active power, the machine is operated at a very high power angle in steady state. The cases of 200 nF/km and 300 nF/km are transiently unstable when following the $\delta_{lim} = 180^\circ$ definition. However, the two cases would be considered steady state unstable in a real system, as the initial power angle is beyond 90° . Thus, the result highlight the necessity for local reactive power compensation.

As the capacitance is increased, the power angle oscillations following the fault increases, as it can be seen by comparing the case of 0 nF/km and 100 nF/km. The oscillations can be seen as the effect of a severe change in network topology and reactive power, when changing between the three network states, pre-fault, faulted and post-fault.

1. **Pre-fault:** Increased capacitance results in an increased power angle due to under-excitation of the SG.
2. **During fault:** The reactive power generated by the transmission line drops as the voltage drops due to the fault. The machine changes from being under-excited to over-excited, as the system requires reactive power in order to maintain voltage.
3. **Post-fault:** The faulted line is switched out of service, and the reactive power generated by the two parallel lines is essentially halved compared to the pre-faulted state. The difference between pre-faulted and post-faulted reactive power increases as the capacitance goes up. The power angle continues to increase after the fault is cleared due to the mechanical and electrical unbalance. When the fault is cleared the active power output of the machine spikes, as the P, δ -curve recovers from a faulted condition to post-faulted condition while δ is large.

The sensitivity study of transmission line capacitance indicates that the SMIB power system stability is influenced by uncompensated reactive power, which must be balanced by the two generation units: The SG and the external grid. Increasing capacitance lowers the stability limit, as the synchronous machine experience big changes in excitation mode when exposed to disturbances. Figure 3.13 show the excitation voltage and the excitation current (field current) of the synchronous machine. Increasing the capacitance of the system has a direct impact on the voltage control of the machine. When the capacitance of the system is low, the AVR is able to regulate the excitation level back to steady state shortly after the fault is cleared. However, at high values of capacitance the terminal voltage of the machine is exposed to the changes in reactive power of the system, and it takes more than 5 s to regulate the excitation level back to a steady state condition. The behaviour is highly dependent on the AVR system of the individual synchronous machine, in this case IEEEEX1 AVR.

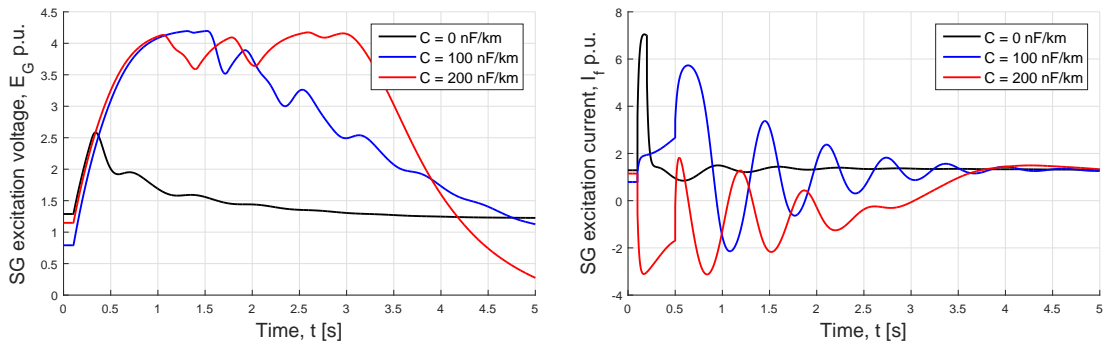


Figure 3.13. SG excitation voltage and excitation current with AVR IEEEEX1 in response to a fault. The fault is applied at $t_{f,0} = 0.1$ s and cleared at $t_c = 0.5$ s, so that $t_f = 0.4$ s. The fault location is $d_f = 25$ km.

3.3.3 Sensitivity of transmission line AC resistance

Now AC resistance is added to the transmission line. The sensitivity of resistance is studied in the case of an equivalent OHL. The constant L and C values are based on the example given in [37]. The values are:

- **Equivalent OHL:** $L = 0.858$ mH/km, and $C = 13.3$ nF/km

Figure 3.14 show the CCT sensitivity of increasing transmission line AC resistance. Typical values of AC resistance are in the area of $0.01 \Omega/\text{km}$ to $0.03 \Omega/\text{km}$. In this area the CCT improves as the resistance is increased. The CCT is more sensitive to changes in resistance when the fault is located at 99 km compared to when it is located at 1 km. When the fault is located far from the SG, there is a higher absolute value of resistance between the SG and the fault, and the faulted topology of the system is affected more by the increase in resistance. Similar behaviour was observed with line reactance, as both are series components. The positive influence of resistance is likely to be caused by a dampening effect. The dampening is analogous to the case of a RLC-circuit with series resistance, where the dampening is directly proportional to the resistance of the circuit.

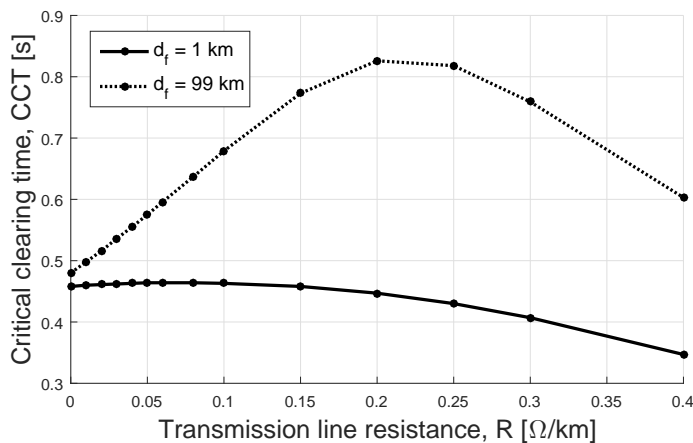


Figure 3.14. CCT sensitivity of line AC resistance R in the SMIB system. Two cases of fault distance d_f are displayed.

When the resistance is increased above a certain value, the CCT is lowered, and the stability limit of the SMIB system is decremented. Figure 3.15 show how the power angle response is changing as the resistance is increased. The fault distance of the cases displayed is 99 km for comparability to the case displayed in Figure 3.14. As the resistance is increased, the steady state power angle increases. The reason is that it requires an increasing angle δ to output 100 MW, due to the resistive part of the impedance seen by the generator. When the resistance is increased, the maximum angle δ_m reached after fault clearing is lowered, and the following oscillations are damped. The red line is the response at $R = 0.2 \Omega/\text{km}$. This is the tested case with best CCT, and it also displays the most damped power angle oscillations. Increasing the resistance to $R = 0.4 \Omega/\text{km}$ as exemplified by the dotted line, displays larger power angle oscillations and lowered CCT.

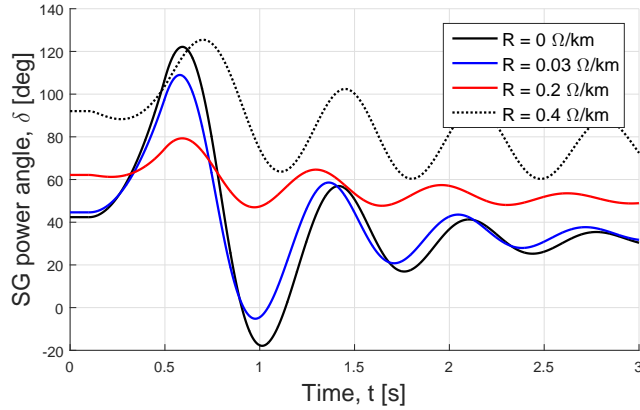


Figure 3.15. SG power angle for various values of R . The fault is applied at $t_{f,0} = 0.1$ s and cleared at $t_c = 0.5$ s. The fault location is $d_f = 99$ km.

An interesting observation is that in the $R = 0.2 \Omega/\text{km}$ case, and more distinct in the case of $R = 0.4 \Omega/\text{km}$, the power angle starts by decreasing when the fault occurs, rather than increasing. The effect is also observed in Figure 3.16, showing that the power output of the SG increases when the fault occurs, whereas it normally drops. This effect is only observed as the fault is located near the external grid. A decrease in power angle following a large disturbance is normally related to the loss of generation or a sudden increase in load, causing the remaining units to initially decelerate.

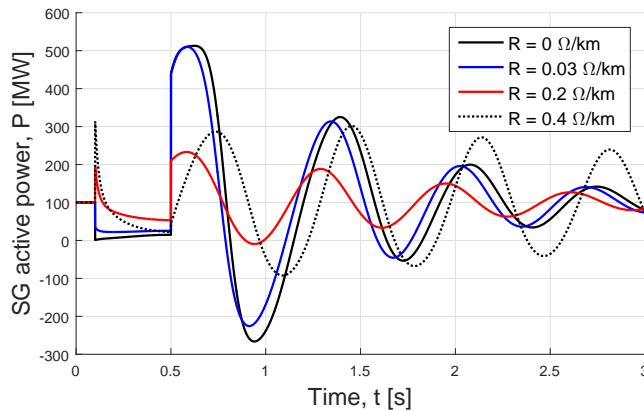


Figure 3.16. SG active power output for various values of R . The fault is applied at $t_{f,0} = 0.1$ s and cleared at $t_c = 0.5$ s. The fault location is $d_f = 99$ km.

As the resistance of the transmission line is increased, the $\frac{X}{R}$ -ratio approaches 1. The line reactance is $0.2695 \Omega/\text{km}$, and it is when R_l is close to this value, that the CCT changes behaviour. This is without accounting for the synchronous reactance, transformer reactance and the negative shunt reactance. The observation that the decrementing behaviour in CCT happens around this value could be an indication that the positive effect of resistance is suppressed as the losses of the system, and the voltage drop associated with the transmission of active power, goes beyond a certain limit.

However, the influence of line resistance and the effects observed is not investigated further. The influence of line resistance is not significantly sensitive in the range of $0.01 \Omega/\text{km}$ to $0.03 \Omega/\text{km}$, where most OHL and cables for HVAC transmission lies. Additionally the behaviour is linear with good approximation in this area, which limits the risk of unexpected behaviour in stability limits.

As to the overall influence of line resistance in stability studies, it can be argued that resistance should not be considered a controlled variable. In order to minimize steady state active power losses, any given transmission line is designed to have as little resistance as possible within the given constraints. Thus, accounting for transmission line resistance is unnecessary in sensitivity studies of system stability.

3.4 Comparison of OHL and cable transmission lines in the SMIB system

The sensitivity studies of transmission line L , C and R showed that for the SMIB system increasing either L and C has a negative impact on the transient stability limits. Higher L results in higher impedance seen by the SG while the main influence of C comes from the balance of reactive power and the control of voltages. Thus impacting the excitation levels of the SG, leading to increased changes in P , δ -operation points, as the system is disturbed and the topology of the network changes. In the SMIB system, L and C are increased from a point where the SG is operating close to unity power factor. If the sensitivities are carried out on a system in different operating conditions, increasing L or C , is likely to have a positive impact in a certain range.

In this section the stability of the SMIB system is evaluated when changing the transmission lines from OHL to un-compensated cables, and when changing from cables to compensated cables with different simple schemes of shunt reactor switching. The electrical parameters of the equivalent OHL and cables are chosen based on [37], and are shown in Table 3.2.

Table 3.2. Equivalent OHL and cable electrical parameters used in SMIB modelling and stability comparison [37].

	L [mH/km]	C [nF/km]	R_{AC} [m Ω /km]
OHL	0.858	13.3	23.1
Cable	0.576	234	13.3

The results of the sensitivity study in Section 3.3.2 support the fact that it is necessary to compensate the reactive power generated by the capacitive cable at high voltage levels. Thus the SMIB model in DIgSILENT PowerFactory is expanded to include four switchable shunt reactors divided between the sending and receiving end of the two parallel lines in the SMIB system. Figure 3.17 show the single-line diagram of the SMIB system with shunt reactors.

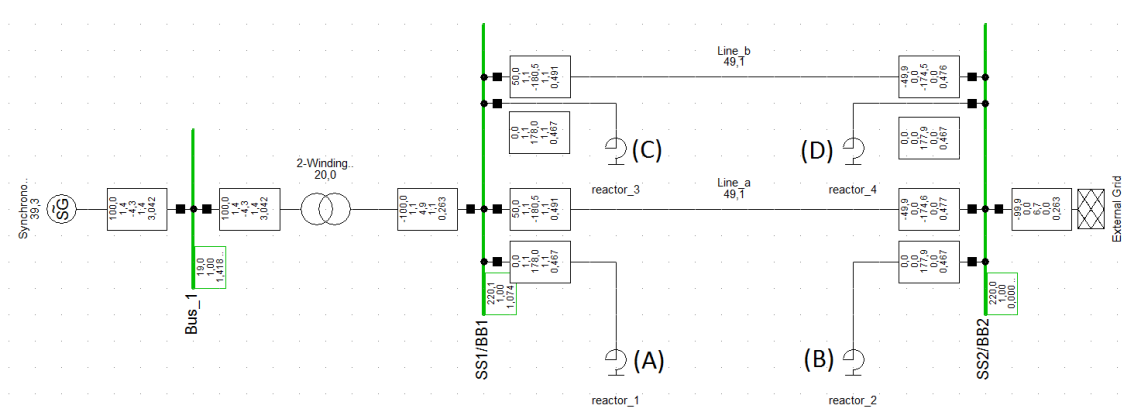


Figure 3.17. Single-line diagram of the SMIB system modelled in DiGSILENT PowerFactory. A, B, C and D indicate the four switch-able shunt reactors.

The four shunt reactors are dimensioned, such that each of them compensate 50 % of the reactive power generated by one of the two parallel cables. The reactive power of each shunt reactor is denoted Q_{SR} and is calculated in (3.7). As a consequence of implementing four shunt reactors of 177.9 Mvar, the reactive power generated by the cable transmission system is compensated 100 %, with a distribution of 50 % at each end.

$$\begin{aligned} \text{Shunt reactor dimensioning: } Q_{SR} &= \frac{1}{2} Q_c \Rightarrow & (3.7) \\ Q_{SR} &= \frac{1}{2} (220 \cdot 10^3 \text{V})^2 \cdot 2\pi \cdot 50 \text{ Hz} \cdot 234 \cdot 10^{-9} \frac{\text{F}}{\text{km}} \cdot 100 \text{ km} \\ Q_{SR} &= 177.9 \text{ Mvar} \end{aligned}$$

For analysis and comparison of stability performance, six different cases of transmission lines and switching of shunt reactors are defined:

1. **OHL base case:** Both lines are modelled with equivalent OHL parameters, with all four shunt reactors disconnected in every operation state.
2. **Un-compensated cables:** Both lines are modelled with equivalent cable parameters. The system is un-compensated, as the four shunt reactors are disconnected in every operation state.
3. **SR, no switching:** Lines are cables with 100 % compensation. The four shunt reactors are connected in every operation state.
4. **SR fault-switch-out:** Lines are cables with 100 % compensation in steady state. When the fault occurs at $t_{f,0}$, all four shunt reactors (A B C D) are disconnected. All shunt reactors remain disconnected for the remaining simulation.
5. **SR A-B fault-switch-out:** Lines are cables with 100 % compensation in steady state. When the fault occurs at $t_{f,0}$, shunt reactors of the faulted line (A and B) are disconnected for the remaining simulation time. Shunt reactors of the healthy line (C and D) stay connected.
6. **SR A-B-C-D switch-out, C-D reconnect:** Lines are cables with 100 % compensation in steady state. When the fault occurs at $t_{f,0}$, shunt reactors of the faulted line (A and B) are disconnected for the remaining simulation time. Shunt reactors of the healthy line (C and D) are likewise disconnected at $t_{f,0}$, but are reconnected at t_c , when the fault is cleared by taking the faulted line out of service.

The CCT for the different cases is calculated by the use of a DPL script in PowerFactory. For cases 4 and 5, the switching of shunt reactors is independent of the fault duration, and is easily set up by defining static switch events occurring at the fault incident time $t_{f,0}$. However, in case 6, the disconnection of shunt reactors (SR) must be timed with the removal of the faulted line, at t_c . In the DPL script for calculation of CCT t_c is incremented in iterations, till the stability limit δ_{lim} is reached. Thus, the switching of SR C and D must be incremented concurrently. The procedure is visualised by a flow diagram in Figure 3.18.

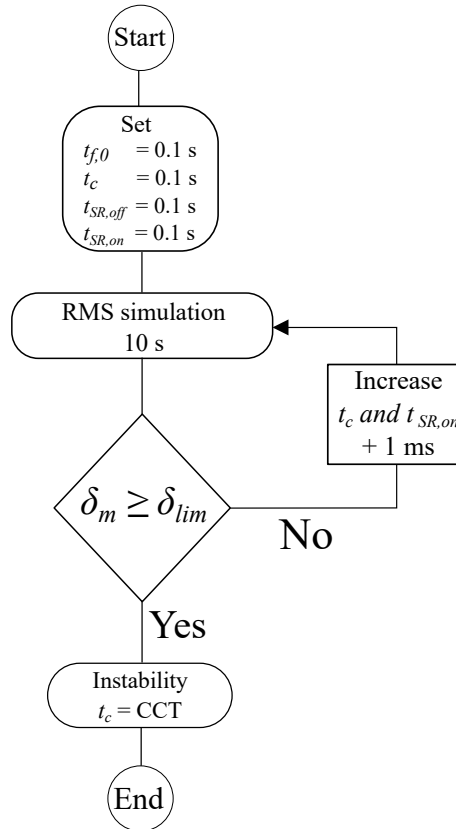


Figure 3.18. Flow diagram of the CCT method used for Case 6 on the SMIB system.

The CCT values of the case studies are compared in Figure 3.19. The results shown are for a three-phase fault at 1 km, with removal of the fault by switching the faulted line out. Placing the fault at 99 km leads to similar results. As expected, when changing from an OHL system in Case 1 to a un-compensated cable system in Case 2, the CCT of the system drops to just 17 ms and it is considered unstable, both in steady state and transiently. As the transmission line is compensated in Case 3, the CCT is significantly improved and in this case just above the equivalent OHL case.

Case 4 show the impact of disconnecting all four shunt reactors at the fault incident $t_{f,0}$. As the system is faulted, it absorbs an increased amount of reactive power. Shunt reactors consume reactive power, thus disconnecting shunt reactors in a faulted system condition is expected to have a positive stability effect, as it should be analogous to injecting reactive power. However, the results in Figure 3.18 show that disconnecting all shunt reactors at $t_{f,0}$ leads to a transiently unstable system.

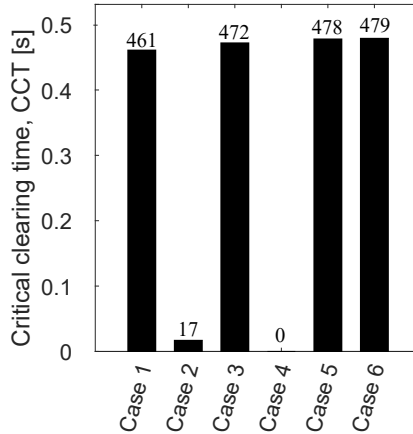


Figure 3.19. Simulated CCT values for different cases of transmission lines and switching of shunt compensation. The values above each bar is the actual CCT in ms.

Observing the power angle δ for Case 4 in Figure 3.20 reveals that the SG does not lose synchronism in the first-swing. Actually Case 4 display similar first-swing behaviour as case 3, 5 and 6, all of which has a high CCT value. In Case 4, following the second power swing, the angle separation of the SG and the external grid increases. Thus the instability of Case 4 is likely to be the consequence of not reconnecting the compensation of the healthy transmission line, leading to an unstable post-faulted system.

In Case 5, the shunt reactors of the faulted line are disconnected, while the shunt reactors of the healthy parallel line stay in operation. Case 5 display slightly better CCT performance, than Case 3, where all shunt reactors stay in operation during the fault. This indicates that lowering the required reactive power during a fault, by disconnecting shunt reactors, does have an improving effect on transient stability, as long as the healthy lines are still compensated. Case 4 exemplifies the importance of reconnecting shunt reactors. The small improvement of just 6 ms, between Case 3 and Case 5, indicates that the lowered reactive power demand due to shunt reactor switching, is not providing sufficient leverage to make a significant difference in the case displayed. Although it is important to note that the fault is located at 1 km, which causes a severe voltage drop at the bus, which can be seen in Figure 3.21. Case 6 displays a very small improvement in CCT, and is the best of all the tested cases. Case 6 is similar to the transiently unstable Case 4, as all shunt reactors are disconnected initially. The important difference is that the shunt reactors (C and D) of the healthy line are reconnected, when the fault is cleared by removal of the faulted line.

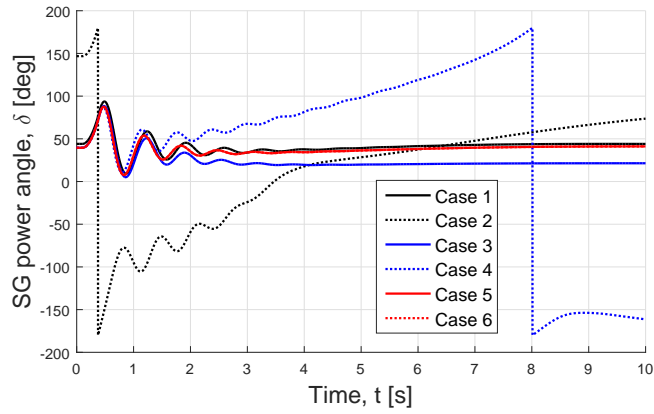


Figure 3.20. Comparison of power angle behaviour for Cases 1-6. The fault is located at $d_f = 1$ km and is cleared at $t_c = 0.4$ s, so that $t_f = 0.3$ s.

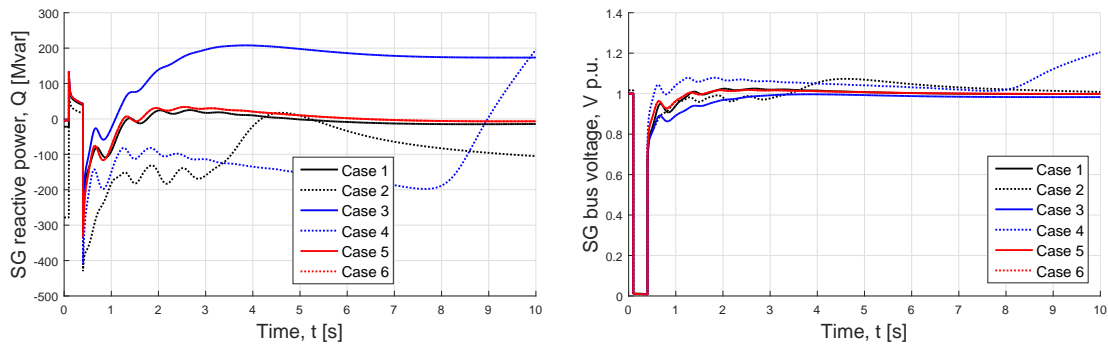


Figure 3.21. Comparison of SG reactive power and bus voltage for Cases 1-6. The fault is located at $d_f = 1$ km and is cleared at $t_c = 0.4$ s, so that $t_f = 0.3$ s.

Transient stability analysis 4

This chapter proceeds with transient stability analysis on generic multi-machine systems. The systems used in the study are IEEE 9-bus and 39-bus systems, and the PowerFactory simulation models are briefly described. The investigated cases consist of OHL and equivalent cable with compensation. The stability index used for the analysis is CCT based upon a three-phase fault on the lines close to the busbars and the observations are compared and discussed. The discussion is done in relation to the analysis carried out in Chapter 3.

4.1 Introduction

Transient stability is a subcategory of power angle stability when the system experiences a severe disturbance as stated in Section 1.2.1. Therefore, the study is mainly focused on the power angle of generators and voltage instability is not investigated in this chapter.

The IEEE 9-bus and 39-bus systems are generally used in literature as test models to perform stability studies. The 9-bus system is first introduced in [25] while the 39-bus system is simplified from the transmission system in the New England Area, USA. Being established systems, the transmission network in both are made up of only OHL.

IEEE 9-bus system represents a small sized multi-machine system which is used for analysis in the project and is shown in Figure 4.1. The 230 kV grid consists of three generators with transformers and three loads interconnected by six transmission lines in the network. A corresponding built-in simulation model is available from the DIgSILENT PowerFactory library and is used in this thesis. The loads in the system comprises entirely of constant Z type. Explanation about the load type and its characteristics can be found in Section 5.1. The relevant parameters of each element are located in Appendix C.

Contrary, the IEEE 39-bus test system is a relatively large and complex interconnected system with 10 generators in the network. Figure C.1 shows the graphical representation of the system. A corresponding model is also obtained from the DIgSILENT PowerFactory library. The nominal operating voltage is 345 kV while the loads are modelled with constant I for P and constant Z for Q . The fault event setup is a three-phase ideal fault initiated at $t_{f,0} = 0.1$ s at 1 % and subsequently 99 % of a line. In DIgSILENT PowerFactory the starting point of distance measurement for the lines is Terminal i as presented in Table C.1. These specific locations are used because it would simulate conditions that are close to the worst case scenario for line fault analysis. The initial clearing time, t_c is also set to 0.1 s. CCT of each event is determined by the same method used in the SMIB analysis presented in Section 3.2.3.

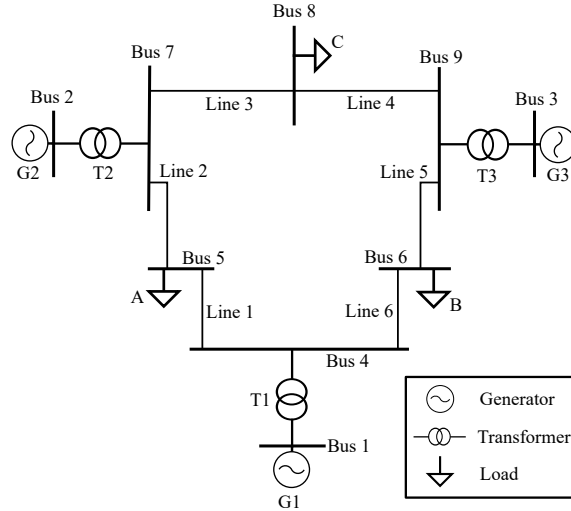


Figure 4.1. IEEE 9-bus system single-line diagram.

Since multi-machine systems are investigated, the number of machines detected to be unstable is also recorded and denoted by n_s . The process is repeated for all the lines in the system. The duration of simulation is chosen to be 11 seconds for each iteration. This is done to ensure that it would cover both first-swing instability and interarea instability as explained in Section 1.2.1. The effects of the interarea oscillations would be more likely detected in the 39-bus system due to its larger scale. The process flow of determining the CCT of an event is shown in Figure 4.2.

It is important to note that the CCT method is used to find the stability limit of a generator which may not necessarily reflect the stability of the system as a whole. In practice, when a generator loses synchronism it would be disconnected from the grid after which the system may still be able to maintain stability. Nevertheless the CCT values found are taken to be the stability indicators of a system in the project.

As mentioned in Section 1.3.2, the stability defining parameter of a multi-machine system is the angular separation between generators. Consider a simple system with various identically placed generators of different ratings, when the system is subjected to severe disturbance, there is typically one candidate generator or a group of generators in the system likely to deviate from the remaining machines which are known as critical machines. These critical machines are generally the weak machines responsible for any loss of synchronism. One of the ways to identify such machines is to compare the inertia constant H or short-circuit power of the machines in the system.

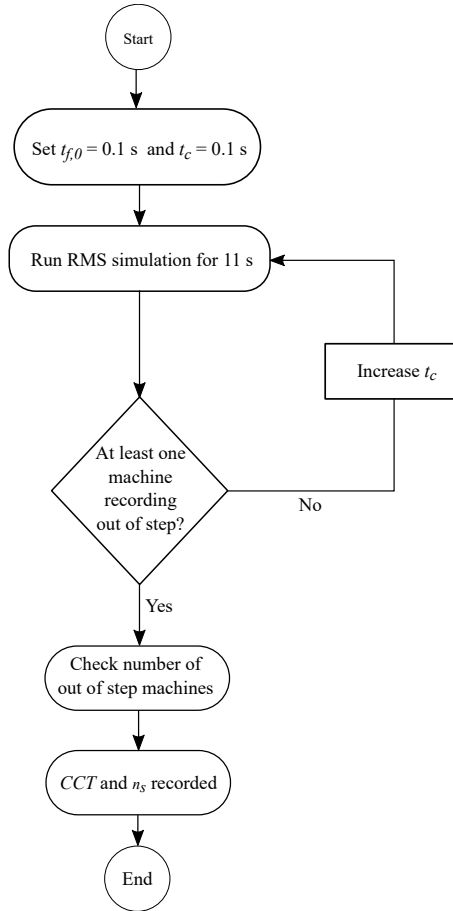


Figure 4.2. Flow diagram of the CCT method for a single event in multi-machine system.

4.2 IEEE 9-bus transient stability analysis

This section presents the analysis of all the study cases carried out on the IEEE 9-bus system with regards to transient stability. The default DIGSILENT PowerFactory 9-bus model is used as the base model for initial sensitivity study. It is followed by increasing line shunt capacitance, replacing OHL with cable and introducing compensation to the cable-based system.

4.2.1 IEEE 9-bus transient stability base case

In this case, the fault conditions as described in Section 4.1 are simulated using the base model. The model is set to operate at default settings and G1 being the generator with the highest H by referring to Table C.2, is used as the reference machine. The angular separation of machines are measured relative to the angle of the reference machine. CCT is determined for each event and tabulated in Table 4.1 in accordance to the line at which fault is applied. The subscript notation of CCT refers to the location of the fault. For example, CCT_1 stands for the CCT when fault is initiated at 1 % of the line. Terminal i is included in the table for convenience. Maximum of n_s is 2 as unstable detection is not possible for G1.

Table 4.1. CCT recorded for fault applied at each line in base case.

Faulted Line	Terminal i	CCT ₁ [ms]	n_s [-]	CCT ₉₉ [ms]	n_s [-]
Line 1	Bus 5	248	1	197	1
Line 2	Bus 7	85	2	172	2
Line 3	Bus 7	117	1	182	1
Line 4	Bus 8	200	1	152	1
Line 5	Bus 9	127	2	228	2
Line 6	Bus 6	275	2	200	2

Based on Table 4.1, the CCT tends to be higher when the fault is located at a distance farther away from generators. This observation is expected and it verifies the principle explained in Section 1.3.1 because the generator could transfer more active power with increase in the fault distance away from the sending end, thus having a greater power curve during fault and improving system stability.

Furthermore, the system has a higher stability margin when the fault happens nearer to generator G1 as observed by the higher average CCT values recorded when fault is simulated at Line 1 and Line 6. This is due to G1 having the highest inertia constant, H as compared to G2 and G3. In any fault event, the generator that is most affected by the disturbance is the one located nearest to the fault location. Higher H translates into slower increase in power angle when subjected to disturbance according to (1.2) and therefore able to sustain fault for a longer period before exceeding the stability limit.

A similar investigation is carried out by changing the reference machine of the base model to G2 which can be found in Appendix F. In summary, the new case study records the same CCT values found in the base case.

4.2.2 Increasing line capacitance

This section investigates the influence of increasing line capacitance of the base model on the system stability. The sensitivity study can be treated as a transitional analysis to the equivalent cable-based system. As mentioned in Section 1.1, the main difference in using cables is the much higher capacitance value. When using the parameter transformation ratios as proposed by [37] in the process of replacing the lines with equivalent-cables which is shown in Section 4.2.3, the model becomes steady-state unstable and power flow simulation is not possible. Instead the capacitance of each line is multiplied initially by a small capacitance factor, F_c and increased in steps further because in this way simulations could be performed until a certain limit of F_c is reached.

Figure 4.3 shows the CCT sensitivity with line capacitance obtained from simulations performed with fault at 1% of the first three lines. A general observation can be made that the stability performance of the system has a negative tendency with increase in line capacitance. This is in coherence with the findings in the SMIB analysis and is explained in Section 3.3.2.

The system has no stability tolerance margin when F_c reaches 5 which is well below the typical cable-OHL capacitance ratio, thus it is imperative that compensation devices be placed together with cables in the network.

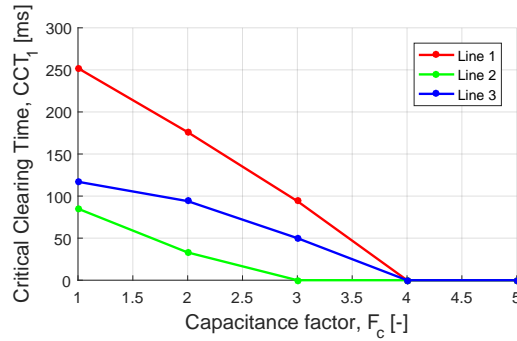


Figure 4.3. CCT₁ versus F_c . Base case is indicated by $F_c = 1$.

4.2.3 Equivalent cable system with full reactive power compensation

In this section the case is presented whereby all the lines are considered to be replaced with corresponding equivalent cables. The reactive power generated by the capacitance of the cables is fully compensated with shunt reactors. The equivalent cables are modelled by multiplying the electrical parameters of the OHL lines in the base model with the respective coefficients. The coefficients are calculated from the values given in [37] as follow:

$$\text{Capacitance coefficient, } k_c = \frac{C_{Cable}}{C_{OHL}} = \frac{234 \frac{\text{nF}}{\text{km}}}{13.3 \frac{\text{nF}}{\text{km}}} \approx 17.6 \quad (4.1)$$

$$\text{Inductance coefficient, } k_l = \frac{L_{Cable}}{L_{OHL}} = \frac{0.576 \frac{\text{mH}}{\text{km}}}{0.858 \frac{\text{mH}}{\text{km}}} \approx 0.671 \quad (4.2)$$

$$\text{Resistance coefficient, } k_r = \frac{R_{Cable}}{R_{OHL}} = \frac{13.3 \frac{\text{m}\Omega}{\text{km}}}{23.1 \frac{\text{m}\Omega}{\text{km}}} \approx 0.576 \quad (4.3)$$

The new line parameters would be computed according to the following:

$$C_{new} = C_{base} \cdot k_c \quad (4.4)$$

$$L_{new} = L_{base} \cdot k_l \quad (4.5)$$

$$R_{new} = R_{base} \cdot k_r \quad (4.6)$$

where subscript *new* refers to the new parameters whereas *base* is for the base case.

Next the reactive power generated by each equivalent cable is calculated using equation (4.7). This is necessary to determine the sizing of the shunt reactors. Using 230 kV and $2\pi 50$ rad/s for V_{LL} and ω respectively, computation of (4.7) for each line yields its reactive power generation as presented in Table 4.2.

$$Q_c = V_{LL}^2 \cdot \omega C_{new} \quad (4.7)$$

In order to accomplish full reactive compensation of a line, shunt reactors have to be able to absorb all the reactive power generated by the line.

Table 4.2. Reactive Power generated from uncompensated equivalent cables.

Line	Q_c [Mvar]
Line 1	309.8
Line 2	538.6
Line 3	262.2
Line 4	367.8
Line 5	630.1
Line 6	278.1

Therefore the total rating of shunt reactors are assumed to be equal to the reactive power generated by the line capacitance. This is done by not taking into consideration the reactive power demand by the line itself. The allocation of the shunt reactors should in practice be based on economic feasibility as well as steady state and transient stability studies. However, symmetrical arrangement is deployed whereby the reactive load are distributed equally between two shunt reactors and placed on both ends of each line. The procedure is repeated likewise for all the lines and the new case schematic representation is presented in Figure 4.4. The shunt reactor on each side of any line is sized half the reactive power generation of the respective line as listed in Table 4.2.

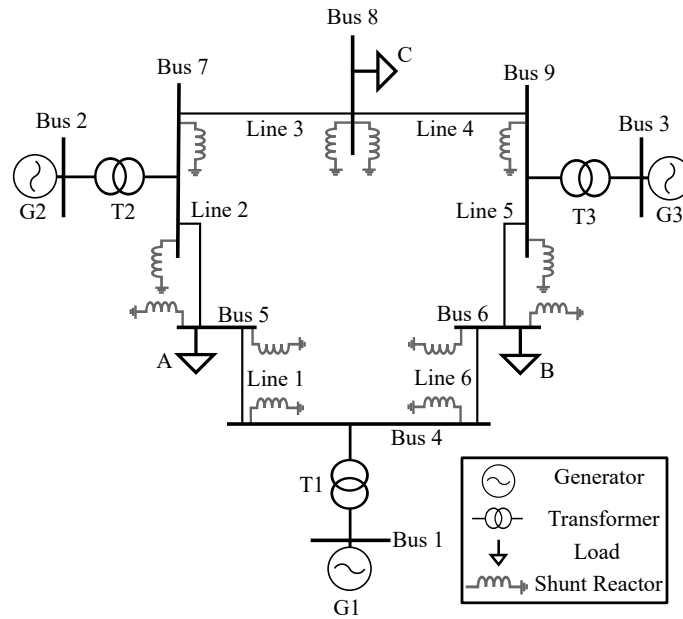


Figure 4.4. Fully compensated equivalent cable-based 9-bus model.

The DIgSilent PowerFactory model is modified into the one presented in Figure 4.4, after which simulations are performed on the case model to determine the CCT of the system. G1 is set to be the reference machine in the simulations. The results of the simulations can be seen in Table 4.3.

Looking at the CCT values in the table and comparing with the base case presented in Table 4.1, there appears to be some degree of agreement between the two cases.

Table 4.3. CCT of the 100 % compensated equivalent cable system.

Faulted Line	Terminal i	CCT_1 [ms]	n_s [-]	CCT_{99} [ms]	n_s [-]
Line 1	Bus 5	241	2	190	1
Line 2	Bus 7	49	2	101	2
Line 3	Bus 7	137	1	196	1
Line 4	Bus 8	198	1	162	1
Line 5	Bus 9	101	2	177	2
Line 6	Bus 6	268	2	195	2

Ignoring Line 2 and Line 5, the overall mean deviation in CCT values for all other events is just approximately 5.78 %.

On the other hand, faults on Line 2 and Line 5 have a relatively large impact in terms of stability of the cable-based system. When the fault is located at either side of these two lines, the CCT values decrease by more than 30 % on average in comparison with the base case indicating a significant reduction in stability margin.

Figure 4.5 shows the G2 power angle and active power output for a stable event when a fault is applied at Line 2 for both cases. Although the initial steady-state operating power angle of G2 is higher in the base case, the compensated system reaches a much higher peak value during the first swing period. Therefore rendering the latter being more susceptible to first swing instability. This observation can be explained by the large surplus of reactive power consumption from the shunt reactor connected at Bus 7 after Line 2 is disconnected. As a result, G2 has to supply for the reactive power deficit. As much more reactive power is needed to be generated by G2, the active power output is limited by the generator capability. This is applicable for all the lines but the effects are substantially more noticeable for Line 2 and Line 5 due to the much higher reactive power generation by the lines as shown in Table 4.2. Referring to Figure 1.9 with a post fault power curve the generator would need a longer time in order to recover from the accelerating power caused by the fault and thus recording higher power angles.

Shunt reactor switching

Further investigation is conducted in order to justify the explanation made concerning shunt reactors being the main cause of the bigger power angle swing seen in Figure 4.5. For the same stable event, a special case is simulated with the shunt reactor at Bus 7 which is initially deployed to compensate Line 2, turned off simultaneously with the initiation of fault at $t_{f,0} = 0.1$ s. The power angle and active power curves of generator G2 for this case are shown in Figure 4.6 together with the case where shunt reactor remains connected. It can be seen that the power angle of G2 recovers much faster when the shunt reactor is disconnected as compared to the case that the shunt reactor is connected. This is because the post fault active power transfer of G2 is much higher in this case, which mean more decelerating torque on the generator to counter the accelerating effect of the fault.

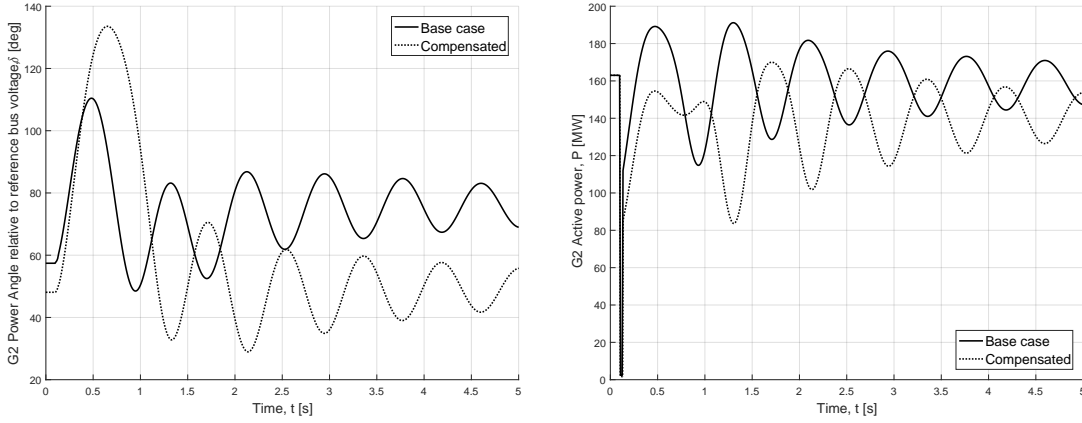


Figure 4.5. Comparison of G2 power angle [left] and active power output [right] between base case and compensated cable case. The fault is applied at $t_{f,0} = 0.1$ s and cleared at $t_c = 0.13$ s, so that $t_f = 0.03$ s. The fault location is at 1 % of Line 2.

This observation indicates that the shunt reactive allocation may have a direct impact on the lines. There is the possibility that fixed symmetrical distribution may not be the best compensation scheme in certain scenarios. In view of that, it also paves the way to consider dynamic shunt compensation schemes that are beneficial to the system stability. It could be done in the form of switching in and out of the shunt reactors or using FACTS devices by which the output could be regulated. Considering that this strategy relates mainly to the balancing of reactive power and has a direct impact on voltage regulation, it is covered with more detail in the voltage stability analysis chapter.

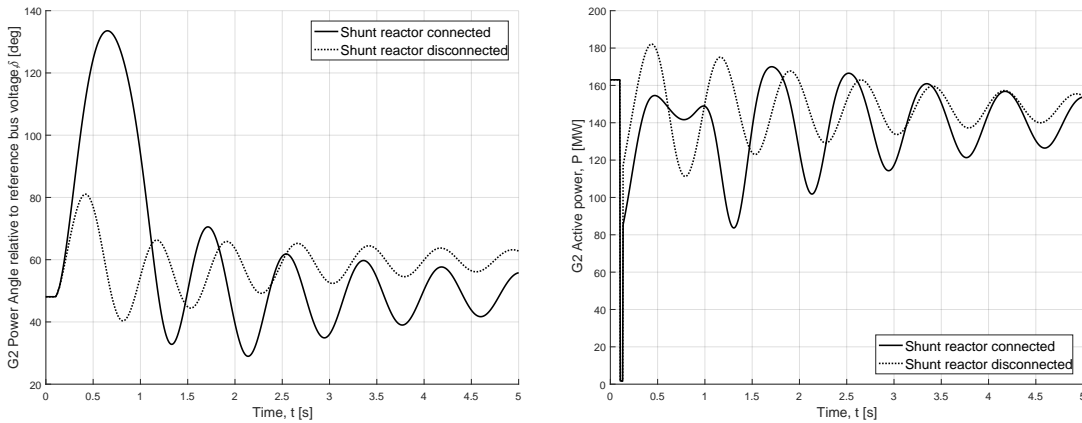


Figure 4.6. Comparison of G2 power angle [left] and active power output [right] between non SR switching case and SR switching case. The fault is applied at $t_{f,0} = 0.1$ s and cleared at $t_c = 0.13$ s, so that $t_f = 0.03$ s. The fault location is at 1 % of Line 2.

4.2.4 Variation of reactive power compensation degree

In this section, the degree of reactive power compensation of the equivalent cable system is varied and the effects on stability are studied. The compensation levels applied from 95% to 115% of the reactive power requirement for each line as listed in Table 4.2.

The motivation is to observe the transient stability performance tendency of the system under different compensation levels.

The CCT values for the case with 95 % compensation are obtained and recorded in Table 4.4. ΔCCT refers to the change in CCT written in % based on the values found in the 100 % compensated case. According to the table, all the CCT values in the 95 % case are lower for every scenario, thus worsening the transient stability. This is because a reduction in compensation degree would require SGs to balance out the extra reactive power generated by the lines. It results in SGs operating in under-excitation mode and thus increasing the power angle of the machines. Higher initial operating angles have lower stability margin and therefore more susceptible to angle instability when subjected to a disturbance with reference to the SMIB studies conducted in Section 3.3.2.

Table 4.4. CCT of 95 % compensated equivalent cable system.

Faulted Line	Terminal i	CCT ₁ [ms]	ΔCCT [%]	CCT ₉₉ [ms]	ΔCCT [%]
Line 1	Bus 5	199	-17.4	163	-14.2
Line 2	Bus 7	0	-100.0	0	-100.0
Line 3	Bus 7	123	-10.2	172	-12.2
Line 4	Bus 8	172	-13.1	146	-9.9
Line 5	Bus 9	56	-44.6	99	-44.1
Line 6	Bus 6	224	-16.4	170	-12.8

In contrast, simulations performed with increasing compensation levels yield an improvement to the transient stability in all events. Figure 4.7 presents the CCT tendencies with fault located at 1 % of the first three lines. The improvement is attributed to the increased reactive power demand by the system which has to be supplied by the generators. Therefore, the generators are operating in increasing levels of over-excitation mode which would in turn lead to a steeper active power curve and beneficial to transient stability. Unless specified in DIGSILENT, the MVA capability of the synchronous generators is unlimited under steady-state conditions, and the generators will supply the required active and reactive power. MVA limiting according to capability curves is discussed in Chapter 5.

According to Figure 4.7, it is observed that there are crossover points between the CCT curves of Line 1 and Line 2 with the respective CCT value obtained in the base case with OHL. These points are indicated by P_1 and P_2 in the figure. In the case of Line 3, the cross point is projected to be at a lower compensation degree range which is not part of the investigation. The observation implies that there exists a specific compensation degree where OHL and cable systems display an equal transient stability performance for each line. This occurrence is dependant on the balance of reactive power in the system and the sensitive interdependence between RLC line parameters and fault location.

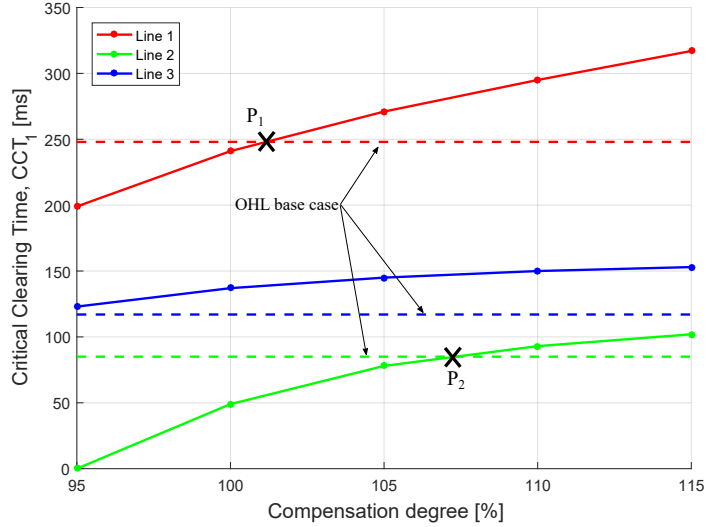


Figure 4.7. Compensation degree sensitivity comparison. Fault location is at 1% at the line.

4.3 IEEE 39-bus transient stability analysis

This section proceeds with the transient stability analysis on the IEEE 39-bus system. The system is analysed in a similar manner as in the 9-bus system. The essence of the study is to determine whether the observations from 9-bus would also hold true for the 39-bus system, which is more comparable to a real interconnected power system. As a summary, the 9-bus study presented in Section 4.2 indicates that the fully shunt compensated cable system is comparable to the uncompensated OHL system in terms of transient stability performance. Further improvement could be observed by over-compensating, whereas under-compensation gives rise to an opposite effect.

Taking into account that the 39-bus system is much larger and has a far more complex nature, much of the investigation would be focused on certain significant events instead on all the lines. This is done in order to narrow down the analysis and comparison to the most important cases.

4.3.1 39-Bus transient stability base case

For the base case, the default DIgSILENT PowerFactory model of the 39-bus system is used as the base model. Simulations are performed under default settings and G1 is selected as the reference machine due to its highest inertia constant value. The CCT values obtained from all the simulated events are shown in Table F.2.

Based on the table, it is evident that the CCT is significantly higher when the fault is applied near to G1 which is located at Bus 39. This observation is also consistent with the findings in the 9-bus study and is explained in Section 4.2.1. Furthermore there are some events that have resulted in multiple machines recording unstable detection during the simulation period. The events with a CCT value lower than 250 ms are selected and shown in Table 4.5 for ease of reference.

Table 4.5. CCT of multiple pole slip events under 250 ms.

Faulted Line	Location [%]	CCT [ms]	n_s [-]
2-25	99	115	2
4-5	99	239	2
5-6	1	239	2
5-6	99	227	2
6-7	1	238	2
15-16	99	173	4
16-17	1	136	2
16-21	1	172	2
21-22	1	108	2
21-22	99	92	2
23-24	1	170	2

There is a possibility, especially in a large system, that a certain unstable machine may have negative influence on the other machines causing more severe oscillations due to the interaction between all the machines in the system. As a result, some machines would go into unstable operation due to the influence of another machine instead of the disturbance. Therefore the first unstable machine is disconnected to avoid any detrimental impact to the system. Taking that into consideration, an event with multiple pole-slip record from the list in Table 4.5 is used for further investigation in a separate simulation case. The case where the fault is applied at 99 % of Line 15-16, is selected due to its highest number of pole-slip incidents. In this separate case, the first machine which reaches 180 degrees, is disconnected at CCT. In other words, the critical generator (G4 in this case) is disconnected at the same instant as the line. The outcome of the simulation is shown and compared to the original event in Figure 4.8.

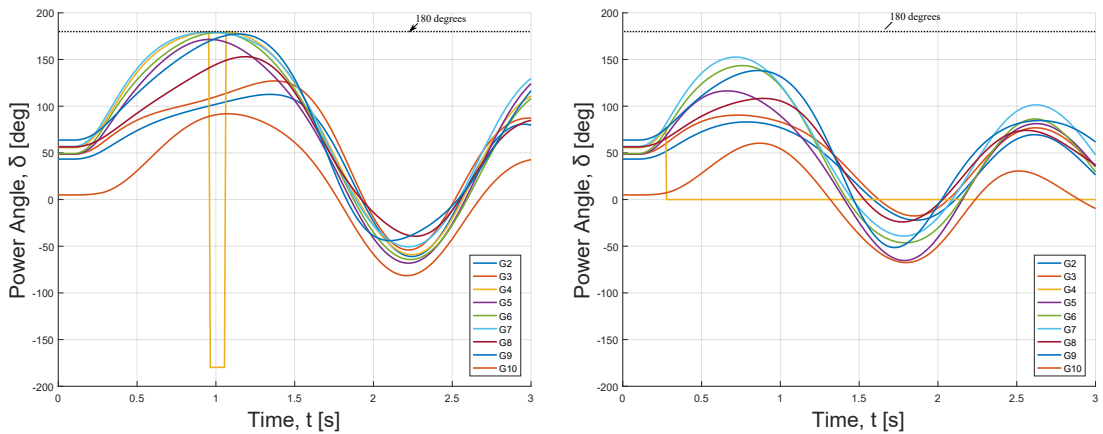


Figure 4.8. Power angle of machines for base case [left] and the case where G4 is disconnected with the line [right]. The fault is applied at $t_{f,0} = 0.1$ s and cleared at $t_c = 0.273$ s, so that $t_f = 0.173$ s. The fault location is at 99 % of Line 15-16.

The simulation reveals that all the machines oscillate fairly below the critical angle of 180 degrees and has a higher stability margin in this case. This observation indicates that the disconnection of an unstable generator is indeed beneficial in terms of system-wide transient stability. The reason being the disruption of the interaction between the critical machine and other machines, thus any negative impact is reduced. Nonetheless, such a method, though it performs better in transient stability, may present other problems in the network e.g. line overloading and voltage drop. This is because when a generator from one area is disconnected, the local power supply of that area would need to come from other areas through the transmission lines therefore increasing the loading of certain lines. Overloading is more likely when the lines are already loaded substantially high under normal operating scenario which can lead to a chain of events.

Transient instability in large power systems could be manifested in a relatively slower form as a result of the inter-area oscillations instead of from the first swing as mentioned in Section 1.2.1. When a fault is applied and cleared, the disturbance would affect all the machines behaviour in a corresponding manner with respect to the location of the fault. Some machines will behave like a cluster and oscillate in near synchronisation. When multiple clusters are present in the system, the oscillations between the clusters would cause a certain machine to oscillate beyond its first swing oscillation.

An example of such a scenario in the 39-bus system is presented in Figure 4.9. It can be seen in this scenario that a group of machines form a cluster and display similar oscillatory behaviour. In contrast, G9 is not part of the cluster and the inter-area oscillation effect is noticeable for this machine where it can be observed from the figure that the first swing peak, P_1 is lower than the subsequent peak P_2 . The type of transient instability for this particular event is not of first swing nature but rather an outcome of subsequent swings and therefore would require a much longer simulation time for detection.

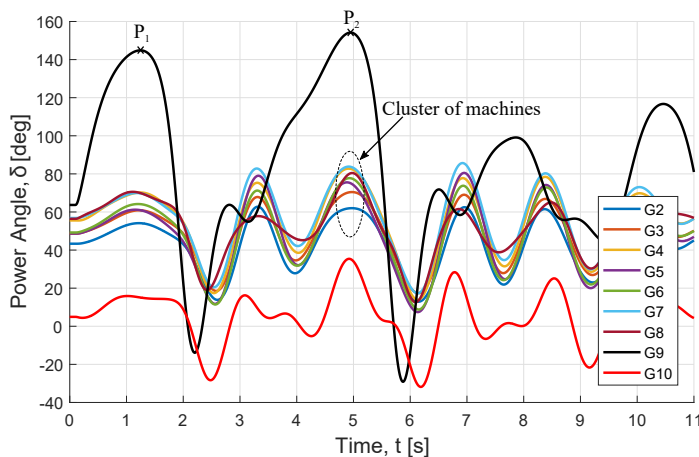


Figure 4.9. Power angle fault response of the machines. The fault is applied at $t_{f,0} = 0.1$ s and cleared at $t_c = 0.1525$ s, so that $t_f = 0.0525$ s. The fault location is at 99 % of Line 28-29.

4.3.2 Change of reference machine

In this section, simulations are performed with G2 as the reference machine to obtain CCT values. The complete findings of this case is presented in Table F.3. The values in most cases are found to be slightly different from the values found in the base case. This observation is contrary to the findings of the 9-bus study in which the CCT values remain identical regardless of reference machine. This is because the reference machine in the 39-bus system is made to operate like a slack bus to provide the power required due to the fault where the generators capability is limited. Thus, altering the power transfer of G2 and also its interaction with the other machines in the system.

Aside from CCT values, the number of machines entering into unstable operating region also shows a degree of variation between the two cases of reference machine. A few examples of such observation are selected and illustrated in Table 4.6. The difference can be seen by comparing the generator power angle curves of each case. Figure 4.10 shows the angle behaviour for both cases. The reference machine is omitted from the figure as all angles are measured relative to the power angle of the reference machine. For the base case, G2 is one of the critical machines in the system and when it is made the reference machine, all the other machines would appear to be unstable as shown on the right figure. A strong indicator is the negative first swings of the other generators relative to G2. Hence the higher number of unstable occurrences in such case is due to the instability of the reference machine being reflected on the other machines. The observation indicates that it would be better to carry out the preceding investigations using G1 as the reference machine which displays a higher transient stability characteristic.

Table 4.6. Comparison between base case and G2 as reference machine case.

Faulted line	Base case		G2 case	
	CCT ₁	n_s	CCT ₁	n_s
4-5	279	2	279	9
4-14	287	1	293	8
5-6	239	2	239	8
16-17	136	2	138	8

4.3.3 Equivalent cable system with reactive power compensation

This section shows the investigation done on the equivalent cable-based model of the 39-bus system. In an identical manner as the 9-bus study, the simulation system is first modelled into a cable-based system using the same transformation coefficients shown in Section 4.2.3. Simulations are unable to be performed on the new equivalent model without any compensation. The steady state operating condition is unstable with severe violation of voltages across the network. Therefore compensated systems are introduced and used for the analysis.

The dimensioning of the shunt reactors is carried out as in Section 4.2.3, such that two shunt reactors are used to compensate one equivalent cable.

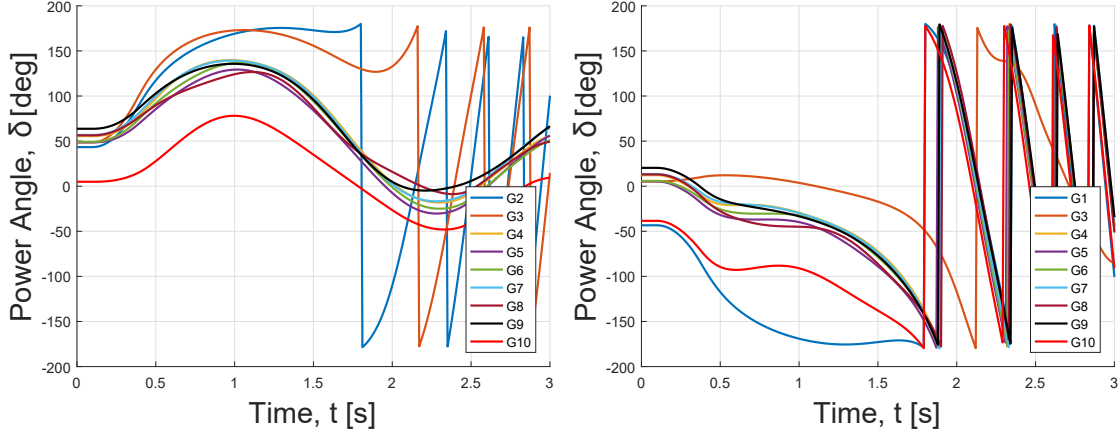


Figure 4.10. Power angle of machines for base case [left] and the case where G2 is reference machine [right]. The fault is applied at $t_{f,0} = 0.1$ s and cleared at $t_c = 0.379$ s, so that $t_f = 0.279$ s. The fault location is at 1 % of Line 4-5.

The simulated compensation degree variation is from 95 % to 115 %. The variation is applied to all the lines of the network. The compensation degree is calculated in proportion to the reactive power generation of each line as listed in Table F.4.

CCT values of the compensated system are recorded and tabulated in Table F.5. Figure 4.11 shows the increasing CCT tendency of five faulted lines when the compensation degree is increased. These lines are chosen on the basis of where they are distributed across the network. The positive influence of increasing compensation level on the CCT is generally observed for all lines, except Line 26-29. This observation is coherent with the 9-bus system which displays a similar tendency. The determining factor is due to the change of excitation state in the generators which could be referred to in Section 4.2.4.

As for the events involving Line 26-29 (which is a 250 km line), generator G9 will become unstable regardless of the compensation levels. The problem lies in the disconnection of the line while keeping the shunt reactors connected. This action is equivalent to losing 1509.20 Mvar of reactive power generation in the area. Though such a scenario is good for transient stability in most cases by driving the generator into over-excitation mode, this case is unique as the bus voltages in the area experience a much larger drop because the huge reactive power demand is not provided locally. Based on the P, δ -characteristic equation shown in 4.8, an increase in excitation voltage E_g is undermined by a large drop in the receiving end voltage V_b . As a result, a much flatter P, δ -curve would have a negative impact on the transient stability performance of the generator. This case exemplifies the phenomenon where transient instability is an outcome of voltage instability which displays the coupling between the phenomena as mentioned in Section 1.2.1.

$$P = \frac{E_g V_b}{X} \sin(\delta) \quad (4.8)$$

Lastly, the rate of increase in CCT for each line is different and it depends on multiple factors. For instance, the total reactive power generation of the line and its location relative to the generators.

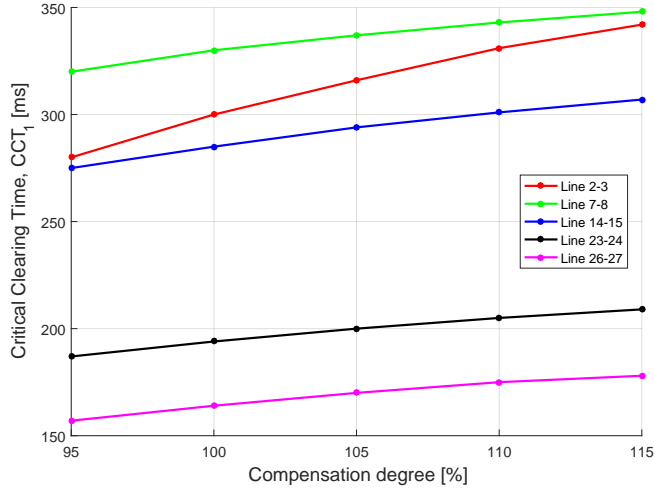


Figure 4.11. Power angle fault response of the machines. The fault is applied at $t_{f,0} = 0.1$ s and cleared at $t_c = 0.1525$ s, so that $t_f = 0.0525$ s. The fault location is at 99 % of Line 28-29.

These factors determine the reactive power imbalances that would need to be balanced by the generators and the distribution is based on the location of the lines relative to the generators. This influences indirectly the behaviour of the critical generator in different cases.

Shunt reactor switching

Similar to the 9-bus study, the impact of switching out the shunt reactors of the faulted line on the transient stability performance in the 39-bus system is investigated. A few events from the 100 % compensation case are selected and tested in this case study as defined below:

- **Switching case:** When the fault is applied at $t_{f,0} = 0.1$ s, the shunt reactors which are compensating the faulted line are disconnected at the same time and remain disconnected for the remaining simulation.

Simulations are performed to obtain the CCT at 1 % fault location for this case and Table 4.7 presents a comparison between the original case and switching case. It is observed that CCT of all events are higher for the switching case recording an improvement between 3 % and 7 % over the original case where shunt reactors remain connected. Figure 4.12 shows the SG power angle swing response in a stable condition for both cases. By comparing the figures, it can be observed that the first swing peak angle of critical generator G3 is slightly reduced in the switching case, therefore displaying a higher transient stability margin than the original case. This observation is predicted and explained in Section 3.4. Hence, it further supports the indication that disconnecting shunt reactors of faulted line would lead to transient stability improvement even for a large system.

Table 4.7. CCT comparison between cases with and without switching of shunt reactors.

Faulted Line	CCT without switch [ms]	CCT with switch [ms]	Improvement [%]
3-4	330	342	3.6
2-25	217	232	6.9
9-39	845	897	6.2
14-15	285	308	5.3
22-23	225	240	6.7

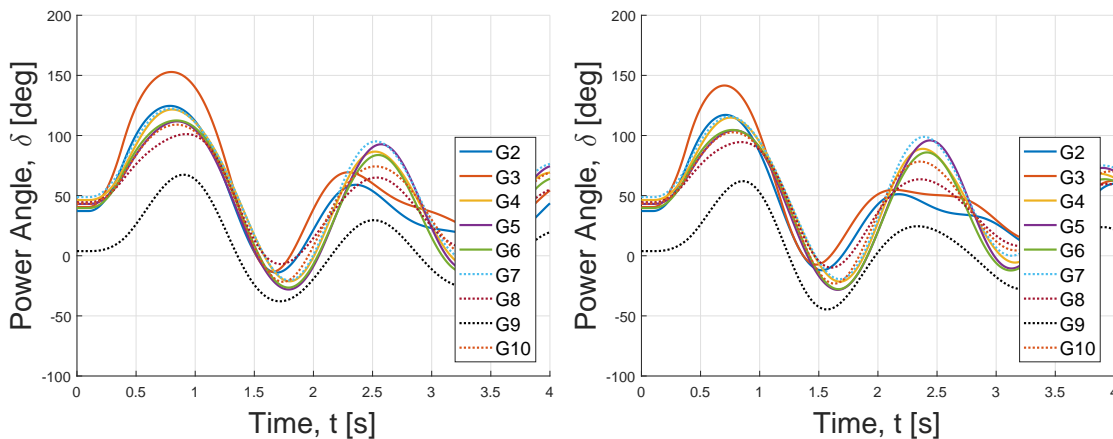


Figure 4.12. Power angle of machines for original case [left] and switching case [right]. The fault is applied at $t_{f,0} = 0.1$ s and cleared at $t_c = 0.380$ s, so that $t_f = 0.280$ s. The fault location is at 1 % of Line 14-15.

4.4 Transient stability summary

This section gives an overview of the transient stability study carried out for the SMIB, IEEE 9-bus and 39-bus test systems. The large disturbance scenario is created by applying a three-phase fault on a line and fault clearing by disconnecting the line. The following are the conclusions of the transient stability analysis in this thesis:

- **Location of the disturbance is crucial:** Transient stability performance is better when the faults are located farther away from generators. The system stability margin is higher when the faults are near to strong machines.
- **Influence of line parameters:** When the generator is initially supplying only active power across the transmission lines, increasing series inductance and shunt capacitance of the lines would have a negative impact on CCT. This conclusion is also applied for system with inductive loads.
- **The equivalent cable system should be compensated:** In SMIB, transient stability is significantly improved by compensating the transmission lines consisting of cables. As for the 9-bus and 39-bus systems, the equivalent cable-based system is transiently unstable without compensation. In addition, the steady state operation of each uncompensated system would also be considered unstable.

- **Sizing of shunt reactors matters:** Increasing the compensation degree generally improves transient stability to a certain extent. The reason is the increasing over-excitation state of the generators. However in reality this positive effect is limited by the AVR design of generators and the MVA capability. Likewise, undervoltage issues may also arise that would counter the positive impact of compensation increment.
- **Effect of dynamic reactor switching:** By disconnecting the shunt reactors of the faulted line during and after fault, leads to improvement in CCT.
- **Impact of machine controls:** AVR and excitation system in the generator model are important factors influencing the dynamic change of states - pre, during and post disturbance. Cables and compensation are strongly influenced by the control model.

Large-disturbance voltage stability analysis: IEEE 9-bus system 5

This chapter describes the study of large-disturbance voltage stability on the IEEE 9-bus system. Similarly to the presented transient stability analysis in Chapter 4, the OHL base case is compared to cases of equivalent cable transmission lines. Different strategies for reactive power compensation is analysed, with focus on switching in response to large-disturbances and dynamic compensation. The analysis also includes the comparison of different load models and their impact on the results in voltage stability studies.

- **Load modelling:** Comparison of different load models in voltage stability studies.
- **Q, V-characteristics:** Producing and analysing Q, V -curves to locate system weak-points.
- **Voltage trajectories:** Analysis of voltage trajectories following large-disturbances.
- **Reactive power compensation:** Analysis of different reactive power compensation strategies for improvement of voltage stability.

5.1 Load modelling in voltage stability analysis

In stability studies load modelling plays an essential role, as it affects the dynamic response of the system. Just like it is typical practice in power system analysis, loads are represented involving simplifications and by summation of the characteristics of several different loads, such as induction motors, heaters, compressors, lights and so forth. Where induction motors are estimated to account for 60-70 % of the total load [2]. A widely used load modelling method, which is described in both [2] and the DIgSILENT PowerFactory version 15.1.6 documentation [38], is the polynomial model:

$$P = P_0 \left(p_1 \left(\frac{v}{v_0} \right)^{e_{p,1}} + p_2 \left(\frac{v}{v_0} \right)^{e_{p,2}} + p_3 \left(\frac{v}{v_0} \right)^{e_{p,3}} \right) \quad (5.1)$$

$$Q = Q_0 \left(q_1 \left(\frac{v}{v_0} \right)^{e_{q,1}} + q_2 \left(\frac{v}{v_0} \right)^{e_{q,2}} + q_3 \left(\frac{v}{v_0} \right)^{e_{q,3}} \right) \quad (5.2)$$

Expressions (5.1) and (5.2) model the load bus P, Q as a nonlinear function of the bus voltage v . Both expressions can be expanded to include dependency on the electrical frequency. However, frequency variations are not accounted for in the study of voltage stability in this thesis. The term v_0 is the initial bus voltage under normal operation conditions, where $P = P_0$ and $Q = Q_0$.

The coefficients p_1 , p_2 , p_3 , q_1 , q_2 and q_3 determine the relative proportion of each component of the polynomial, and must fulfil $p_1 + p_2 + p_3 = q_1 + q_2 + q_3 = 1$.

The exponents of each component $e_{p,1}$, $e_{p,2}$, $e_{p,3}$, $e_{q,1}$, $e_{q,2}$ and $e_{q,3}$ allow for altering the dynamic behaviour of the load. The model is designed such that the exponents approximate the $\partial P/\partial V$ and $\partial Q/\partial V$ behaviour of the specific load components. Generally, if $e_p = e_q = 0$ the load is represented as constant power, while $e_p = e_q = 1$ represents constant current, and $e_p = e_q = 2$ is considered constant impedance. The model is also referred to as the ZIP model, as it allows for modelling of constant impedance (Z), constant current (I) and constant power (P) components of the load. However, the exponents are not limited to values 0, 1 and 2. For realistic representation of specific load components for composite models, the values of the exponents vary depending on the dynamic $\partial P/\partial V$ and $\partial Q/\partial V$ characteristics. Example values can be found in Chapter 7 of [2] and in [39].

In order to chose a load modelling strategy for the voltage stability studies in this thesis, V, Q -trajectories in response to a three-phase fault on the IEEE 9-bus system are compared for different load models. The models and their parameters are shown in Table 5.1. The composite model is based on data given in [39] and resembles a load with 70 % induction motor, 20 % fluorescent bulb and 10 % light bulb. In order to avoid confusion, it is important to note that the use and order of coefficients p_1 , p_2 , p_3 , q_1 , q_2 and q_3 does not influence the dynamic behaviour, but provides the ability for composition.

Table 5.1. Load modelling parameters used in equations (5.1) and (5.2) for comparison on IEEE 9-bus system in DIgSILENT PowerFactory.

	Relative load composition						Exponentials $\partial P/\partial V$ and $\partial Q/\partial V$					
	p_1	p_2	p_3	q_1	q_2	q_3	$e_{p,1}$	$e_{p,2}$	$e_{p,3}$	$e_{q,1}$	$e_{q,2}$	$e_{q,3}$
Constant P	1	0	0	1	0	0	0	0	0	0	0	0
Constant I	0	1	0	0	1	0	0	1	0	0	1	0
Constant Z	0	0	1	0	0	1	0	0	2	0	0	2
Composite	0.7	0.2	0.1	0.7	0.2	0.1	0.1	1.2	1.6	0.6	3.0	0.0

A three-phase fault is placed on Line 2 in the IEEE 9-bus system, while the voltage and reactive power is observed at Bus 5, which is a load bus. In steady state the load is absorbing $S_{3ph} = 125 \text{ MW} + j50 \text{ Mvar}$. Figure 5.1 shows the voltage response and the reactive power at the load bus.

The case of constant P modelling reveals that the system is leading to instability. When the load is modelled as constant P , equations 5.1 and 5.2 are reduced to functions that are voltage independent, such that $P = P_0$ and $Q = Q_0$. When the voltage drops locally due to the fault, the power absorbed by the nearby loads is not adjusted, and the drawn current is increased to account for the lower voltage. A consequence is further voltage drop due to increased flow of active and reactive current through system impedances. As the faulted Line 2 is taken out of service, the synchronous generators with AVR systems are trying to recover terminal voltage by regulation of excitation level.

However, the immediate demand in both active and reactive power of the loads, combined with a voltage suppressed system, leads to instability.

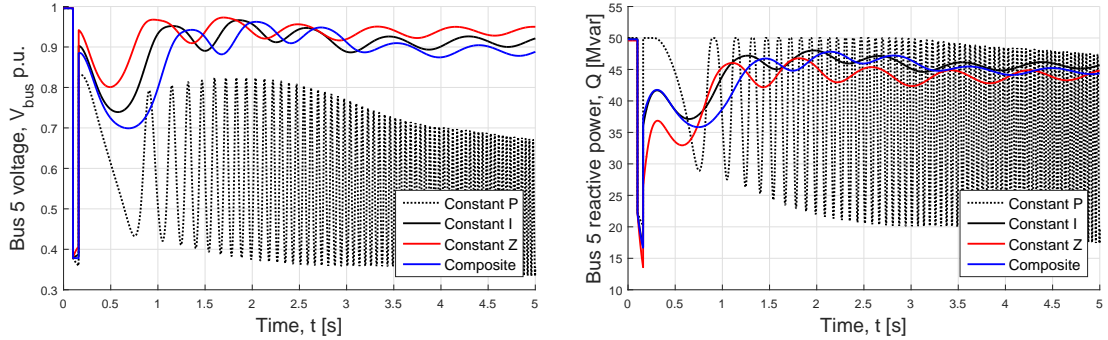


Figure 5.1. IEEE 9-bus system Bus 5 voltage and reactive power trajectory for a fault at 99 % on Line 2. The duration of the fault is $t_f = 60$ ms. Four cases of load modelling are compared. All three loads in the 9-bus system are equally modelled.

In the case of constant current, the power absorbed by the load following the disturbance is dependant on the restoration of the voltage. Here, the load P and Q become linear functions of the voltage, rather than non-linear polynomial expressions, due to the exponent of 1. The best case in terms of voltage recovery is modelling by constant impedance. This is expected as the loads will decrease the drawn current as the voltage drops, while the power demand will restore concurrently with restoration of the voltage. The composite model display voltage recovery performance which is a compromise between the worst case constant P , and the idealized constant Z and I in terms of voltage stability. By observing the values in Table 5.1 it can be seen that the chosen composite model consists 70 % of a term with a $\partial P/\partial V$ exponent of 0.1, which is close to the constant P value of 0. In other words, the inductions motors resemble behaviour close to constant P , while the light bulb and fluorescent bulb elements introduce $\partial P/\partial V$ and $\partial Q/\partial V$ -characteristics closer to constant I and constant Z .

The transient stability simulations in Section 4.2 are performed with constant Z load models, which can be argued to be adding positively to stability limits in a way that does not resemble realistic power system behaviour. Thus, the voltage stability studies are performed with the composite model with values given in Table 5.1.

5.2 Q,V-characteristics of load buses in the IEEE 9-bus system

In order to examine the voltage stability of the IEEE 9-bus system Q, V -curves are produced for the three load buses of the system: Bus 5, Bus 6 and Bus 8. The characteristics of Q, V -curves are introduced in Section 1.4. The Q, V -curves is an indicator of the steady state voltage stability of the system. The shape of the Q, V -curve for a given load and the characteristics of $\partial Q/\partial V$ in relevant intervals of bus voltages can act as an indicator towards weak points in the system. Thus, analysis of Q, V -characteristics is performed to determine weak points of interest for large-disturbance analysis in the IEEE 9-bus system.

The Q, V -curves are produced in DIGSILENT PowerFactory by inserting a variable source of reactive power at the bus of interest. The injected reactive power Q_i is incremented, first as being capacitive (positive injection) and followed by inductive (negative injection). The power flow is solved for every value of Q_i , while the resulting change in bus voltage V_B is observed.

Figure 5.2 shows the Q, V -characteristic of Bus 8. It is important to note the difference between the rated value of shunt reactive power and the actual injected reactive power Q_i . Due to the non-linear relation of reactive power with the voltage, $Q_i = V^2/X$, the difference between rated and actual values increases as the voltage differs further from the rated 1 p.u. value. When the bus voltage is in the range of 0.85 to 1.15 p.u. the slope dQ/dV is approximately constant, and the difference in rated and actual values is small. Evidently, the two curves intersect at $Q_i = 0$. The difference between the actual injected reactive power Q_i and the net flow of reactive power is due to the presence of the composite modelled load at Bus 8. The load is inductive and consumes 35 Mvar when the voltage is 1 p.u. However, The reactive power characteristics of the load is dependent on the $\partial Q/\partial V$ exponents of the model according to Table 5.1. The difference between the two curves increase as the voltage moves further away from 1 p.u. as the voltage dependency of the load scales according to the modelled exponents.

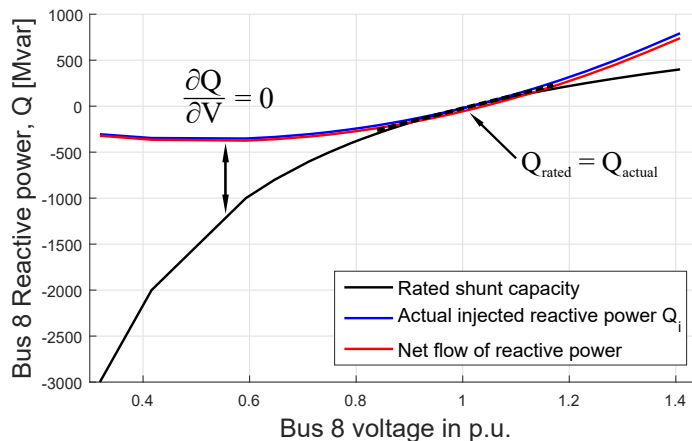


Figure 5.2. Q, V -characteristic of Bus 8 in the IEEE 9-bus system. The loading of the system is in accordance to the composite model of Table 5.1.

Based on the Q, V -characteristic, Bus 8 proves to have a high voltage stability margin in steady state, as it requires around 1000 Mvar of rated inductive shunt reactance to bring the voltage down to the critical voltage level, where $\frac{\partial Q}{\partial V} = 0$. For Bus 5 and Bus 6, the required rated inductive shunt reactance is likewise around 1100 Mvar to 1200 Mvar. In other words, even though Bus 8 is considered the weakest bus based on the Q, V -characteristics, it displays a large stability margin, and does not differ significantly from Bus 5 and Bus 6.

Figure 5.3 show the Q, V -characteristic of the three load buses in the IEEE 9-bus system. Bus 5 and Bus 6 display very similar behaviour with equal critical voltages around 0.51 p.u.

Bus 5 and Bus 6 are both connected to SG1, which is the machine in the 9-bus system with the highest MVA rating and acts as slack bus for the power flow solution. Bus 8 has a slightly higher critical voltage of 0.53 p.u. Thus, Bus 8 is chosen as point of interest in the 9-bus system for analysis of large-disturbance voltage stability. However, for the tested load level all three system nodes display satisfactory steady state voltage stability margin as the critical voltages are far from typical under-voltage limits in steady state.

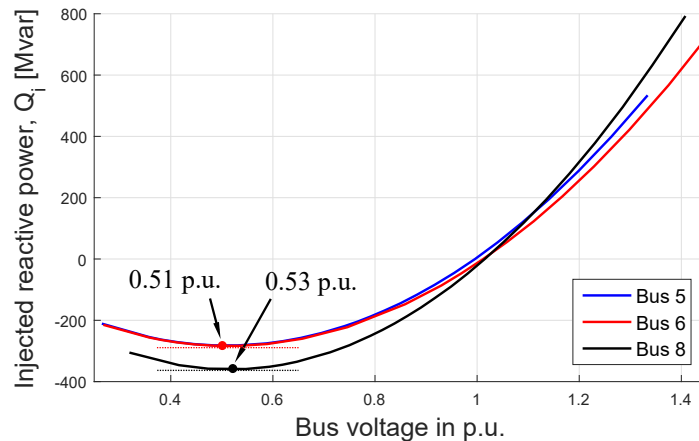


Figure 5.3. Q,V-characteristic of the three load buses in the IEEE 9-bus system produced in DlgSILENT PowerFactory. The loading of the system is in accordance to the composite model of Table 5.1.

5.3 Voltage stability of Bus 8 in the IEEE 9-bus system

The voltage stability is analysed for the IEEE 9-bus system with use of the discussed composite load model and by using Bus 8 as point of interest in the system. The stability is assessed in the case of an OHL based system, and compared to cases of equivalent cable systems with various degrees of reactive power compensation. The modelling of the equivalent cable cases and sizing and location of shunt reactors is done according to the method described in Section 4.2.3.

Figure 5.4 compares the V, P -characteristics of Bus 8 in the OHL base case with three cases of cable based system. The cables of the system are 100 % compensated. The two cases referred to as 75 % and 125 % compensation, only involves under and over-compensation of Line 3 and Line 4 connecting Bus 8 in the ring network. The compensation degree of the remaining lines remains 100 %. The power factor at Bus 8 is held constant at 0.9438 lagging, which is the nominal value. Thus, as the active power loading is increased, the reactive power loading is increased coherently. Attention should be directed towards the difference between the solid and the dotted lines in Figure 5.4. Due to the voltage dependency of load P and Q according to the composite load modelling by (5.1) and (5.2), there is an increasing difference in V, P -characteristics between composite model and the nominal P_0, Q_0 values as the voltage is decreased by the increased loading. It is important to be aware of this *double response*, as changes in nominal P_0 and Q_0 affects the voltage, which affects the actual P and Q loading.

Figure 5.4 show that under-compensation has a positive effect on the steady state voltage stability limit, as P_{max} is largest in the case of 75 % compensation. This result is incoherent with the findings of the transient stability analysis and CCT values for different compensation degrees. The reason for this observation is discussed in Chapter 7.

The critical voltage when comparing the OHL base case and the 100 % compensated cable case is very similar. However, the load-ability (the active power load at which critical voltage is reached) is roughly 100 MW lower in the OHL case. When comparing the OHL base case with the 100 % compensated cable it is important to note that the equivalent cable has lower line reactance and line resistance. This is due to the use of scaling factors in equation (4.1) in Section 4.2.3. The difference in series parameters represent a realistic distinction between equivalent OHL and cable transmission lines mainly due to their geometrical differences. Due to the lower series resistance and series reactance of the cable, there is a lower voltage drop proportional to the transmission of active and reactive power. Thus, the load-ability of the cable is higher in terms of voltage stability.

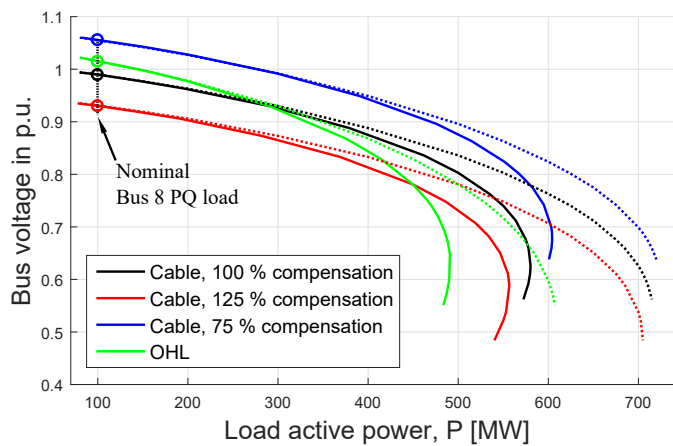


Figure 5.4. V,P -characteristic of Bus 8 in four different cases of system transmission lines and reactive power compensation degree. The solid lines represent the actual load characteristic due to voltage dependency of the composite model. The dotted lines represent the voltage independent P_0 and Q_0 loading.

Figure 5.5 repeats the results illustrated in Figure 5.4, but with the voltages normalized by the voltage at nominal load for each case. The AVR systems in the 9-bus system are controlling the voltage at the terminals of the synchronous generators. Bus 8 is a load bus, located 100km away from the nearest SG. Thus, when the power factor at Bus 8 changes due to over or under-compensation, the voltage is not regulated back to 1 p.u. locally at Bus 8. By normalizing the voltages, the locus of the critical voltages becomes more comparable between the different cases. The figure shows that the critical voltage is lowered as the inductive compensation is increased. This result is in coherence with the characteristics of Figure 1.16 in Section 1.4, showing that capacitive load power factor give rise to a higher critical voltage and that inductive load power factor give rise to a lower critical voltage. Under-compensation of the reactive power produced by the cable, leads to a capacitive power factor locally at Bus 8, while over-compensation leads to an inductive power factor. Thus, the tendencies of Figure 1.16 are supporting the results displayed in Figure 5.5.

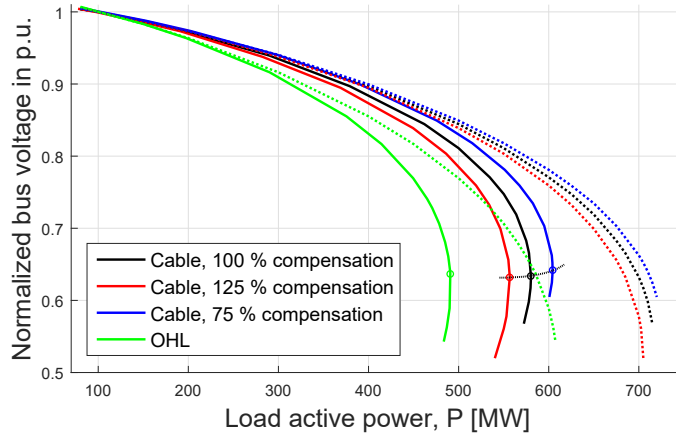


Figure 5.5. Normalized V,P -characteristic of Bus 8, under the same conditions as in Figure 5.4.

Additionally, the un-compensated OHL is inductive, and thus absorbs reactive power. Hence, the OHL case is comparable to the over-compensated cable, which likewise consumes reactive power. This similarity is observed in Figure 5.5 when comparing the load-ability of the different compensation degrees to the OHL case.

Figure 5.6 shows the Q, V -curves for the same cases presented in Figure 5.4. The loading of the shown cases is the nominal loading highlighted by a line in Figure 5.4. However, it is important to note that the loading does not remain completely constant in the displayed cases, as the injection of reactive power affects the voltage, which in turn affects the voltage dependent load. Thus, as the voltage is affected the operational point on the V, P -curve is affected. The figure shows that increasing the compensation level of the cables offsets the Q, V -curves in a positive direction. This is expected, as changing the static compensation level is equivalent of changing the reactive power injected at the bus, which is how the Q, V -curves are produced. The figure shows how the critical points where $dQ/dV = 0$ are found at lower voltages as the degree of compensation is increased. However, it is important to note that over-compensation of cables reduces the active power load-ability displayed by the V, P -characteristics.

5.4 Discussion of reactive power capability limits in the IEEE 9-bus system

A limitation of the results displayed in Figure 5.4 is the unmodelled reactive power capability limits of the synchronous machines of the system. When the loading at Bus 8 is increased beyond 272 MW in the case of a 100 % compensated cable, the synchronous generators begin to exceed their limits. Without modelling of reactive power capability limits, the machines will keep outputting the required active and reactive power needed for the power flow solution. In DIgSILENT PowerFactory the MVA limits of the synchronous generators can be modelled by defining the capability curves under 'Reactive Power Operational Limits' in the Load Flow tab of each SG. In the IEEE 9-bus system, values for defining capability curves can be found under 'Advanced' in the Load Flow tab.

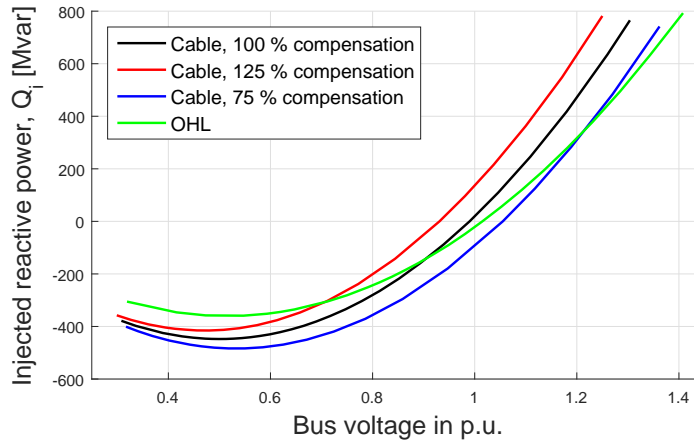


Figure 5.6. Q,V-characteristic of Bus 8 in four different cases of system transmission lines and reactive power compensation degree. The system loading of the displayed case is the nominal loading of the system.

The capability curves defined using these values are displayed in Figure 5.7.

Two capability curves for SG1 are displayed. The dotted line represent the capability curve of SG1 directly using the values in PowerFactory, whereas the solid line represent a capability curve modified to match the shape of SG2 and SG3. Due to the unconventional shape of SG1, DIgSILENT support was contacted in order to clarify the origin of the values given in the 'Advanced' tab:

"The capability curves are normally provided by the manufacturer. However, the drawing (i.e. capability curves based on the values in the advanced tab) is the theoretical representation using the machine parameters. The parameter x_d for this machine (i.e. SG1) is small compared to the other machines, that's the reason for such a drawing." - Karla Mendez, DIgSILENT support, 04.05.2016

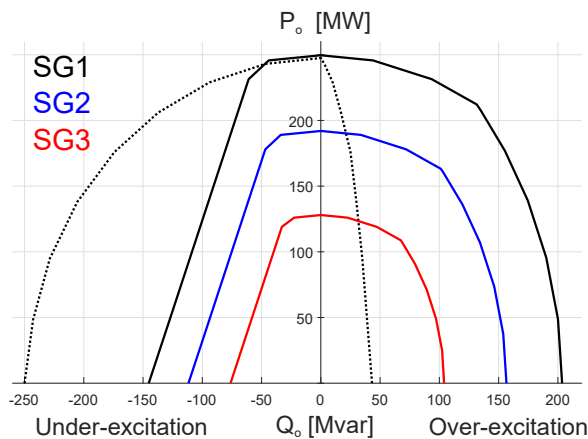


Figure 5.7. Reactive power capability curves of the synchronous machines in the IEEE 9-bus system in PowerFactory. The capability curves for SG2 and SG3 are directly defined from the values given in PowerFactory. The capability curve of SG1 is modified (solid line). The unmodified line is shown as dotted.

Thus, the capability curves in Figure 5.7 do not represent real synchronous machines, but are estimates based on the machine parameters. Nevertheless, the characteristics are applied in order to exemplify the influence of limits to reactive power capabilities.

Figure 5.8 shows the V, P -characteristic of Bus 8 in the IEEE 9-bus system in the 100 % compensated cable case. Three cases are displayed, 1) without capability limits (similar to the characteristics in Figure 5.4, 2) with capability limits on all three generators, and 3) with the un-adjusted SG1 capability curve. Figure 5.8 shows that when reactive power capability limits are modelled, there exists a load level where all three synchronous generators are operated at their limits.

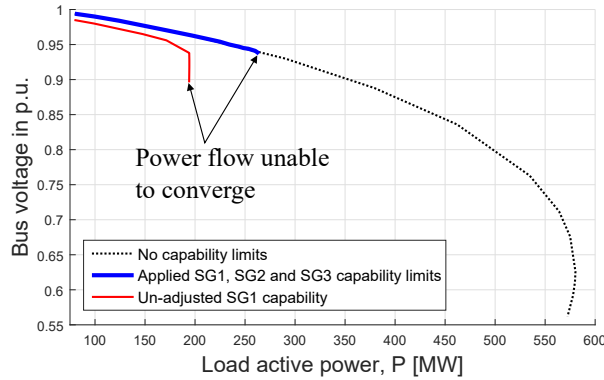


Figure 5.8. Comparison of V, P -characteristics of Bus 8 in the IEEE 9-bus system.

Increasing the loading at Bus 8 beyond this point, result in the inability to solve the power flow in PowerFactory. SG1 is acting as slackbus for the power flow solution, thus attempting to balance active and reactive power beyond the capability of SG1 leads to failure. It is important to note that this is a general limitation of the power flow solution. The expected response in a real power system would be an increasing drop in voltage and frequency as the load level exceeds the generation limits, and not an abrupt system failure.

The apparent power output S_o of each synchronous machine, at the loading limit leading to power flow failure on the next increment, is shown in Figure 5.9. The loading of each machine at this operating point is:

$$\mathbf{SG1: } S_{o,lim} = 231.9 \text{ MW} + j91.9 \text{ Mvar} \quad (5.3)$$

$$\mathbf{SG2: } S_{o,lim} = 163.0 \text{ MW} + j97.0 \text{ Mvar} \quad (5.4)$$

$$\mathbf{SG3: } S_{o,lim} = 85.0 \text{ MW} + j81.8 \text{ Mvar} \quad (5.5)$$

By observing Figure 5.8 it can be seen that there is a significant difference in the loading leading to power flow failure, dependent on the capability curve of SG1. If the over-excitation level of SG1 is very low, it changes the power flow of the system even at low loading. The result is a lower voltage in the area of Bus 8, as SG2 and SG3 must supply the majority of reactive power for the entire system. The inability of SG1 to supply sufficient reactive power with this capability characteristic, leads to power flow failure at a lower load level.

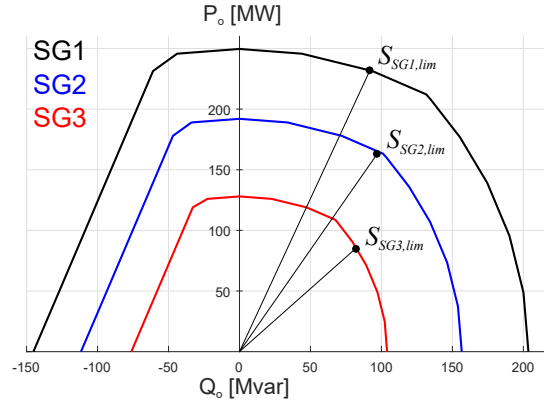


Figure 5.9. Reactive power capability curves of the SGs in the IEEE 9-bus system. The operating points indicate the apparent power output of the machines when the loading at Bus 8 is increased to $S_{load,C} = 272 \text{ MW} + j95.2 \text{ Mvar}$.

As stated, the un-modified reactive power capability curve of SG1 is expected to be unrealistic. However, the case illustrates the consequence of limited reactive power capabilities of synchronous machines with respect to system voltages.

Now, recalling the comparison of normalized V, P -characteristics for OHL networks and cable based networks in Figure 5.5. It can be argued that the difference in critical voltages and load-ability of the different transmission line topologies in the 9-bus system is trivial. The MVA limits of the synchronous machines are exceeded before the loading is increased to a level where any significant difference is observed. Thus, if the 9-bus system represents a real power system, the V, P -characteristics would be dominated by the reactive power capability of the generators.

However, the V, P -characteristics still provide useful indications towards the voltage stability margins of the system, as basis for further analysis.

5.5 Voltage trajectory analysis of Bus 8 in the IEEE 9-bus system

For the initial study of large-disturbance voltage stability, the voltage trajectory method presented in Section 1.6.4 of the introduction is conducted. The goal is to quantify and compare the voltage recovery ability for the OHL base case and cable based systems with different reactive power compensation.

For the purpose of making example, Figure 5.10 show the voltage trajectory of Bus 8 for a three-phase fault on Line 4 in the 9-bus system. The fault is cleared after 60 ms by removal of Line 4. Two cases are displayed, the voltage trajectory of an OHL transmission system and the equivalent 100 % SR compensated cable case. The under-voltage limit is defined according to Figure 1.29 in Section 1.6.4 of the introduction.

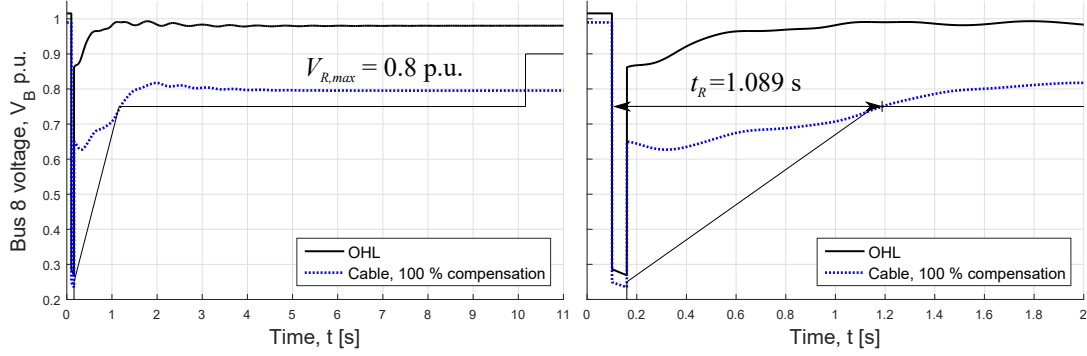


Figure 5.10. Voltage trajectory analysis of Bus 8 in the IEEE 9-bus system. The disturbance is a three-phase fault on Line 4, 99 km from Bus 8. The thin solid line represent the under-voltage limit according to Figure 1.29.

The voltage recovery ability is quantified by defining the voltage recovery time t_R as the time from fault incidence to the time at which the voltage has recovered to 0.75 p.u. and the post fault recovered voltage V_R .

$$\text{OHL: } t_{R,OHL} = 0.16 \text{ s} - 0.1 \text{ s} = 60 \text{ ms} \quad \text{and} \quad V_R = 0.980 \quad (5.6)$$

$$\text{Cable: } t_{R,Cable} = 1.189 \text{ s} - 0.1 \text{ s} = 1089 \text{ ms} \quad \text{and} \quad V_R = 0.795 \quad (5.7)$$

In the case of the OHL based system, the voltage at Bus 8 is able to recover beyond 0.75 p.u. immediately after fault clearing. Furthermore, the voltage is able to recover to 0.98 p.u. which is just below the pre-faulted value of 1.015 p.u. In the case of the 100 % SR compensated system, the voltage trajectory slightly violates the under-voltage limit of reaching 0.75 p.u. 1 s after clearing the fault. However, the worse part is that the voltage is unable to recover beyond 0.8 p.u. Thus, violating the condition of reaching minimum 0.9 p.u. 10 s after clearing the fault.

Now, the question may be raised, why is the voltage able to recover in the OHL case, but unable in the equivalent cable case? The answer is the local deficit of reactive power due to the presence of shunt reactors in the post-faulted condition. Figure 5.11 repeat the case shown in Figure 5.10, but with switching of shunt reactors in response to the disturbance. The result shows that in order to achieve similar voltage trajectory as the equivalent OHL case, shunt reactors should be switched off concurrently with the switching of the cable. Naturally it must be so, as the purpose of the shunt reactors is to compensate the reactive power generated by the cable, which is no longer connected. If the shunt reactors are not switched off, there will be a local unbalance in reactive power, which must be balanced by the remote synchronous machines. Figure 5.11 displays a case of switching off both SRs at Bus 8, that is the SR compensating 50 % of Line 4 and the SR compensating 50 % of Line 3. As it has been discussed earlier, the removal of SR is equivalent of injecting reactive power locally by reducing the demand. In this case, the sudden abundance in reactive power at Bus 8 causes a voltage overshoot as the excitation level of SG2 is high in response to the faulted condition. After approximately 4 s, the AVR of SG2 has settled, and the voltage at Bus 8 has reached a steady state condition.

However, the voltage is not controlled to 1 p.u. due to the reactive power imbalance at Bus 8, as the voltage is only controlled at the terminals of the synchronous generators.

Thus, SR and transmission lines should be disconnected simultaneously. Disconnecting additional SR may improve the recovery time, but at a risk of transient voltage overshoots and steady state over voltage. Ideally, the SR capacity should be variable and controlled according to the local voltage, with the ability to respond fast to changes in load and excitation level of nearby synchronous generators.

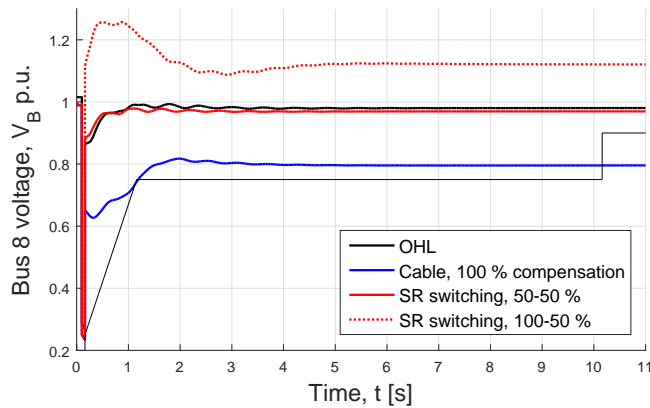


Figure 5.11. Voltage trajectory analysis of Bus 8 in the IEEE 9-bus system. The disturbance is a three-phase fault on Line 4, 99 km from Bus 8. The thin solid line represent the under-voltage limit according to Figure 1.29.

5.5.1 Varying the fault location in the proximity of Bus 8

In Section 5.5 it is shown how the voltage recovery at Bus 8 is dependent on the balance of reactive power in the post-disturbed condition, and the excitation control of synchronous generators in the proximity of Bus 8.

An important note about the IEEE 9-bus base system in DIgSILENT PowerFactory is regarding the difference in AVR systems between the three synchronous generators. Table 5.2 shows the so called amplifier gain K_A and the amplifier time constant T_A of the SG plant models. Primarily, K_A is much higher for SG2. As a result, the excitation of SG2 has a powerful dynamic response to terminal voltage deviations, whereas SG1 and SG3 respond by changing the excitation level significantly less. Practically, the magnitude of K_A for SG1 and SG3 implies a negligible large-signal dynamic response. This can be observed in Figure 5.13, where each SG of the 9-bus system in turn are exposed to a permanent three-phase fault located 1 km from its terminals. The simulation is performed without over-excitation limiter (OEL). SG2 displays a fast excitation response with a high ceiling level, while excitation systems of SG1 and SG3 responds weakly.

Table 5.2. Selected AVR system constants of the SGs in the IEEE 9-bus system in DIgSILENT PowerFactory. K_A is the voltage controller gain, while T_A is the time constant.

	K_A [-]	T_A [s]
SG1	0.001	0.2
SG2	400	0.05
SG3	0.001	0.2

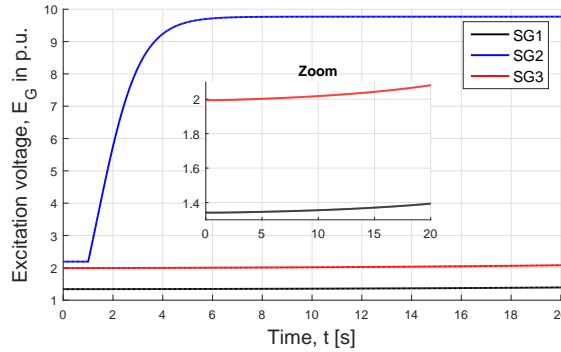


Figure 5.12. Excitation system response of the synchronous generators in the IEEE 9-bus system in response to a permanent three-phase fault located 1 km from the SG terminals in each respective case.

The difference in AVR system between the synchronous generators in the 9-bus system implies another asymmetry in the network, which influences the voltage stability limits. Basically, it can be argued that with the base AVR systems, SG2 is the only unit in the 9-bus system with dynamic reactive power and voltage control capabilities. Thus, any large-signal voltage disturbances would need to rely on the capability of SG2.

Based on this observation, it is relevant to discuss the strength of the network buses, as it was presented in Section 5.2. Based on the Q, V -curves presented in Figure 5.3, Bus 8 is argued to be the weakest bus in the network. However, the method of producing Q, V and V, P -curves is a steady state method of assessing voltage stability. Thus, assessing the strength of the nodes based on the Q, V -curve does not reveal limitations in the dynamic response of nearby synchronous generators.

Now, it can be argued that Bus 6 is the dynamically weakest bus of the 9-bus system, as it is the most distant bus relative to SG2, and recalling that SG2 is the only dynamic regulator of reactive power in the network. However, the important conclusion of this discussion is not which bus of the 9-bus system is the weakest. Rather, the importance is how the strength at a given node is affected by the topological change of the network in post-faulted condition.

Figure 5.13 show how the voltage trajectory at Bus 8 is dependent on the post-faulted topology relative to SG2. Line 3 is the direct connection between Bus 8 and SG2. Thus, when Line 3 is faulted and switched out of operation, the voltage trajectory is unable to satisfy the post-disturbance under-voltage limit.

Due to the post-faulted topology of the network in this case, the only dynamic reactive power controller (i.e. SG2) is distanced far from Bus 8. In contrary, when Line 4 is faulted, which connects Bus 8 and SG3, the voltage trajectory at Bus 8 is improved as the direct connection between Bus 8 and SG2 is maintained. Thus, any bus which is separated from SG2 will be weakened with respect to voltage stability.

The voltage is unable to recover to 1. p.u. due to the post-faulted topology of the network and the fact that SGs regulate the terminal voltage and not the distant voltage at Bus 8.

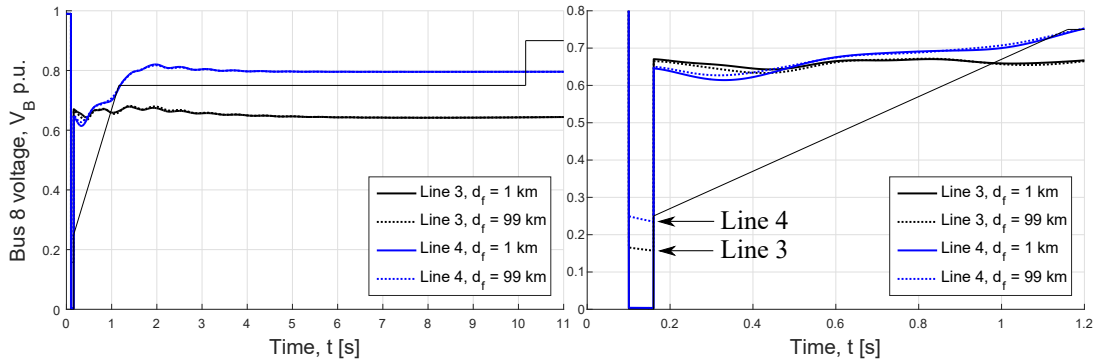


Figure 5.13. Voltage trajectory analysis of Bus 8 in the IEEE 9-bus system. Four cases of line faults are displayed with distances measured from Bus 8. The thin solid line represent the under-voltage limit according to Figure 1.29.

The AVR systems in the 9-bus system in PowerFactory could simply be changed to have similar performance. However, as the purpose is to compare the performance of OHL and cable networks, the difference in AVR system is just something to be aware of when assessing the dynamic voltage performance. The discussion highlights that voltage stability is a local phenomena, which is highly dependent on the reactive power capabilities of units in the proximity of the area. Based on which the discussion of switching of shunt reactors in response to large-disturbances becomes relevant.

5.6 Forcing voltage instability in the IEEE 9-bus system

It is desired to investigate if switching of shunt reactors in the cable based HVAC transmission network provides the ability to stabilize a potential voltage collapse. In order to realize this study in the IEEE 9-bus system, the system must be disturbed in such a way that one or more bus voltage does not satisfy the under-voltage limits within the specified time restrictions.

Such an event can be obtained when applying a series of disturbances to the network. Initially Line 3 is exposed to a three-phase fault located at 1 % line distance from Bus 8. After 60ms the fault is cleared by taking Line 3 out of service, while the shunt reactors of the line are switched-off correspondingly. However, faulting the system and removal of a transmission line and SRs does not lead to low system voltage alone, as it is discussed in Section 5.5. Thus, a load event is introduced where the P, Q loading of Bus 8 start increasing with a ramp increment in which the load is increased proportionally by 70%.

This means that Bus 8 P_0 is increased from 100 MW to 170 MW, and Q_0 is increased from 35 Mvar to 59.5 Mvar. The total duration of the ramp increment is 3 s, and is initiated at $t = 0.3$ s, 140 ms after removal of Line 3.

The nature of the disturbance is highly unrealistic, as a load increase of 70 % within 3 s is far from any expected load profiling. However, the disturbance forces a condition of unsatisfactory voltage profiles in the 9-bus system, which is needed for analysing possible methods for avoiding a total voltage collapse.

As to why instability is unobtainable following a more natural disturbance, it is expected to be partly due to the topology of the network and due to the simplicity of the model. Voltage instability in a real power system is typically recognized as a cascading event of disturbances, which includes the interactions of transformer tap changing, over-excitation limitations, under-voltage protection and the performance of dynamic loads such as induction machines.

Figure 5.14 shows the voltage instability scenario forced by the described disturbance. The voltage drop is not limited to Bus 8 where the load is increased, but is observed throughout the system. Only the voltage at the terminals of SG2 is kept at 1 p.u. due to the AVR, which is observed as an improved voltage trajectory at Bus 7 compared to the more distant buses.

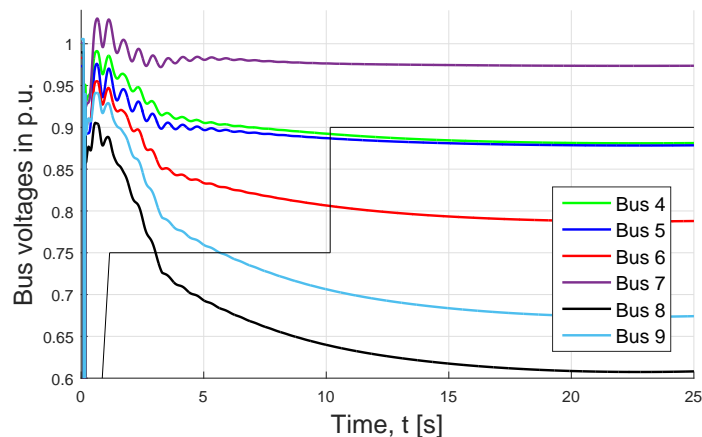


Figure 5.14. Voltage trajectories of the six transmission system buses in the 9-bus system following a large disturbance, including a line fault and a 70% load ramp disturbance at Bus 8. The thin solid line represent the under-voltage limit according to Figure 1.29.

The cause of the voltage instability following the disturbance is due to the increasing flow of active and reactive current over long distances in the network. The loads of the system are modelled as a composition of ZIP as described in Section 5.1. Thus, when the voltage drops locally at Bus 8 due to the load increment, the load will draw more active and reactive current due to the constant power component. Figure 5.15 shows the 9-bus network topology in the post-faulted condition. The ring-network topology is weakened and changed to a radial network, where Bus 8 and Load C are separated far from SG2.

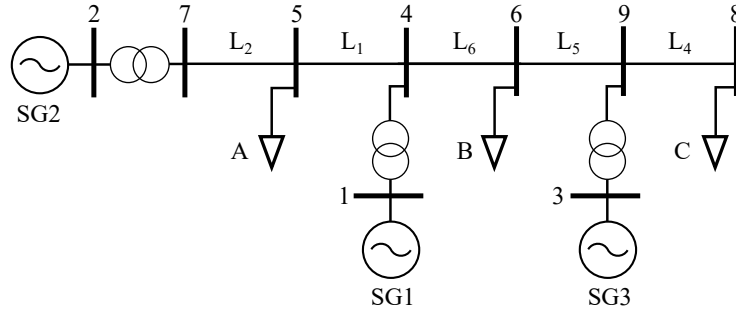


Figure 5.15. Post-disturbance 9-bus system. The system topology is changed from a ring-network to a radial string configuration due to the removal of Line 3.

Due to the dynamic excitation inability of SG3 the reactive current is not supplied near Bus 8, but is injected farther away. Figure 5.16 shows the terminal voltage V_T and the active output current $I_{P,o}$ and the reactive output current $I_{Q,o}$ of the synchronous generators. SG3 is unable to keep the voltage at its terminals due to the dynamically unchanged excitation voltage E_G , as shown in Figure 5.12. Due to the drop in terminal voltage, the reactive power output of SG3 decreases, and the active power output P_o is not increased proportionally with the increase in active output current $I_{P,o}$. Consequently more reactive current must be supplied from SG1 and SG2 in order to achieve a new steady state operating point. The result is that the system voltages, shown in Figure 5.14 are increasingly suppressed when observing the buses in Figure 5.15 from Bus 7 (left) towards Bus 8 (right).

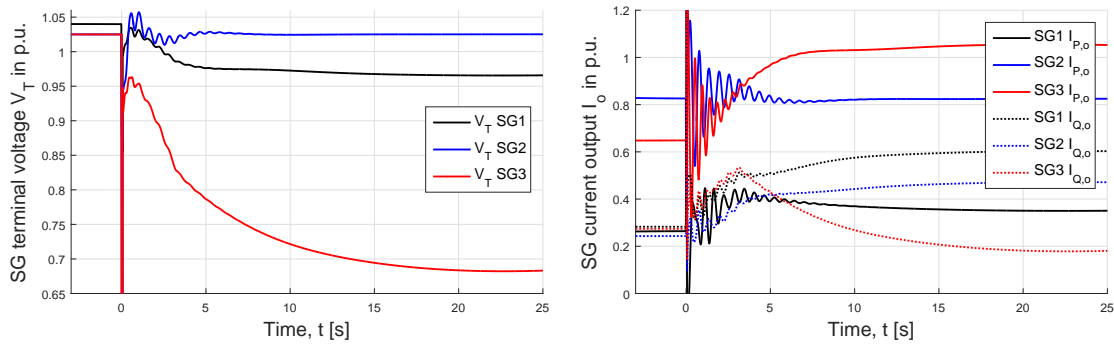


Figure 5.16. Left: SG terminal voltages. Right: SG active output current $I_{P,o}$ (solid lines), and reactive current output $I_{Q,o}$ (dotted lines).

5.6.1 Modelling considerations for load-increment in RMS simulations

In Section 5.6 it is described how the IEEE 9-bus system voltages can be forced below the under-voltage limits by increasing the loading following a large disturbance. In order to simulate this event with expected system behaviour, it is necessary to add speed governors to the synchronous generators in the system. Without speed regulation in the modelled system, even a small increase or decrease in load will eventually make the system unstable, as the balance between load and generation is unable to recover to an equilibrium.

Figure 5.17 display the mechanical power and shaft speed of SG1 in response to a load increment at Bus 8 while performing RMS simulation in DIgSILENT PowerFactory. Two cases are compared 1) with speed governor IEEEG1 applied to all three synchronous generators, and 2) without speed governors on any of the three synchronous generators.

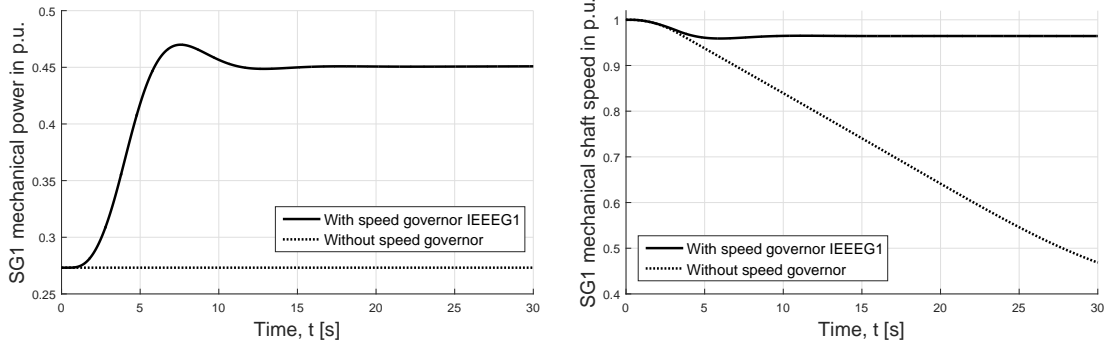


Figure 5.17. Comparison of mechanical power and shaft speed with and without governor IEEEG1 applied to the SG plant models in DIgSILENT PowerFactory in response to a system load increment.

When the system experiences an increase in load, more mechanical power must be supplied in order produce the active power required to balance generation and load and keep the electrical frequency. The purpose of the speed governor is to measure the shaft speed deviation following the change in load, and control the turbine driving the SG to produce more torque. If the turbine does not deliver more torque on the shaft, the speed will decrease and thus the electrical frequency will drop.

Figure 5.18 shows the field current I_f of SG2 and the load bus voltage in the 9-bus system. The inability to find an equilibrium between generation and load without the speed governor leads to voltage instability of the system. As the shaft speed decreases towards zero, the terminal voltages drops simultaneously. The excitation system of SG2 tries to restore voltage by increasing the field current I_f , but inevitably the system voltage drops due to the unbalance in mechanical power required and the demand of the loads, which draws increased current as the voltage drops. If the loads are modelled as constant impedance, this effect will not be observed, as the load P_o will be reduced as the voltage drops.

Without regulation of mechanical power an increment in system loading is impossible for dynamic simulations in PowerFactory without slowly losing stability. Thus, if governor models or similar controls are not included, a study case may falsely be interpreted as an event of power system instability which does not represent real system behaviour. Hence, the results displayed in Section 5.6 and the following sections and chapters are produced by including governor models. The results displayed in Chapter 3 and Chapter 4 are unaffected by the presence of the governor, as no dynamic load change is performed.

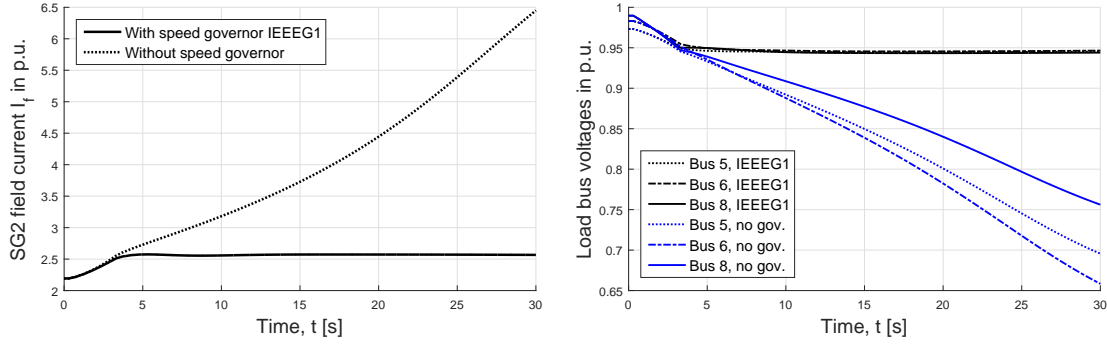


Figure 5.18. Comparison of SG2 field current and bus voltages with and without governor IEEE1 applied to the SG plant models in DIGSILENT PowerFactory in response to a system load increment.

5.6.2 Effects of shunt reactor switching

Shunt reactor switching is regarded as a relief to large voltage drops by utilizing the reactive power generated by the cables. By switching off certain portion of the shunt reactors, the additional reactive power by the cables could supply the inductive loads locally, thus decreasing the reactive power transfer from a more distant point in the system. This would in turn reduce the voltage variation between connecting terminals. The switching of SRs is done using a tap event in PowerFactory where the tap position of SRs could be changed during the simulation. The SR model is assumed to have 20 tap positions and operating at the top position initially. Hence each step change is analogous to switching out five percent of the SR total Mvar rating.

Different SR-switching schemes would produce varying degree of improvements to the system. Location and amount of compensation are some factors to be taken into consideration with respect to the improvement and operating limits. In this section, these considerations are investigated and shown by performing various case studies on the forced event as described in Section 5.6. The investigation focuses on the voltage level of the load buses and the main criteria is that it should be able to satisfy the under-voltage operating limits as defined in Figure 1.29. The following SR switching cases are carried out assuming that there is no restriction on the number of steps that can be changed at the switching instant:

For Case A, the location of SR switching is chosen at Bus 8 because the load disturbance occurs at that terminal and also where the most severe voltage drop is recorded. The entire SR is switched out for an initial study. The new voltage trajectory of the load buses is shown in Figure 5.19. After SR switching, all the load buses are able to satisfy the under-voltage operating condition and their voltages settle at 1.0 p.u. and above. Nonetheless there is a noticeable voltage difference between Bus 8 and the other two. This observation is expected as the SR switching at Bus 8 results in an excess of reactive power at Bus 8 which is at one end of the system as can be seen in Figure 5.15. Therefore excessive reactive power flow through the transmission lines to the other loads and generators in the system would in turn cause substantial voltage variation across the single-line network.

In fact, the new operating voltage of more than 1.2 p.u. at Bus 8 would have otherwise violated the over-voltage operating limit though it is not covered in the thesis. Hence this switching case is not considered a viable improvement for the system.

Table 5.3. Definition of switching cases with respective events. All the switching events are applied at $t = 3.019$ s. SR4 refers to the shunt reactor that is used to compensate Line 4. Switching % refers to the compensation amount of that particular SR being switched out. The rating of each SR can be calculated by dividing the respective line reactive power values found in Table 4.2 by 2.

	Location	SR-switching [%]	Total Mvar Disconnection [Mvar]
Case A	Bus 8	SR4 - 100	183.90
Case B	Bus 8	SR4 - 50	91.95 + 92.94 = 184.89
	Bus 4	SR1 - 60	
Case C	Bus 8	SR4 - 45	82.75 + 54.22 + 48.67 = 185.64
	Bus 5	SR1 - 35	
	Bus 6	SR6 - 35	

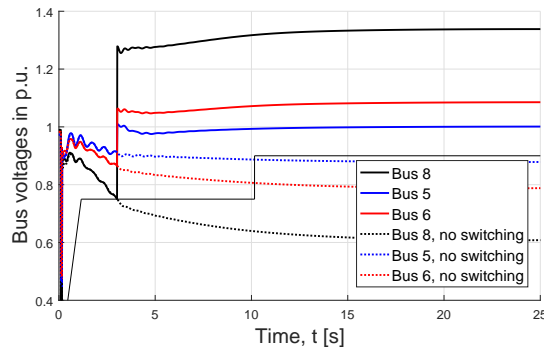


Figure 5.19. Voltage trajectories of the three load buses with Case A SR switching following a 70% load ramp disturbance at Bus 8. The trajectories of the non-switching case is also included for comparison.

The same voltage trajectory curves obtained from Case B and C are presented in Figure 5.20. Referring to Table 5.3, both these cases are used based on the total SR compensation disconnected of each case in order to match closely with Case A and thus highlighting the importance of the location. The locations are chosen depending on their proximity with respect to the load buses. The idea is to distribute the excess reactive power more evenly and not be transferred from a specific point in the network. It can be observed from the left side of the figure that the resulting load voltages in Case B are much closer to one another in comparison with Case A. Moreover, the peak voltage of Bus 8 has been greatly reduced to a level below 1.04 p.u. indicating a much higher margin from a possible over-voltage violation.

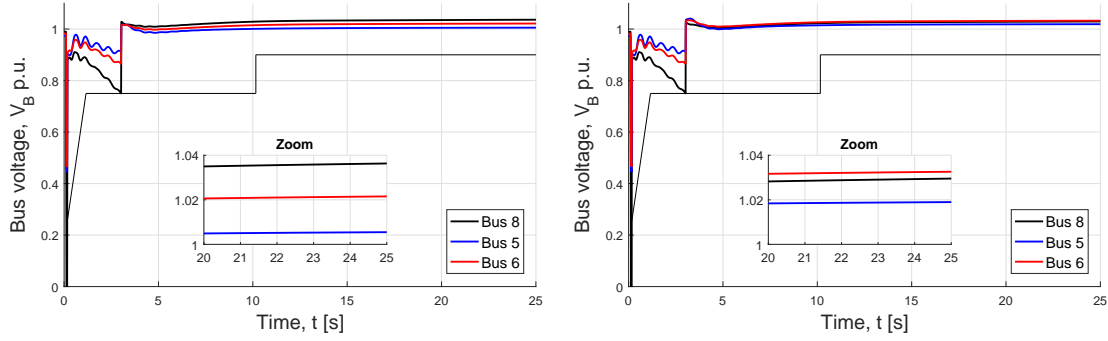


Figure 5.20. Voltage trajectories of the three load buses with two SR switching cases (Left: Case B and Right: Case C) following a 70 % load ramp disturbance at Bus 8.

The observed improvement in Case B is attributed to a more distributed reactive power flow in the system as Bus 4 is situated between Load A and B shown in Figure 5.15. There is no large reactive power flow across long distance that would cause a large voltage deviation and thus more beneficial for a more uniform voltage levels. Further improvement could be explored when reactive power is directly supplied at the load buses. This is the main motivation behind Case C where the SR-switching events are located at these specific buses. By comparing the trajectory curves in Figure 5.20, the load voltages in Case C settle slightly closer to one another as compared to Case B. However a more significant impact on the loading of Line 1 is observed and presented in Figure 5.21 when varying between the two switching schemes. There is a reduction in the loading of more than 10 % in Case C which is due to reactive demand of the load at Bus 5 being supplied locally in contrast with being transferred from Bus 4 in Case B. Besides smaller voltage deviation, a decrease in loading also reduces active power losses in the network. This factor is vital because the active demand of the loads could only be supplied from the generators in the system. From a voltage perspective, higher losses would incur a larger deviation from the sending end to the receiving end. Hence highlighting the importance of supplying reactive power locally for voltage support in the system.

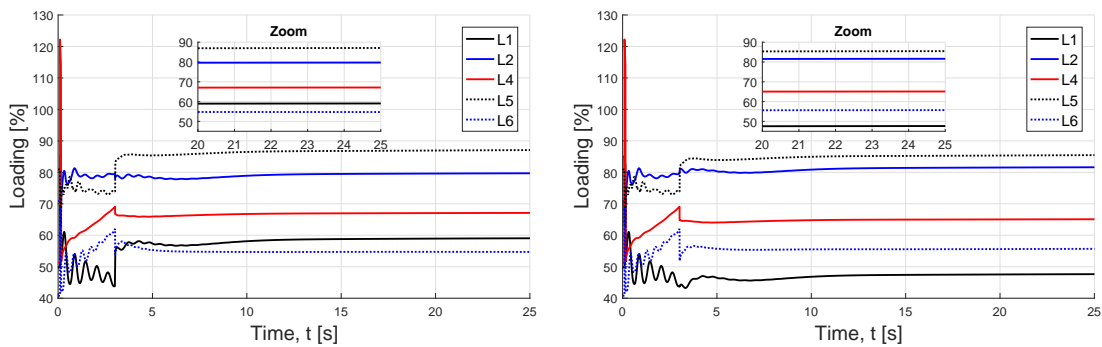


Figure 5.21. Line loadings of the six transmission lines with SR switching cases (Left: Case B and Right: Case C) following a 70 % load ramp disturbance at Bus 8. The loading is computed based on its rating and each line is rated at 1 kA.

5.6.3 Improving the dynamic voltage regulation in the IEEE 9-bus system

In Section 5.6.2 it is presented how tap switching of SRs can improve the voltage trajectory following a large disturbance. However, the technical feasibility of implementing sufficiently fast and flexible SR-switching is an open question. Assuming that cables were compensated by variable SRs with the ability to regulate within a few seconds, it would still be natural to consider the SR-switching as an emergency tool in events of collapsing system voltages. For long HVAC cables, the SRs are dimensioned for several hundreds Mvar.

Dynamic voltage regulation by including STATCOM

In modern power systems FACTS devices can be implemented (flexible AC transmission systems), such as the static synchronous compensator (STATCOM) or thyristor-controlled shunt and series devices such as SVC (Static-var-compensator) and TCSC (thyristor controlled series capacitor). Within their capacity limits these devices provide the ability to control the voltage and the power factor at a given node in the system independent of the voltage. However, if the capability limit of the device is reached, it will be voltage dependent and display similar behaviour as a simple shunt capacitor or reactor, with a dependency of: $Q = V^2/X$ [2].

In an event of cascading system voltages, a hypothesis is that SR-switching can act as a recovery tool. Large amounts of reactive power supplied from under-compensated cables may recover system voltages to satisfy voltage limits. By letting cables inject the majority of the necessary reactive current, the dependency on FACTS devices may be relieved.

A generic STATCOM model is inserted at Bus 8 in the IEEE 9-bus system. The purpose is to compare and discuss the combination of SR-switching and improved dynamic voltage control. A brief discussion of the STATCOM and the PowerFactory model is located in Appendix G.

Figure 5.22 presents a comparison of the voltage trajectories at Bus 8 with STATCOM included. It is evident that the presence of STATCOM has a significant improvement on the bus voltage. In each case the STATCOM is set to voltage control mode which would inject or absorb reactive power for dynamic regulation. However, there exists a limit in the reactive power injection from the STATCOM even though the voltage at the controlled terminal has not been brought back to its voltage set point which is 1.0 p.u. in this case. This limit is dependent on the rating of the STATCOM. Hence the figure also illustrates that a better voltage trajectory is observed in the case of 50 MVA rated STATCOM as compared to the 25 MVA rated case plus the 0.9 p.u. under-voltage limit is not violated.

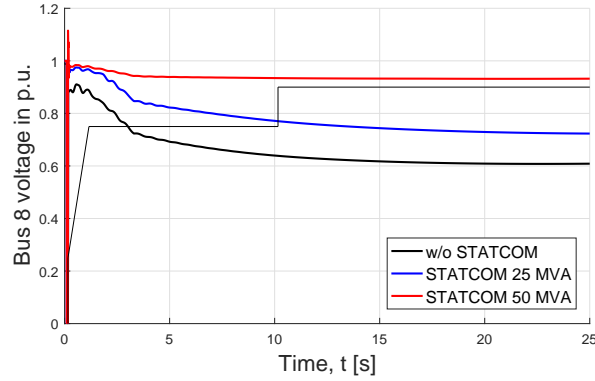


Figure 5.22. Comparison of voltage trajectories of Bus 8 in the IEEE 9-bus system with 25 MVA and 50 MVA rated STATCOM included at Bus 8.

While the most improvement is observed with a higher rated STATCOM, the goal is not to have large capacity STATCOM installed at every node in the system due to economical constraints. Instead it is desired to investigate if a smaller capacity STATCOM is sufficient by coupling with SR-switching. For this reason the same cases are repeated with SR-switching and the voltage trajectories are displayed in Figure 5.23. It can be seen that the final operating point of both cases are the same though with varying amount of SR-switching. This result proves that SR-switching could be employed in order to reduce the need for reactive support by STATCOM. This observation is important as it provides the possibility of using SR-switching as the primary voltage recovery tool in the cable network while the use of STATCOM could be limited.

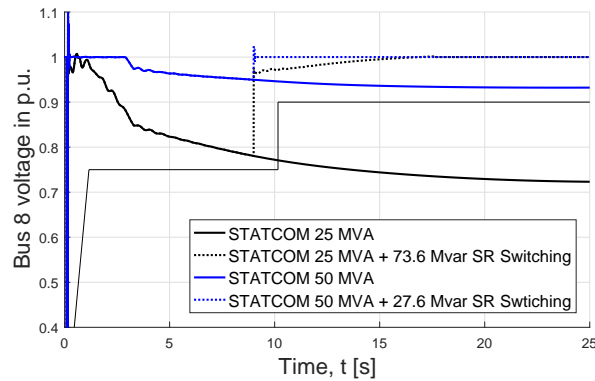


Figure 5.23. Voltage trajectory of Bus 8 in the IEEE 9-bus system with 25 MVA and 50 MVA rated STATCOM and switching of SR4 at Bus 8. The switching time instant is at $t = 9$ s.

Dynamic voltage regulation by improved AVR

As mentioned throughout Chapter 5 the dynamic voltage regulation of SG1 and SG3 in the IEEE 9-bus system is very poor due to the modelled AVR constants. Another way of improving the voltage trajectory of Bus 8 in the 9-bus system is by changing the excitation system of SG3. In reality excitation systems cannot simply be changed, but it is done here to illustrate the influence of a better AVR system.

Figure 5.24 show how the voltage trajectory at Bus 8 is significantly improved by changing the AVR system of SG3. The time constants and gains of the excitation system are changed from the default values in the 9-bus model in DIGSILENT PowerFactory, to the values of the standard IEEE X1 model.

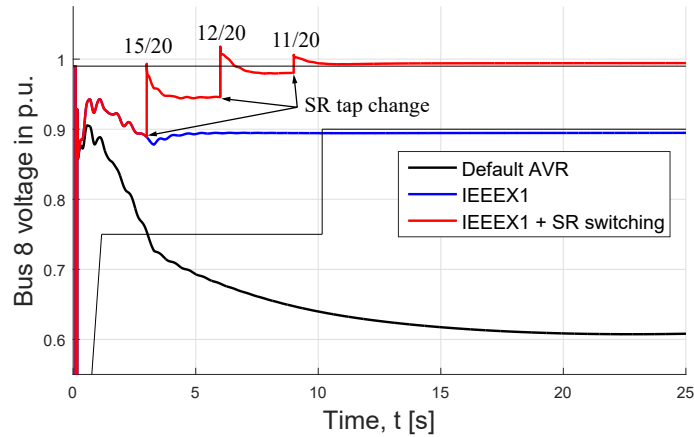


Figure 5.24. Voltage trajectory of Bus 8 in the IEEE 9-bus system with improved excitation system AVR for SG3 and tap change switching of SR4a located at Bus 8.

When the excitation system is improved, the terminal voltage of SG3 is regulated to 1 p.u. and the SG is able to supply active and reactive power to Bus 8 at lower current. Hence, improving the AVR system of SG3 changes the power flow of the entire system, as power to a greater extent is supplied locally.

However, the AVR system regulates the voltage at the terminal of the generator. Hence, despite being improved, the voltage at the 100 km distant Bus 8 is not regulated back to its initial voltage.

The voltage at Bus 8 can be regulated close to 1 p.u. by utilizing tap changing of the SRs connected at Bus 8. Figure 5.24 show a case where the voltage at Bus 8 is regulated to 0.995 p.u. by changing the taps of SR4a at Bus 8 in 3 steps with 3s between each tap change. SR4a is rated to 183.9 Mvar, and when divided into 20 taps, each step corresponds to 9.195 Mvar at 1 p.u.

Figure 5.24 show that even though the AVR systems of SGs are improved, there is still a need for local voltage control at distant buses. SRs with the capability to dynamically switch can provide local control.

5.7 Summary of voltage stability analysis in the IEEE 9-bus system

This section gives an overview of the large-disturbance voltage stability study carried out in the IEEE 9-bus system. The following are the conclusions of the voltage stability analysis based on the 9-bus system:

Conclusions on the modelling procedure:

- **Load modelling:** The voltage instability phenomenon is highly dependent on the load characteristics. The $\partial P/\partial V$ and $\partial Q/\partial V$ behaviour of loads will influence the flow of active and reactive power in the network, and thus affect the system voltage.
- **SG reactive power capability limits:** Modelling of reactive power capability limits influences the power flow of the system and thus the V, P -characteristics of the network. For realistic representation, V, P -curves should be produced with capability curves. However, due to the small scale of the 9-bus network, power flow convergence failure occurs before load-ability differences can be distinguished between the OHL base system and the equivalent cable system. For a larger network it is possible to obtain critical-voltage levels in power flow solutions with capability limits, and hereby obtain a more meaningful V, P -curve. This is shown in Chapter 6.
- **Load and generation balance in RMS simulation:** Speed governors must be included in the model in order to avoid system collapse when changing the system loading in RMS simulations. Without speed governing the inevitable system collapse may be mistaken for an event of cascading voltage instability.
- **Excitation system modelling:** The dynamic response of excitation systems of voltage controlled synchronous generators is crucial for the power systems ability to remain voltage stable. Thus, realistic models of excitation systems and AVR is necessary for realistic representation of system dynamics.

Conclusions on the voltage stability comparison of OHL systems and equivalent cable systems:

- **Load-ability:** V, P -characteristics show that the cable based system has higher load-ability margin P_{max} , due to the lower series inductance and resistance resulting in lower equivalent impedance between generation and load.
- **SR compensation degree:** By under-compensating the cable based system, the overall load-ability can be increased, as the cables will supply reactive power for the inductive loads, line inductance and transformers. A consequence of over-compensating is slightly increased critical voltages due to the overall capacitive behaviour of the network. However, as discussed by the authors of [40], the load-ability P_{max} in V, P -curves, is more meaningful than the critical voltage.
- **Voltage trajectories following line faults:** When 100 % compensated, the equivalent cable system displays equal fault response as the OHL base system if SRs of the faulted line are disconnected. Changing the compensation degree will induce a difference in system responses.

- **Switching of shunt reactors:** When the 9-bus system is severely weakened by the removal of a transmission line and an increase in load, the system voltage can be recovered by switching of shunt reactor capacity. This ability is unavailable in the OHL base system, where compensation for steady-state operation is unnecessary.
- **Combining dynamic voltage regulation and SR-switching:** Switching of shunt reactors can aid dynamic voltage regulators such as locally placed FACTS or AVR systems of SGs. If voltage support in the form of a STATCOM is combined with SR-switching, the necessary STATCOM capacity may be reduced.

Large-disturbance voltage stability analysis: IEEE 39-bus system 6

This chapter describes the study of large-disturbance voltage stability in the IEEE 39-bus system. Line modelling is done according to Chapter 4, including replacement of the OHL base system with an equivalent HVAC cable transmission system. The IEEE 39-bus system is more representative of a real power system compared to the 9-bus system as discussed in Chapter 5. Hence, more emphasis will be on the characteristics of the network strength and dividing the network into areas for the voltage stability analysis. The topics and analysis presented in the chapter are:

- **Localizing and characterization of weak areas:** Identification of weak areas by short-circuit analysis and characterization of AVR of nearby synchronous generators.
- **Steady state analysis of weak areas:** Comparison of V, P and Q, V -characteristics for the OHL and cable cases.
- **Large disturbance voltage trajectories:** Analysis of voltage trajectories following large-disturbances.
- **Reactive power compensation:** Analysis of different reactive power compensation strategies for improvement of voltage stability.

Modelling considerations for voltage stability analysis in the IEEE 39-bus system

Based on the 9-bus system analysis the following models are included in the 39-bus model in DIgSILENT PowerFactory:

- **Equivalent cable system and shunt reactors:** The equivalent cable system is modelled according to the coefficients presented in Section 4.2.3. Shunt reactors are initially dimensioned for 100 % compensation according to equation (4.7), with a 50-50 % line-end distribution.
- **Reactive power capability curves:** P, Q -curves are included in the model of the ten synchronous generators in the system. The limits are defined following the procedure described in Section 5.4, using the theoretically based values provided by DIgSILENT. The reactive capability limits of the synchronous generators changes the steady state power flow of the system, as individual generators reach their limits. This behaviour is relevant for producing V, P and Q, V -characteristics of the network.

- **Load modelling:** Every load in the network is modelled according to the composition described in Section 5.1. Changing the composition and the $\partial P/\partial V$ and $\partial Q/\partial V$ coefficients will affect the steady state results as well as the dynamic behaviour of the network.
- **Excitation systems:** Synchronous generators SG2-SG10 of the IEEE 39-bus system in DIgSILENT PowerFactory have predefined AVR systems. SG1 is excluded as it represents an external network, rather than an actual synchronous machine. Each of the AVR system is unique and dynamically responsive, unlike SG1 and SG3 in the 9-bus system. The performance of each excitation system is shown in Figure 6.2.
- **Speed governors:** In order to be able to perform load increments in RMS simulation each of the synchronous generators are modelled with speed governors, which are included in the model provided by DIgSILENT.

6.1 Identification and characterization of weak areas in the IEEE 39-bus system

The voltage stability analysis of the 39-bus system is limited to a few selected network areas. Thus, a short-circuit analysis is performed in DIgSILENT PowerFactory with the purpose of calculating the apparent short-circuit power at each load bus in the network. The strength of a power system node (in a SG based system) is a combination of the Thevenin equivalent impedance Z_{th} seen from the node, and the mechanical inertia J of nearby generation units [2]. Hence, a weak node or area is characterized by a high Thevenin impedance and low mechanical inertia. In relation to voltage stability analysis, a low short-circuit power at a load bus indicate a possible large impedance between the load and the generating units. Thus, short-circuit power is an indicator of the distance between the load and generation, and as such provides information regarding the V, P -characteristics and the voltage sensitivity to load increments.

Table 6.1 show the results of the short-circuit calculations. The calculations are performed for the equivalent cable case with 100 % compensation. Thus, all lines are modelled according to the scaling coefficients presented in Section 4.2.3. The equivalent cable case display slightly larger short-circuit powers S_{SC} , due to the lower line resistance and line inductance in comparison to the OHL base case. However, the overall relative strength between the buses and areas remain unchanged.

SG1, which is feeding Bus 39, displays a very large short-circuit power in comparison to the other buses. This is because SG1 is modelled to represent the interconnection between the New England power system and the rest of USA and Canada. For the same reason, SG1 is modelled without any AVR system, whereas the remaining 9 synchronous generators have individual AVR models.

Based on the short-circuit results, the load buses of the system are divided into areas from A to G based on their short-circuit power and their location in the network. Area A represent the grouping of load buses in close proximity displaying the highest short-circuit powers. While, Area G represent the grouping of load buses in close proximity displaying the lowest short-circuit powers.

Load buses 20, 24 and 39 do not share similar short-circuit characteristic with their connected buses, and are not regarded as part of an area. It is important to note that the areas are solely based on the short-circuit analysis performed in this thesis. The purpose of defining the load bus areas A to G is easier referencing and to simplify the voltage stability analysis.

Table 6.1. Short-circuit current and apparent power at the load buses in the IEEE 39-bus system calculated in DIGSILENT PowerFactory according to the IEC 60909 standard.

Load bus no.	S_{SC} [MVA]	I_{SC} [kA]	Area
Bus 3	10824.42	18.11	
Bus 4	10181.91	17.04	A
Bus 18	9532.17	15.95	
Bus 25	10009.72	16.75	
Bus 15	9380.62	15.70	
Bus 16	12497.60	20.91	B
Bus 24	9505.65	15.91	
Bus 8	8979.67	15.03	C
Bus 7	8639.21	14.46	
Bus 21	8585.50	14.37	D
Bus 23	8279.45	13.86	
Bus 26	7765.95	13.00	E
Bus 27	7553.91	12.64	
Bus 28	4902.76	8.20	F
Bus 29	5927.31	9.92	
Bus 12	3479.15	14.56	G
Bus 31	6748.71	236.14	
Bus 39	58794.88	98.39	
Bus 20	6091.60	15.29	-

Based on the results displayed in Table 6.1, three load bus areas are selected for the voltage stability analysis. Area F and G are chosen as they are considered the weakest, while Area A is chosen for the ability to compare to a stronger area. Figure 6.1 show Area A, Area F and Area G marked on a single-line diagram of the IEEE 39-bus system.

As it was stated, the short-circuit power gives indications towards the voltage stability by being a function of the system impedance and the inertia of the synchronous machines. However, as it was discussed in Chapter 5 the performance of the AVR systems play an essential role in keeping the system voltage stable. In the system model used the controlled excitation systems are the only reactive power regulating devices in the network. Thus, it is relevant to evaluate the speed and the ceiling value of the AVR systems in the model.

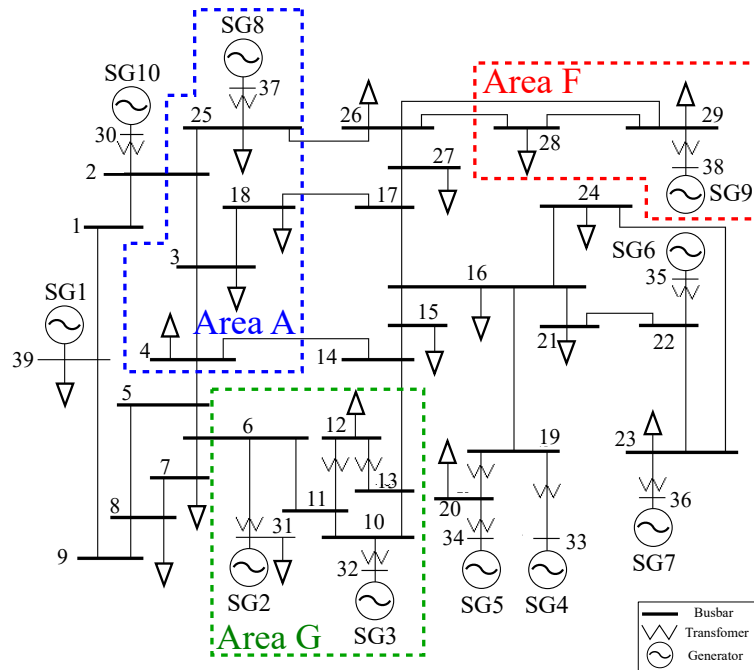


Figure 6.1. Single-line diagram of the New England IEEE 39-bus system with marking of the Areas A, F and G.

Figure 6.2 show the excitation voltage response of the synchronous generators in the system when in turn exposed to a three-phase fault located at 1 % line distance from the respective SG.

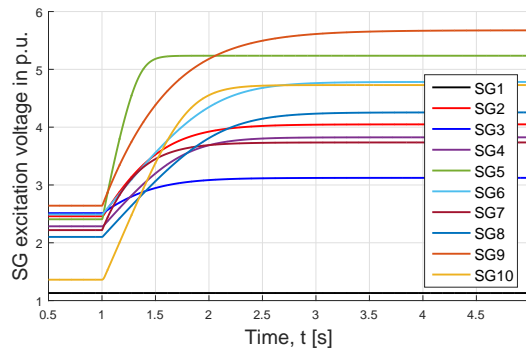


Figure 6.2. Excitation response of the synchronous generators in the IEEE 39-bus system following a permanent three-phase short-circuit located at 1 % line distance from each SG respectively.

SG3, which is located in Area G, displays the lowest excitation voltage E_G ceiling value compared to the other machines. SG2, also located in Area G, has an average ceiling value. Neither of the two reaches their ceiling values fast in comparison to the excitation systems of the other machines. SG9, which is located in Area F, has the highest ceiling value of the excitation systems. The dependency of excitation system controls will not be expressed in the V, P and Q, V -curves produced by steady state analysis, but will influence the dynamic voltage trajectory analysis.

6.2 V,P-characteristics of areas in the IEEE 39-bus system

With reference to Figure 6.1, three areas are subsequently selected for voltage sensitivity analysis: Areas A, F and G. The V, P -characteristics of these specific areas are obtained in the OHL case along with three different compensation levels of cable system, shown in Figures 6.3, 6.4 and 6.5. The 75% and 125% compensation cases are done in the same manner as described in Section 5.3 for the IEEE 9-bus system. The normalized curves of each area in the figures are only represented for the most significant bus in the area. Power flow simulations are performed where the loading at the bus is progressively increased with constant power factor and the power capability curve included in the SG models. The normalization of both voltage and load active power is done by scaling upon their respective nominal values in each case. The nominal values can be found in Table 6.2.

Table 6.2. Nominal and critical values of Areas A, G and F in different cases of system transmission lines. Cable case is referring to the 100% compensation level.

	Area	P_n [MW]	V_n [-]	PF, $\cos \theta$	P_{max} [MW]	V_{crit} [-]
Bus 3 Cable	A	322	1.010	0.99997 ind.	3382.32	0.806
Bus 3 OHL		322	1.025	0.99997 ind.	2661.84	0.812
Bus 12 Cable	G	7.5	0.986	0.08491 ind.	84.56	0.444
Bus 12 OHL		7.5	0.996	0.08491 ind.	76.28	0.477
Bus 28 Cable	F	206	1.018	0.99114 ind.	1703.11	0.725
Bus 28 OHL		206	1.043	0.99114 ind.	1433.37	0.775

According to the table, there is a significant difference between the nominal loading at Bus 12 in Area G and the other two areas. The nominal active power, P_n of Bus 12 in that area is merely 7.5 MW which is at least 25 times less than the nominal values of the other two areas. In contrast, Bus 3 in Area A has the highest nominal active load among the three buses at 322 MW. Another peculiarity of the load at Bus 12 is its PF of 0.08491. The low PF value indicates that it is almost equivalent to a purely reactive load element.

Generally, the V, P -characteristic of the three areas display a similar tendency between the investigated cases. It is important to note that the curves are consistent with the results observed from the 9-bus analysis in Section 5.3. This observation confirms that the OHL system has a lower load-ability, and that under-compensation of the cable-based system is beneficial in terms of load increment.

Bus 28 has a unique behaviour with a larger sensitivity in active power loading P with a change in compensation degree, which can be seen in Figure 6.3. On the other hand, Bus 12 and Bus 3 both display relatively small influence of the compensation degree over their load-ability. The difference in tendencies is due to the substantially larger reactive power generated by the cables connected to Bus 28 which can be found in Table F.4. As a result the absolute size of the SR at Bus 28 is much larger and therefore a variation of 25% in compensation degree at the bus leads to a larger excess, or deficit of reactive power supply, and has a greater influence on the V, P -characteristic.

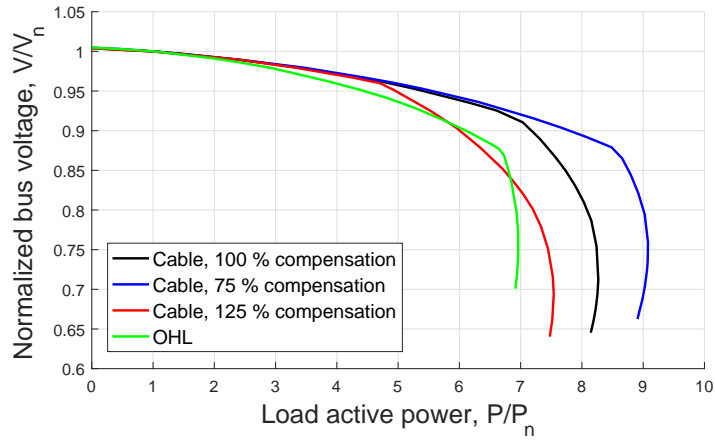


Figure 6.3. Normalized V, P -characteristic of Bus 28 in Area F in four different cases of system transmission lines and reactive power compensation degree.

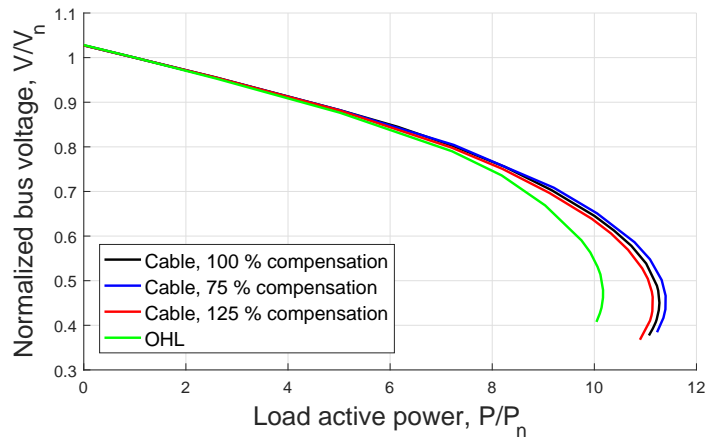


Figure 6.4. Normalized V, P -characteristic of Bus 12 in Area G in four different cases of system transmission lines and reactive power compensation degree.

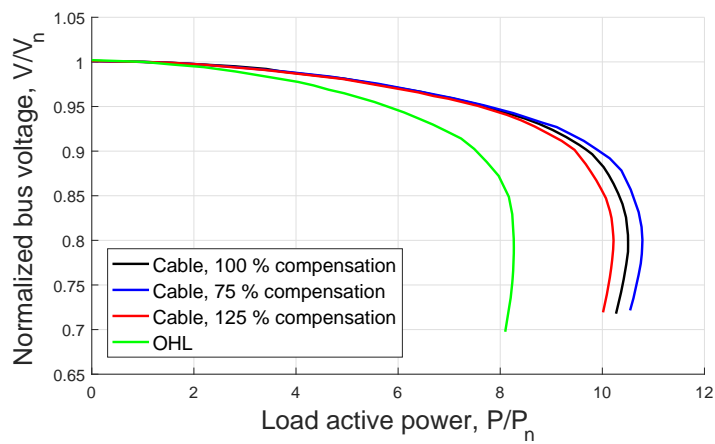


Figure 6.5. Normalized V, P -characteristic of Bus 3 in Area A in four different cases of system transmission lines and reactive power compensation degree.

Lastly, a comparison of the V, P -characteristic between areas is presented in Figure 6.6 for two different cases according to the type of transmission lines. The same tendency is observed for both the 100% compensated cable and the OHL case. Bus 12 in Area G is found to attain the highest relative load-ability when reaching its critical point V_{crit} . However the high load-ability value is due to its extremely low nominal value which is used as the scaling factor and can be verified by the absolute P_{max} value shown in Table 6.2. Even at P_{max} , it is still much lower than the nominal values of the other areas. Furthermore, the voltage starts to experience a significant drop even at low load increments. All these observations suggest that the high relative load-ability of Bus 12 is not completely indicative of its voltage stability margin. In contrast, Bus 3 of Area A has the largest absolute P_{max} value and its voltage appears to be the least sensitive to load increment as its curve is able to remain flat for the widest range of load levels. Therefore Area A is considered most robust to voltage instability. Meanwhile Area F has the lowest relative load-ability among all the areas and thus rendering it the worst performing area in the analysis.

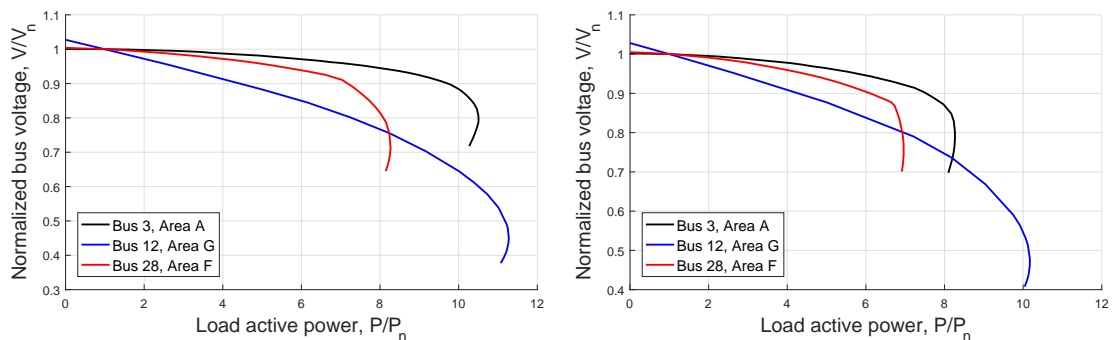


Figure 6.6. Normalized V, P -characteristic of Areas A, F and G in two different cases of system transmission lines. Left: 100% compensated cable. Right: OHL.

6.3 Q, V -characteristics of areas in the IEEE 39-bus system

Further investigation is carried out on Areas A, F and G by developing the Q, V -characteristic of these areas. The Q, V -relationship of an area shows how variation of reactive power Q affects voltage stability in that particular area. This characteristic complements well with the voltage sensitivity with respect to P variation established by the V, P -curves in Section 6.2, because voltage is both dependent on the change of Q as well as P . The Q, V -curves in three different loading cases of each area for both OHL and cable systems are presented in Figures 6.7, 6.8 and 6.9. The various P load values can be found by referring to Table 6.2. These curves are obtained by varying injection of reactive power Q_i at the bus.

It can be observed from Figure 6.7 that Bus 28 in Area F behaves differently as compared to the other areas. For each of the cases the curve undergoes two drastic bends at two different Q_i levels. These bends are due to the local generator SG9 in the area reaching its over- and under-excitation capability limits respectively at those levels, as highlighted in the figure. As a result, the power flow beyond these limits in the network changes drastically and the voltage at the connected terminal of the SG could not be maintained further, thus changing the voltage levels in the area abruptly.

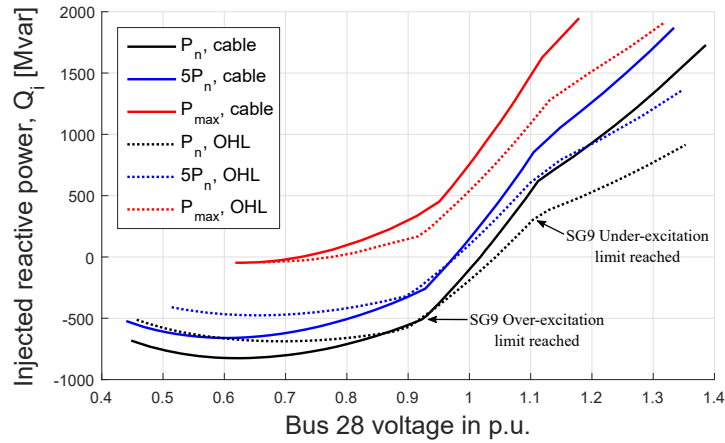


Figure 6.7. Q, V -characteristic of Area F in three different loading levels for both OHL and cable systems. Dotted line refers to the OHL case.

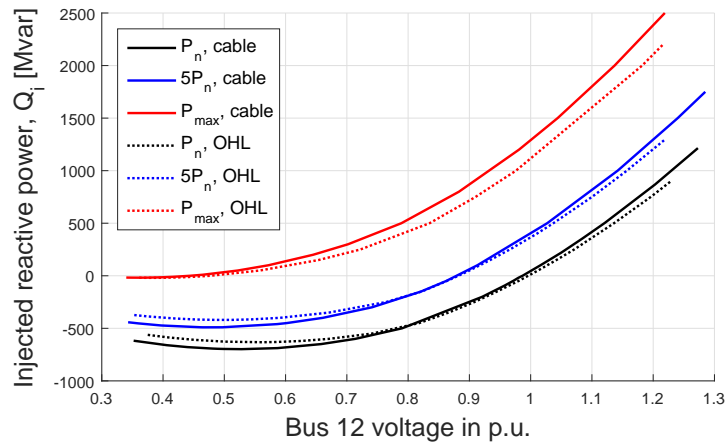


Figure 6.8. Q, V -characteristic of Area G in three different loading levels for both OHL and cable systems. Dotted line refers to the OHL case.

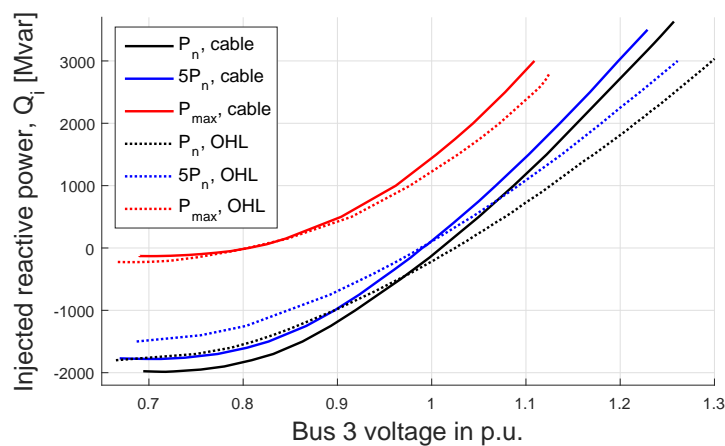


Figure 6.9. Q, V -characteristic of Area A in three different loading levels for both OHL and cable systems. Dotted line refers to the OHL case.

Figure 6.10 presents and compares the Q, V -characteristics of all the areas at two different loading levels, P_n and P_{max} . Area A is noticeably the best performing area as its curve has the highest gradient at all loading levels. The steeper the curve the less sensitive the voltage is to Q variation which is an indicator of good voltage stability performance. On the other hand, Areas F and G behave similarly at nominal load P_n and both are much weaker than Area A with a much flatter curve displayed. It indicates that the bus voltage is more sensitive to a change in Q_i which is undesirable. However when operating at their respective maximum loading state of P_{max} , the two areas behaves significantly different from one another. Due to the overwhelming difference in P_{max} between the two areas as presented in Table 6.2, the influence of the P variation could not be neglected therefore the curves at the P_{max} level are not directly comparable.

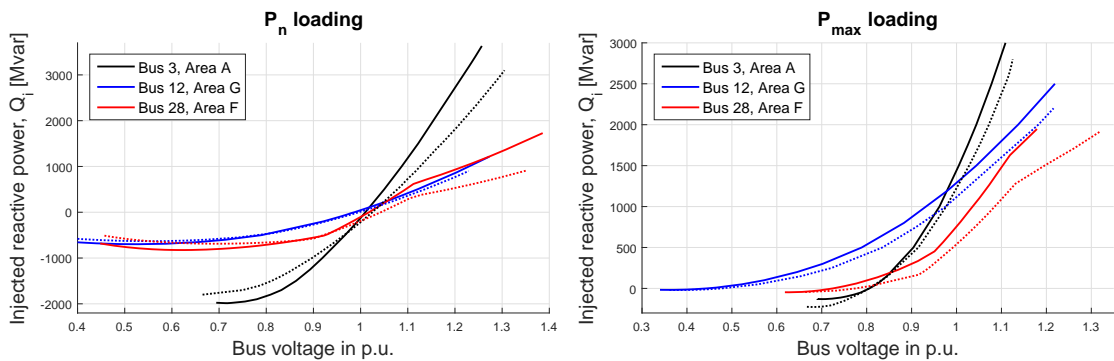


Figure 6.10. Comparison of the Q, V -characteristics of Areas A, F and G at two different load levels: P_n and P_{max} . Dotted line refers to the OHL case.

6.4 Large-disturbance case studies in the IEEE 39-bus system

In Section 6.2 and Section 6.3 V, P and Q, V -curves of selected system buses are discussed. The network nodes are Bus 28 (Area F), Bus 12 (Area G) and Bus 3 (Area A). It is concluded that the cable based system display larger V, P -load-ability and steeper Q, V -curves. The tendency is observed at all three buses.

In continuation of the voltage trajectory analysis presented in Chapter 5, a series of case studies are performed in the 39-bus system. The analysis is continued for Bus 28, Bus 12 and Bus 3.

Six different study cases are presented, all of which involves different disturbances, buses and ways of investigating SR-switching. Hence, the analysis may seem disorganized and random, while the perspective may be lost. Although, initially the goal was to verify the benefits of SR-switching in multiple cases, while observing any common tendencies between as many cases as possible. Retrospectively it is experienced that the analysis would have profited from a more structured and systematic approach with less cases.

Properties of SR-switching

The focus is on improving the system voltages following large disturbances by utilizing SR-switching. It is desired to investigate if SR-switching can be improved and generalized for large-disturbances with respect to three properties:

1. **Amount:** The necessary amount (i.e. quantity) of switched shunt reactor capacity Q_{sw} necessary for voltage recovery at a given bus or area.
2. **Location:** Procedural switching of SRs in the area of and in the proximity of the most weakened bus (i.e. lowest voltage bus).
3. **Timing:** Timing of the necessary shunt reactor switching Q_{sw} with respect to satisfying both under-voltage and over-voltage trajectory limits (i.e. limiting temporary voltage over-shoot).

Although SR-switching is to be improved for these properties, an actual optimization is not performed. Instead, the goal is to provide pointers towards guidelines and future work within SR-switching for improved voltage stability in large-disturbance events. Thus, the study cases are designed to imitate large-disturbances in the network, while investigating possible tendencies towards the mentioned properties.

The study cases involves a combination of one or more of the following disturbances:

- Pre-disturbance steady-state load increase to simulate a high-load condition.
- Dynamic load ramp in specific areas to simulate load-restoration.
- Switching of transmission lines to simulate events of over-loading.
- Switching of transmission lines in the event of permanent faults.
- Loss of generation due to permanent faults near generation units.

Each large-disturbance study case is designed to involve at least one of the discussed areas: Area A, Area F and Area G.

6.4.1 Large-disturbance Case 1: Dynamic load increase, loss of generation and transformer in Area G

The area of interest in this case is Area G with reference to Figure 6.1. The large-disturbance is applied in the form of sequential events as follow:

- Load ramp increase of 50 % in the area over a duration of 10 s starting from $t = 0.1$ s.
- Three-phase fault at the terminal bus of SG3, $t = 4$ s.
- Permanent disconnection of SG3 and transformer, $t = 4.06$ s.
- Permanent disconnection of Transformer 12-13, $t = 7.0$ s.

The outcome of the described disturbance can be seen by the bus voltages in the area in Figure 6.11. There are certain buses that are not shown in the figure as they display similar characteristics. The voltage trajectory of Bus 12 ends at a level below the under-voltage limit thus violating continuous operating conditions. Two SR-switching schemes are introduced to keep the voltages above the limit and to recover back to approximately 1.0 p.u. The two schemes are basically the same in terms of the amount and location of switching. However, one is an instantaneous switching where the entire quantity is switched out instantly, whereas the other alternative divides the switching into two separate instants. The SR-switching events are shown in Table 6.3.

The effects of both SR-switching schemes can be seen in Figure 6.11. It is observed that the resulting final operating states of both schemes are identical. This is due to the same amount being disconnected at the same location, and thus the resulting power flow in the system is equal. Nevertheless, there is a significant difference in the peak voltage at Bus 11 between them. The instantaneous switching produces an overshoot value of over 1.1 p.u. while it is limited below 1.07 p.u. with the progressive one. This observation indicates that it is more advantageous to distribute the SR-switching amount into a few instants which results in a higher tolerance margin from the over-voltage limits.

There still appears to be a substantial voltage difference between Bus 12 and Bus 11 even after SR switching. This is because the two terminals are connected via a transformer, and no reactive power is supplied by cables directly at Bus 12. Hence no SR-switching could be carried out to compensate the voltage drop across the transformer.

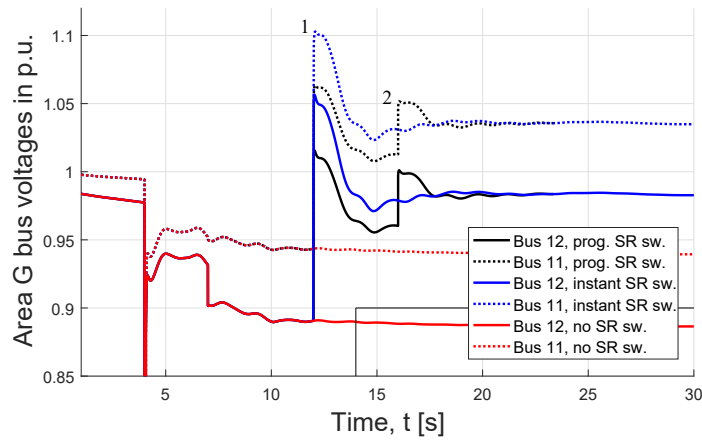


Figure 6.11. Voltage trajectories of Bus 12 and Bus 11 in Area G for large-disturbance Case 1. Number indicates the switching sequence according to Table 6.3.

6.4.2 Large-disturbance Case 2: Fault and loss of generation in Area G

This study case is centred around Area G with reference to Figure 6.1. The study case is carried out for 25 % increased steady-state loading, such that $P = 1.25P_n$ at all load buses in the system. The power factor is kept constant. The events of the disturbance are:

- Three-phase fault at the terminal bus of SG3, $t = 1$ s.
- Permanent disconnection of SG3 and transformer, $t = 1.060$ s.
- Permanent disconnection of Line 13-14 and shunt reactors due to overloading, $t = 3$ s.
- Permanent disconnection of transformer at SG2 due to overloading, $t = 4$ s.

SR-switching with the purpose of voltage recovery is initiated at $t = 6$ s. Figure 6.12 show a sensitivity of switching either 25 %, 50 %, 75% or 100% of the available Q_{SR} amount in Area G, when accounting for the SRs taken out of service due to line disconnection. As expected, the voltage recovers to an increasing value as more reactive power is switched Q_{sw} . However, in this case, 100 % SR-switching in Area G is insufficient for full voltage recovery. Due to the nature of the disturbance, the neighbouring buses in Area C are affected by the event and requires compensation as well as Area G.

Table 6.3. Sequence of events for the progressive SR-switching scheme. The time instant of each step is indicated in Figure 6.11. Total bus Q_{SR} indicates the total SR amount available for switching.

SR no.	Bus	Total bus Q_{SR} [Mvar]	Q_{sw} [Mvar] switching sequence	
			1	2
SR11-10	11	155.4	53.5	-
SR11-6	11	155.4	101.9	-
SR10-11	10	107.0	53.5	-
SR10-13	10	107.0	53.5	-
SR13-10	13	179.8	53.5	-
SR13-14	13	179.8	126.3	-
SR6-5	6	216.6	31.8	-
SR6-11	6	216.6	101.9	-
SR14-15	14	496.1	-	201.3
Total Q_{sw} switched			777.2 Mvar	

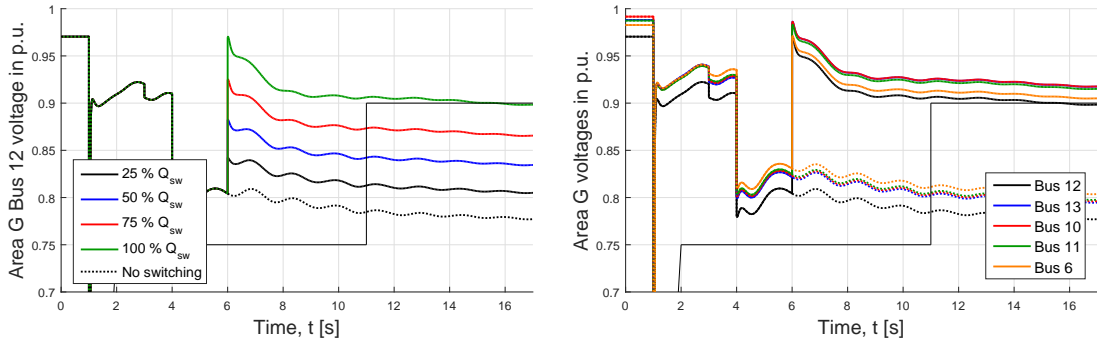


Figure 6.12. Left: Bus 12 (representing Area G) voltage sensitivity to increased switched amount Q_{sw} . Right: Voltage of buses following 100 % Q_{sw} in Area G.

Figure 6.13 show how the voltage trajectories in Area G are improved by switching 25 % or 50 % of the SRs at buses 8, 7, 5 and 4 in the neighbouring area. By switching 25 %, the buses in Area G recovers to a voltage range between 0.95 to 0.97 p.u. By switching 50 %, the voltages recover to a range of 1.01 to 1.03 p.u.

However, a problem of switching the shunt reactors in the neighbouring area by 50 % in one step, is a voltage over-shoot to just above 1.1 p.u. at $t = 8$ s. This is observed in Figure 6.13(Right).

The voltage over-shoot can be avoided by increasing the number of steps in which the SRs in the neighbouring area are switched. In this way the voltage recovery becomes more progressive and smooth. This is shown in Figure 6.14, where the 50 % Q_{sw} at buses 8, 7, 5 and 4 are divided into two steps of 25 % each. Now, the voltages recover to the same level (1.01 to 1.03 p.u.), but the voltage over-shoot is only just above 1.05 p.u. Further division of the SR-switching into progressive steps would eliminate the over-shoot.

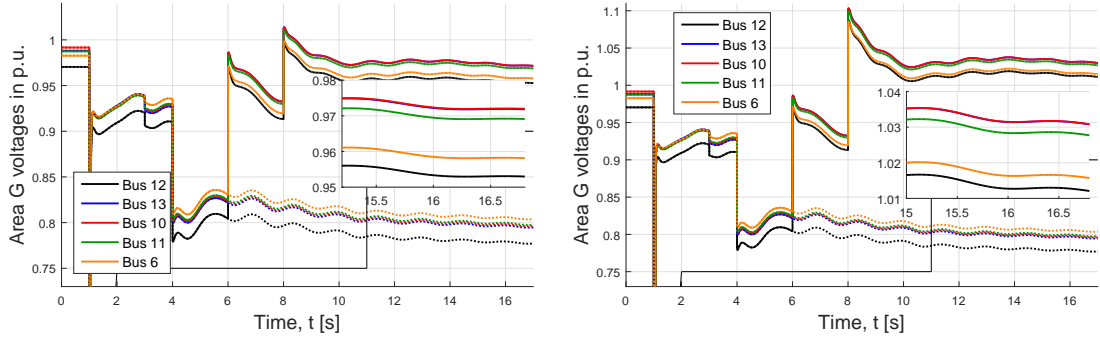


Figure 6.13. Left: Area G voltages following 100 % Q_{sw} in the area and 25 % at Bus 8, 7, 5 and 4 in the neighbouring area. Right: Equivalent case, but with 50 % Q_{sw} in the neighbouring area. The zoomed area show the voltage magnitudes at the end of the simulation.

Figure 6.14(Right) show the voltages at the buses in the neighbouring area. It is important that the voltage at all buses in the network is within a satisfactory range when SRs in a neighbouring area are switched to aid the disturbed area. Thus, focusing on the most weakened area alone is insufficient.

Table 6.4 show the exact SR-switching sequence of Area G and the neighbouring area leading to the voltage recovery shown in Figure 6.14. The total switched amount Q_{sw} is 1125 Mvar. Noting that the lines in Area G are relatively short with lower Q_{SR} in comparison to other parts of the 39-bus system. Hence, in this study case it is necessary to switch 100 % of the capacity in the disturbed area. This may not be necessary in areas with large Q_{SR} capacity due to long cables with high capacitance.

The study case show that voltage can be efficiently recovered by initial switching of SRs near the disturbance, followed by progressive switching of shunt reactors at farther substations. Although voltage instability typically is characterized as a local phenomenon, it impacts the power flow of the system as a whole. Voltage regulation by injection of reactive current in point A has an improving effect of the voltage in point B, and vice versa.

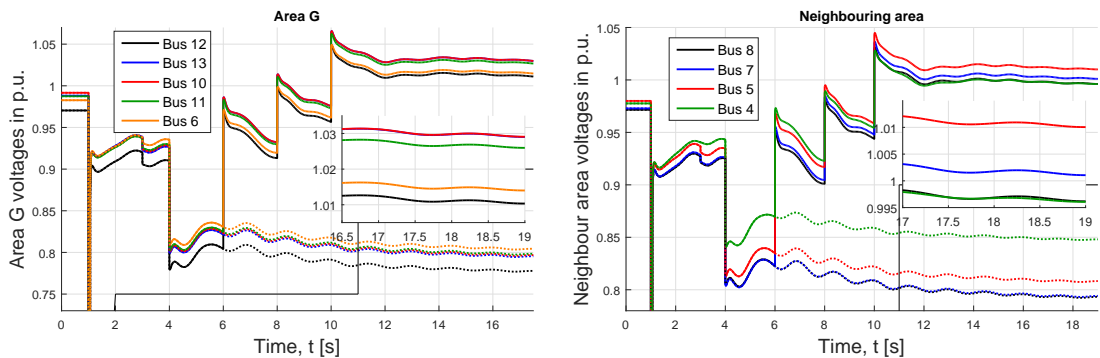


Figure 6.14. Left: Area G improved voltage trajectory by dividing the Q_{sw} into two steps of 25 % each in the neighbouring area. Right: Voltage trajectories in the neighbouring area (Bus 8, 7, 5 and 4). The zoomed area show the voltage magnitudes at the end of the simulation.

Table 6.4. SR switching sequence of the voltage recovery displayed in Figure 6.14.

Area G			Switching sequence		
SR no.	Bus	Q_{SR} [Mvar]	1	2	3
SR13-10	13	53.5	100 %	-	-
SR10-11	10	53.5	100 %	-	-
SR10-13	10	53.5	100 %	-	-
SR11-6	11	101.9	100 %	-	-
SR11-10	11	53.5	100 %	-	-
SR6-7	6	82.9	100 %	-	-
SR6-5	6	31.8	100 %	-	-
SR6-11	6	101.9	100 %	-	-
Neighbouring area					
SR8-5	8	108.2	-	25 %	25 %
SR8-7	8	57.2	-	25 %	25 %
SR8-9	8	278.9	-	25 %	25 %
SR7-8	7	57.2	-	25 %	25 %
SR7-6	7	82.9	-	25 %	25 %
SR5-8	5	108.2	-	25 %	25 %
SR5-4	5	98.4	-	25 %	25 %
SR5-6	5	31.8	-	25 %	25 %
SR4-3	4	162.4	-	25 %	25 %
SR4-14	4	101.4	-	25 %	25 %
SR4-5	4	98.4	-	25 %	25 %
Total Q_{sw} switched			1125 Mvar		

6.4.3 Large-disturbance Case 3: Dynamic load increase and disconnection of lines in Area F

This case study focuses on Area F with reference to Figure 6.1, and a large-disturbance is simulated, which would have a significant impact on the buses in the area. The description of the disturbance is given:

- Load ramp increase of 50 % in the area over a duration of 10 s starting from $t = 0.1$ s.
- Permanent disconnection of Line 28-29 and shunt reactors due to overloading, $t = 5$ s.
- Permanent disconnection of Line 25-26 and shunt reactors due to overloading, $t = 5$ s.
- Permanent disconnection of Line 16-17 and shunt reactors due to overloading, $t = 7$ s.

There are three switching combinations conducted for this case study and are listed in Table 6.5. The motivation is to showcase the effects of switching-location on the overall voltage trajectories of the buses in the area. All the switching cases are done at the same instant and for a similar total amount of Q_{sw} .

The first scheme involves SR-switching at only one location which is selected to be Bus 28 because it records the lowest voltage in the area following the disturbance. For the second scheme, the total amount is distributed almost equally among Bus 28 and Bus 26. Lastly, Bus 27 is included as one of the locations in the third case. The composition of all the different switching cases can also be found in the table.

Table 6.5. Three different switching cases at various locations for large-disturbance Case 3.

Case name	SR no.	Bus	Total bus		Total Q_{sw} switched [Mvar]
			Q_{SR} [Mvar]	Q_{sw} [Mvar]	
1 SR switching	SR28-26	28	572.2	314.71	314.71
2 SR switching	SR28-26	28	572.2	171.66	321.00
	SR26-27	26	1502.5	149.34	
3 SR switching	SR28-26	28	572.2	114.44	316.50
	SR26-27	26	1502.5	105.42	
	SR27-26	27	411.5	96.64	

Figure 6.15 presents and compares the voltage trajectories of the buses in Area F with the different SR-switching schemes following the described large-disturbance. All three schemes help to boost the voltage levels with varying degree of impact. The largest voltage deviation between the two buses is observed for the first scheme whereas it becomes smaller with increasing switching locations. Furthermore, the temporary overshoot value recorded is also highest when all the Q_{sw} amount is disconnected at a single bus instead of distributing between more locations in the area. These observations are consistent with the 9-bus analysis as presented in Section 5.6.2 for a similar situation. In order to reduce voltage deviation between buses, it is beneficial to perform switching across several buses in the area. This procedure helps to distribute the flow of reactive power generated by the cables and not concentrated from a single terminal.

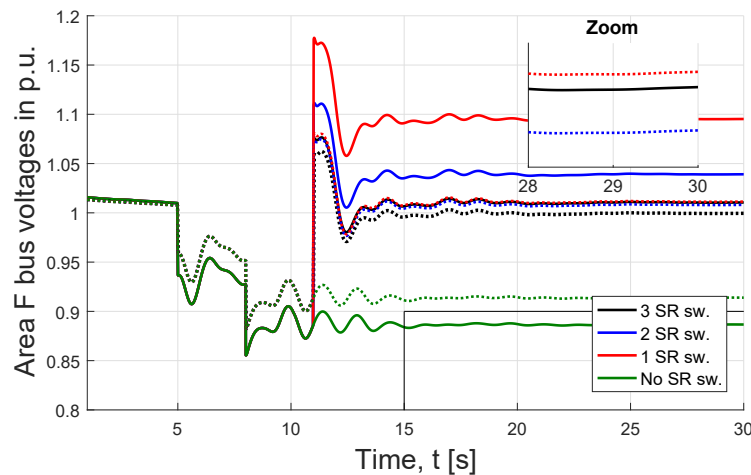


Figure 6.15. Voltage trajectories of Bus 28 and Bus 26 in Area F for large-disturbance Case 2. Solid line refers to the trajectory of Bus 28 whereas dotted line represents Bus 26.

6.4.4 Large-disturbance Case 4: Transmission line over-loading in Area A

This study case is centred around Area A with reference to Figure 6.1. The study case is carried out for 25 % increased steady-state loading, such that $P = 1.25P_n$ at all load buses in the system. The power factor is kept constant. The events of the disturbance are:

- Disconnection of Line 1-39, $t = 1$ s.
- Disconnection of Line 4-14, $t = 3$ s.
- Disconnection of Line 2-3, $t = 4$ s.
- Disconnection of Line 17-18, $t = 6$ s.

SR-switching with the purpose of voltage recovery is initiated at $t = 8$ s. The consequence of the described disturbance is that the voltage at Bus 3, 4 and 18 is lowered to approximately 0.8 p.u. The topological change of the system weakens these buses, by reducing their connection to the remaining system to just one transmission line. In the post-disturbed condition these buses are connected radially, where Bus 18 is at the extreme end, Bus 3 is in the middle and Bus 4 connects to the network.

Thus, as it is shown in Figure 6.17, Bus 18 has the lowest post-disturbed voltage without SR-switching, although the difference between the buses is within 0.02 p.u.

Now the question is how this radial string configuration should be compensated by SR-switching with respect to location. Figure 6.16 show the difference between the three buses (3, 4 and 18), as they in turn are switched by an equal amount $Q_{sw} = 300$ Mvar.

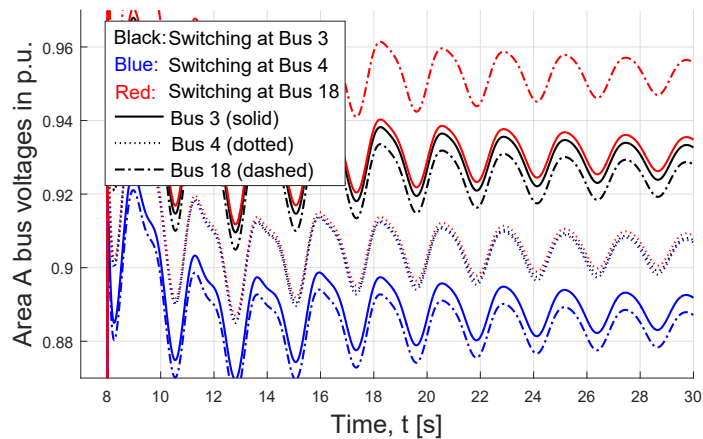


Figure 6.16. Comparison of voltage trajectories for three cases of 300 Mvar SR-switching. Black lines: Switching at Bus 3 only, Blue lines: Switching at Bus 4 only and Red lines: Switching at Bus 18 only. The voltages at all three buses are shown for each case, marked by solid, dotted and dashed lines.

Naturally in each case, the bus at which the switching is done recovers to the highest voltage among the three buses. Being the SRs locally switched out, the reactive power from the cables will flow away from the bus, rather than towards it (i.e. towards the SRs).

However, the voltages at all three buses recover to their maximum value when the SR-switching is done at the extreme of the radial configuration (i.e. Bus 18).

When the SR is switched out at Bus 18, the reactive power from the cable will support the weakest point directly and flow towards the stronger buses.

The example show that when switching a fixed amount of Q_{SR} it is beneficial to do it at the location of lowest voltage as it will improve the area voltage the most. However this may not be true for every disturbance. If the topology of the post-faulted network is meshed the optimal location is dependent on the reactive power flow elsewhere in the system.

It is not strictly necessary to switch the shunt reactors at the weakest point to obtain voltage recovery at every node. Figure 6.17 show how the voltage can be recovered by switching the middle bus (i.e. Bus 3) and Bus 4. Excluding the weaker Bus 18. Table 6.6 show the three-step switching sequence used to obtain the improved voltage trajectory. Switching out the full SR capacity at the middle of the string allows the cables to supply reactive power to the middle as well as both ends of the string.

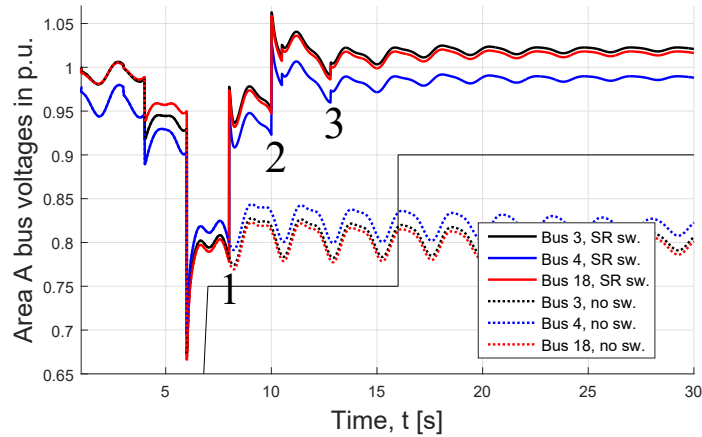


Figure 6.17. Improved Area A voltage trajectory by the switching sequence shown in Table 6.6.

Table 6.6. Switching sequence used for the improved voltage trajectory displayed in Figure 6.17. Total bus Q_{SR} is the total available shunt reactor capacity at the given bus, deducting the disconnected SRs due to line outage. Q_{sw} is the switched amount for each SR.

SR no.	Bus	Total bus Q_{SR} [Mvar]	Q_{sw} [Mvar] switching sequence		
			1	2	3
SR3-4	3	507.8	162.4	-	-
SR3-2	3	507.8	188.6	-	-
SR3-18	3	507.8	156.8	-	-
SR4-3	4	362.2	-	138.4	24.36
SR4-5	4	362.2	-	73.8	24.6
Total Q_{sw} switched			768.6 Mvar		

6.4.5 Large-disturbance Case 5: Dynamic load increase and disconnection of lines in Area A.

This study case focuses on Area A with reference to Figure 6.1. The events of the disturbance are:

- Load ramp increase of 50 % in the area over a duration of 10s starting from $t = 0.1$ s.
- Permanent disconnection of Line 2-3 and shunt reactors, $t = 5$ s.
- Permanent disconnection of Line 17-18 and shunt reactors, $t = 5$ s.

An attempt is made to plan an approach to calculate the amount of Q_{sw} at certain buses to minimize the voltage deviation between them. The post-disturbance Area A topology is presented in Figure 6.18. Buses 18, 3 and 4 are now connected similar to a radial line network. Under this condition it is possible to approximate the necessary Q_{sw} at Buses 3 and 18 to obtain a very small deviation across the whole area.

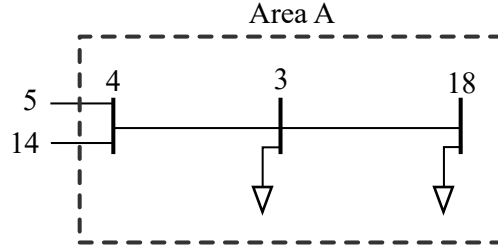


Figure 6.18. Simplified post-disturbance topology of Area A

Referring to the voltage drop equation derived for two terminals connected through a transmission line in (1.11), a simplified version is repeated here for convenience assuming that the imaginary part is negligible and excluded. P_R and Q_R represent the receiving end active and reactive power while X and R represents the line series resistance and impedance.

$$\Delta V = \left(\frac{P_R}{V_R} \right) R + \left(\frac{Q_R}{V_R} \right) X \quad (6.1)$$

Based on the equation, there is a component that is caused by active power and the other by reactive power. Assuming that $\Delta V = 0$, equation (6.2) is obtained which gives a relationship between active and reactive power at the receiving end necessary to have zero voltage deviation. The reactive power would have to flow in the opposite direction of the active power to counter balance each other. The knowledge of the $\frac{R}{X}$ ratio of the corresponding transmission line is also needed for this approach.

$$Q_R = - \left(\frac{R}{X} \right) P_R \quad (6.2)$$

Applying this approach to the post-disturbance network of Area A, as shown in Figure 6.18, the amount of Q_{sw} at Buses 3 and 18 can be approximated using (6.2), as the total load demands at the buses are known. The new power flow of the network with this approach is illustrated in Figure 6.19. It should be noted that the voltage dependency of the power demand is unaccounted for. Q_{bal} is the new reactive power flow in counter direction to balance the drop due to active power. The $\frac{R}{X}$ ratios of Line 3-18 and Line 3-4 are 0.0708 and 0.0524 respectively.

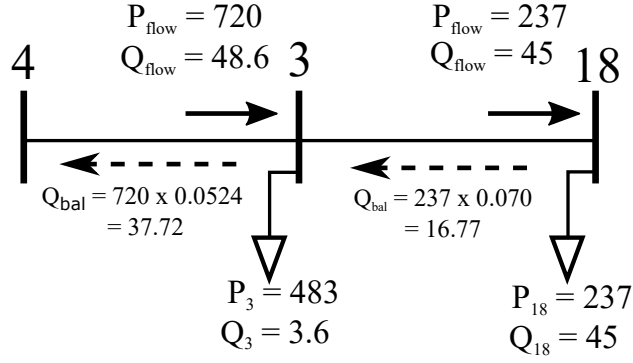


Figure 6.19. Illustration of the planned power flow of Area A

Beginning from Bus 18, the total amount of switching necessary $Q_{SR,18}$ is equal to the addition of Q_{bal} and Q_{flow} , which is computed to be 61.77 Mvar. When the amount at Bus 18 is fixed, it is possible to proceed with the calculation at Bus 3. $Q_{SR,3}$ is computed to be 69.55 Mvar taking into account the additional reactive power flow from Bus 18 after SR-switching. However due to the discrete nature of the tap switching, a similar amount of Q_{sw} at both buses is used instead. Q_{sw} at Bus 18 and Bus 3 is 62.72 and 70.56 Mvar respectively.

$$Q_{SR,18} = 45 + 16.77 = 61.77 \text{ Mvar} \quad (6.3)$$

$$Q_{SR,3} = 48.6 + 37.72 - 16.77 = 69.55 \text{ Mvar} \quad (6.4)$$

Continued SR-switching would have to come from Bus 4 and other nearby buses in order to increase the voltage further. Two switching cases are presented in Table 6.7. For the first switching case, all the SRs available at Bus 4 are disconnected, while additional SR-switching at Bus 5 is included as well.

Figure 6.20 presents the comparison of the voltage trajectories of the buses in Area A. Firstly it can be observed that the final voltage levels achieved in the second switching scheme is higher around the range of 0.99 p.u. while the voltages could only recover up to 0.96 p.u. with the first switching scheme. This is expected as the positive effect is caused by additional Q_{sw} carried out at Bus 5. Moreover, it can be noticed that the bus voltages are moving very close to each other in both switching cases. This observation supports that the $\frac{R}{X}$ ratio planning approach, of the SR-switching amount Q_{sw} at Buses 3 and 18, produce a more uniform voltage in the area. However, this method is only applicable for a radial network.

Table 6.7. Two different switching cases in Area A for large Disturbance Case 5. The second scheme includes all the events in the first and only the extra events are shown.

Balance SR switching 1			Switching sequence	
SR no.	Bus	Q_{SR} [Mvar]	1	2
SR4-5	4	98.4	100 %	-
SR4-14	4	101.4	100 %	-
SR4-3	4	162.4	100 %	-
SR18-3	18	156.8	-	40 %
SR3-18	3	156.8	-	45 %
Total Q_{SW}			495.48 Mvar	
Balance SR switching 2				
SR5-4	5	98.4	100 %	-
SR5-8	5	108.2	100 %	-
Total Q_{SW}			702.08 Mvar	

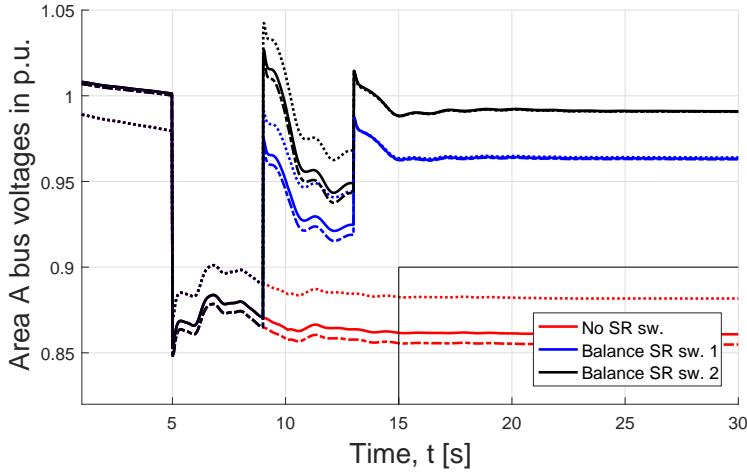


Figure 6.20. Voltage trajectories of the buses in Area A for large-disturbance Case 5. Solid line: Bus 3. Dotted-line: Bus 4. Dashed-line: Bus 18.

6.4.6 Large-disturbance Case 6: Loss of generation and transmission line in Area F

The disturbances in this study case are imposed on Area F with reference to Figure 6.1. The study case is carried out for 25 % increased steady-state loading, such that $P = 1.25P_n$ at all load buses in the system. The power factor is kept constant. The events of the disturbance are:

- Three-phase fault at the terminal bus of SG9, $t = 1$ s.
- Permanent disconnection of SG9 and transformer, $t = 1.060$ s.
- Permanent disconnection of Line 26-29 and shunt reactors due to overloading, $t = 2$ s.
- Permanent disconnection of Line 25-26 and shunt reactors due to overloading, $t = 3$ s.

The described disturbance lowers the voltages in Area F to a level between 0.7 p.u. and 0.8 p.u. However, the voltage is not only affected locally. Due to the loss of generation and two transmission lines, the power flow of the network has been significantly changed. As power is no longer supplied locally in Area F, a larger amount of power must be supplied from farther away. As a consequence the voltage in the opposite end of the network (Bus 8, 7, 6, 5 and 4) is lowered to just above 0.9 p.u.

Post-disturbance voltages at Bus 28 in Area F, Bus 27 neighbouring Area F, and distant buses 4 and 8, are shown in Figure 6.21.

Due to the nature of the disturbance it is insufficient to perform SR-switching in Area F alone. Thus, the sequential SR-switching shown in Table 6.8 is performed. The result of the SR-switching is likewise shown in Figure 6.21. Noting that improving the voltage at distant buses by SR-switching has an increasing effect on the voltage in Area F as well. Hence, the sequential method progressively switches Q_{sw} starting from Area F towards distant buses. The amount of Q_{sw} is steadily reduced as the voltages at all buses approaches 1 p.u.

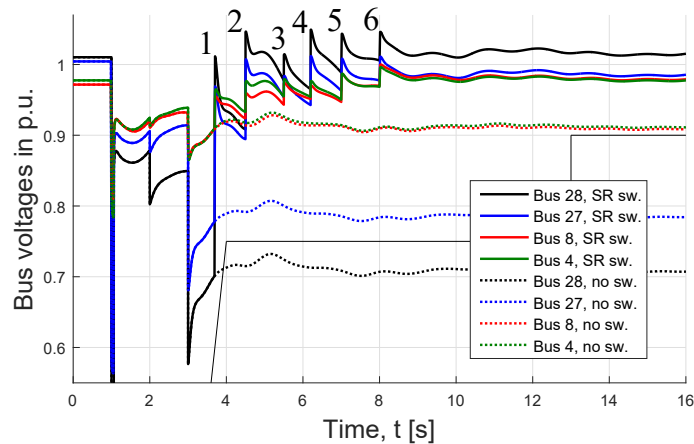


Figure 6.21. Comparison of voltage trajectories across the network with sequential SR-switching and without SR-switching.

Table 6.8. Shunt reactor switching sequence in six steps involving shunt reactors in multiple network areas.

SR no.	Bus	Total bus Q_{SR} [Mvar]	Q_{sw} [Mvar] switching sequence					
			1	2	3	4	5	6
SR29-28	29	182.6	182.6	-	-	-	-	-
SR28-26	28	758.8	85.83	-	-	-	-	-
SR26-27	26	1878.7	-	70.28	-	26.36	-	-
SR27-26	27	411.5	-	70.28	-	70.28	-	-
SR4-3	4	362.2	-	-	64.96	-	56.84	40.6
SR7-6	7	140.1	-	-	33.16	-	29.02	20.73
SR8-9	8	444.30	-	-	111.56	-	97.67	69.73
Total Q_{sw} switched			1029.9 Mvar					

If the sequence is performed faster, the voltage at all buses will recover faster. However, a consequence of switching a high amount of SRs within a short time span is the risk of over-voltages. Figure 6.22 show the result of switching the total $Q_{sw} = 1029.9$ Mvar of the sequence instantly in comparison to the progressive method. The voltages settle at an equal equilibrium value, but the electromechanical transient is different. In the case of instant switching, the high amount of reactive power supplied by the cables causes the voltage to over-shoot before synchronous generators has time to adjust the excitation level. Thus, ideally the SR-switching is performed in several small steps with a regulated amount in each step.

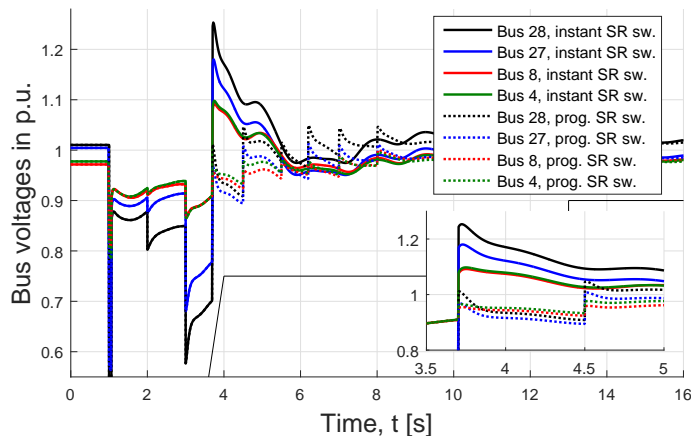


Figure 6.22. Comparison of progressive sequential switching and instantaneous switching of an equal amount: 1029.9 Mvar.

6.4.7 Combining shunt reactor switching with STATCOM

In continuation of the 9-bus analysis presented in Section 5.6.3, the combination of SR-switching with dynamic voltage regulation is investigated in the 39-bus system. The focus is on how dynamic switching of shunt reactors may replace the need for FACTS devices, such as STATCOMs, by allowing cables to inject the necessary reactive current in emergency situations. Hence, the question is if FACTS devices are necessary for large-disturbance when shunt reactors are assumed controllable.

Based on the steady state V, P and Q, V analysis, and the voltage trajectory case studies, it is decided to analyse the impact of placing two STATCOMs in the 39-bus system. Both STATCOMs have a 50 Mvar rating. Two different combinations of STATCOM locations are chosen:

- **Location 1, center of weak areas:** The two STATCOMs are placed at Bus 12 and Bus 28. Bus 12 is the weakest bus in Area G, while Bus 28 is the weakest bus in Area F.
- **Location 2, area borders:** The two STATCOMs are placed at the borders of the weak areas of the network. Here Bus 5 and Bus 27 are chosen. Bus 5 is a connection point of Area G and Area C (which proved to be a voltage sensitive area in the case studies). Bus 27 is a connection point of Area F to the remaining network.

The six study cases are repeated with the STATCOMs placed at the mentioned locations with and without SR-switching. The focus is on observing if the combination of SR-switching and STATCOM has an improving effect on the voltage trajectory in certain cases, and if the combination of both is redundant in other cases.

Disturbance in Area F, observing Bus 28

Figure 6.23 compares SR-switching and STATCOM for the disturbances in Area F, where the voltage at Bus 28 is observed. For disturbance Case 3 (left), it is shown that the presence of the STATCOM directly at Bus 28 is unnecessary when SR-switching is performed. The STATCOM could be relocated with benefit, or the capacity of the STATCOM could be reduced.

If the STATCOM is placed at the area border (i.e. Bus 5), the combination of STATCOM and SR-switching has a small improving effect on the voltage trajectory. However, for disturbance Case 3 it can be concluded that either SR-switching or the presence of a 100 Mvar STATCOM is sufficient.

An important observation is the voltage spike occurring in the case of combining STATCOM and SR-switching. Due to the switching of SRs, the combination of reactive power supplied by the cables and the STATCOM at that instant causes the voltage to spike. It is possible that this observation is a consequence of the simplified STATCOM model used in RMS-simulation. It should be investigated in future work if this result is due to incorrect modelling, or if its an indication of the need to coordinate SR-switching and the control of the STATCOM.

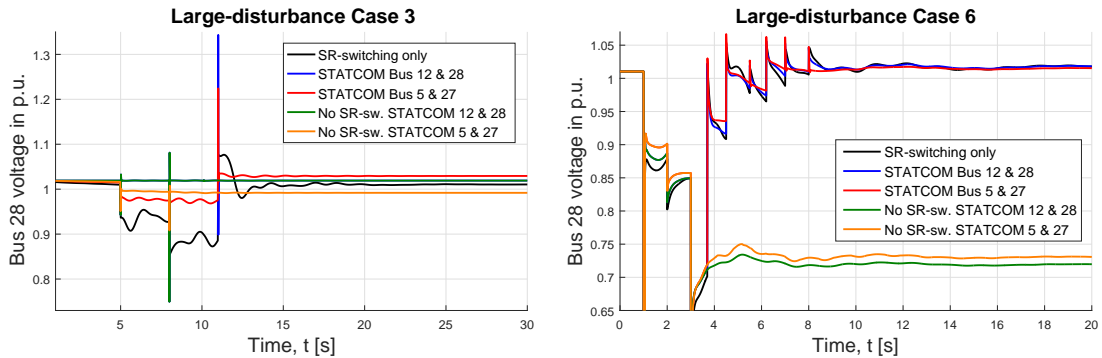


Figure 6.23. Comparison of voltage trajectories at Bus 28 with STATCOMs in the network, with and without SR-switching. Left: Large-disturbance Case 3. Right: Large-disturbance Case 6.

Figure 6.23(right) show a more severe disturbance in Area F. For this disturbance the 100 Mvar STATCOM is unable to keep the voltage without SR-switching. This case show that the STATCOM can be placed at the area border (i.e. Bus 27), and that the last two steps of the SR-switching sequence are unnecessary in the presence of the STATCOM.

The main result of this comparison is that if the amount of SR-switching is unrestricted, the STATCOMs may be unnecessary for large-disturbances. However, the STATCOM allows for less steps in the SR-switching sequence by smoothing the voltage trajectory.

Locating STATCOMs directly in weak areas is unnecessary in the tested cases, as shunt reactors can be switched to let the cables supply the critical reactive power locally.

Similar analysis of SR-switching and STATCOMs performed for Area G and Area A is located in Appendix H

6.5 Summary of voltage stability analysis in the IEEE 39-bus system

This section presents an overview of the large-disturbance voltage stability study carried out in the IEEE 39-bus system. Since the investigation is done in a similar manner to the 9-bus study repetitive conclusions are not elaborated. Instead, the following provides the additional conclusions of the 39-bus voltage stability analysis.

Conclusions on the voltage stability comparison of OHL systems and equivalent cable systems:

- V, P -characteristics show that the tendency observed in the 9-bus system is confirmed in the 39-bus system.
- Q, V - characteristics show that the cable-based system has higher slope (i.e. $\partial Q/\partial V$) in the voltage range of 1.0 p.u. at nominal loading levels. This indicates that its voltage is less sensitive to the variation of reactive power at the bus. The Q, V -characteristics of the investigated areas are also consistent with the area characterization according to short-circuit calculations.

Conclusions on the guidelines for SR-switching. SR-switching is shown to help voltage recovery. Considerations should be taken with focus on the following three elements:

1. **Timing:** Instants at which SR-switching is initiated
 - Progressive SR-switching is able to limit the voltage over-shoot and reduce the risk of over-voltages. A smoother voltage characteristic could be achieved by this method.
 - Smooth voltage trajectories may be achieved by switching shunt reactors in multiple steps.
2. **Location:** Location of switching with respect to disturbed area
 - SR-switching at any bus in an area improve the voltage levels of all buses in the area. Switching at the bus displaying the lowest voltage is a good strategy, but may not be optimal for every case. If the system is highly meshed, injecting reactive current in other nodes may be more beneficial for the overall power flow.
 - Distributing the same amount of SR-switching among multiple buses would reduce voltage deviations between buses and thus produce a much more uniform voltage characteristic in the area.

3. **Amount:** The amount necessary to achieve voltage improvement in an area.

- Larger amount of SR-switching would result in a higher post-disturbance voltage.
- Dependent on the availability of the area, areas with low capacitance due to short lines may have insufficient amount of SR capacity for voltage recovery. In this case SR-switching may be performed in neighbouring areas.
- Planning of amount at certain buses to minimize voltage deviations between buses in the area could be done by utilizing R/X ratio of the cables. This approach is more easily applicable in radial type of network.
- It is likely that $\partial Q/\partial V$ -sensitivities can be utilized to design SR-switching. Due to time constraints of the project presented in this thesis, a study of $\Delta Q/\Delta V$ -based planning of SR-switching is not realised. This should be investigated in future work. A brief discussion of linearised $\Delta Q/\Delta V$ slopes and their possible use for SR-switching is located in Appendix I.

Conclusions on combining STATCOM with SR-switching:

- SR-switching may remove the necessity for FACTS such as STATCOM when assuming similar controllability.
- If located in the disturbed area, the MVA rating of the STATCOMs may be reduced if combined with SR-switching.
- STATCOMs can be used to fine tune the voltage trajectory by smoothing the voltage. Therefore the amount of SR-switching steps in a sequence may be reduced. To provide this ability, STATCOMs do not need to be located in the disturbed area but instead can be located at the borders between areas.

Additional conclusions: Short-circuit test is not an explicit indicator of network strength for voltage stability

- Area C recorded large voltage drops during RMS simulations conducted in study cases contrary to the short-circuit results which indicates that it is a stronger area. The observed contradiction is assumed due to its close proximity to SG1 that mainly contributes short-circuit power to the area. On the other hand, SG1 is modelled with no AVR included and therefore the dynamic regulation in that area is greatly reduced in RMS simulation.

Discussion of results

7

In this chapter the main results presented in this thesis are discussed. The focus is on the limitations of the methodology, and comparison with published research on the topic: stability of cable based HVAC power systems.

7.1 Comparison of results with published research

The authors of [19] compare CCT values of an OHL based SMIB system and a mixed cable-OHL SMIB system. It is concluded that if the cable transmission line is compensated, the CCT difference of the OHL and the mixed line system is insignificant. Furthermore, it is concluded that if the cable stretch of the mixed line is short (approximately 20 km), the CCT values are equal even without compensation by SRs. The deviation between the OHL system and the mixed-line system increases as the length of the cable stretch is increased, unless corresponding compensation is introduced.

In this thesis CCT values of a SMIB system are compared for the OHL case and equivalent cable case with and without SRs and SR-switching. Here it is found, that if the cable system is uncompensated the CCT values are significantly lower. However, it is important to note that the system is a pure cable system, as opposed to the mixed line system, and that the length of the lines is 100 km. In [19] the uncompensated generated reactive power of the short cable stretch acts as compensation for the inductive OHLs in the system. Hence, the results presented in this thesis confirms that increasing the length of uncompensated cables lowers the CCT of the system, while introducing compensation in the form of SRs equalizes the performance between OHL and cable systems. As presented in Chapter 4, the difference in CCT between the OHL base system and equivalent cable system is approximately 6 % in the case of 100 % compensation. For large power systems, such as the 39-bus system, it is found that the power flow cannot be solved unless cables are compensated.

The authors of [19] find that over-compensation of cable stretches longer than 20 km has an improving effect on CCT, however no explanation as to why is given. A similar tendency is observed in the transient 9-bus and 39-bus analysis in this thesis. The reason why is presumably due to steeper P, δ -curves when SGs are operating in over-excitation mode, resulting in reduced power-swing oscillations following large-disturbances. However, this assumption should be confirmed in future work.

It is very important to note that the steady-state voltage stability analysis in the form of V, P -curves yields the opposite result. In Chapter 5 and Chapter 6 it is shown that under-compensating the cable system yields a higher load-ability with respect to voltage stability margins. The author of [2] shows that the load-ability is higher for capacitive networks, which confirms the tendency observed in V, P -curves for under-compensated cables.

This contradicts the dynamic CCT analysis, which shows that over-compensation is beneficial. Thus, when analysing the influence of changing compensation degree, one should be aware of this when choosing stability index and methodology.

In reality the effect of increasing or decreasing the compensation degree should be a relationship between improving the operation state of synchronous machines with respect to P, δ and excitation level, and the balance of reactive power and voltage control in the network. Naturally, the compensation degree cannot be increased indefinitely while observing an improved CCT. At a certain limit the arising problem of voltage instability will dominate the system performance, and the CCT must necessarily drop in case of further increment of the compensation degree. In other words, it can not be concluded whether over- or under-compensation is better, as it is dependent on the parameters on which the analysis is based and the operating condition of the system.

The authors of [19] do not discuss switching of SRs for improving CCT. In this thesis it is found that in a SMIB system, switching of SRs in an electromechanical transient following a fault may improve CCT. Furthermore, it is found that SRs of disconnected lines should be disconnected concurrently for improved CCT.

In [21] the authors find that transmission cables should be sufficiently compensated to avoid under-excitation of synchronous machines and to avoid over-voltages. Furthermore it is found that SRs should be switched together with lines to avoid voltage steps exceeding $\pm 3\%$, while it is argued that it is beneficial to reconnect SRs before reconnecting a cable line. In this thesis the order of disconnecting and reconnecting lines and their SRs is not investigated. However, it can be confirmed that it is necessary to disconnect SRs of long cables that are taken out of service.

The authors of [22] propose a method to calculate the cable length required to compensate inductive OHLs in mixed-line configurations. This is not investigated in this thesis, as the entire OHL base system is replaced by an equivalent cable system. However, it is found that under-compensation of cables improve V, P -load-ability, by allowing reactive power to be supplied nearer inductive loads and compensation of line inductance. This effect is similar to finding an optimal under-compensation degree (or cable length), which matches the reactive power demand locally in the network.

In agreement, the authors of [41] and [42] conclude that under-compensation may be beneficial in the case of short cable lines. It is argued how SRs with tap changing ability can be used to regulate the voltage, by letting the cables supply reactive power. However the analysis is performed for steady-state analysis and load-ability, and is not extended to large-disturbance.

The authors of [32] seek to optimize the location and size of dynamic reactive power compensation. The method presented is based on identifying the network node displaying the weakest voltage trajectories for various disturbances. The authors argue how compensating the weakest point entail the largest overall voltage improvement of the network by indirect improvement the neighbouring nodes. Although intuitive, this effect is confirmed in the study of SR-switching presented in this thesis, where immediate compensation in the area of lowest voltage is most effective for the tested cases.

The work done in [32] focuses on FACTS devices. However, a similar method could be adopted in future work in regards to fast tap-changing and switching of SRs.

In this thesis the voltage stability is assessed by comparing voltage trajectories against an under-voltage limit and by steady state analysis of V, P and Q, V -characteristics. An issue of this methodology is that the actual stability margins, of the various study cases and line parameters, are undefined for large-disturbances. In other words, the methods used do not provide a comparable index which provides information about the so called distance to instability. The authors of [34] compare several stability indices based on analysing the power flow Jacobian and eigenvalues, and propose a new improved index. The proposed method is designed for large-disturbance and utilizes dV/dQ to identify nodes where the voltage is most sensitive to injection of reactive power (i.e. weak point) combined with time domain solutions to include electromechanical dynamics of generation and loads. Adopting the method proposed in [34], may be advantageous in future work of the topic presented in this thesis. With a well defined stability index the effects of SR-switching may be more systematically assessed and compared.

7.2 Discussion of methodology and validity of results

Modelling reflections:

1. The dynamic models of electrical machinery, excitations systems and governors are not developed specifically for this thesis. Instead, standard models from the DIGSILENT library and the included 9-bus and 39-bus systems are used. Alternatively the analysis could be based on a model of a real modern power system. In [21] the analysis is carried out using a model of the Dutch power system. The benefit of using the model of a real modern power system is up-to-date and representative model parameters of generation, transmission and loads.
2. Several dynamic power system components are not included in the models. The list includes transformer OLTC, under- and over-voltage protection, OEL and UEL, and dynamic load models such as induction machines. Especially, the voltage stability results may be affected by the lack of these models, as their presence is expected to alter the cascading voltage instability events. In this thesis voltage instability is assumed when the bus voltages does not satisfy an under-voltage limit following the given disturbance. However, an actual collapse of the system voltages is not observed.
3. In this thesis the simulations were performed for up to 30-40 seconds at the most. If slow dynamics such as OLTC and OEL/UEL are included in the models, the time frame should be included to capture a cascading event.
4. The infinite bus of the SMIB system is not modelled in the classical way, with an ideal voltage source behind a reactance. Thus, the voltage at the end bus is not kept at 1 p.u. as the external grid used has a finite short-circuit power. This should be kept in mind when comparing the results presented in this thesis to other SMIB studies.

5. The transmission lines are π -modelled such that the capacitance is lumped to the line ends. Thus, the reactive power generated by cable capacitance is supplied directly at the ends, where the shunt reactors are located. In reality the capacitance is distributed, and the reactive current flows through line inductance towards the end points. Lumped modelling is briefly discussed in Section 3.3.2. It may be relevant to test if there is a notable difference in the stability tendencies for SR-switching whether capacitance is distributed or lumped in future work.
6. The CCT analysis is performed without reactive power capability limits of the synchronous generators. The power flow (i.e. initial conditions of the RMS-simulation) is affected by the capability limits, which would reflect on the studies of over- and under-compensation of cables.
7. The CCT calculations are performed using a power-angle limit of $\delta = 179^\circ$. Another limit can be argued for and chosen, which will affect the CCT values. However, the tendencies should remain.
8. In the transient stability analysis (i.e. power angle and CCT), the composite polynomial model is not used. In the 9-bus system all loads are modelled as constant Z , while in the 39-bus the loads are modelled as constant current I for P , and constant Z for Q . These are the basic settings in the system. Changing to the composite model presented in voltage stability analysis is expected to lower the obtained CCT values.

Assumptions for equivalent cable system and shunt-reactors:

1. The shunt reactors are dimensioned to compensate 100 % of the reactive power generated by the cable capacitance. This is done without considering any deviation in system voltages between the OHL case and cable case after compensation. In [21], compensation is designed such that the bus voltages does not deviate by more than 2 % between the cable case and the OHL case. Furthermore the reactive power output of SGs does not deviate more than 1 % between the OHL case and cable case. Table F.6 and Table F.7 in Appendix F compare the reactive power output of SGs Q_o and the load bus voltages between the 39-bus system base case and the equivalent cable system. The majority of the load buses satisfy the maximum 2 % deviation criterion given in [21]. Three buses violate the criterion, but with a maximum deviation of 2.68 %. However, the Q_o deviations are significantly larger. In the worst case the reactive power output is increased by 400 %. Generally the reactive power output of most SGs is increased by 14 % to 56 % in the cable case. A reason may be the fact that the capacitance of the OHL base case is uncompensated and thus the lines are generating reactive power. A more significant impact are observed for the longer lines.
2. When replacing the OHL base system with the equivalent cable system it is assumed that one OHL is replaceable by one equivalent cable. However, due to differences in ampacity between cables and OHLs it may be necessary to have more cables in parallel in the equivalent case. The guidelines in [37] used for the creating the equivalent case do not compare the ampacity for the given OHL and cable. If more cables needs to be put in parallel it will change the network impedance and affect the results.

3. It is assumed that shunt reactors can be disconnected and reconnected instantaneously, and that all shunt reactors have the ability to tap change within few seconds. According to [20] tap changing of commercial shunt reactors has a time delay of approximately 10s. The feasibility of fast SR-switching and the technical challenges should be investigated in future work.

7.3 Future work

Following the discussion of the results and methods of this project, this section lists an overview of the future work that could be done for further studies and to provide a more comprehensive analysis of the relevant topics.

Voltage stability index

An important issue that is lacking in the project is the ability to predict large-disturbance voltage instability. This can be solved by utilizing a voltage sensitivity index that assesses stability margins of the system. Possibly an index which is based on dV/dQ method may be used as it gives indications on how much SR-switching is necessary to prevent a voltage collapse.

Location of SR placement

Only one configuration of the SR distribution is considered in the project, which is 50 % at each end of the cable. The analysis could be expanded to include more SR configurations in the system for further comparison of stability tendencies and performance.

Optimisation of SR switching

Several properties have been considered with regards to SR-switching in order to improve the overall performance of the system following a disturbance. However a general approach to the planning of switching as a function of voltage magnitude and time is not established. Therefore an optimised SR-switching strategy based on bus voltage magnitude and dV/dQ sensitivity could be explored.

Dynamic SR modelling

SR-switching is performed manually in the project by utilizing a tap event. An automated alternative could be used by implementing dynamic modelling of each SR element in DIgSILENT PowerFactory. This could be done by developing a DSL model with measured voltage as the input signal. Appropriate time delays and droop controls could be included in the modelling. This way sensitivity studies could be performed of the permissible SR-switching time delay and the size of discrete tap steps. Hence the SR-switching would be more comparable with FACTS devices.

Feasibility study of SR switching

In this project SR tap-switching is assumed to be fast acting without any restrictions on the amount of switching. This assumption is in contrast to a typical behaviour of tap-changer with long delays and limited tap-position per movement due to mechanical limitations. There may also be other implications due to fast action detrimental to the system that need to be considered.

Nonetheless results indicate that fast SR switching would improve the voltage stability performance of the system significantly therefore its feasibility and potential is worth investigating. An instant switching SR has essentially the same behaviour as FACTS devices.

Over-compensation on CCT improvement

Transient analysis show that over-compensation of cable system has an improving transient stability tendency and presumably explained by the steeper P, δ -curves which is a result of increasing over-excitation level of SGs. This explanation should be questioned with the purpose of confirming or disproving.

π modelling

All the transmission lines are modelled as π -models with lumped parameters. Distributed parameters could be used to emulate a more realistic representation of cables, especially when big voltage variations between the terminals are observed. As such the reactive power flow would be influenced significantly. Hence, it should be investigated if distribution of line parameters of long HVAC cables influence the assessed stability margins significantly compared to lumped modelling.

Realistic power system model

The stability analysis could be done on a more modern and comprehensive power system model, for example by modelling a part of the Danish transmission network. By modelling a modern power system, the influence of many existing components such as HVDC, wind turbines and PV generators would be included. Such components are typically absent in conventional standard models such as the IEEE 9-bus and 39-bus systems. Another advantage of investigating a realistic system is that the actual stability margins (such as CCT) obtained may represent the expected behaviour of the real system.

STATCOM modelling

Emphasis should be placed on valid modelling of the STATCOM. Thus making the comparison between SR-switching and STATCOM performance more conclusive.

Conclusion

8

The goal of this thesis is to investigate how undergrounding of long HVAC transmission lines affect the stability limits of multi-machine power systems. This is accomplished by simulating large-disturbance electromechanical transients in DIgSILENT PowerFactory. The stability is assessed for generic power systems by the classical definitions of transient stability and voltage stability. The analysis is initiated on a simple single-machine infinite bus system, and is expanded to the IEEE 9-bus and 39-bus multi-machine power systems. The stability performance of the OHL base case system is compared against an equivalent cable system. The main findings of the thesis are hereby presented.

Theoretical sensitivity studies of transmission line L and C are performed in a SMIB system. The theoretical observations are indicative for the comparison of OHL and equivalent cable lines including compensation. In reality the line parameters are determined by the transmission line design, and is not simply changed. The tendencies show that increasing either L or C has a transiently destabilizing effect, expressed by decreasing CCT, when the SG is initially operated at unity power factor. Increasing series parameters may improve the faulted P, δ -state due to increased fault loop impedance, similarly to increasing the fault distance. However, topological differences between pre- and post-faulted systems give rise to larger power angle oscillations as line parameters are increased. Being a pi-modelled shunt parameter, the influence of C is insensitive to fault location as opposed to L . Increasing C may reduce CCT by significantly increasing the steady-state power angle due to under-excitation of the synchronous generator. Compensation of the reactive power generated by the capacitance reduces the power angle and the CCT is improved.

Comparison of the transient stability performance in both SMIB and multi-machine systems show that the equivalent cable system with 100 % compensation has consistently longer CCT than the OHL base system, provided that the corresponding SRs of the faulted line are disconnected when the line is taken out of service. In some cases the CCT of the cable case is longer, even without switching of shunt reactors. This is a natural consequence of lower L due to the geometrical differences of OHL and equivalent cables.

Increasing the SR compensation degree has an improving effect on the CCT. This is tested up to 115 %, and is a confirmation of the findings in [19]. Inductive behaviour of the network requires increased excitation level of synchronous machines, which results in a steeper P, δ -curve and smaller power angle oscillations. However, this result is not explicitly conclusive for every aspect power system stability. In contradiction the voltage stability analysis show that under-compensation of cables improve the V, P load-ability of the network. Being under-compensated, the cables supply reactive power to line inductance, inductive loads and transformers locally.

Hence the optimal compensation degree must necessarily be a balance of both synchronous generator excitation level and the ability to supply reactive power locally in the network.

The V, P -characteristics in both 9-bus system and 39-bus system show that the 100 % compensated equivalent cable system display higher steady state load-ability than the OHL base system. Furthermore, the stability margin of the cable system is significantly larger, even when the SR compensation is increased by 25 %. Similarly Q, V -curves of the equivalent cable systems prove to be slightly steeper. Hence a high $\partial Q/\partial V$ indicating lower voltage sensitivity to changes in reactive power flow.

Dynamically the voltage stability is assessed through case studies of voltage trajectory analysis. The bus voltages following large-disturbances are evaluated against an under-voltage limit. An advantage of the cable based system is the presence of SRs. The cable based system is equipped with a significant amount of local reactive power support, by assuming that SRs can be tap changed and switched in and out of service as fast as necessary. By decreasing the shunt reactance during an electromechanical transient, the large amount of capacitive current generated by the cables is injected into the network inductance and thereby imposing a voltage.

It is shown for various cases that SR-switching can improve voltage trajectories to satisfy the under-voltage limit. This ability is unavailable in the OHL base system, where compensation for steady state operation is unnecessary. However, the real question is how to generalize the planning of SR-switching for large-disturbance events. Three different properties of SR-switching are investigated through case studies: Amount, location and timing.

It is concluded that the SR-switching should be performed progressively to reduce the risk of transient over-voltages. A smooth voltage recovery can be achieved by sequentially switching the buses measuring the lowest voltages. The overall system improvement should be considered and not limited to the lowest voltage nodes. Distributing the amount of SR-switching among multiple buses and areas reduce voltage deviations and produce a more uniform voltage characteristic. The amount of SR-switching necessary should be based on the magnitude of the post-disturbed voltage. However, the results of SR-switching presented in this thesis only bring indications towards improving the voltage trajectory. Further work is required in order to generalize and quantify the properties of SR-switching.

Lastly it is shown how SR-switching may reduce the need of dynamic voltage regulation in the form of FACTS. By performing SR-switching the necessary capacity of STATCOMS may be significantly reduced or completely substituted.

Bibliography

- [1] “First report of power system stability,” AIEE Subcommittee on Interconnections and Stability Factors, pp. 51 – 80, 1926.
- [2] P. Kundur, Power System Stability and Control. McGraw-Hill, 1994.
- [3] P. Kundur, J. Paserba, V. Ajjarapu, G. Andersson, A. Bose, C. Canizares, N. Hatziargyriou, D. Hill, A. Stankovic, C. Taylor, T. V. Cutsem, and V. Vittal, “Definition and classification of power system stability,” IEEE Transactions on Power Systems, vol. 19, pp. 1387 – 1401, may 2004.
- [4] “Final report on the august 14, 2003 blackout in the united states and canada: Causes and recommendations,” U.S.-Canada Power System Outage Task Force, apr 2004.
- [5] REN21, “Renewables 2015 global status report,” pp. 30–32, 2015. [Online]. Available: http://www.ren21.net/wp-content/uploads/2015/07/REN12-GSR2015_Onlinebook_low1.pdf
- [6] D. Gautam, V. Vittal, and T. Harbour, “Impact of Increased Penetration of DFIG-Based Wind Turbine Generators on Transient and Small Signal Stability of Power Systems,” IEEE Transactions on Power Systems, vol. 24, pp. 1426 – 1434, aug 2009.
- [7] ing.dk, “Et blaesende 2015 gav rekord i vindkraft,” Ingenioeren, January 2016. [Online]. Available: <http://ing.dk/artikel/et-blaesende-2015-gav-rekord-i-vindkraft-181552>
- [8] S. Eftekharnejad, V. Vittal, G. T. Heydt, B. Keel, and J. Loehr, “Impact of Increased Penetration of Photovoltaic Generationon Power Systems,” IEEE Transactions on Power Systems, vol. 28, pp. 893 – 901, may 2013.
- [9] Energinet.dk, “Cable to the Netherlands - COBRACable,” www.energinet.dk, jun 2015. [Online]. Available: <https://www.energinet.dk/EN/ANLAEG-OG-PROJEKTER/Anlaegsprojekter-el/Kabel-til-Holland-COBRA/Sider/Kabel-til-Holland-COBRA.aspx>
- [10] Nationalgrid and Energinet.dk, “Vikinglink,” www.viking-link.com, feb 2016. [Online]. Available: <http://viking-link.com/the-project/>
- [11] Energinet.dk, “Tennet and Energinet.dk to reinforce electricity connection across the Danish-German border,” www.energinet.dk, apr 2015. [Online]. Available: <http://energinet.dk/EN/ANLAEG-OG-PROJEKTER/Nyheder/Sider/TenneT-og-Energinet-dk-vil-forstaerke-el-forbindelse-over-tysk-dansk-graense.aspx>
- [12] Energinet.dk, “Kriegers Flak: Combined Grid Solution,” www.energinet.dk, nov 2015. [Online]. Available:

<http://energinet.dk/EN/ANLAEG-OG-PROJEKTER/Anlaegsprojekter-el/Forbindelse-til-Tyskland-Kriegers-Flak-CGS/Sider/default.aspx>

- [13] L. Zhang, L. Harnefors, and H.-P. Nee, "Interconnection of Two Very Weak AC Systems by VSC-HVDC Links Using Power-Synchronization Control," IEEE Transactions on Power Systems, vol. 26, pp. 344 – 355, feb 2011.
- [14] Energinet.dk, "Netudviklingsplan 2013," vol. Dok. 46329/13, Sag 10/7196, May 2013. [Online]. Available: <http://www.energinet.dk/SiteCollectionDocuments/Danske%20dokumenter/El/Netudviklingsplan%202013.PDF>
- [15] Energinet.dk, "Kabelhandlingsplan 2013," vol. Dok. 21597/13, Sag 10/7196, May 2013. [Online]. Available: <http://www.energinet.dk/SiteCollectionDocuments/Danske%20dokumenter/El/Kabelhandlingsplan%202013.PDF>
- [16] "Statistics of AC underground cables in power networks," CIGRE Technical Brochure, vol. 338, dec 2007.
- [17] "General Guidelines for the Integration of a New Underground Cable System in the Network," CIGRE Working Group B1.19, 2004.
- [18] F. F. da Silva and C. L. Bak, Electromagnetic Transients in Power Cables. Springer, 2013.
- [19] M. G. Ippolito, F. Massaro, G. Morana, and R. Musca, "Transient Stability Assessment of SMIB System with Mixed Overhead-Cable Line - Sensitivity Analysis," Universities Power Engineering Conference (UPEC), vol. 44, sep 2009.
- [20] C.-J. Chou, C.-Y. Han, Y.-K. Wu, and C.-Y. Lee, "Study on Voltage Stability of Island Grid Supplied by Large Grid with Long Submarine Cables Considering Different Load Patterns." Utility Exhibition on Power and Energy Systems: Issues and Prospects for Asia (ICUE), sep 2011.
- [21] H. Khalilnezhad, M. Popov, J. A. Bos, and K. P. J. Jansen, "Influence of partial undergrounding on the transient stability of EHV power transmission systems," Electric Power Systems Research, vol. 131, pp. 126 – 138, 2016.
- [22] U. Karki, D. Gunasekaran, and F. Z. Peng, "Reactive Compensation of Overhead AC Transmission Lines using Underground Power Cables," Power and Energy Society General Meeting, may 2015.
- [23] P. W. Sauer and M. A. Pai, Power System Dynamics and Stability. Stipes Publishing Co., 1997.
- [24] M. W. Mustafa and M. R. Ahmad, "Transient Stability Analysis of Power System with Six-Phase Converted Transmission Line," in IEEE International Power and Energy Conference, 2006 (PECON '06), Putrajaya, Malaysia, Nov. 2006, pp. 262–266.
- [25] P. M. Anderson and A. Fouad, Power System Control and Stability. IEEE Press, 1994.

- [26] M. J. Basler and R. C. Schaefer, "Understanding of power system stability," in Pulp and Paper Industry Technical Conference, 2007. Conference Record of Annual, Williamsburg, VA, June 2007, pp. 37–47.
- [27] F. Lu and J.-L. Yu, "Using Critical Machine Couple Equal Area Criterion to Assess Multi-Machine System Stability," in Power and Energy Engineering Conference, 2009. APPEEC 2009. Asia-Pacific, Wuhan, March 2009, pp. 1–4.
- [28] N. Yorino, A. Priyadi, H. Kakui, and M. Takeshita, "A New Method for Obtaining Critical Clearing Time for Transient Stability," IEEE Transactions on Power Systems, vol. 25, pp. 1620–1626, Aug 2010.
- [29] A. Paul and N. Senroy, "Critical clearing time estimation using synchrophasor data-based equivalent dynamic model," IET Generation, Transmission and Distribution, vol. 9, pp. 609–614, Apr 2015.
- [30] L. G. W. Roberts, A. R. Champneys, K. R. W. Bell, and M. di Bernardo, "Analytical Approximations of Critical Clearing Time for Parametric Analysis of Power System Transient Stability," IEEE Journal on Emerging and Selected Topics in Circuits and Systems, vol. 5, pp. 465–476, Sept 2015.
- [31] D. K. Cheng, Field and Wave Electromagnetics. Pearson, 1989.
- [32] R. Xia, Z. Hu, and Q. Zhou, "Optimal Planning of Dynamic VAR Compensation Based on Transient Voltage Stability Analysis," POWERCON, pp. 916–921, Oct 2014.
- [33] F. A. Althowibi and M. W. Mustafa, "Voltage Stability Calculations in Power Transmission Lines: Indications and Allocations," IEEE International Conference on Power and Energy, pp. 390 – 394, dec 2010.
- [34] S. Konar, D. Chatterjee, and S. Patra, "V-Q sensitivity-based index for assessment of dynamic voltage stability of power systems," IET Generation, Transmission and Distribution, vol. 9, pp. 677–685, 2015.
- [35] N. Qin, V. Akhmatov, T. Lund, H. Abildgaard, and M. K. Jørgensen, "Voltage Stability Analysis of the Eastern Danish Power System with a High Share of Wind Energy," 10th International Workshop on Large-Scale Integration of Wind Power into Power Systems as well as on Transmission Networks for Offshore Wind Power Plants, vol. 10, oct 2011.
- [36] DIgSILENT, "DIgSILENT PowerFactory Technical Reference Documentation: Synchronous Machine, ElmSym, TypSym," www.digsilent.net, 2016. [Online]. Available: <http://www.digsilent.de/index.php/downloads.html>
- [37] "Cable Systems Electrical Characteristics," Working Group B1.30 CIGRE, apr 2013.
- [38] DIgSILENT, "DIgSILENT PowerFactory Technical Reference Documentation: General Load, ElmLod," www.digsilent.net, 2016. [Online]. Available: <http://www.digsilent.de/index.php/downloads.html>

- [39] “IEEE Guide for the Application of Protective Relays Used for Abnormal Frequency Load Shedding and Restoration,” IEEE, aug 2007.
- [40] P. Kundur, K. Morison, and B. Gao, “Practical considerations in voltage stability assessment,” IEEE Electrical Power and Energy Systems, vol. 15, pp. 205–215, 1993.
- [41] F. M. Gatta and S. Lauria, “Very long EHV cables and mixed overhead-cable lines. Steady-state operation,” Power Tech, 2005.
- [42] S. Lauria, F. M. Gatta, and L. Colla, “Shunt compensation of EHV Cables and Mixed Overhead-Cable Lines,” Power Tech, pp. 1344–1349, 2007.
- [43] IEEE Power Engineering Society, “IEEE Recommended Practice for Excitation System Models for Power System Stability Studies.” 2005.
- [44] F. M. Gonzalez-Longatt and J. L. Rueda, PowerFactory Applications for Power System Analysis. Springer, 2014.

Accounting for capacitance in SMIB systems

A

This chapter present considerations regarding expanding the classical P, δ -expression of a radial system to include transmission line capacitance.

In equation (1.1) in Section 1.3.1, the classical P, δ relationship is expressed. The model can be derived from Figure 1.5, by considering the machine transient reactance X'_d , transformer transient reactance X_T and the line impedance X_l . Traditionally lines in the SMIB system are represented as purely inductive. However, for a transmission system consisting of cables or EHV OHL, such an assumption would not be accurate for the reasons discussed in 1.5. Instead considering the system represented in Figure A.1, a better approximation is achieved by lumping the distributed capacitance to each end of the line. This approximation is inaccurate in comparison to distributed modelling, but provides a better dynamic understanding compared to complete neglect of capacitance.

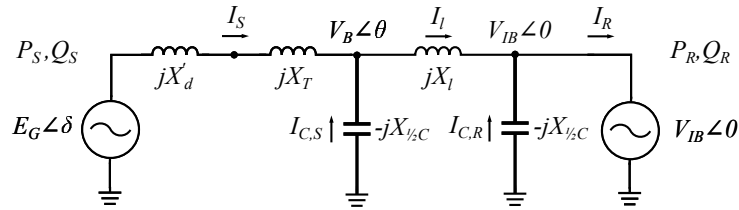


Figure A.1. Single-line diagram SMIB system with the distributed line capacitance lumped to the line ends.

By defining the sending end bus voltage magnitude V_B with angle θ , such that the power angle δ appears from the superposition of \tilde{V}_B and \tilde{E}_G with reference to the infinite bus voltage \tilde{V}_{IB} , a P, δ relationship considering capacitance can be derived following the method used for obtaining (1.1). From Figure A.1 jX'_d is the transient impedance of the SG, jX_T is the transformer impedance, $-jX_{C,1/2}$ is the impedance of the lumped capacitance at each end, and finally jX_l is the line impedance. The system is modelled as lossless such that:

$$P_S = P_R = \text{Re} \left\{ \tilde{V}_{IB} \tilde{I}_R^* \right\} \quad (\text{A.1})$$

By applying KCL and expanding to complex form, an expression for the receiving end current I_R is obtained. Since \tilde{V}_{IB} is the reference voltage, with angle 0° , it only has a real

component, such that $\tilde{V}_{IB} = V_{IB} \cos(0) + jV_{IB} \sin(0) = V_{IB}$.

$$\tilde{I}_R = \tilde{I}_S + \tilde{I}_{C,S} + \tilde{I}_{C,R} \Rightarrow \quad (\text{A.2})$$

$$\tilde{I}_R = \frac{\tilde{E}_G - \tilde{V}_B}{j(X'_d + X_T)} + \frac{0 - \tilde{V}_B}{-jX_{C,1/2}} + \frac{0 - \tilde{V}_{IB}}{-jX_{C,1/2}} \Rightarrow \quad (\text{A.3})$$

$$\tilde{I}_R = \frac{\tilde{E}_G - \tilde{V}_B}{j(X'_d + X_T)} + \frac{\tilde{V}_B}{jX_{C,1/2}} + \frac{\tilde{V}_{IB}}{jX_{C,1/2}} \quad (\text{A.4})$$

$$\begin{aligned} \tilde{I}_R = \frac{(E_G \cos(\delta) + jE_G \sin(\delta)) - (V_B \cos(\theta) + jV_B \sin(\theta))}{j(X'_d + X_T)} \\ + \frac{(V_B \cos(\theta) + jV_B \sin(\theta))}{jX_{C,1/2}} + \frac{V_{IB}}{jX_{C,1/2}} \end{aligned} \quad (\text{A.5})$$

$$\begin{aligned} \tilde{I}_R = \frac{-jE_G \cos(\delta) + E_G \sin(\delta) + jV_B \cos(\theta) - V_B \sin(\theta)}{X'_d + X_T} \\ + \frac{-jV_B \cos(\theta) + V_B \sin(\theta)}{X_{C,1/2}} + \frac{-jV_{IB}}{X_{C,1/2}} \end{aligned} \quad (\text{A.6})$$

$$P_S = \text{Re} \left\{ \tilde{V}_{IB} \tilde{I}_R \right\} \Rightarrow P_S = V_{IB} \text{Re} \left\{ \tilde{I}_R^* \right\} \quad (\text{A.7})$$

By complex conjugation and substitution of (A.6) into (A.7), the expression for $P(\delta)$ is obtained in (A.8). The expression assumes the total capacitance is equally lumped at each end, such that $X_{C,1/2} = \frac{1}{2}X_C$.

$$P_S = \frac{V_{IB}E_G \sin(\delta) - V_{IB}V_B \sin(\theta)}{X'_d + X_T} + \frac{2V_{IB}V_B \sin(\theta)}{X_C} \quad (\text{A.8})$$

At a first look it may seem odd that the expression in (A.8) is independent of the line reactance X_l . However, the dependency of X_l appears indirectly from the sending end bus voltage \tilde{V}_B as expressed in (A.9).

$$\tilde{V}_B = \tilde{V}_{IB} - \tilde{I}_R(jX_l) \quad (\text{A.9})$$

The capacitance lumped at the receiving end of the line does not have an impact on the P, δ -characteristic, as it is cancelled when taking the real part of the expression in (A.6). This is a consequence of the model, assuming that the voltage at the receiving end is constant $V_{IB} \angle 0$, despite the presence of the capacitor. However, it is reasonable that the capacitance lumped at the sending end bus, will have a greater impact on the P, δ -characteristic of the local SG in a real system.

Expanding (A.8) yields (A.10), where the term highlighted by a box is the classical $P(\delta)$ expression, with the exception of the inductive line reactance X_l . The model is still dependent on the field voltage E_G and the power angle associated with the flow of active and reactive power through X'_d and X_T . However, the two additional terms imply that the presence of the capacitor at the sending end of the line changes the non-linear power-angle relationship. The extra terms are independent of E_G , and are primarily associated with the voltage at the sending end of the line, $V_B \angle \theta$. The bus voltage $V_B \angle \theta$ is dependent on the

transfer of active and reactive power between the sending end of the line and the receiving end. In other words, $V_B \angle \theta$, is affected by the balance of injected and drawn capacitive and inductive current. Thus, changing the line parameters to include capacitance will effectively change the P, δ -relationship for any given sending and receiving end power factor.

$$P_S = \boxed{\frac{V_{IB} E_G}{X'_d + X_T} \sin(\delta)} - \frac{V_{IB} V_B}{X'_d + X_T} \sin(\theta) + \frac{2V_{IB} V_B}{X_C} \sin(\theta) \quad (\text{A.10})$$

Applying the power equation

A relevant question is how big the impact is of the two additional terms occurring when including transmission line capacitance. In order to evaluate (A.10) an example is calculated.

Table A.1 show examples of all the parameters in (A.10) in two cases of line capacitance. The values are obtained by solving the power flow for a SMIB system in DIgSILENT PowerFactory. The system is introduced in Section 3.2. The values are obtained without a parallel line topology of the SMIB, so that the system is exactly equal to the one presented in Figure A.1 for which the equation was derived. The steady state synchronous reactance X_d is used, rather than the transient reactance X'_d , as the cases are solved for steady state. The p.u. voltage values of Table A.1 are given on their respective line-to-line ratings as base values.

Table A.1. Steady state values of a SMIB system with one line in DIgSILENT PowerFactory at two different values of transmission line capacitance.

	$C = 13.3 \text{ nF/km}$	$C = 234 \text{ nF/km}$
δ [deg]	41.03	103.04
θ [deg]	2.1	2.1
E_G p.u.	1.233	0.812
V_B p.u.	1.0	1.01
V_{IB} p.u.	1.0	1.0

In order to apply (A.10) all the reactance per unit values must be referred to the SG by base change according to (A.11). The converted p.u. values are displayed in Table A.2.

$$Z_{pu,new} = Z_{pu,old} \cdot \frac{S_{b,new}}{S_{b,old}} \cdot \left(\frac{V_{b,old}}{V_{b,new}} \right)^2 \quad (\text{A.11})$$

The line-to-line voltage base of the SG is $V_{LL} = 19 \text{ kV}$, while the SG three-phase apparent power base is $S_b = 255 \text{ MVA}$. The base values of the transmission line are determined by the rated voltage 220 kV and rated current 1 kA.

Equation (A.10) computes the single-phase power output of the machine, and the voltages are line-to-neutral. The total three-phase power output can be calculated by inserting the line-to-line voltages, due to the reduction when going from (A.12) to (A.13).

Table A.2. Reactance base change by equation (A.11) on the SMIB system. The new p.u. values are referred to the SG.

Component	$S_{b,old}$	$V_{b,old}$	$X_{pu,old}$	$X_{pu,new}$
X_d	255 MVA	19 kV	2.01	2.01
X_T	500 MVA	19 kV	0.03	0.0153
X_C ($C = 13.3$ nF/km)	$\sqrt{3}$ 220 MVA	220 kV	18.84	1690.4
X_C ($C = 234$ nF/km)	$\sqrt{3}$ 220 MVA	220 kV	1.071	96.05

$$P_{S,3ph} = 3 \left(\frac{V_{IB,LL} E_{G,LL}}{\sqrt{3}\sqrt{3}(X_d + X_T)} \sin(\delta) - \frac{V_{IB,LL} V_{B,LL}}{\sqrt{3}\sqrt{3}(X_d + X_T)} \sin(\theta) + \frac{2V_{IB,LL} V_{B,LL}}{\sqrt{3}\sqrt{3}X_C} \sin(\theta) \right) \quad (\text{A.12})$$

$$P_{S,3ph} = \frac{V_{IB,LL} E_{G,LL}}{X_d + X_T} \sin(\delta) - \frac{V_{IB,LL} V_{B,LL}}{X_d + X_T} \sin(\theta) + \frac{2V_{IB,LL} V_{B,LL}}{X_C} \sin(\theta) \quad (\text{A.13})$$

The result of applying (A.13) with the values in Table A.1 and Table A.2 is shown in Table A.3. The p.u. value of each of the three terms in (A.13) is displayed together with the total active power output $P_{S,3ph}$, which is the sum of the three terms.

Table A.3. Calculated values of the terms in equation (A.10) based on the values given in Table A.1.

Term	$C = 13.3$ nF/km	$C = 234$ nF/km
(1) $\frac{V_{IB} E_G}{X_d + X_T} \sin(\delta)$	0.39965	0.39059
(2) $-\frac{V_{IB} V_B}{X_d + X_T} \sin(\theta)$	-0.018093	-0.018274
(3) $\frac{2V_{IB} V_B}{X_C} \sin(\theta)$	0.00004336	0.00077068
Total $P_{S,3ph}$	0.3816	0.37309

The active power output of the SG in PowerFactory is 100 MW. Converting the per unit power values in Table A.3 yields:

$$P_{S,3ph}(C = 13.3 \text{ nF/km}) = P_{S,3ph,pu} \cdot S_b = 0.3816 \cdot 255 \text{ MVA} = 97.308 \text{ MW} \quad (\text{A.14})$$

$$P_{S,3ph}(C = 234 \text{ nF/km}) = P_{S,3ph,pu} \cdot S_b = 0.37309 \cdot 255 \text{ MVA} = 95.138 \text{ MW} \quad (\text{A.15})$$

There is an error of approximately 3 % and 5 % on the values calculated by (A.13) compared to the actual power output in PowerFactory (100 MW). The error is bigger when the capacitance is increased to 234 nF/km. One reason for the increased error is likely to be inconsistencies between the more accurate reference frame based $dq0$ model in PowerFactory and the classical SG model. The $dq0$ model accurately represent the inductances of the electrical machinery and the flux linkages arising due to increased field current. The modified classical expression may not correctly represent the relationships between E_G and δ as the excitation is changed due to under-excitation.

Despite the error, the main importance is the relationship between the three terms of the expression. Term (1), which is the classical expression, account for the majority of the power output. Term (2) and Term (3) account for just 0.05% of the total power output, with a slight increase as the capacitance is increased. Due to the negative sign of Term (2), Term (2) and (3) have a cancelling effect on each other, and collectively contribute in a negligible decrease in active power output. The insignificance of Term (2) and Term (3), lies in the fact that Term (1) accounts of the change in δ and E_G , which is influenced by the line capacitance. The angle δ is significantly larger than θ , and the bus voltage V_B is hardly influenced as the AVR is controlling the voltage by E_G .

Conclusively, modelling of line capacitance has a negligible effect on the classical P, δ -equation. This indicates that the influence of capacitance on transient stability is likely to be indirect, by affecting the control of reactive power and voltages.

Basic voltage regulation and reactive power control of synchronous generators

B

The purpose of this appendix is to provide a basic understanding of how the reactive power output of synchronous machines is controlled with respect to the terminal voltage and how it influences the power system stability. Voltage regulation through excitation control is an essential element in power system stability studies, as it constitutes the link between transient stability and voltage stability. Thus, understanding how changes in reactive power demand affects the electromechanical behaviour of synchronous machines is important when studying the impact of cable based transmission networks and reactive power compensation on large-disturbance stability.

B.1 Control of active and reactive power

In this section is presented a brief overview of the principles behind SG active and reactive power control in relation to its excitation voltage and field current. The classical equivalent circuit of SG is repeated in Figure B.1 for illustration purpose.

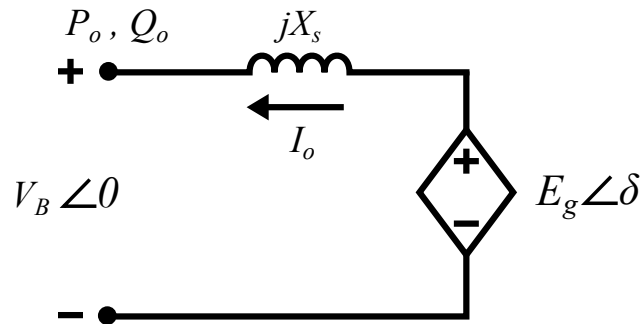


Figure B.1. Classical equivalent circuit of generator.

The excitation and terminal voltages of generators are represented by E_g and V_B while the terminal or output current is denoted by I_o in the circuit. The vector diagram of the equivalent circuit is shown in Figure B.2 for lagging power factor scenario.

The active and reactive output power of SG is expressed by equation B.1. Based on the convention used in [2] and PowerFactory, lagging power factor means SG is generating reactive power ($+Q_o$) whereas leading power factor consumes reactive power ($-Q_o$).

$$P_o = V_B I_o \cos(\theta) \quad \text{and} \quad Q_o = V_B I_o \sin(\theta) \quad (\text{B.1})$$

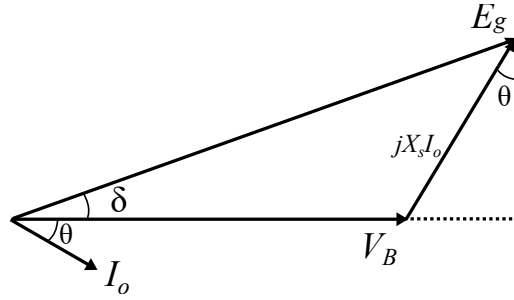


Figure B.2. Vector diagram of E_g , V_B and I_o . The power factor is lagging, so that the current is lagging the voltage by θ .

Firstly the case of unity power factor is considered, where the terminal voltage and current are in phase with one another ($\theta = 0$) and no reactive power is generated or consumed. The phasor diagram of this case is presented in Figure B.3(a). The active output power is assumed to be P_1 . Figure B.3(b) shows a lagging power factor case with the same active power P_1 while generating Q_1 of reactive power. This condition is considered to be over-excited. Lastly, the corresponding leading power factor case is presented in Figure B.3(c) with output powers P_1 and Q_2 . Q_2 is the same magnitude as Q_1 but consumed instead. The terminal voltage V_B is assumed to be the same for all cases as the voltage of the connected terminal is normally regulated.

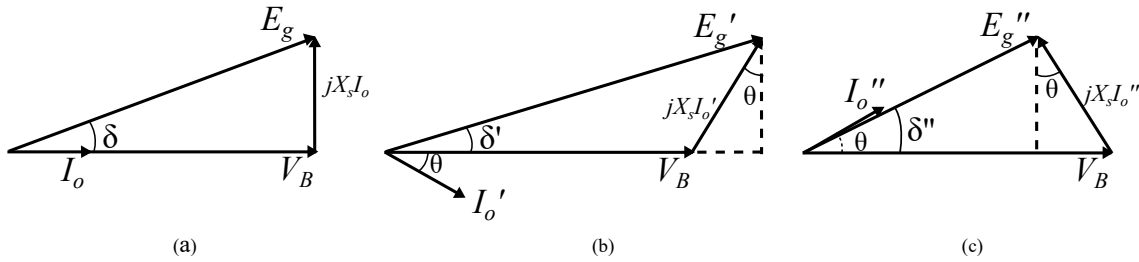


Figure B.3. Phasor diagram of three different power factors (a) Unity power factor with output power P_1 (b) Lagging power factor with output power P_1 and Q_1 (c) Leading power factor with output power P_1 and Q_2 ($-Q_1$)

According to the scaled figures, while maintaining the same active power output, the magnitude of the SG excitation voltage E_g is varying with power factor. The direction of change depends on whether reactive power is generated or absorbed by the SG. If the generator needs to produce reactive power to regulate the voltage for instance, magnitude of E_g is increased. The opposite phenomenon is observed for reactive power consumption. The behaviour of E_g is ultimately dependent on the excitation system and thereby the excitation system plays an important role in reactive power control of a generator.

An excitation system basically provides and regulates DC current to the field windings in order to produce magnetic fields [2]. The design of the system is unique for each machine and tailored specially according to the requirement of the generator and power system. A typical excitation system for a large synchronous generator consists of multiple elements including exciter, regulator and protective limiters which can be seen in Figure B.9.

The exciter is the element that is responsible for providing DC current to the field windings and thus controlling the excitation voltage. The relationship between field current I_f and excitation voltage E_g is shown in B.2, whereby magnetic saturation is neglected. M refers to the mutual inductance between stator and rotor and ω_s is synchronous speed. Both of these are constant parameters and therefore constituting a linear form of relationship.

$$E_{g,rms} = \frac{\omega_s M I_f}{\sqrt{2}} \quad (\text{B.2})$$

With equation B.2 being established, it is then possible to showcase the effects of power control on field current I_f . Figure B.4 shows the phasor diagram of two over-excited cases with a constant lagging power factor. It can be seen that an increment in output power is followed by increasing magnitude of E_g thereby I_f also rises proportionally.

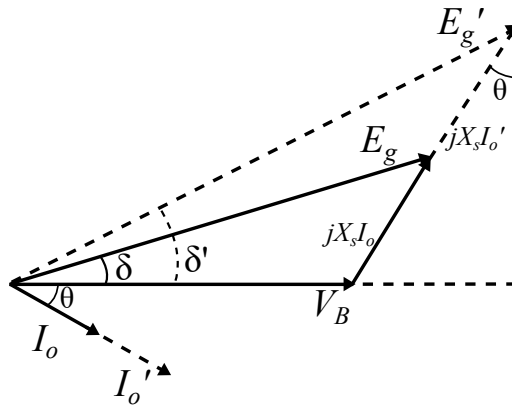


Figure B.4. Phasor diagram of constant power factor over-excitation cases. The power factor is lagging, so that the current is lagging the voltage by θ . Dotted line refers to a higher power operating state.

However for under-excited cases with a constant leading power factor the relationship is not as straightforward. Referring to Figure B.5, starting from a low operating point, increasing output magnitude would result in an initial decrease in E_g up to a minimum point. Beyond this point the magnitude of E_g would begin to increase back again together with the increment in output power. This explains the shape of the dotted red lines shown in Figure B.6. This is only observed when the generator is operating under power factor control.

As for voltage control operation where the active power is kept constant while reactive power is varied accordingly, E_g and I_f tend to increase during over-excited conditions within the operating limits and vice versa. The general behaviour of field current I_f with respect to power control of the generator can be summarized by the I_o - I_f curves presented in Figure B.6 [2]. Output current I_o is analogous to output power magnitude assuming constant terminal voltage V_B .

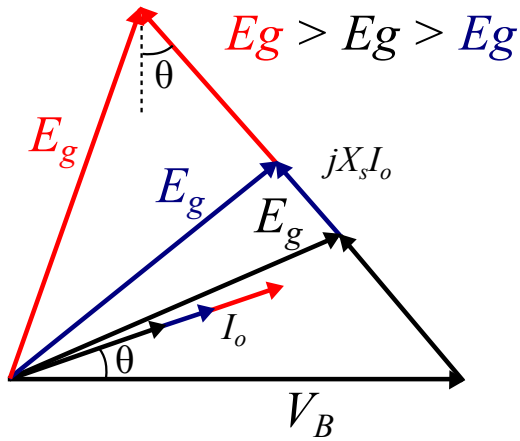


Figure B.5. Phasor diagram of constant power factor under-excitation cases. The power factor is leading, so that the current is leading the voltage by θ . Red line refers to a highest power operating state while blue is the second highest.

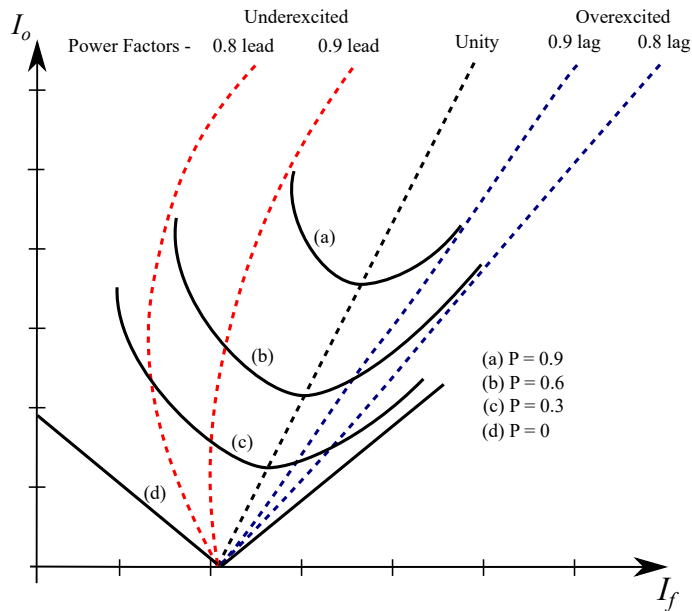


Figure B.6. I_o - I_f characteristics of the SG at four active power operating points. The power values are arbitrarily selected to illustrate the tendency of increasing active power over field current.

B.2 Automatic voltage regulator

Synchronous generators at large power stations are voltage controlled, such that the voltage at the output terminals, or a nearby bus, is regulated to 1 p.u. within specific limits. In order to achieve this, a control system is implemented, often referred to as excitation system with automatic voltage regulator (AVR). In simple terms, the measured terminal voltage is fed to the AVR, where it is compared to the set reference voltage. Based on the difference between the two values, the AVR will control the excitation voltage of the generator E_G by increasing or decreasing the field current I_f . A highly simplified diagram of the control scheme is illustrated in Figure B.7.

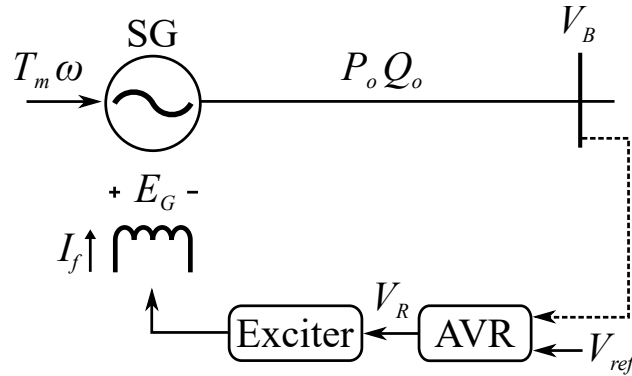


Figure B.7. Simplified diagram of a voltage controlled synchronous generator.

Up until a certain level of field excitation there exist a linear relationship between E_G and I_f by equation (B.2), and as illustrated in Figure B.8. However, due to magnetic saturation of the field windings, the excitation system is limited to a certain range [2]. The non-linearity due to saturation can be accounted for in the excitation control by methods described in [25] and [2]. But, inevitably it is a limitation to the excitation capability of the individual synchronous machine, dependent on the machine design.

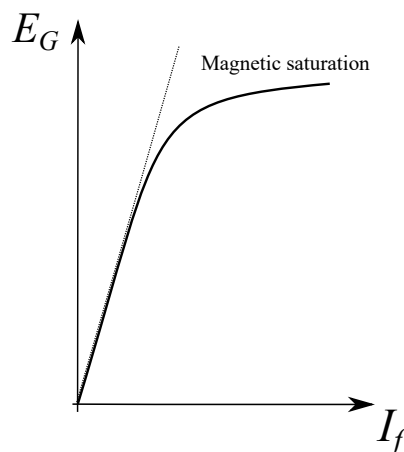


Figure B.8. Relationship between E_G and I_f . The non-linear region represents magnetic saturation of the field windings.

Figure B.9 show a more detailed, but yet simplified block diagram of a voltage regulated excitation system. The elements of the block diagram are chosen based on the most essential components described in [43]. Describing the system from the left to the right of Figure B.9:

1. The control system receives the measured terminal voltage of the synchronous generator as control signal. The signal is delayed by a first order delay, which represent any measurement time delay in the system.
2. A signal error is calculated by comparison with the reference voltage value (1 p.u.), while accounting for possible input signals from over-excitation limiter (OEL) or under-excitation limiter (UEL).
3. At the next summing junction, the signal is regulated by a stabilizing feedback V_f and a possible input from a power system stabilizer (PSS) if implemented. The feedback is a first-order lag controller, which stabilizes the AVR system by reducing any steady state error in the signal.
4. Amplifier: A first-order forward regulator with gain K_A and time constant T_A . The main function of this element is to amplify the control signal for the excitation system to change the field current I_f . The limits $V_{R,MAX}$ and $V_{R,MIN}$ incorporates limitations to the amplifier power supply or possible saturation [43].
5. The excitation system of the synchronous generator which can be designed in several ways. Examples of both DC and AC excitation systems are given in [2] and [25]. However, the main purpose is to produce the DC field current I_f in the field windings of the rotor to produce the excitation voltage E_G . The excitation has gain K_E and time constant T_E .

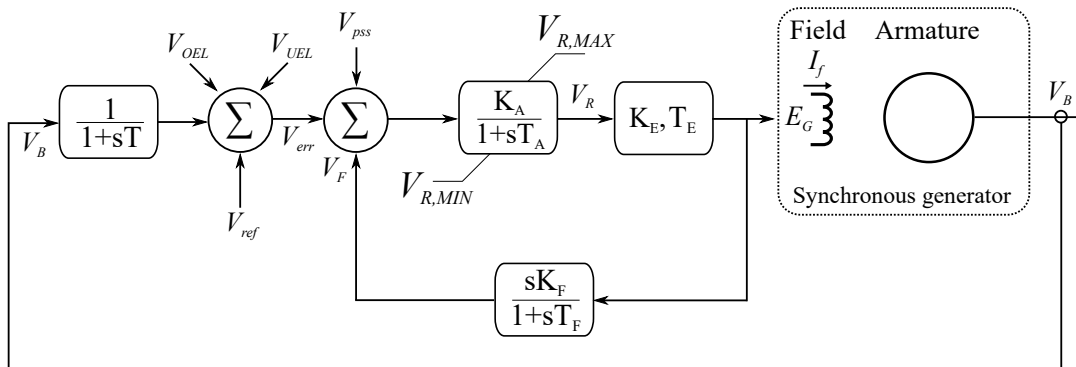


Figure B.9. AVR and excitation system with feedback control and amplifier.

B.3 Excitation system influence on power system stability

The speed and maximum level of the excitation system are of great importance for the transient stability of the power system [25]. If the voltage V_B at the terminals of the synchronous generator drops due to a faulted condition, E_G must be increased in order to supply active and reactive power to maintain voltage at a reasonable level. When the fault is removed by switching of a line, the thevenin equivalent impedance seen by the generator changes, and the excitation system must react.

Thus, the described AVR and excitation system illustrated in Figure B.9 must be able to respond as fast as possible with low time constants T_A and T_E . Standard values for T_A and T_E in the IEEEEX1 excitation system are 0.2s and 0.5s respectively, with a measurement delay 1 ms. Besides speed, the maximum possible excitation level of E_G is of great importance, also referred to as ceiling value. Imagining an excitation system which reacts instantaneously, with a total time constant of 0s, and with no limitation to E_G , then there would not exist a P, δ stability limit, and the terminal voltage V_B would be kept at 1 p.u. in any operating condition [25]. During electromechanical transients following large disturbances, the synchronous generators experience P, δ -oscillations as it is described in Section 1.3. If the excitation system is too slow, it will have a destabilizing effect on the system, as the delayed control will interact with the system oscillations. Thus, the delay of poorly designed excitation systems can in some cases result in worse oscillations, than if the SG excitation was uncontrolled [25].

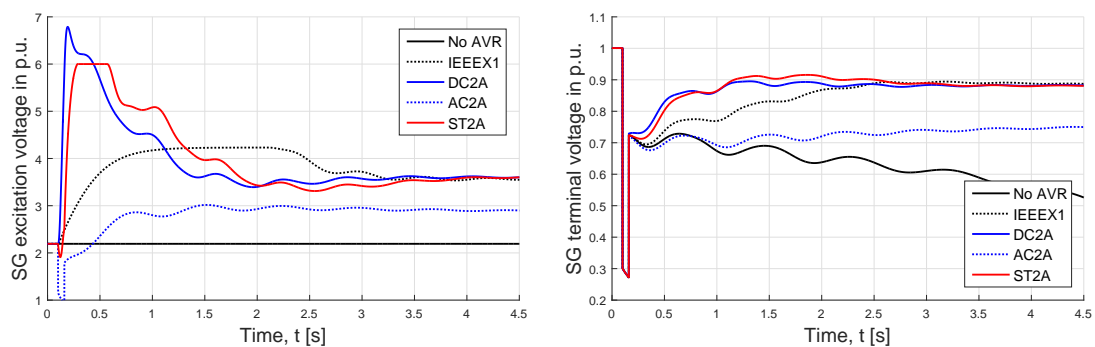


Figure B.10. Time response of E_G and V_B of SG2 following a three-phase fault on Line 4 in the IEEE 9-bus system. The fault is kept for 60 ms, after which Line 4 is taken out of service. Various cases of AVR systems are displayed according to [43].

- IEEEEX1: The 1979 IEEE type 1 (IEEEEX1) excitation system model corresponds to the 1981 IEEE type DC1 model. Field-controlled DC commutator exciters with continuously acting voltage regulator. Few new synchronous machines are being equipped with Type DC exciters, which have been superseded by AC and ST systems. However many such systems are still in service [43].
- DC2A: Field-controlled DC commutator exciters with continuously acting voltage regulators. It differs from the Type DC1A model only in the voltage regulator output limits, which are now proportional to terminal voltage.
- AC2A: These excitation systems use an AC-alternator and either stationary or rotating rectifiers to produce the DC field required [43].
- ST2A: Static excitation system model utilizing both current and voltage sources (generator terminal quantities) to control the excitation. In these excitation systems, voltage and current is transformed to an appropriate level. Rectifiers, either controlled or non-controlled, provide the necessary direct current for the generator field. For many of the static systems, exciter ceiling voltage is very high. For such systems, additional field current limiter circuits may be used to protect the exciter and the generator rotor [43].

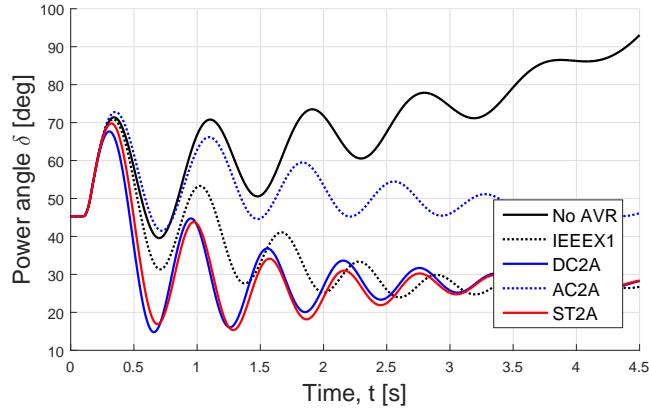


Figure B.11. Time response of δ of SG2 for the same cases as displayed in Figure B.10.

In order to illustrate the significance of excitation systems and their modelling in large-disturbance stability studies, the fault response of different AVR system are compared. The disturbance is a three-phase fault on Line 4 in the IEEE 9-bus system, while observing the terminal voltage of SG2, the excitation voltage of SG2 and the power angle of SG2. Figure B.10 display V_B and E_G responses, while Figure B.11 show δ . Each AVR system is modelled with its standard parameters in DIgSILENT PowerFactory version 15.1.6. Detailed descriptions of each individual system can be found in [43]. The purpose here is not to discuss the attributes of each system, but to recognize that there exist a significant difference in system response depending on the excitation system. Unless regulated the excitation voltage E_G remains constant during any operation condition, and the system becomes transiently unstable after a few power swings and the system voltage drops. With the AVR systems, the voltage is able to recover back to 1 p.u. Focusing on the electromechanical dynamics on the timescale from 1s to 10s it can be seen that there are significant differences in how fast the excitation systems respond in the control of E_G and how it is affecting the bus voltage and power angle.

In relation to the studies presented in this thesis, the main importance is to be aware that stability limits are affected by the excitation systems of the synchronous generators. Thus, it should be expected that changes in voltage stability limits due to undergrounding of HVAC networks and variations in reactive power compensation, are affected differently dependent on the topology of nearby synchronous generators and excitation controls.

B.4 Influence of governors and power system stabilizers compared to AVR

Besides AVR and excitation systems, synchronous generators in conventional power plants can be equipped with speed governors which controls the mechanical shaft speed of the rotor. Thus, speed governors has the ability to provide frequency control. In this thesis it is found that modelling of speed governors is important when loads are changed in dynamically. This is discussed in Section 5.6.1.

Another synchronous generator control are power system stabilizers (PSS) for the excitation systems. The power system stabilizer is a controlled input the excitation system which seeks to dampen oscillations. The typical inputs to the power system stabilizer is the electrical frequency, the shaft speed and the power output of the generator. However, as discussed in [2] the stabilizing effect of PSS is typically in regards to small-signal stability. In order to discuss the importance of the different controls, the impact of AVR, governor and PSS on the dynamic power swings are compared in Figure B.12.

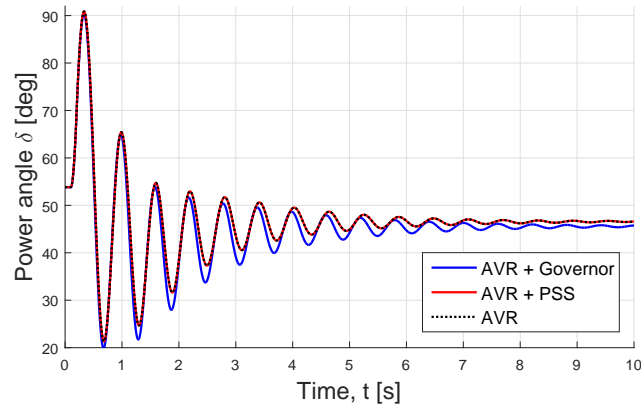


Figure B.12. Time response of δ of SG2. Comparison of a case with AVR as only control with cases of added governor and PSS.

The modelled Governor is the IEEEESGO from the DIgSILENT library, while IEEEEST is chosen as stabilizer. The figure shows that for the tested case the PSS has no influence on the power oscillations following the fault. The governor has a small impact, as the speed regulation of the shaft influences the imbalance of mechanical and electrical power which is related to the power angle oscillations. However, by comparison of Figure B.12 and Figure B.11 it is clear that the AVR is the most influential SG control on large-disturbance stability in the displayed case. It can not be excluded that cases exist where the PSS model will have an important impact, but [2] and [25] supports that the excitation system is of most importance.

Modelling parameters in 9-bus and 39-bus systems



This appendix is done for reference purpose of the test systems used in the thesis. Both 9-bus and 39-bus system models are obtained directly from PowerFactory with a certain set of element parameters. Nonetheless the only elements included in this appendix are line, synchronous generator (SG) and load.

For the line element, the parameters shown are as follow:

- **Terminal i and j:** Terminals to which the line is connected
- **Length:** Total length of the line
- **R:** AC resistance at 20 °C per-km
- **L:** Line inductance per-km
- **C:** Line capacitance per-km

As for the SG element, the parameters shown are as follow:

- **S_n and V_n:** Nominal power and voltage ratings
- **H:** Inertia time constant of the machine
- **P:** Active power dispatch
- **V_{set}:** Voltage setpoint for voltage control mode

Finally, for the load element, the parameters shown are as follow:

- **P:** Nominal active power
- **Q:** Nominal reactive power
- **Power Factor:** Nominal Power factor

C.1 9-bus system

With reference to Figure 4.1, the parameters of each line is shown in Table C.1.

Table C.2 presents the steady-state parameters and the inertia constant, H of the SGs in the system. The dynamic modelling parameters of the generator models are not included in the table. In PowerFactory version 15.2, there are two types of SG model available in the RMS simulation tab: Classical and Detailed. Detailed model includes transient and subtransient modelling (dq0) which is not included in classical model. Choosing the classical mode yields coherent results as in [25] from which the IEEE 9-bus is first introduced with classical representation of SG for transient stability study. On the other hand, the SG models used in the project are taken from version 15.1 which only includes the detailed model. Therefore there exists a difference between the results in this project and in [25] even when subjected to the same disturbance.

One important difference in the AVR design between the generators is that G1 and G3 have a very low gain K_A as shown in Figure B.7 which renders the excitation system insignificant during the transient period. It is fair to conclude that only G2 has an active excitation system.

Lastly the load parameters are presented in Table C.3.

Table C.1. Line parameters of 9-bus model

Line	Terminal i	Terminal j	Length [km]	R [Ω /km]	L [mH/km]	C [μ F/km]
Line 1	Bus 5	Bus 4	100	0.0529	1.431	0.01059
Line 2	Bus 7	Bus 5	100	0.1693	2.711	0.01841
Line 3	Bus 7	Bus 8	100	0.0449	1.212	0.00896
Line 4	Bus 8	Bus 9	100	0.0629	1.697	0.01257
Line 5	Bus 9	Bus 6	100	0.2063	2.862	0.02154
Line 6	Bus 6	Bus 4	100	0.0899	1.549	0.00951

Table C.2. Generator parameters of 9-bus model

Generator	S_n [MVA]	V_n [kV]	H [s]	P [MW]	V_{set} in p.u.
G1	247.5	16.5	4.775	163	1.04
G2	192	18.0	1.77	163	1.025
G3	128	13.8	1.175	85	1.025

Table C.3. Load parameters of 9-bus model

Load	P [MW]	Q [Mvar]	Power Factor
A	125	50	0.928 ind.
B	90	30	0.948 ind.
C	100	35	0.943 ind.

C.2 39-bus system

In a similar manner the elements of the 39-bus system is presented in this section. The elements can be located in the systems layout in Figure C.1. Table C.4 shows the line parameters whereas generators and loads are presented in Table C.2 and Table C.3 respectively.

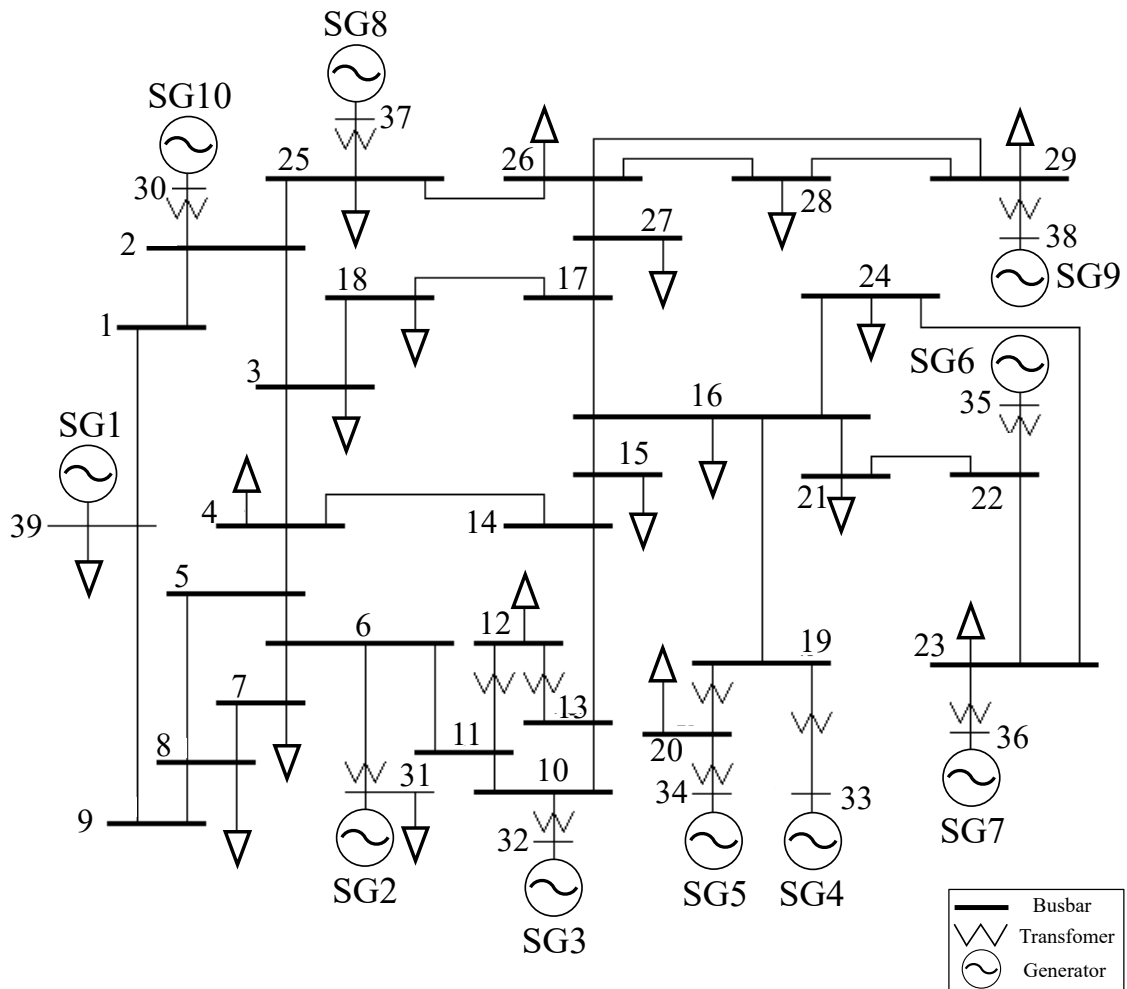


Figure C.1. IEEE 39-bus system model.

Table C.4. Line parameters of 39-bus model

Line	Terminal i	Terminal j	Length [km]	R [Ω /km]	L [mH/km]	C [μ F/km]
1-2	Bus 1	Bus 2	163.06	0.0255	0.7958	0.00954
1-39	Bus 1	Bus 39	99.188	0.0120	0.7958	0.01685
2-3	Bus 2	Bus 3	59.909	0.0258	0.7958	0.00956
2-25	Bus 2	Bus 25	34.120	0.2442	0.7958	0.00953
3-4	Bus 3	Bus 4	84.508	0.0183	0.7958	0.00583
3-18	Bus 3	Bus 18	52.768	0.0248	0.7958	0.00902
4-5	Bus 4	Bus 5	50.784	0.0187	0.7958	0.00588
4-14	Bus 4	Bus 14	51.181	0.0186	0.7958	0.00601
5-6	Bus 5	Bus 6	10.316	0.0231	0.7958	0.00937
5-8	Bus 5	Bus 8	44.436	0.0214	0.7958	0.00740
6-7	Bus 6	Bus 7	36.501	0.0196	0.7958	0.00689
6-11	Bus 6	Bus 11	32.533	0.0256	0.7958	0.00951
7-8	Bus 7	Bus 8	18.251	0.0261	0.7958	0.00952
8-9	Bus 8	Bus 9	144.02	0.0190	0.7958	0.00588
9-39	Bus 9	Bus 39	99.188	0.0120	0.7958	0.00269
10-11	Bus 10	Bus 11	17.063	0.0279	0.7958	0.00952
10-13	Bus 10	Bus 13	17.063	0.0279	0.7958	0.00952
13-14	Bus 13	Bus 14	40.072	0.0268	0.7958	0.00958
14-15	Bus 14	Bus 15	86.095	0.0249	0.7958	0.00947
15-16	Bus 15	Bus 16	37.294	0.0287	0.7958	0.01021
16-17	Bus 16	Bus 17	35.311	0.0236	0.7958	0.00846
16-19	Bus 16	Bus 19	77.366	0.0246	0.7958	0.00875
16-21	Bus 16	Bus 21	53.561	0.0178	0.7958	0.01060
16-24	Bus 16	Bus 24	23.408	0.0153	0.7958	0.00647
17-18	Bus 17	Bus 18	32.533	0.0256	0.7958	0.00903
17-27	Bus 17	Bus 27	68.638	0.0225	0.7958	0.01044
21-22	Bus 21	Bus 22	55.545	0.0171	0.7958	0.01029
22-23	Bus 22	Bus 23	38.088	0.0188	0.7958	0.01080
23-24	Bus 23	Bus 24	138.86	0.0188	0.7958	0.00579
25-26	Bus 25	Bus 26	128.15	0.0297	0.7958	0.00892
26-27	Bus 26	Bus 27	58.322	0.0286	0.7958	0.00915
26-28	Bus 26	Bus 28	188.06	0.0272	0.7958	0.00924
26-29	Bus 26	Bus 29	247.97	0.0274	0.7958	0.00924
28-29	Bus 28	Bus 29	59.909	0.0278	0.7958	0.00926

Table C.5. Generator parameters of 39-bus model

Generator	S_n [MVA]	V_n [kV]	H [s]	P [MW]	V_{set} in p.u.
SG1	10000	345	5	1000	1.03
SG2	700	16.5	4.329	520.8	0.982
SG3	800	16.5	4.475	650	0.9831
SG4	800	16.5	3.575	632	0.9972
SG5	300	16.5	4.333	254	1.0123
SG6	800	16.5	4.35	650	1.0493
SG7	700	16.5	3.771	560	1.0635
SG8	700	16.5	3.471	540	1.0278
SG9	1000	16.5	3.45	830	1.0265
SG10	1000	16.5	4.2	250	1.0475

Table C.6. Load parameters of 39-bus model

Load	P [MW]	Q [Mvar]	Power Factor
3	322	2.4	0.99997 ind.
4	500	184	0.93847 ind.
7	233.8	84.	0.94110 ind.
8	522	176.	0.94758 ind.
12	7.5	88.	0.08491 ind.
15	320	153	0.90218 ind.
16	329	32.3	0.99521 ind.
18	158	30	0.98244 ind.
20	628	103	0.98681 ind.
21	274	115	0.92207 ind.
23	247.5	84.6	0.94624 ind.
24	308.6	-92.2	0.95815 cap.
25	224	47.2	0.97851 ind.
26	139	17	0.99260 ind.
27	281	75.5	0.96574 ind.
28	206	27.6	0.99114 ind.
29	283.5	26.9	0.99552 ind.
31	9.2	4.6	0.89442 ind.
39	1104	250	0.97530 ind.

DIgSILENT Programming Language used in studies



This appendix presents the DIgSILENT Programming Language (DPL) scripts that have been used to obtain the critical clearing time in transient stability analysis of IEEE 9-bus and 39-bus system. Three DPL scripts of coding that are used extensively throughout are labelled as LineSweep, CCT and AngleLimit. LineSweep is the main script and CCT and AngleLimit are sub-scripts that are automatically executed within the main script.

LineSweep: DPL script for sweeping across all the lines in the system

```
set S_gen, L, Events; % Define set variables
double i, Step; % Define double variables
int Step_2, Step_3, p; % Define integer variables
object Initial, RMS, o_gen; % Define object variables
object o_result, o_clear;
object A, o_fault, o_trip, pEvent, fault, f_clear;
string Name, Pathway; % Define object variables

ClearOutput(); % Clear output window
EchoOff(); % Turn off graphical interface – speed up simulation

Initial = GetCaseCommand('ComInc'); % Assign initial conditions
RMS = GetCaseCommand('ComSim'); % Assign RMS simulation command

!Setting the switching event for fault
pEvent = Initial:p_event; % Assign event of initialization
Events=pEvent.GetContents(); % Assign set of events
fault = Events.FirstFilt('Fault'); % Assign fault event
f_clear = Events.FirstFilt('Clear'); % Assign fault clearing event
Pathway = OHL_Result:f_name; % Folder pathway for saving results

L=Lines.Get(); % Assign set of lines

% Loop to change location of the fault on the lines (1% and 99%)
for(p=99; p<100; p=p+98){

% Resetting dpll of all lines – description parameter of the lines
A=L.First(); % Assign A the first line in lines set
while(A){
    A:dpll=0; % Reset dpll to 0
```

```

        A:fshcloc = p;      % Set fault location
        A=L.Next(); % Proceed with next line in L set
    }
% Setting up the simulating events for finding CCT
A=L.First(); % First line
while(A){ % Loop over all lines
    fault:p_target=A; % Assign faulted line
    f_clear:p_target=A; % Assign line to be cleared
    CCT.Execute(); % Execute CCT script
    A:dpl1=CCT:t_crit; % Assign CCT to each line
    A:dpl1=A:dpl1-0.1; % Minus duration before fault
% Assign name for each result file
Name = sprintf( '%s_%i_%s_%f_%i%s', Pathway, A: fshcloc, A: loc_name,
A: dpl1, CCT: Step, '. csv' );
OHL_Result:f_name = Name; % Assign result export file name
OHL_Result.Execute(); % Export as CSV file
A=L.Next(); % Proceed with next line
}

% Print the CCTs of each line at different locations
A=L.First();
while(A){
    printf( 'CCT_of_%s_with_fault_at_%i_percent_is_%5.3f_seconds',
A: loc_name, A: fshcloc, A: dpl1);
    A=L.Next();
}
printf( '' );
printf( '_____');

OHL_Result:f_name = Pathway; % Reset path for result command
}

```

CCT: DPL script for increasing fault time to obtain CCT

```

set Events; % Define set variables
double i; % Define double variables
object Initial, RMS, Results; % Define object variables
object pEvent, fault, f_clear;
string Name; % Define string variables

EchoOff(); % Turn off user interface to speed up process

Initial = GetCaseCommand( 'ComInc' ); % Assign initial condition
RMS = GetCaseCommand( 'ComSim' ); % Assign RMS simulation
Results = Initial:p_resvar; % Assign simulation result file

% Setting the switching events for fault

```

```

pEvent = Initial:p_event; % Assign events used in initialization
Events=pEvent.GetContents(); % Assign set of events
fault = Events.FirstFilt('Fault'); % Assign fault event
f_clear = Events.FirstFilt('Clear'); % Assign fault clearing event

Step = reset; % Reset unstable case variable

% For loop to increase fault time and stop when step signal >= 1
for(i=0.25; Step<1; i=i+0.001){ % Increment of 1 ms per iteration
Initial.Execute(); % Initial condition calculated
f_clear:time = i; % Fault clearing time set to i

RMS.Execute(); % Run rms simulation
AngleLimit.Execute(Results); % Run AngleLimit script
Step = AngleLimit:unstable; % Assign no. of unstable from script

t_crit = i; % Assign critical clearing time
}

```

AngleLimit: DPL script for detecting power angle reaching 180 limit

```

int nval, nvar; % Define integer variables
int ivar, ival;
double val; % Define double variables

LoadResData(ResFile); % Load data of simulation result file
nvar= ResNvars(ResFile); % Returns number of columns/variables
nval= ResNval(ResFile,0); % Returns number of values in column 0

unstable=0; % Reset unstable count to 0
ivar=0; % Reset variable count to 0
while ({ivar<nvar}){ % Loop over all variables
for(ival=0;ival<nval;ival=ival+1){ % Loop over all data points
GetResData(val,ResFile,ival,ivar); % Read value at specific data
if ({abs(val)>179}){ % Unstable Condition Detected (ang>179)
unstable=unstable+1; % Count the no. of unstable cases
break; % Break from for loop
}
}
ivar= ivar+1; % Proceed with next variable
}

```


Pole-slip function in PowerFactory E

DIgSILENT PowerFactory has a built-in function for detection of pole-slip for transient stability analysis. However, in the work presented in this thesis it was found that this tool should be used with caution.

Prior to changing the CCT procedure in this thesis, the pole-slip function was utilized in a DPL script to calculate CCT values. The script uses a function in the synchronous machine, which changes a binary value from 0 to 1, if the machine loses synchronism. This function is recognized as "out of step detection" or "pole-slip", and is defined in the DIgSILENT documentation [36]. The DPL script runs a for-loop, which performs RMS simulations while increasing the clearing time t_c , and thus the fault duration t_f . This procedure is iterated until the pole-slip is detected, and the fault duration t_f reached in that iteration is the CCT.

An important note is that the pole-slip function is defined differently depending on the version of DIgSILENT PowerFactory. By correspondence with Stefan Weigel from the DIgSILENT support on the 5th of April 2016, the following definition for pole-slip in PowerFactory for all versions prior to 2016 was given:

"Till version 2016 the outofstep signal was calculated in a very simple, but not consistent way: If the machine angle (firel) has two zero crossings in the same direction, then the outofstep flag is set. This can mean that the outofstep flag is set in a range between 360° and 719° angle change. Dependent on the starting position of the machine angle (positive or negative). This behavior was changed with version 2016 to a more consistent way".

In the 2016 version of the software, the out of step detection (pole-slip) is detected when the rotor angle of the machine is changed 360° from its original operating point, with reference to the local reference machine (in this case the infinite bus).

Figure E.1 illustrates the difference between the 2016 version of PowerFactory and older versions. The consequence of the difference is that CCT values calculated by the pole-slip definition is dependent on the version of the software used. In the older versions of PowerFactory the initial value of δ influences the CCT directly, whereas the pole-slip detection is independent of the initial value in version 2016. In any case the CCT will always be influenced by the initial power angle δ of the generator. The reason is that the initial conditions influence the P, δ characteristics and the change of states, illustrated in Figure 1.9 in Section 1.3.1. In other words, the initial conditions should determine the CCT together with the characteristics of the disturbance. However, the purpose of the pole-slip function is to indicate when the machine is considered unstable beyond recovery.

If δ changes 360° in one direction from its initial point it should be considered unstable, and not when it reaches 719° , as it is possible in the worst case scenario.

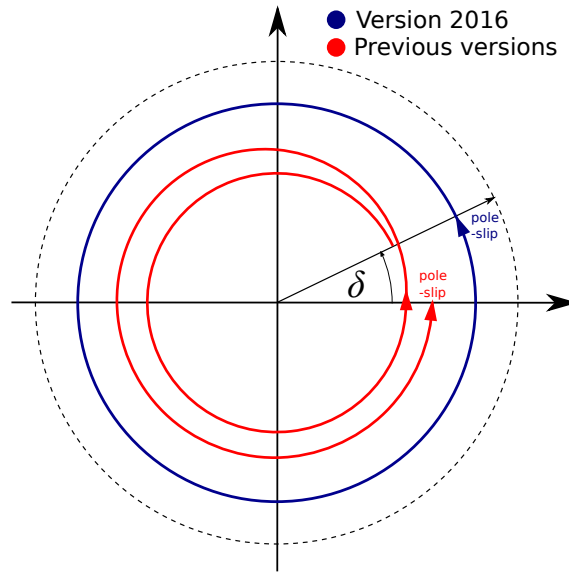


Figure E.1. Illustration of the change in δ leading to a pole-slip following a large disturbance. The δ -trajectory marked in blue leads to pole-slip in version 2016, whereas the δ -trajectory marked in red leads to pole-slip in older versions.

Problems encountered when using PowerFactory version 15.1.6

Inconsistent CCT results were observed when using the pole-slip definition for sensitivity studies of line parameters. Table E.1 show how increasing the line capacitance result in discontinuous behaviour in fault clearing time. Using the pole-slip definition, a simulation may display as transiently stable for $t_c = 0.6$ s and $t_c = 0.8$ s, but not for $t_c = 0.7$ s. This behaviour is not expected to represent real system behaviour, and is interpreted as an issue of the numerical solution and the pole-slip definition used.

Figure E.2 show the sensitivity study of C by using the pole-slip defintion in DIgSILENT PowerFactory v. 15.1.6.

An alarming observation is that going from having no line capacitance $C = 0$ nF/km, to having just $C = 1$ nF/km improves the CCT from 0.63s to 1.08s. However, further increasing the capacitance beyond this point decreases the CCT exponentially. The CCT values displayed at $C = 0$ nF/km is exactly equal to the case represented in Figure E.3 at $X_l = 0.181 \Omega/\text{km}$.

The reason behind the inconsistent results are not investigated further in this thesis due to time constraints. As explained in Chapter 3 another definition of pole-slip is used. However, users of DIgSILENT PowerFactory for stability studies should be aware of the problem observed.

Table E.1. Discontinuous behaviour of pole-slip detection

	Clearing time, t_c						
	0.5 s	0.6 s	0.7 s	0.8 s	0.9 s	1.0 s	1.1 s
Version 15.1.6							
$C = 0 \text{ nF}$	✓	✓	✗	✓	✓	✓	✗
$C = 1 \text{ nF}$	✓	✓	✗	✓	✓	✓	✗
$C = 100 \text{ nF}$	✓	✓	✓	✓	✗	✗	✗
$C = 200 \text{ nF}$	✓	✓	✗	✗	✗	✗	✗
Version 2016							
$C = 0 \text{ nF}$	✓	✗	✗	✗	✗	✗	✗
$C = 1 \text{ nF}$	✓	✗	✗	✗	✗	✗	✗
$C = 100 \text{ nF}$	✗	✗	✗	✗	✗	✗	✗
$C = 200 \text{ nF}$	✓	✓	✗	✗	✗	✗	✗

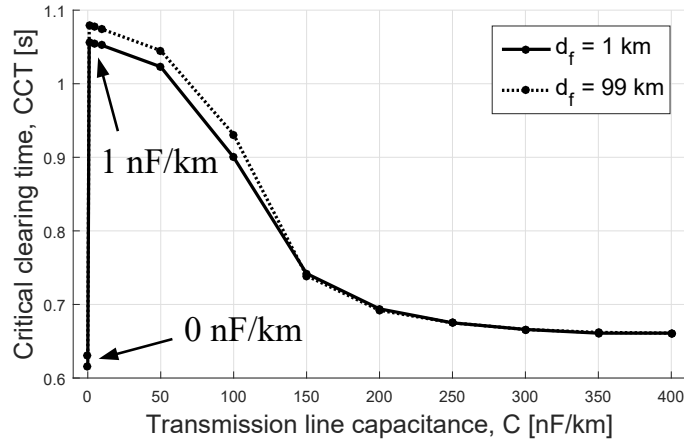


Figure E.2. CCT sensitivity of line capacitance C in the SMIB system. The line is lossless, with $X_l = 0.181 \Omega/\text{km}$. Total length of the line, $l = 100 \text{ km}$.

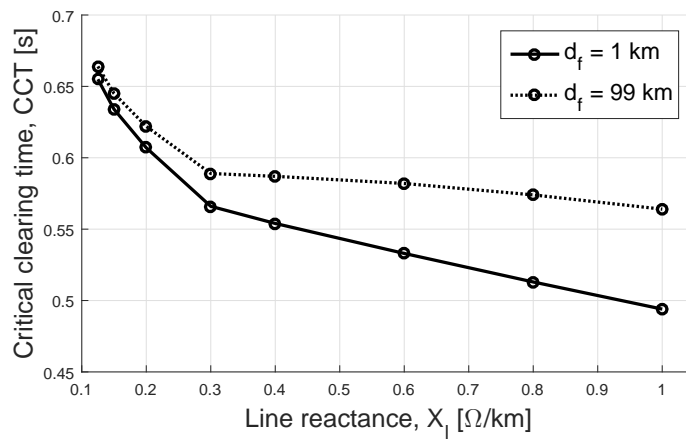


Figure E.3. CCT sensitivity of line reactance X_l in the SMIB system. The line is purely inductive, so that $R = C = G = 0$. Total length of the line, $l = 100 \text{ km}$.

PowerFactory simulation results for 9-bus and 39-bus system



In this appendix is presented the studies and simulation results that are not included in the main report and basically for ease of reference, if necessary.

Change of reference machine in 9-bus system

The effects of changing the reference machine in the 9-bus model is investigated. The motivation for this case is to compare the observations made in the base case. G1 is now replaced by G2 as the reference machine. In addition, the active and reactive power output of G1 are set to 71.6 MW and 27 Mvar respectively. These values are used to reproduce the same steady state operating conditions as in the base case.

The results are recorded and tabulated in Table F.1. The CCT values match exactly with the base case. This is because the power dispatch of each generator in any event remains identical after setting G2 as the reference machine. An example of the generators active power output from both cases is given in Figure F.1. As a result, the internal rotor angle of each generator would have a corresponding behaviour thus yielding the same angular separation mathematically and CCT values. Nevertheless a different phenomenon would occur if the reference machine behaves like a slack bus to balance out the power imbalances when the capability of the other generators is exceeded. Furthermore n_s is almost completely inverse of the base case. The reason is that in the event both G2 and G3 become unstable, the angular separation between them is small and bounded therefore if one of the generator is made the reference, the other would be detected as being stable. On the other hand, if n_s is 2 in this case, it means that the unstable occurrence in the base case is caused by G2.

Table F.1. CCT with G2 as reference machine

Faulted Line	Terminal i	CCT_1 [ms]	n_s [-]	CCT_{99} [ms]	n_s [-]
Line 1	Bus 5	248	1	197	1
Line 2	Bus 7	85	1	172	1
Line 3	Bus 7	117	2	182	2
Line 4	Bus 8	200	2	152	1
Line 5	Bus 9	127	1	228	1
Line 6	Bus 6	275	1	200	1

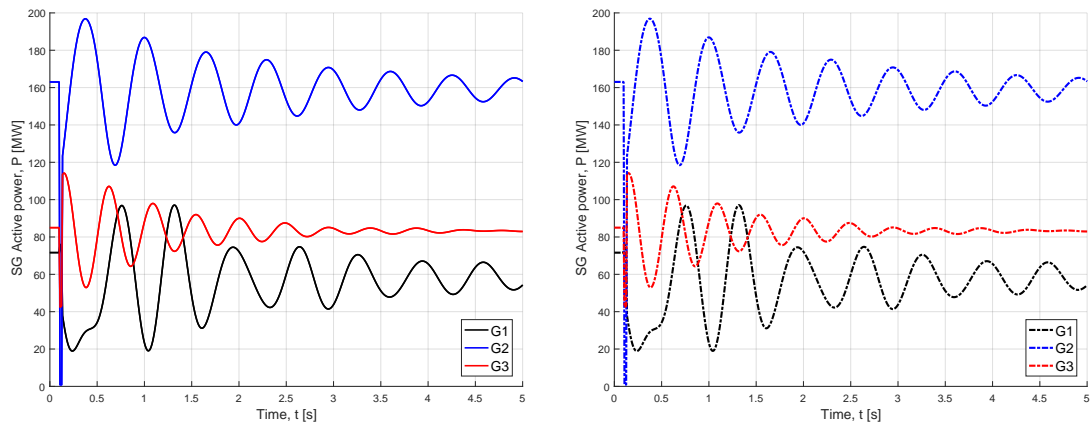


Figure F.1. SG active power output for base case [left] and the case when G2 is reference machine [right]. The fault is applied at $t_{f,0} = 0.1$ s and cleared at $t_c = 0.13$ s, so that $t_f = 0.03$ s. The fault location is at 1 % of Line 2.

Table F.2. CCT values of the base model in DIgSILENT PowerFactory.

Faulted Line	Terminal i	CCT_1 [ms]	n_s [-]	CCT_{99} [ms]	n_s [-]
1-2	Bus 1	639	1	197	1
1-39	Bus 1	630	1	851	1
2-3	Bus 2	264	1	317	2
2-25	Bus 2	158	1	115	2
3-4	Bus 3	315	2	263	1
3-18	Bus 3	315	1	307	1
4-5	Bus 4	279	2	239	2
4-14	Bus 4	287	1	284	1
5-6	Bus 5	239	2	227	2
5-8	Bus 5	253	2	300	2
6-7	Bus 6	238	2	301	2
6-11	Bus 6	236	1	234	1
7-8	Bus 7	304	1	300	2
8-9	Bus 8	298	1	848	1
9-39	Bus 9	863	1	960	1
10-11	Bus 10	217	1	238	1
10-13	Bus 10	209	1	233	1
13-14	Bus 13	224	1	254	1
14-15	Bus 14	266	1	285	2
15-16	Bus 15	272	1	173	4
16-17	Bus 16	136	2	197	1
16-19	Bus 16	191	1	358	1
16-21	Bus 16	144	1	172	2
16-24	Bus 16	183	1	224	1
17-18	Bus 17	227	1	295	1
17-27	Bus 17	241	1	201	1
21-22	Bus 21	108	2	92	2
22-23	Bus 22	202	1	188	1
23-24	Bus 23	170	2	198	1
25-26	Bus 25	206	1	125	1
26-27	Bus 26	139	1	211	1
26-28	Bus 26	110	1	102	1
26-29	Bus 26	96	1	71	1
28-29	Bus 28	68	1	53	1

Table F.3. CCT values of the base model in DIgSILENT PowerFactory with G2 as reference machine.

Faulted Line	Terminal i	CCT_1 [ms]	n_s [-]	CCT_{99} [ms]	n_s [-]
1-2	Bus 1	753	1	225	1
1-39	Bus 1	740	1	1012	8
2-3	Bus 2	278	1	318	1
2-25	Bus 2	158	1	115	2
3-4	Bus 3	315	8	263	1
3-18	Bus 3	318	1	317	1
4-5	Bus 4	279	9	239	9
4-14	Bus 4	293	8	290	1
5-6	Bus 5	239	8	227	8
5-8	Bus 5	253	1	300	1
6-7	Bus 6	238	8	301	1
6-11	Bus 6	237	9	234	1
7-8	Bus 7	304	1	300	1
8-9	Bus 8	306	1	879	1
9-39	Bus 9	896	1	961	1
10-11	Bus 10	217	1	238	1
10-13	Bus 10	209	1	233	1
13-14	Bus 13	224	1	254	1
14-15	Bus 14	266	1	298	9
15-16	Bus 15	274	1	173	1
16-17	Bus 16	138	8	197	1
16-19	Bus 16	192	3	444	1
16-21	Bus 16	145	2	172	2
16-24	Bus 16	192	8	238	8
17-18	Bus 17	227	1	295	1
17-27	Bus 17	241	1	201	1
21-22	Bus 21	108	2	92	2
22-23	Bus 22	208	8	191	1
23-24	Bus 23	170	2	208	2
25-26	Bus 25	207	1	125	1
26-27	Bus 26	139	1	211	1
26-28	Bus 26	110	1	102	1
26-29	Bus 26	96	1	71	1
28-29	Bus 28	68	1	53	1

Table F.4. Reactive power Q_c generated due to line capacitance C in the equivalent cable system in the 39-bus system at 345 kV and 50 Hz.

Faulted Line	Q_c [Mvar]
1-2	1024.75
1-39	1099.98
2-3	377.24
2-25	214.13
3-4	324.74
3-18	313.59
4-5	196.82
4-14	202.70
5-6	63.65
5-8	216.49
6-7	165.73
6-11	203.72
7-8	114.40
8-9	557.89
9-39	1759.99
10-11	106.92
10-13	106.92
13-14	252.69
14-15	536.80
15-16	250.79
16-17	196.83
16-19	445.87
16-21	373.71
16-24	99.73
17-18	193.45
17-27	471.68
21-22	376.19
22-23	270.74
23-24	529.50
25-26	752.38
26-27	351.39
26-28	1144.33
26-29	1509.20
28-29	365.21

Table F.5. CCT of compensated cable-based system. The value with the parenthesis refers to the CCT in the event where fault is at 99% of the line.

Faulted Line	Compensation degree [%] // CCT_1 (CCT_{99}) [ms]				
	95	100	105	110	115
1-2	865 (224)	970 (239)	1072 (252)	1166 (263)	1249 (271)
1-39	882 (751)	988 (804)	1090 (850)	1186 (890)	1271 (925)
2-3	280 (307)	300 (327)	316 (344)	331 (358)	342 (371)
2-25	200 (157)	217 (166)	230 (172)	240 (176)	248 (179)
3-4	310 (279)	330 (291)	347 (300)	360 (307)	372 (314)
3-18	309 (304)	329 (323)	346 (340)	361 (355)	374 (368)
4-5	295 (257)	306 (264)	315 (269)	323 (274)	329 (277)
4-14	299 (296)	311 (307)	320 (316)	328 (324)	335 (330)
5-6	263 (251)	270 (257)	275 (262)	280 (266)	283 (269)
5-8	269 (313)	276 (322)	282 (330)	286 (336)	290 (341)
6-7	256 (317)	262 (327)	267 (334)	271 (340)	274 (345)
6-11	254 (251)	260 (258)	265 (263)	268 (267)	271 (269)
7-8	320 (316)	330 (325)	337 (332)	343 (338)	348 (343)
8-9	308 (791)	318 (863)	326 (929)	332 (987)	337 (1038)
9-39	772 (787)	845 (845)	913 (894)	973 (936)	1025 (973)
10-11	242 (263)	247 (269)	251 (275)	254 (279)	257 (282)
10-13	231 (255)	236 (262)	241 (268)	244 (272)	247 (276)
13-14	244 (271)	252 (282)	258 (291)	263 (298)	267 (304)
14-15	275 (280)	285 (295)	294 (307)	301 (318)	307 (328)
15-16	280 (192)	295 (200)	307 (205)	318 (210)	327 (214)
16-17	164 (219)	174 (234)	181 (246)	187 (257)	192 (266)
16-19	208 (365)	214 (370)	219 (374)	220 (377)	224 (380)
16-21	165 (196)	174 (206)	180 (213)	185 (220)	189 (224)
16-24	201 (241)	208 (250)	213 (257)	218 (264)	221 (269)
17-18	243 (303)	255 (322)	266 (339)	275 (353)	283 (366)
17-27	248 (214)	263 (228)	275 (240)	286 (250)	295 (258)
21-22	164 (142)	174 (150)	182 (156)	189 (160)	194 (164)
22-23	219 (204)	225 (208)	230 (212)	234 (214)	236 (216)
23-24	187 (207)	194 (217)	200 (226)	205 (233)	209 (239)
25-26	209 (133)	224 (139)	234 (144)	242 (147)	248 (149)
26-27	157 (223)	164 (237)	170 (249)	175 (259)	178 (268)
26-28	31 (31)	48 (48)	63 (60)	72 (69)	79 (76)
26-29	0 (0)	0 (0)	0 (0)	0 (0)	0 (0)
28-29	98 (79)	109 (87)	118 (94)	124 (98)	129 (102)

Table F.6. Comparison of the 39-bus system SGs reactive power output Q_o in the OHL base case and the equivalent cable case.

	SG Q_o [Mvar]		relative difference, d_r %
	OHL case	100 % SR cable case	
SG1	88.15	325.6	269 %
SG2	213.16	242.85	14 %
SG3	222.52	271.19	22 %
SG4	124.27	186.42	50 %
SG5	171.86	200.35	17 %
SG6	233.96	313.79	34 %
SG7	113.99	153.50	35 %
SG8	21.68	108.70	401 %
SG9	57.74	189.91	229 %
SG10	168.06	262.43	56 %

Table F.7. Comparison of the 39-bus system load bus voltages in the OHL base case and the equivalent cable case.

Load bus no.	Load bus voltage in p.u.		relative difference, d_r %
	OHL case	100 % SR cable case	
3	1.025	1.010	-1.46 %
4	0.999	0.992	-0.7 %
7	0.993	0.988	-0.5 %
8	0.992	0.987	-0.5 %
12	0.996	0.986	-1.0 %
15	1.009	1.001	-0.79 %
16	1.026	1.014	-1.17 %
18	1.024	1.009	-1.46 %
20	0.990	0.985	-0.51 %
21	1.027	1.018	-0.88 %
23	1.042	1.031	-1.06 %
24	1.032	1.019	-1.26 %
25	1.053	1.033	-1.9 %
26	1.043	1.015	-2.68 %
27	1.029	1.008	-2.04 %
28	1.043	1.018	-2.4 %
29	1.045	1.024	-2.0 %
31	0.982	0.982	0 %
39	1.030	1.030	0 %

Simple model of a generic STATCOM in DIgSILENT PowerFactory



The static synchronous compensator (STATCOM) included in the case studies presented in Chapter 5 and Chapter 6 is a simplified generic model provided by DIgSILENT support. The model is available in the DIgSILENT Knowledge base on the following link: <http://faq.digsilent.de/faq-reader-powerfactory/do-you-have-a-model-for-a-statcom-2/searchfaq/STATCOM.html> - 19.05.2016

The purpose of this appendix is not to provide a full description of the STATCOM and its applications in power systems, but rather to present the generic model introduced in this thesis and to briefly discuss its limitations.

For further information about modelling of FACTS in DIgSILENT PowerFactory, including the STATCOM, the author of [44] has published detailed guidelines.

The simplified STATCOM model is designed for the application in stability studies with electromechanical transients. Hence, the simplified model does not include modelling of the power electronics and modelling of the converter firing angle control. The model is designed to only include the control response to the fundamental power frequency.

The simplified STATCOM operates as a controlled source of reactive power. The main purpose of the STATCOM is to provide voltage support without using large banks of capacitors and reactors in order to supply or absorb reactive power [44]. The injected or absorbed reactive power is developed within the STATCOM, which is able to generate a synchronous voltage at its terminals by the control of power electronics and a DC energy storage. Thus, the simplified STATCOM has the ability to control its capacitive or inductive current independently of system voltage, within its capability limits. A single-line diagram of the STATCOM introduced in DIgSILENT PowerFactory is shown in Figure G.1.

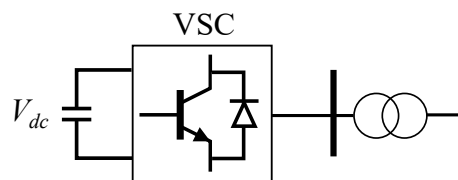


Figure G.1. Single-line diagram representation of STATCOM for power system applications.

As described in [44], when the bus voltage is below the reference voltage, the STATCOM will absorb a current that leads the voltage by 90° . In this way, the STATCOM injects reactive power into the network to increase the voltage, presenting a capacitive behaviour. When the bus voltage is above the reference voltage, the STATCOM must absorb a current that lags the voltage by 90° . Thus, the STATCOM consumes reactive power from the grid in order to decrease the bus voltage. In this case, the STATCOM presents an inductive behaviour.

G.1 Modifications to the generic model

The generic STATCOM model comes without any steady-state capability curve. A suitable capability curve is computed and added to the model as shown in Figure G.3. In addition, the control mode is also changed to "Vac-Vdc" where the AC voltage of Bus 8 and DC voltage of capacitor are regulated.

However, this capability curve is not applicable in the dynamic RMS simulation. In RMS simulation the reactive power capability of the STATCOM is limited by ceiling values to the injected or absorbed reactive currents, as shown in the block diagram in Figure G.2. When the Mvar rating of the STATCOM is changed, the ceiling values of the reactive current are correspondingly altered as the values are given in p.u. The reactive current ceiling values are ± 2.67 p.u.

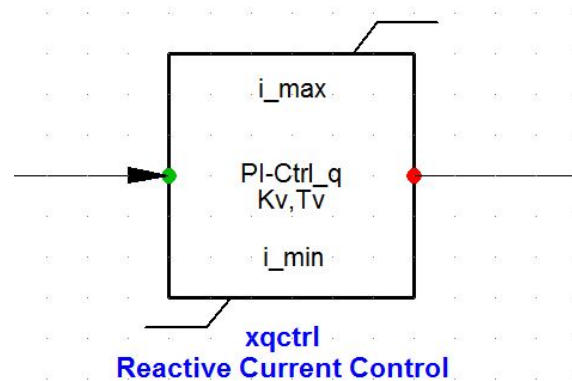


Figure G.2. STATCOM current controller block diagram in DIgSILENT PowerFactory.

The model is operating to regulate AC-voltage with a droop controller of 5% setting. This droop value will determine the final voltage operating point of the controlled terminal based upon the change in both active and reactive power at that terminal. An illustration of the V-Q characteristic curve is presented in Figure G.4. This curve is obtained from the generic PowerFactory model by varying the reactive power injected at the controlled node. The gradient of the curve is determined by the droop value.

However, the objective of the project in using STATCOM is the ability to regulate the controlled terminal at a constant voltage value within its capability limits following a power change at the terminal. Therefore the droop value is changed to zero percent and constant voltage is observed at the regulated terminal.

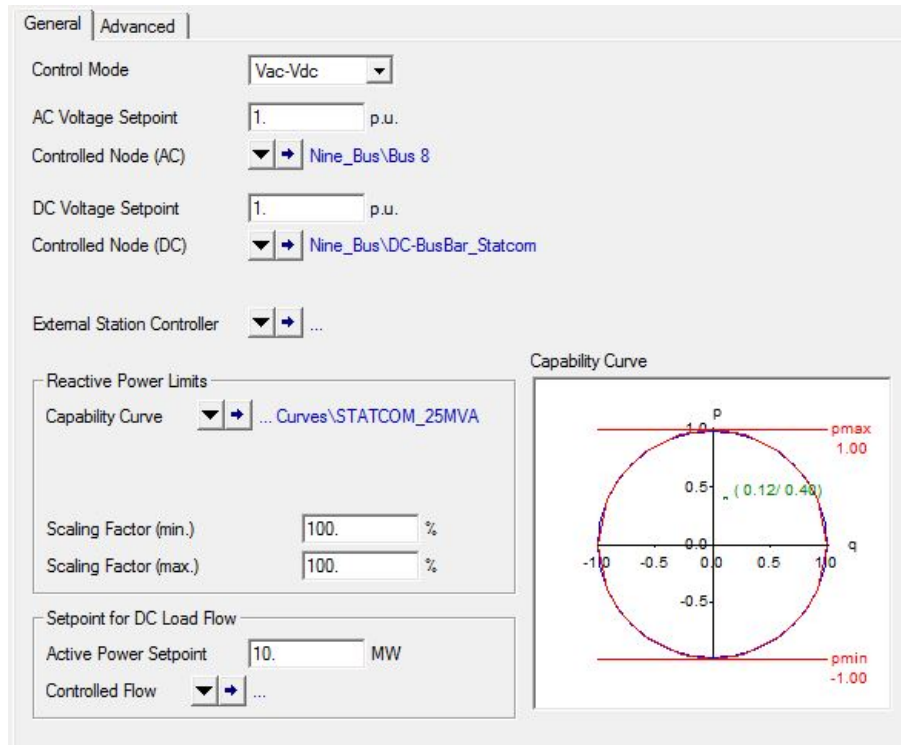


Figure G.3. Screenshot of the load flow tab in the STATCOM model.

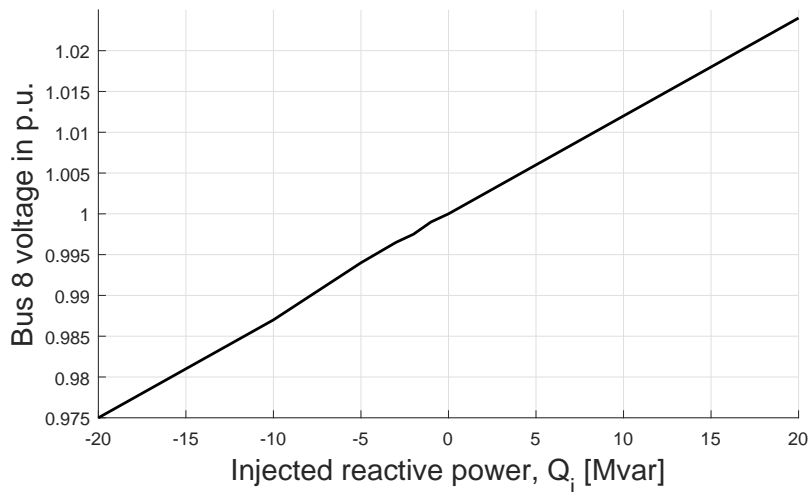


Figure G.4. V-Q characteristic .

Additional case studies of SR-switching and STATCOM H

This appendix present additional study cases of SR-switching and STATCOM similar to the one presented in Section 6.4.7.

Disturbance in Area G, observing Bus 12

Figure H.1 compares SR-switching and STATCOM for the disturbances in Area G, where the voltage at Bus 12 is observed. In support of the results show in Figure 6.23, this case reveal that the STATCOM is over-dimensioned in combination of SR-switching if it placed directly in the weakened area. To benefit from the combination, the capacity of the STATCOM could be reduced or the STATCOM could be relocated to the area border (Bus 5). The presence of the STATCOM at either locations smoothens the voltage trajectory, but the aforementioned problem of voltage spikes at the instant of SR-switching remains.

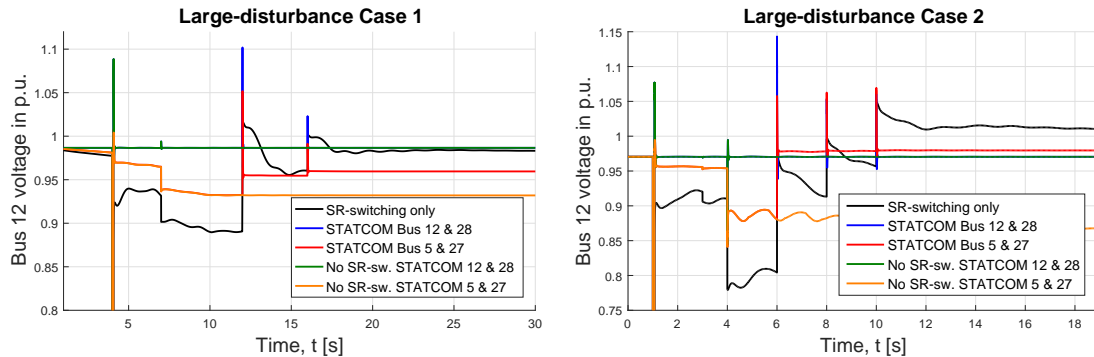


Figure H.1. Comparison of voltage trajectories at Bus 12 with STATCOMs in the network, with and without SR-switching. Left: Large-disturbance Case 1. Right: Large-disturbance Case 2.

Disturbance in Area A, observing Bus 3

Figure H.2 compares SR-switching and STATCOM for the disturbances in Area A, where the voltage at Bus 3 is observed. A STATCOM is not placed directly in Area A as it was defined as a strong area in the short-circuit analysis and by the Q, V -curves. The nearest STATCOM is at Bus 5, when the *area border* STATCOM placement is used. Thus, the most improved voltage trajectory at Bus 3 is observed when there is a STATCOM located at Bus 3.

For both disturbance Case 4 and Case 5 it is shown that the STATCOM is unable to supply sufficient reactive power without the aid of the SR-switching. In the combination of SR-switching and STATCOM the voltage trajectory is smooth and stabilizes quicker.

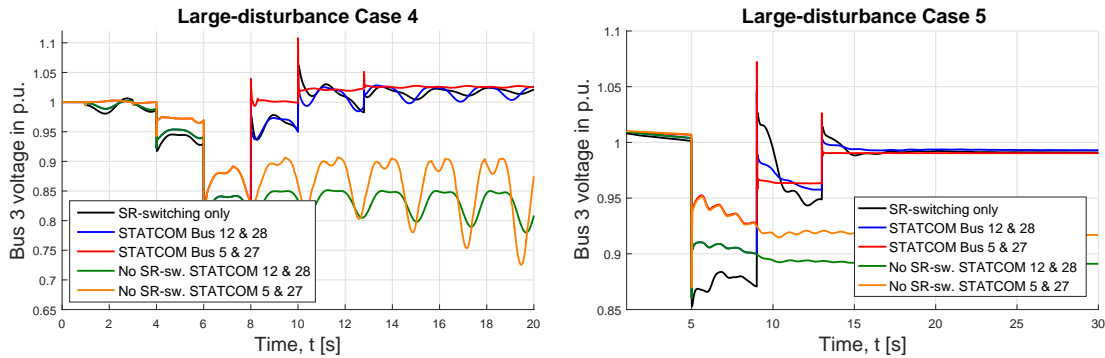


Figure H.2. Comparison of voltage trajectories at Bus 3 with STATCOMs in the network, with and without SR-switching. Left: Large-disturbance Case 4. Right: Large-disturbance Case 5.

Figure H.2(left) show that without SR-switching, disturbance Case 4 leads to transient instability. Recalling Section 6.4.4, power angle oscillations are observed, but without the STATCOMs the system finds a stable equilibrium. In other words, when STATCOMs are included in the system model, Case 4 leads to transient instability unless the shunt reactors are switched. It is highly likely that this result is due to limitations of the simple STATCOM model used for this study. However, due to time constraints of the project work presented in this thesis, this event is not investigated further. Though, caution should be paid towards the behaviour of the STATCOM model in future work.

Utilizing Q, V -characteristics for SR-switching I

This appendix present the unsolved and very basic thoughts behind dQ/dV based SR-switching. The purpose is to support the argument that further analysis of this concept should be investigated in future work.

Recalling the Q, V -curves presented in Section 6.3. The gradients dQ/dV describes how the voltage at a given bus reacts to changes in reactive power locally. Switching of SRs is analogous to injecting reactive power by letting the cables supply Q , and thus move in positive voltage direction on the Q, V -curve, as long as the system is operating above critical level.

Thus, it is relevant to discuss if there exist a relation between the dQ/dV -sensitivities of the network, and the necessary Q_{sw} required to restore voltages in a large-disturbance event. Hence, the question is if utilizing Q, V -characteristics is a possible method for developing sequential switching schemes of SRs.

It is important to note that the Q, V -curves are produced for steady-state condition where the topology of the network is intact. Thus, a difference must be expected between the voltage response to the injection of Q_i in the steady-state and the electromechanical transient. In the transient state, the Q, V -sensitivity is affected by topological changes due line switching, loss of generation and interactions of AVR systems.

Using the data presented in Figures 6.7, 6.8 and 6.9, linearised $\Delta Q/\Delta V$ -slopes are defined for three different voltage ranges. Figure I.1 show the basic concept of the linearisation.

For simplicity three ranges of voltage are defined, for which the $\Delta Q/\Delta V$ -slope are specified. Table I.1 show the $\Delta Q/\Delta V$ for the three different areas in three different voltage ranges.

Table I.1. Linearised $\Delta Q/\Delta V$ slopes based on Q, V -curves. The values indicate the necessary Q_i in Mvar to increase the voltage by 0.1 p.u.

Bus	Area	$\Delta Q/\Delta V$ [Mvar/0.1 p.u.]		
		$V_{crit} < V < 0.8$	$0.8 < V < 0.9$	$0.9 < V < 1.0$
3	A	242.42	714.29	1119.4
12	G	156.25	271.17	393.01
28	F	110.81	181.76	549.79

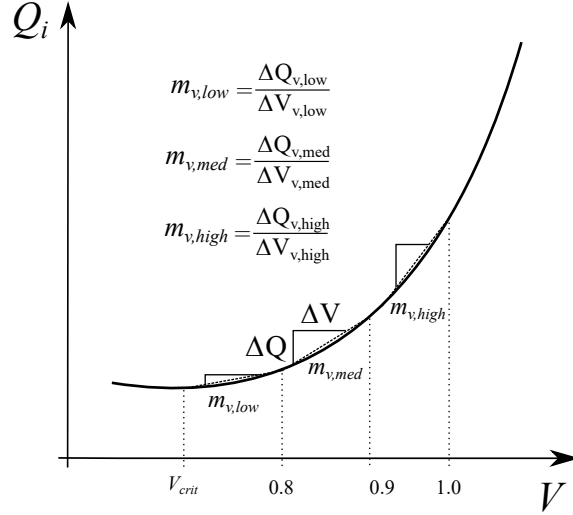


Figure I.1. Concept of linearisation of Q, V -curves to obtain $\Delta Q/\Delta V$ -slopes for specified voltage operation ranges.

To make an example, the assumption based on the Q, V -curves is that in order to change the voltage from 0.8 p.u. to 0.9 p.u. at Bus 28 in Area F, the inductive shunt reactor capacity at Bus 28 must be reduced by 181.76 Mvar by tap switching. However, accounting for increased excitation levels of nearby SGs, line-switching and load increments, the necessary Q_i required by SR-switching is likely to be different. Thus, the SR-switching and its adjustments is investigated through large-disturbance case studies.

In each of the case studies presented in Section 6.4 the total necessary sequential Q_{sw} is registered together with the post-disturbance voltages without SR-switching. Case 2 and Case 6 are excluded here as they evolve switching of buses in multiple areas.

Table I.3 present the $\Delta Q/\Delta V$ [Mvar/0.1 p.u.] values of the dynamic analysis from the case studies in comparison to the values from the Q, V linearisation. Rough assumptions were made in order to calculate $\Delta Q/\Delta V$ from the dynamic cases in a simple way. First of all it was assumed that all the buses in the area display the same voltage behaviour. Secondly it is assumed that each of the buses are compensated equally.

Comparing the values of the dynamic analysis to the steady state values reveal that they are highly different, especially in the high voltage range from 0.9 to 1.0 p.u. The method used for comparison presented here is insufficient and too simplistic to conclude if $\Delta Q/\Delta V$ -characteristics can be used for designing SR-switching.

Table I.2. Characteristics of the SR-switching in the study cases presented in Section 6.4.

Case no.	Area	No. of buses	V_{avg} area	Total Q_{sw} [Mvar]	Q_{sw} [Mvar] per bus
1	G	5	0.89	777.2	155.4
3	F	3	0.88	316.5	105.5
4	A	3	0.79	768.6	256.2
5	F	4	0.86	702.1	175.5

Table I.3. Comparison of $\Delta Q/\Delta V$ between dynamic analysis (i.e. case studies) and steady-state Q, V -characteristics.

Case no.	Area	$1 - V_{avg}$	$\Delta Q/\Delta V$ [Mvar/0.1 p.u.]			
			Dynamic analysis	$V_{crit} < V < 0.8$	$0.8 < V < 0.9$	$0.9 < V < 1.0$
1	G	0.11	141.3	156.25	271.17	393.01
3	F	0.12	87.9	110.81	181.76	549.79
4	A	0.21	122	242.42	714.29	1119.4
5	F	0.14	125.4	110.81	181.76	549.79

CD content J

The CD contains the following:

Data and plots in Matlab	File location
SMIB	\Matlab scripts\ SMIB
9bus_voltage_stab	\Matlab scripts\9-bus
9bus_transient_stab	\Matlab scripts\9-bus
39bus_voltage_stab	\Matlab scripts\39-bus
39bus_transient_stab	\Matlab scripts\39-bus

DIgSILENT PowerFactory models	File location
SMIB_eqcable	\Models
9-bus_eqcable	\Models
39-bus_eqcable	\Models
39-bus_STATCOM	\Models

Misc	File location
Report.pdf	\
Selected figures	\Images